Topology optimization

of

macro-/micro- structures for dynamic problems

（動的問題に対する　マクロ・ミクロ構造のトポロジー最適化）

Sep 2018

Zhang Xiaopeng

HIROSHIMA UNIVERSITY

Topology optimization

of

macro-/micro- structures for dynamic problems

（動的問題に対するマクロ・ミクロ構造のトポロジー最適化）

BY

Xiaopeng ZHANG

Abstract

Topology optimization is an important and challenging topic in structural design. Continuum topology optimization, as an automated conceptual design tool to achieve desired structural performance, has received an ever-increasing attention. In conventional topology optimization, it is assumed that the external loads and environmental conditions are deterministic. In practical applications, however, they usually exhibit large uncertain variability. This raises the need of the topology optimization considering load uncertainties. There are two major non-deterministic structural optimization frameworks, namely reliability-based design optimization (RBDO) and structural robust design optimization. In particular, the latter aims to generate optimal designs that are less sensitive to system variability or perform as required even in the worst-case scenarios.

This dissertation presents topology optimization methods of macrostructures and microstructures against uncertain dynamic loads, random material properties distribution, and random diffuse regions between material phases. In addition, this dissertation also investigates topology optimization of the piezoelectric structure to reduce the energy consumption of active vibration control.

In the robust topology optimization problems of structures subjected to uncertain dynamic excitations, the unknown-but-bounded dynamic loads/accelerations are described with the non-probabilistic ellipsoid convex model. The aim of the optimization problem is to minimize the absolute dynamic compliance for the worst-case loading condition. For this purpose, a generalized compliance matrix is defined to construct the objective function. To find the optimal structural layout under uncertain dynamic excitations, we first formulate the robust optimization problem into a nested double-loop one. Here, the inner-loop aims to seek the worst-case combination of the excitations, and the outer-loop optimizes the structural topology under the found worst-case excitation. To tackle the inherent difficulties associated with such

an originally nested formulation, we convert the inner-loop into an inhomogeneous eigenvalue problem using the optimality condition. Thus, the double-loop problem is reformulated into an equivalent single-loop one. This formulation ensures that the strict-sense worst-case combination of the uncertain excitations for each intermediate design be located without resorting to a time-consuming global search algorithm.

For the topology optimization problems for designing the microstructures of PnCs by considering random-field material properties, this dissertation proposed a robust topology optimization framework for achieving a wide band gap design that is insensitive to the uncertain material distribution. Herein, the spatial distribution of the material properties is first represented by a random field and then discretized into uncorrelated stochastic variables with the expansion optimal linear estimation method; stochastic band gap analysis is then conducted with polynomial chaos expansion. Furthermore, a robust topology optimization formulation of PnCs is proposed on the basis of the relative elemental density, where a weighted objective function handles the compromise of the mean value and standard deviation of the PnCs band gap. The band gap response is analyzed employing the finite element method for each sample of polynomial chaos expansion. In this context, the sensitivities of the stochastic band gap behaviors to the design variables are also derived.

The phase-field based robust topology optimization method for macrostructures and microstructures considering random diffuse-region widths between different material phases are also proposed. The diffuse regions between two material phases are assumed to satisfy a spatial Gaussian random field and discretized into uncorrelated stochastic variables with the EOLE method; then stochastic response analysis is conducted with the PCE. In the optimization formulation, the design domain is represented with the phase-field function and the explicit phase-field curve is updated by solving the Allen–Cahn equation. A weighted summation of the mean value and standard deviation of the structural dynamic performance is taken as the

objective function of the robust optimization problem. For the macrostructures design problem, three types of the dynamic performance functions are considered, including the structural dynamic compliance, the fundamental frequency or frequency gap, and the transient displacement under impact loads. In the robust microstructures design of PnCs, the weighted sum of the mean value and standard deviation of the specified band gap is considered as the objective function.

We also proposed the topology optimization of the electrode coverage over piezoelectric patches attached to a thin-shell structure to reduce the energy consumption of active vibration control under harmonic excitations. The constant gain velocity feedback control method is employed, and the structural frequency response under control is analyzed with the finite element method. In the mathematical formulation of the proposed topology optimization model, the total energy consumption of the control system is taken as the objective function, and a constraint of the maximum allowable dynamic compliance is considered. The pseudo-densities indicating the distribution of surface electrode coverage over the piezoelectric layers are chosen as the design variables, and a penalized model is employed to relate the active damping effect and these design variables. The sensitivity analysis scheme of the control energy consumption with respect to the design variables is derived with the adjoint-variable method.

The proposed optimization methods have been proved with numerical examples, some influence factors that affect the optimal solutions are also discussed. These methods may have good potentials in the mechanical engineering design for vibrating structures and the design of new acoustic metamaterials.

Acknowledgements

Contents

1 Introduction

1.1 Motivation

Optimization techniques are considered effective for enhancing the dynamic properties of vibrating structures and have been studied for several decades. Among optimization methods, topology optimization is regarded a powerful design tool that dramatically improves structural performance Traditional structural topology optimization are mostly based on deterministic assumptions, without considering the inherent uncertainties. In practical applications, however, the inherent uncertainties of the structure usually exhibit large variability and have remarkable even critical effects on the structural performance. This raises the need of the structural optimization considering uncertainties.

There are generally three types of uncertainties for non-deterministic structural optimization problems: (I) material uncertainties, it can be considered simply as uncertain parameters or random fields; (II) boundary conditions, including uncertain loads and imperfect elastic supports [1]; (III) geometry conditions, it can be considered as manufacturing errors [2-4]. These uncertainties are very common during the manufacture and use of the structures and devices.

In the structural dynamic optimization problems, most studies on macrostructures designs have been conducted for deterministic conditions. Dynamic optimization problems present more difficulties than static ones, due to e.g. local optima traps, localized eigenmodes and adjacent eigenfrequencies [5, 6]. These difficulties often result in convergence issues and large grey areas. However, in vibration/dynamic optimization problems, the structural dynamic properties can be affected by many uncertain factors of the real vibration system during its design, manufacturing, and service [17,18]. Therefore, the uncertainties in material distributions, loading conditions, and geometry boundaries usually have more remarkable effect

on the structural dynamic performances and optimal solutions than static ones. There is thus a need to propose a more realistic topology optimization method for the design of vibrating structures subject to uncertainties.

On the other hand, the microstructures design of phononic crystals have attracted more and more attention. Phononic crystals (PnCs) [7] exhibit band gap effects that can obstruct the propagation of sound and elastodynamic waves in specified frequency regimes. The development of analysis and design methods for PnCs is thus an important and challenging topic. However, in the real applications of PnCs, the uncertainties of material properties and manufacturing errors are usually inevitable. The material property uncertainty of PnCs is from the inherent material inhomogeneity and also affected by the changing of the environment. While the manufacturing errors may include the uncertainties of the boundary geometry and diffuse regions between material phases of PnCs, and it has been reported in some literatures as shown in Fig.1.1. These manufacturing errors can remarkably change the band gap prosperities of PnCs, thus considering the uncertainty of diffuse region is necessary and important in the design and optimization of PnCs. How to efficiently handle the diffuse region uncertainties of PnCs and implement the corresponding topology optimization are major tasks of this paper.

(a)　　　　(b)

(c)　　　　(d)
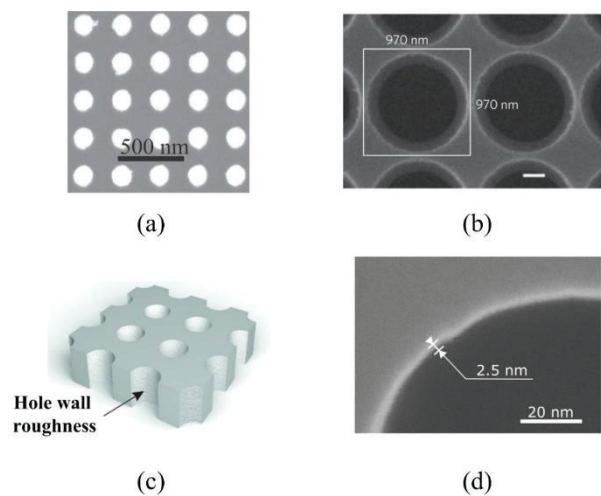
Fig.1.1 Examples of uncertainties of the manufacturing errors of PnCs. (a) Scanning electron microscope (SEM) image of Au-Si PnC [8], which shows the uncertain boundaries exist in each lattice of PnCs; (b) SEM image of a periodic porous film [9], which shows the diffuse regions exist between material phases of PnCs; (c) PnCs with a hole wall roughness of about 7nm [10], where the hole wall roughness may be considered as the uncertain diffuse region between the solid and void phases of the SI membrane type PnCs); (d) SEM image of the hole surface roughness of PnCs [11].

In short, the uncertainties should not be ignored in the structural dynamic optimization problems. This dissertation focuses on the development of robust optimization methods of macrostructures and microstructures (phononic crystals) for achieving an optimal design that has the best dynamic performance and is insensitive to the uncertain variations.

1.2 Continuum structural topology optimization

1.2.1 Development of structural topology optimization

The structural optimization problems usually can be divided into three categories: size optimization, shape optimization, and topology optimization, as shown in Fig.1.2. The study of topology optimization problems first began from the study of the optimal design of truss structures. At the beginning of the 20th century, Michell [12] used analytical methods to optimize the topological configuration of truss structures under stress constraints and proposed the Michell truss and corresponding optimization criterions. This work opened the prelude to the topology optimization.
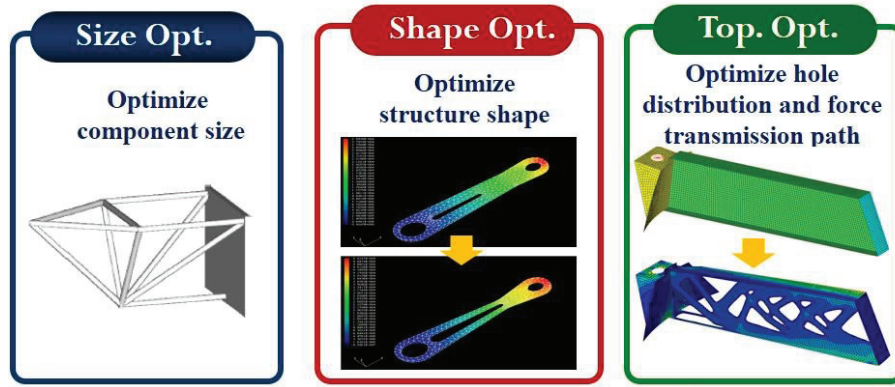
Fig.1.2. Three categories of structural optimization: sizing optimization; shape optimization; topology optimization.

Continuum topology optimization began in the early 1980s, Cheng and Olhoff [13] studied the minimum compliance optimization of solid plates, they first introduced the concept of microstructures into structural topology optimization and achieved the optimal distribution of stiffeners of a variable thickness plate. This is a pioneering work for continuum topology optimization and has attracted the attention of a large number of researchers. In 1988, Bendsoe and Kikuchi [14] introduced the homogenization theory into the continuum topology optimization and proposed homogenization method. In the following years, several popular topology optimization approaches have been developed, including SIMP (Solid Isotropic Material Penalization) method [15], ESO (Evolutionary Structural Optimization) method [16], Level-set method [17, 18], Phase-field method [19, 20], MMC (Moving Morphable Components) method [20, 21] and so on. These methods have been successfully applied to a wide range of structural and multidisciplinary design problems. The detailed introduction and review of these topology optimization methods can be found in some literatures [22-24] and will not be included in this dissertation. In our study, the density-based topology optimization approach (including SIMP and RAMP method) and the phase-field method are used to formulated the optimization problems, so these two optimization methods will be briefly

introduced in the following subsection.

1.2.2 Density-based topology optimization approach

One of the most popular density-based topology optimization approach is Simplified Isotropic Material with Penalization (SIMP) method, which is proposed by Bendsøe [15] and Zhou and Rozvany [25]. In the SIMP method. In this method, the core of this method is to establish a power-law penalty relationship between element density and Young's modulus, it is usually expressed as:

$$E(\rho_i) = \rho_i^p E_0, \tag{1.1}$$

where p is the penalty factor and E_0 is the Young's modulus of the solid material. Usually the penalty factor is suggested to be taken as $p = 3$, the penalty relationship between element density and Young's modulus is illustrated in Fig.1.3.
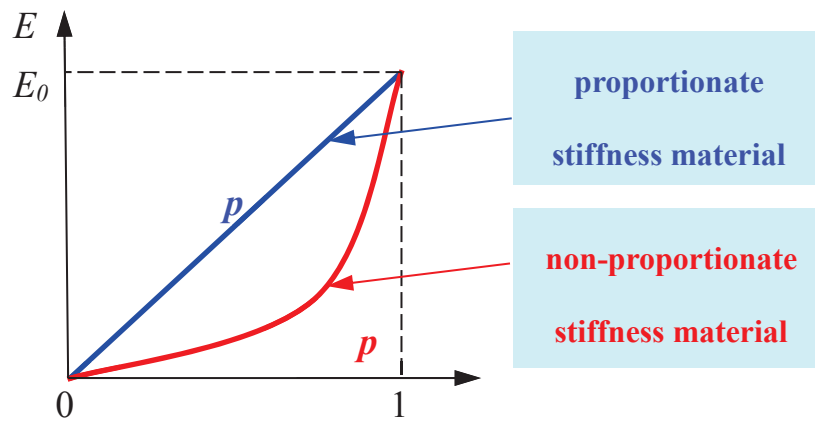
Fig.1.3 Penalty relationship between element density and Young's modulus in SIMP method.

The original intention of the SIMP method is just to reduce the complexity of the homogenization method and make the optimization easier to get a convergence to a 0-1 solution. In the following years, some studies are carried out to complete the theoretical basis of the SIMP method. For example, Bendsøe and Sigmund [26] provided a physical justification of SIMP method. Petersson [27] proved that the topology optimization problem with the compliance objective is a convex problem with a unique solution when the penalty factor $p = 1$. Jog and Haber [28] the essential reason for the checkerboard phenomenon is that the stiffness of the elements with checkerboard pattern is overestimated in numerical modeling. Haber [29] proposed perimeter constraints control method and Sigmund [30] founded a well-known sensitivity filter technique to prevent checkerboard formation and mesh dependency of the optimal solution. In recent years, more and more researches on structural topology optimization problems based on SIMP method have been conducted., and the SIMP method has been applied to the optimization problems of different fields [31].

During the development of SIMP method, some researchers also devoted to propose some different forms of density interpolation schemes. Herein, Rational Approximation of Material Properties (RAMP) [32] is a popular interpolation scheme, the penalty relationship between element density and Young's modulus based on RAMP method can be given as:

$$E\left(\rho_e\right) = E_{\text{void}} + \frac{\rho_e}{1 + p_{\text{E}}(1 - \rho_e)}(E_{\text{solid}} - E_{\text{void}}) \tag{1.2}$$

Where p_{E} is the penalty factor. The original intention of RAMP method is to reduce the non-convex nature brought by SIMP method. The main difference between the RAMP method and the SIMP method is that when $\rho_i = 0$, RAMP method can still provide a non-zero gradient, this may let the optimization problem easier to get a convergence.

On the other hand, the conventional power-law penalization model in the SIMP method

may lead to spurious local vibration modes due to inconsistent penalization of the stiffness and the mass matrices [33]. It has been shown that the RAMP model [34] is capable of removing localized vibration modes. The essential reason of the RAMP method can avoid localized vibration modes is that ratio between penalization on mass and stiffness is still a limited value even when the relative density ρ_e is near to zero. The ratio between penalization on mass and stiffness when $E_{void}=10^{-3}E_{solid}$ and $E_{void}=10^{-3}E_{solid}$ are illustrated in Fig.1.4.
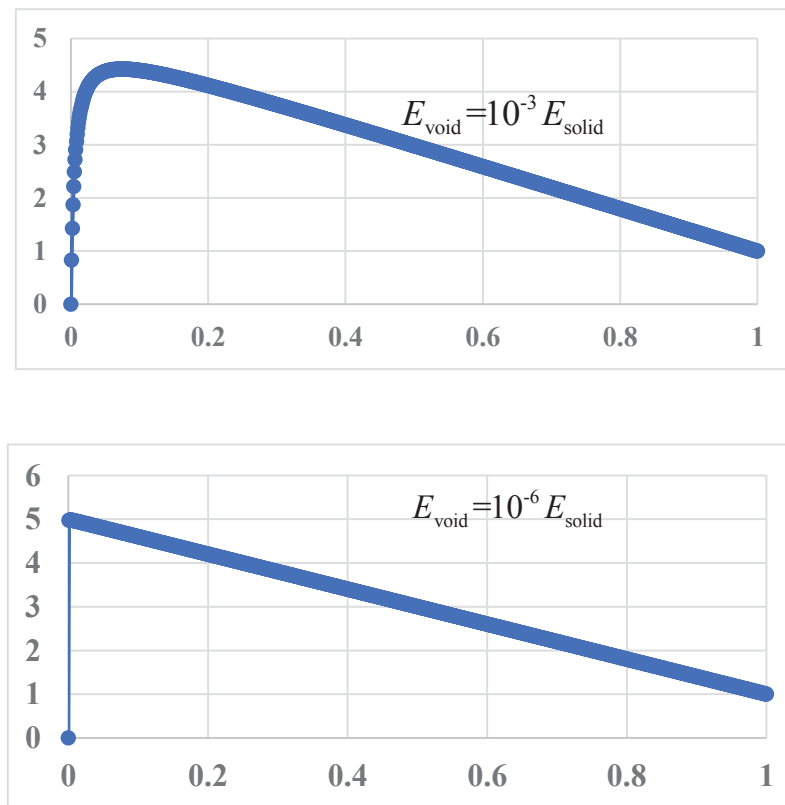
Fig.1.4 Ratio between penalization on mass and stiffness in RAMP method.

1.2.3 Phase-field based topology optimization method

The phase-field method, which was first proposed by Cahn and Hilliard [34], can handle the motion relating to domain states and shapes. A phase-field-based topology optimization method has been proposed [7,35–37] and applied to structural and multi-physics design

problems. Recently, Gain and Paulino [38] employed a fully unstructured polygonal finite element mesh in implementing a phase-field method for structural topology optimization. Jeong et al. [39] developed a stress-constrained topology optimization method using the phase-field model to represent topological changes. Garcke et al. [40] proposed a phase-field-based topology optimization method of finding optimal shapes of fluid domains in stationary incompressible Navier–Stokes problems. Xia et al. [41] first considered topology optimization problems of composites accounting for the complete fracturing process, using the phase-field method to approximately represent propagating cracks. Moreover, Takezawa and Kitamura [42] and Wu et al. [43] employed the phase-field-based topology optimization method for a photonic crystal metamaterial.

This section briefly introduces deterministic topology optimization with the phase-field method for structural vibration problems. More details on the phase-field method can be found in the literature [7,35,37].

In the phase-field method, the shape of the structure in the design domain is represented by two phases Ω_1 and Ω_2 and the boundary layer ξ between the two phases as shown in Fig. 1.5. The boundary layer, which is called the diffuse region, is defined by a smooth interpolation function $\phi(\chi)$ between the two phases. The whole design domain representation D ($D = \Omega_1 \cup \Omega_2 \cup \xi$) can thus be formulated with the phase-field function ϕ as

$$
\begin{cases}
\phi = 1 & \Leftrightarrow \quad \chi \in \Omega_1, \\
0 < \phi < 1 & \Leftrightarrow \quad \chi \in \xi, \\
\phi = 0 & \Leftrightarrow \quad \chi \in \Omega_2.
\end{cases}
\tag{1.3}
$$
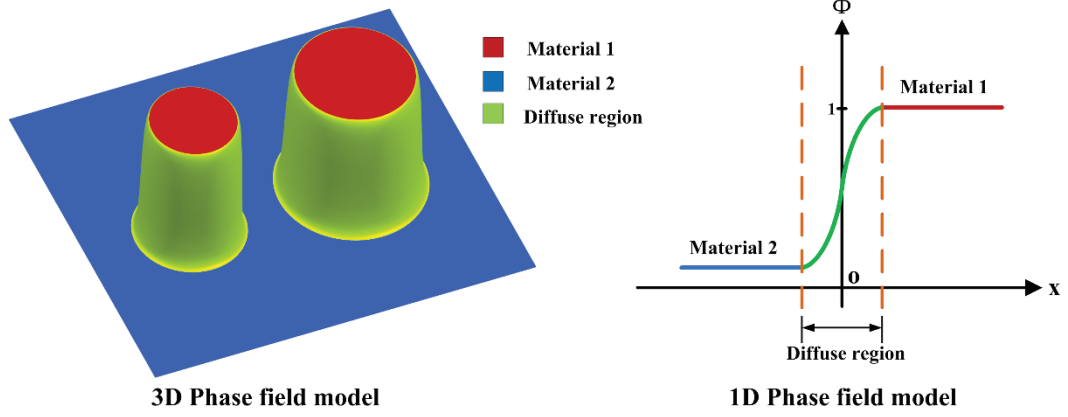
Fig. 1.5 Illustration of the phase-field model.

Here, $\phi = 1$ means that material 1 is chosen while $\phi = 0$ means that material 2 is chosen. A value within the range $0 < \phi < 1$ means that there is a diffuse region (denoted ξ), which consists of both candidate materials. With the above formulation, the state of the design domain can be determined by minimizing the Van der Walls free energy equation:

$$F(\phi) = \int_D \left(\frac{\varepsilon}{2} |\nabla \phi|^2 + \varepsilon^{-1} f(\phi) \right) d\chi, \tag{1.4}$$

where ε is a positive coefficient that determines the effect of each term and controls the width of the diffuse interface region [48,49]. In Eq. (1.4), the first term only affects the diffuse region while $f(\phi)$ in the second term represents a double-well potential function, which should be set to satisfy the conditions

$$f(0) = 0, \quad f(1) = \eta \frac{J'(\phi_t)}{\|J'(\phi_t)\|}, \quad f'(0) = f'(1) = 0, \tag{1.5}$$

where $J'(\phi_t)$ is the sensitivity of the objective function $J(\phi_t)$ with respect to the design variables ϕ at the current virtual time t, and η is a positive scaling coefficient.

To satisfy Eq. (1.5), a double-well potential function can be set as

9

$$f(\phi) = W(\chi) w(\phi) + \eta \frac{J'(\phi_t)}{\|J'(\phi_t)\|} g(\phi).\qquad(1.6)$$

As suggested in [34], the function $w(\phi)$ should satisfy $w(0) = w(1) = w'(0) = w'(1) = 0$,

and $g(\phi)$ should be a function such that $g(0) = 0$, $g(1) = 1$, and $g'(0) = g'(1) = 0$. The

notations $W(\chi)$ and $\eta J'(\phi_t)/\|J'(\phi_t)\|$ are coefficients of these functions. The coefficient

$W(\chi)$ determines the height of the wall of the double-well potential, which affects the

thickness of the diffuse region, and it is set to be $W(\chi) = 1/4$ in this study. The functions

$w(\phi)$ and $g(\phi)$ are chosen following a previous study [50]:

$$w(\phi) = \phi^2 (1-\phi)^2, \quad g(\phi) = \phi^3 (6\phi^2 - 15\phi + 10).\qquad(1.7)$$

The double-well potential function $f(\phi)$ is then expressed as

$$f(\phi) = \frac{1}{4}\phi^2 (1-\phi)^2 + \eta \frac{J'(t)}{\|J'(t)\|}(6\phi^5 - 15\phi^4 + 10\phi^3).\qquad(1.8)$$

The double-well potential $f(\phi)$ and functions $w(\phi)$ and $g(\phi)$ are sketched in Fig. 1.6.
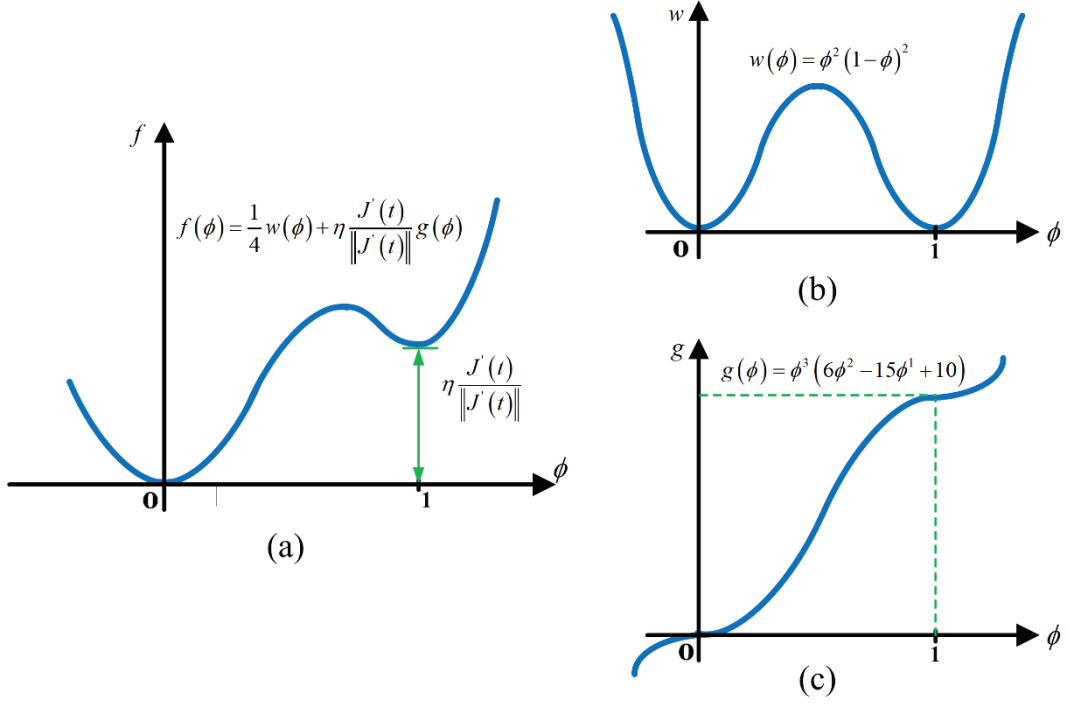
Fig. 1.6. Sketches of (a) double-well potential $f(\phi)$, (b) function $w(\phi)$, and (c) $g(\phi)$.

To minimize the objective function value $J(t)$, the optimization should proceed in the direction in which the van der Walls free energy of Eq. (1.4) is minimized, and the change in the phase-field function ϕ with respect to virtual time t is thus assumed to satisfy the equation

$$\frac{\partial \phi}{\partial t} = -M(\phi)\frac{\delta F(\phi)}{\delta \phi}, \tag{1.9}$$

where $M(\phi)$ is a variation rate. By substituting (1.4) into (1.9) and using the definition of the functional derivative, the time evolution of the phase-field function based on the Allen–Cahn equation [47] can be given as

$$\frac{\partial \phi}{\partial t} = \varepsilon^2 \nabla^2 \phi - f'(\phi). \tag{1.10}$$

Substituting (1.8) into (1.10), the time evolutional equation can be expressed as

$$\frac{\partial \phi}{\partial t} = \varepsilon^2 \nabla^2 \phi + \phi(1-\phi)\left[\phi - \frac{1}{2} - 30\eta \frac{J'(t)}{\|J'(t)\|}\phi(1-\phi)\right]. \tag{1.11}$$

The structural topologies can be expressed with an explicit phase-field curve by employing the phase-field function in Eq. (1.3). In evaluating the structural dynamic performance (e.g., the eigenfrequency or displacement response), the virtual elasticity tensor $\mathbf{D}^*(\phi)$ and the mass density $\rho^*(\phi)$ in the diffuse region are defined using the interpolation functions $k(\phi)$ and $m(\phi)$:

$$\mathbf{D}^*(\phi) = \begin{cases} \mathbf{D}^{(1)} & \text{if } \chi \in \Omega_1, \\ k(\phi)\mathbf{D}^{(1)} + (1-k(\phi))\mathbf{D}^{(2)} & (0 < k(\phi) < 1) \text{ if } \chi \in \xi, \\ \mathbf{D}^{(2)} & \text{if } \chi \in \Omega_2, \end{cases} \tag{1.12}$$

$$\rho^*(\phi) = \begin{cases} \rho^{(1)} & \text{if } \chi \in \Omega_1, \\ m(\phi)\rho^{(1)} + (1-m(\phi))\rho^{(2)} & (0 < \rho(\phi) < 1) \text{ if } \chi \in \xi, \\ \rho^{(2)} & \text{if } \chi \in \Omega_2, \end{cases} \tag{1.13}$$

with

$$k(\phi) = \phi^{p_1}, \quad m(\phi) = \phi^{p_2}, \tag{1.14}$$

where, $\mathbf{D}^{(1)}$, $\mathbf{D}^{(2)}$, $\rho^{(1)}$ and $\rho^{(2)}$ are respectively the usual elasticity matrices and mass density for each material. In Eq. (1.14), p_1 and p_2 are penalty factors, similarly to those used in the solid isotropic material with penalization method [1]. We here set $p_1 = 3$ and $p_2 = 1$ as suggested in the literature [7]. Obviously, when $\mathbf{D}^{(2)} = \mathbf{0}$ and $\rho^{(2)} = 0$, the phase of material 2 reduces to a void phase.

1.3 Macro-/micro- structures optimization design for dynamic problems

1.3.1 Macrostructures design of structural vibration problems

Since large vibrations are harmful to the structural safety and functionality, many studies have been devoted to the control of structural vibration. According to the control mechanisms, structural vibration control methods can be divided into three categories: active control, passive control, and semi-active control, the control categories and common control devices are shown in Fig. 1.7.
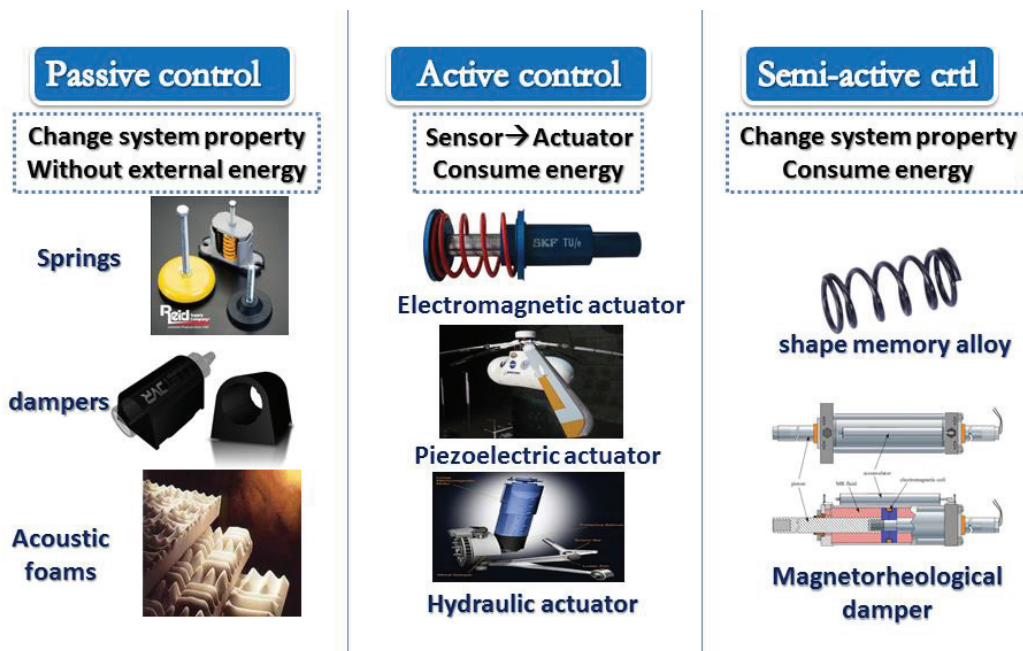
Fig. 1.7 Different control categories and control devices.

(a) Passive control

The passive control, which does not require additional control energy and only needs simple control device, can usually achieve a good control performance. Usually, the passive control devices include damping springs, damping materials, and sound-absorbing/shock absorbing foams.

Structure optimization especially topology optimization is high technology and with great potential for application in structural vibration and noise control. Here, where and how to place the material is the core problem for achieving the best dynamic performance. Taking the eigenfrequency optimization as an example: In 1965, Niordson [35] first proposed the size optimization for a beam section and this is the first attempt of the structure dynamic optimization. After that Olhoff [36] proposed the shape optimization method for the vibrating beams, and in 1992, Diaz and Kikuhci [37] introduced the topology optimization in to the eigenfrequency design for plate structures, these three works are just three major types of structural optimization methods. Nowadays, all the popular topology optimization methods, such as the homogenization method, SIMP method, level-set method, ESO method, phase-field method, and MMC method, have all successfully applied in the structural dynamic optimization [38].

Many researchers have treated dynamic topology optimization of main load-bearing structural components. For instance, Larsen et al. [39] considered the optimal material layout of plates for minimizing the global vibration level and maximizing the energy transport. Yoon [40] compared several model reduction techniques in the SIMP-based structural topology optimization for frequency responses. Du and Olhoff [41, 42] studied the topology optimization for reducing vibration level and sound radiation of bi-material structures under harmonic excitations. Shu et al. [43] investigated structural topology optimization for minimizing frequency response based on level set method, and extended the approach to problems concerning sound radiation properties of vibrating structures. Rosi et al. [44] optimized the positions of piezoelectric patches for reducing the radiated sound power of thin plates using the piezoelectric shunt damping effect. Some studies employed genetic algorithms (Xu and Jin [45] or other biologically inspired optimization approaches (Sabbatini et al. [46] for optimizing the structural configurations to reduce the dynamic responses.

With the purpose of ensuring effective vibration reduction, some studies have been devoted to the layout design of the damping layer attached to the main load-bearing structure (i.e. the host structure made of base material). Zheng et al. [47] studied the optimal placement of damping patches for minimizing the structural vibration level with the Genetic Algorithm. Chia et al. [48] employed the cellular automata algorithm to find the optimal layout of the damping layer. Kang et al. [49] proposed an artificial damping material model-based topology optimization method for minimizing the dynamic response under harmonic excitations, and this model is then extended to topology optimization of damping layers in sound radiation structures [50]. Kim [51] optimized distribution of the damping material attached to a given host structure by maximizing the modal loss factor.

(b) Active control

The active control requires additional control energy. In the implement of the active control, structural vibration is first perceived by the sensors, a certain control strategy is selected and corresponding calculations are performed, then control forces or moments are applied by actuators into the vibration systems. The active vibration control system is mainly composed of three parts: sensors, controllers and actuators. Herein, the sensors sense external force information or system response information; the controllers receive the sensor information and give the control signals to the actuators through a certain control algorithm; actuators produce corresponding control forces into the vibration system; then the vibration reduction can be achieved. Active control strategies have been proved effective in reducing the structural vibration level. Many studies on active vibration control of thin-shell structures focus on arranging the spatial distribution of control transducers (e.g. piezoelectric actuator/sensor patches). To achieve the best control performance, however, finding the optimal layouts of the piezoelectric actuators/sensors patches in accordance with the employed control algorithms

becomes highly important.

Classical and optimal active control algorithms [52, 53] are frequently used to suppress structural vibration in engineering applications. It is clear that the control performance can be significantly improved by optimizing the configuration of the actuator and sensor patches, including their numbers, positions and topologies. Most early studies in this area rely on exhaustive search [54] or heuristic optimization strategies [55] to determine the positions and sizes of the piezoelectric actuator/sensor patches. Onoda and Haftka [56] proposed an exhaustive search method for optimizing the structural stiffness distribution, location of controller, and control gains in a beam-like space structure. In more recent works, Bruant et al. [57] employed different criteria in the optimization of actuator/sensor locations with genetic algorithms. Darivandi [58] optimized the placement of piezoelectric actuators under optimal linear quadratic regulator (LQR) control with a subgradient-based optimization tool. Takezawa et al. [59] proposed a novel optimization methodology for the placement of piezoelectric elements in real-scale truss structures for suppressing multi-modal vibration with semi-active control.

Topology optimization is regarded as a powerful tool for innovative structural design. Among various methods (see review paper [60]), the solid isotropic material with penalization (SIMP) approach [15, 25] has become popular and been widely used. Similarly as the SIMP approach, artificial piezoelectric material models with penalization on piezoelectricity have been introduced to the topological design of piezoelectric structures [61, 62], with which the intermediate densities of piezoelectric materials can be effectively suppressed during the optimization process. Based on these and similar models, the topology optimization of piezoelectric material distribution has been successfully applied in the design of the piezoelectric actuators/sensors [63, 64] and energy harvesters [65-68]. Besides, Ou and Kikuchi [69] proposed an integrated design procedure combining the homogenization-based topology

16

optimization method and an independent modal space control.

Some studies have been devoted to reduce the structural vibration with active control by optimizing the piezoelectric material distribution. For instance, Silva and Kikuchi [70] introduced an electromechanical coupling factor into the topology optimization of piezoelectric material distribution. Wang et al. [71] studied the optimal piezoelectric actuators/sensors distribution under CGVF control with a genetic algorithm. Drenckhan et al. [71] used the homogenization method to optimize the piezoelectric actuator placement on a beam with proportional feedback control. Mello et al. [72] proposed a topology optimization methodology to design the piezoresistive membrane and flexible substrate simultaneously for maximizing the sensor sensitivity to external loading. Zhang and Kang [73] considered the topology optimization of the piezoelectric sensor/actuator distribution with CGVF control for minimizing the steady-state response under harmonic loads.

(c) Semi-active control

Semi-active control is between the active control and the passive control. It also requires additional control energy; however, the energy is not directly applied to the system through the actuator. Instead, the actuator is used to change the system's stiffness effect, damping effect, or local resonance characteristics to achieve control. Semi-active control mainly has the advantages of low price, low energy consumption, small volume and weight. Commonly used semi-active control elements include: controllable elastic and inertial elements (such as shape memory alloys), controllable dampers (such as magnetorheological, electrorheological dampers), controllable dynamic absorbers and so on.

Many studies have been devoted to the vibration control of plate/beam structures incorporating MR or ER fluid layers. Yalcintas and Dai [74, 75] studied the dynamic responses

of a simply supported beam comprising a layer of MR and ER fluid using an energy approach. Ying et al. [76] carried out numerical simulations of the micro-vibration response of a stochastically excited sandwich beam with a MR elastomer core. Rajamohan et al. [77, 78] and Hoseinzadeh and Rezaeepazhand [79] investigated finite element modeling of a laminated composite structures containing fully and partially treated MR fluid layer. Yeh [80] discussed vibration characteristics and MR damping effects of sandwich rectangular plates with MR elastomer damping treatment. These studies have proved that the structural dynamic performance can be improved by including MR or ER fluid layers. It was also shown that the vibration characteristics can be significantly changed by adopting partially treated MR fluid layer [81]. Clearly, for further improving the overall semi-active control performance, it is highly desirable to determine the best locations and geometries of the MR (or ER) segments. This just highlights the need to optimize the layout of MR/ER layers in semi-active control applications.

Layout design optimization of MR/ER layers in sandwich plates has been considered in a few academic studies. An early attempt was done by Gong and Lim [82], who optimized the lengths and locations of the MR fluid segments for achieving relatively higher natural frequencies in a sandwich beam using analytical and experimental results. In more recent studies, Snamina [83] optimized the location of an active MR fluid patch in a sandwich plate for suppressing selected vibration modes with direct search. Rajamohan et al. [84] developed an optimization method based on sequential quadratic programming and genetic algorithms for determining the optimal location of MR fluid segments in a partially treated MR sandwich beam to maximize the modal damping factors. In general, existing optimization methods can only handle a relatively small number of design variables, thus limiting the control performance improvement. For achieving the best overall control performance, more advanced optimization techniques should be developed, such as topology optimization. Up to now, only a few studies considered this topic, for example, Zhang and Kang [85] investigated topology optimization of

the magnetorheological (MR) fluid layer in a sandwich plate for improving the semi-active vibration control performance.

1.3.2 Microstructures design of phononic crystals

Phononic crystals (PnCs) [7] exhibit band gap effects that can obstruct the propagation of sound and elastodynamic waves in specified frequency regimes. PnCs have potential in a wide range of practical applications, such as sound and vibration reduction [86, 87], waveguides and filters [88], and acoustic cloaks [89, 90], their applications can be found in Fig. 1.8 . The microstructures and material components of PnCs, as a class of artificial periodic composite material, should be designed and manufactured to satisfy the requirements of applications. The development of analysis and design methods for PnCs is thus an important and challenging topic.
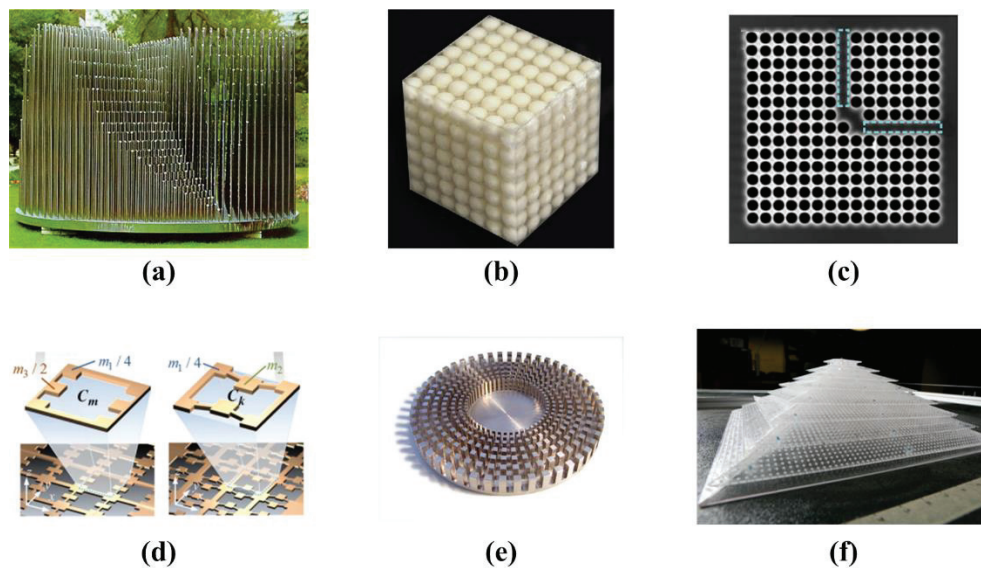
Fig. 1.8 Phononic crystal material and bandgap structure: (a) Kinematic sculpture [91]; (b) Acoustic metamaterials [92]; (c) L-shaped acoustic wave waveguide microstructure [93]; (d) Phononic crystal microstructure with negative stiffness and mass [94]; (e) Cylindrical acoustic cloak for surface waves [95]; (f) Three-dimensional acoustic ground cloak [96].

A general phononic crystal material microstructure design method is: Based on the formation mechanism of phononic crystals (the principle of Bragg scattering [7] and local resonance [2, 8]), Studying the influence of the geometric and physical properties of different material components on the bandgap characteristics, find a kind of initial microstructures with a specified bandgap, and then a microstructure of the PnCs can be obtained through the parameters design and optimization. Some good performance phononic crystal materials have been designed and manufactured in some studies by adjusting the volume fraction of the component materials, lattice constants, the shapes of scatterers. For example, Wen and Wang studied the influence of the volume fraction and lattice size on the start and cutoff frequencies of the bandgap for one-dimensional PnCs. Jensen[97] performed the simulation of acoustic bandgap characteristics of two-dimensional periodic structures with the springs-masses model. Chocano[98] designed the acoustic cloak by optimizing the distribution of aluminum columns in the structure based on genetic algorithms. The above research works provide groundbreaking basis for the analysis and design of the phononic crystal structure, but limited by the total number of variables, it is difficult to achieve a substantial increase of the bandgap performance. Thus, the topology optimization techniques are necessary to be introduced into the microstructure design of PnCs.

Topology optimization has been successfully applied to the design of PnCs [97, 99-101]. In recent years, many novel and attractive designs have been produced using topology optimization methods [102]. For instance, Jensen and Sigmund [97, 103] first proposed a topology optimization method based on solid isotropic material interpolation with penalization (SIMP) for the design of one- and two-dimensional band gap structures and PnCs. Hussein et al. [104] and Dong et al. [105, 106] employed the genetic algorithms based topology optimization method for the design of the unit cell of PnCs with a maximum band gap. Li et al. [107, 108] employed a bidirectional evolutionary structural optimization (BESO) method to optimize the design of phononic band gaps with a specified bulk or shear modulus constraint.

Hedayatrasa et al. [109] presented a study on topology optimization and experimental validation for achieving a maximum band gap and in-plane stiffness design of porous phononic plates. In addition, PnC-based functional devices, such as wave filters [99, 110], waveguide tubes [111], multiphase architected materials for energy dissipation [112], and self-collimation devices [113], have also been designed via topology optimization.

1.3.3 Topology optimization of piezoelectric smart structures under active control

Topology optimization of piezoelectric smart structures has received increasing attention. Early works in this field include topology optimization penalization models for piezoelectric materials [67, 70] and structural static deformation control with piezoelectric actuators [114, 115]. For example, Kögl and Silva [61] proposed a piezoelectric material penalization model for topology optimization of the piezoelectric constant and polarization of piezoelectric actuators. Ruiz et al. [116] proposed a topology optimization method for designing in-plane piezoelectric transducers for static response control by simultaneously optimizing the load-bearing structure and the electrode profile over piezoelectric material. Mello et al. [117] presented topology optimization of a quasi-static piezoelectric transducer configuration attached to a metallic plate. Some researchers also considered topology optimization of piezoelectric structures under active vibration control. Wang et al. [71] studied topology optimization of the piezoelectric actuator/sensor configuration for structural vibration reduction based on constant gain velocity feedback (CGVF) control using a genetic algorithm. Donoso and Sigmund [118] presented a parametric optimization model for finding the optimal thickness and width profile of piezoelectric bimorph actuators with active damping to reduce the tip deflection. Takezawa et al. [59] proposed a method for shape optimization of piezoelectric truss structures for vibration reduction based on an energy recycling-type semi-active control. Zhang and Kang [119] investigated the optimal layouts of piezoelectric actuator/sensor layers to

reduce the transients dynamic response based on active control.

1.4 Robust topology optimization

Robust topology optimization is an important and challenging topic in structural design. In conventional topology optimization, it is assumed that the external loads and environmental conditions are deterministic. In practical applications, however, they usually exhibit large uncertain variability. This raises the need of the topology optimization considering load uncertainties. There are two major non-deterministic structural optimization frameworks, namely reliability-based design optimization (RBDO) [120, 121] and structural robust design optimization [122, 123]. In particular, robust optimization aims to generate optimal designs that are less sensitive to system variability, or perform as required even in the worst-case scenarios.

1.4.1 Robust optimization for different types of uncertainties

There may be three types of uncertainties for non-deterministic structural optimization problems: (I) material uncertainties, it can be considered simply as uncertain parameters or random fields [124, 125]; (II) boundary conditions, including uncertain loads [126-129] and imperfect elastic supports [1]; (III) geometry conditions, it can be considered as manufacturing errors that is important when the structural response is sensitive to the structural topology [2-4].

Robust topology optimization methods have been employed to generate robust structural configurations for these uncertainties. For instance, Jalalpour and Tootkaboni [130] presented a computationally efficient method for reliability-based topology optimization for continuum domains under material property uncertainty, where the response statistics are estimated with

second-order stochastic perturbation. A robust topology optimization algorithm was also proposed by Changizi and Jalalpour [131] for frame structures under geometric or material uncertainties. Wu et al. [132] proposed a new non-probabilistic robust topology optimization approach for structures under interval uncertainty using the expansion of Chebyshev polynomials, and the method was also extended to the level-set based topological design of metamaterials under hybrid uncertainties of material [133].

Among all the uncertainties typically treated in non-deterministic structural optimization problems, the load uncertainty is often considered as the most significant type of uncertainties in practical structural design problems [134]. Given precise statistical information, the load uncertainty can be described by a probability distribution function and well treated with reliability-based method [135, 136]. In this case, some useful techniques can be used to improve the computational efficiency in certain circumstances, including univariate dimension reduction [137] and analytically derived sensitivities [127].

In robust optimization considering manufacturing errors, there are several typical ways to account for spatially varying boundary shapes. In the density-based topology optimization framework, a projection density filter (such as the Heaviside projection function [44,45]) can be employed to simulate the under-etching and over-etching of structural boundary errors during the manufacturing process [21]. In the framework of level-set methods, a random velocity method [46] or a stochastic level set perturbation model [33] can be used to model geometric uncertainties of structural boundaries. The above methods provide sharp and clear boundaries in robust structural design. However, for structures composed of multiple material phases, there are usually continuous diffuse regions between material phases in real applications, and it is thus necessary to introduce diffuse regions into the optimization model when considering manufacturing-related uncertainties.

1.4.2 Robust optimization against probability and non-probability uncertainties

In the analysis and optimization design of engineering structures considering uncertainties, one basic step is to establish a suitable mathematical model to deal with uncertain factors. Usually, there are several types of models, including Mathematical statistics based probability model, non-probabilistic models, and fuzzy models.

Probabilistic models are usually built on the basis of probability density function information. The uncertainty information is generally represented through a random variable or random field with a certain probability distribution, and the response of the structure is also assumed to be a random distribution. Then, the statistical characteristics, such as the mean, the variance, and the failure probability, are solved with the statistical theories. For example, the Material properties uncertainty can be represented through with the probability density function and covariance function, as shown in Fig. 1.9.
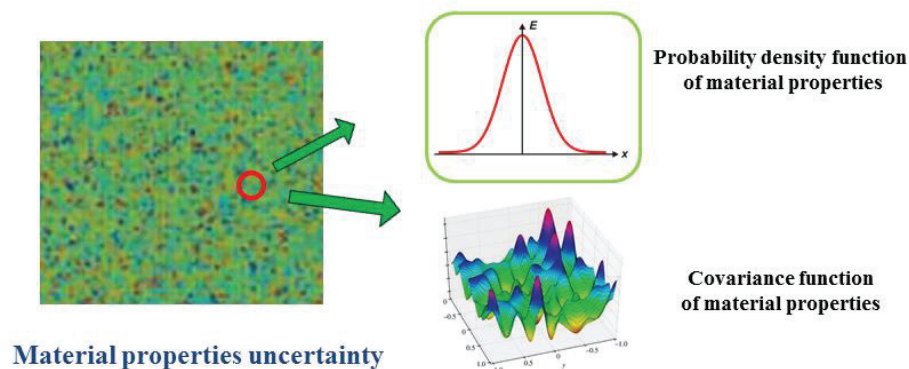
Fig. 1.9 Material properties uncertainty based on random field models.

Previous studies have contributed to structural robust designs with random material distributions. Chen et al. [137], for example, proposed the level-set-based robust shape and topology optimization method for structures and compliant mechanisms, where the Karhunen–Loeve (K-L) expansion is employed to characterize the random material property field and the

univariate dimension-reduction method is adopted in the analysis of the statistical moment. Zhao and Wang [128] proposed a robust topology optimization approach considering random field loading uncertainty based on Karhunen-Loeve expansion. Schevenels et al. [138] presented a robust topology design method of macro-/micro-structures, accounting for spatially varying manufacturing errors. In their method, the random field is discretized into uncorrelated random variables using the expansion optimal linear estimation (EOLE). Tootkaboni et al. [125] proposed the topology optimization method of continuum structures to produce robust designs in the presence of random material properties by combining polynomial chaos expansion (PCE) with the topology optimization method. Keshavarzzadeh et al. [139] comprehensively studied the computational framework for robust- and reliability-based design optimization with intrusive and non-intrusive PCE approaches and extended their method to the topological design of continuum structures under uncertainty [140].

However, in many practical engineering design problems, the precise probability distribution of uncertain fields are not available due to limited number of sample data [141]. A typical example in aerospace engineering is illustrated in Fig.1.10, in which sufficient probability information of uncertain excitations actually exerted on the payload structure during different stages of a launching process can be hardly obtained through ground experiments. Moreover, the load uncertainties are often bounded in nature. For description of these uncertainties, probabilistic models with interval bounds can be applied under certain assumption of probability distribution. However, they may lead to unreliable results when no sufficient samples are available. In such circumstances, a more realistic option is to describe these unknown-but-bounded load uncertainties with ellipsoidal convex models [142]. For example, two types of unknown-but-bounded excitations modelled with ellipsoidal convex models for the dynamic optimization problems are shown in Fig. 1.11. Here, the ellipsoidal models provide a smooth and differentiable mathematical representation of the bounds of the uncertainties, and are thus enable gradient-based optimization algorithms to be used in

reliability analysis and design optimization. However, structural robust optimization considering uncertain-but-bounded loads often leads to optimization problems under worst-case scenario of loading condition, which usually requires to be found by a global optimization algorithm.
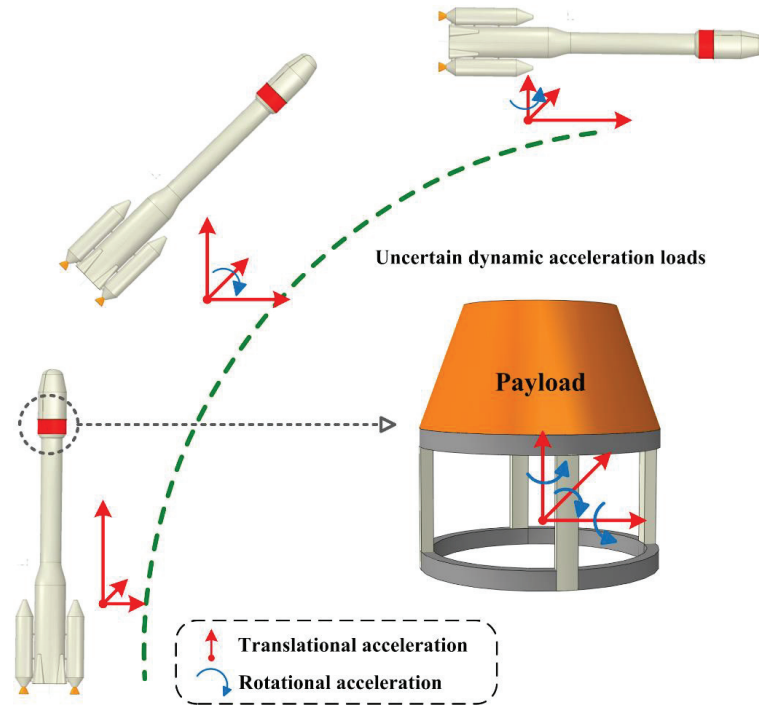
Fig. 1.10 Uncertain dynamic loads exerted on the payload structure during a launch mission.
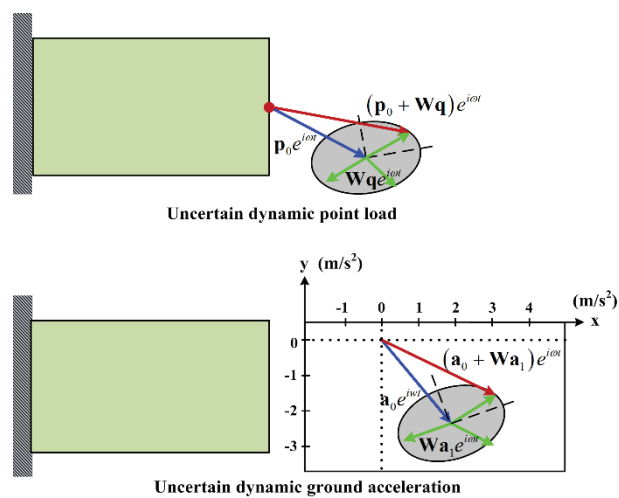
Fig. 1.11 Structures under unknown-but-bounded dynamic loads or dynamic ground accelerations.

In most works on structural optimization regarding the worst-case loading condition, a double-loop optimization formulation is treated [1, 135, 143]. For example, Jung and Cho [144] developed a reliability-based topology optimization of geometrically nonlinear structures under loading uncertainty. Luo et al. [1] performed continuum topology optimization under a non-probabilistic reliability constraint based on the multi-ellipsoidal convex model, and the worst-case load was found by solving the inner-loop mathematical programing problem. In real applications, the double-loop optimization problems will be expensive (if possible) to solve [143], and the sensitivity of the outer-loop optimization is even more difficult to be determined since it has no explicit expression. Thus, some researchers developed various single-loop approaches using the sequential approximation programing (SAP) method [145] to improve the computational efficiency of the optimization problem. However, for robust topology optimization problems with uncertain-but-bounded loads, finding the worst-case loads directly instead of solving the inner-loop problem may be a more reasonable choice [146]. Takezawa et al. [147] first proposed a maximum eigenvalue-based approach for continuum topology optimization under uncertain static loads with zero nominal values. Brittain et al. [148] considered a similar problem by solve the inner-loop problem directly based on Karush-Kuhn-Tucker optimal conditions. Kocvara [149] and Zhao et al. [150] extended these methods into cases of uncertain static loads with nonzero nominal parts.

1.5 Thesis organization

This dissertation presents robust topology optimization of macrostructures and microstructures for dynamic problems, and the topology optimization of piezoelectric smart structures is also

performed. In this chapter, the motivation for this research and some fundamental concepts are briefly introduced. The other chapters are organized as follows.

Chapter 2 investigates robust topology optimization of structures subjected to unknown-but-bounded dynamic loads/ground accelerations. The robust topology optimization formulation considering uncertain-but-bounded excitation is presented using the ellipsoidal convex model. Then the single-loop reformulation of the originally nested problem on the basis of inhomogeneous eigenvalue analysis is proposed. Sensitivity analysis for the worst-case dynamic response is derived. Numerical examples are also presented to demonstrate the validity of the proposed method, and the obtained robust optimal solutions are compared with their deterministic counterparts.

Chapter 3 investigates a robust topology optimization method for designing the microstructures of PnCs by considering random-field material properties. The deterministic band analysis method of PnCs with the FEM is first presented. Then the stochastic response analysis method combining the EOLE method with the PCE approach for the random material property distribution is addressed. The robust formulation of the topology optimization for PnCs with uncertainties and derives the sensitivity analysis for the stochastic band gap response is proposed. Numerical examples is presented to demonstrate the validity of the proposed robust optimization method and discusses robust designs for different band gap orders and different waves propagating modes.

In Chapter 4, a phase-field-based topology optimization method of vibrating structures that reduces the dynamic performance variability under diffuse-region uncertainties is developed. Herein, the spatial distribution of the widths of diffuse regions in a multi-material structure is first represented by a random field and then discretized into uncorrelated stochastic variables using the expansion optimal linear estimation method; stochastic response analysis is then conducted with polynomial chaos expansion. The stochastic structural dynamic responses

28

and the corresponding sensitivities are evaluated by polynomial chaos expansion based on finite element analysis at each sampling point. Numerical examples show that the proposed method generates meaningful optimal topologies for structural dynamic robust optimization problems with the framework of the phase-field method. The phase field-based method is applied into the robust topological microstructural design of PnCs under diffuse region uncertainties.

In Chapter 5, topology optimization of the electrode coverage over piezoelectric patches attached to a thin-shell structure is proposed to reduce the energy consumption of active vibration control under harmonic excitations. The constant gain velocity feedback control method is employed, and the structural frequency response under control is analyzed with the finite element method. In the mathematical formulation of the proposed topology optimization model, the total energy consumption of the control system is taken as the objective function, and a constraint of the maximum allowable dynamic compliance is considered. The sensitivity analysis for total energy consumption of the active control system is derived. Numerical examples are presented to demonstrate the validity of the proposed method, and the differences between the proposed optimization model and the traditional volume minimization model are also discussed based on the numerical solutions.

Finally, Chapter 6 summarizes the findings in this dissertation, and describes promising avenues to explore in future research.

2 Robust topology optimization of vibrating structures subject to uncertain dynamic loads

In this chapter, we consider the robust topology optimization of structures subjected to unknown-but-bounded dynamic loads/ground accelerations. Structural robust optimization considering uncertain-but-bounded loads often leads to optimization problems under worst-case scenario of loading condition, which usually requires to be found by a global optimization algorithm. However, structural dynamic topology optimizations under bounded load uncertainty have not been treated in literature, partly because they have even greater challenges in finding the worst-case scenario. This is due to the fact that the outer-loop optimization problem strongly depends on the solutions of the inner-loop problem, and the worst-case load is also remarkably affected by the material distribution. As a result, the interdependence of the double-loops leads to convergence difficulties and high computational costs.

In this chapter, the excitation uncertainty is described with an ellipsoidal convex model. A nested double-loop problem is first formulated for the robust topology optimization. Since the dynamic compliance may become negative when the external excitation frequency is higher than the structural fundamental frequency, the absolute dynamic compliance is taken as the objective function. We then propose a method to seek the worst-case objective function value directly by evaluating the maximum/minimum eigenvalues and the corresponding eigenvectors of an inhomogeneous eigenvalue problem. Here, a generalized compliance matrix is introduced as a mapping of the structural dynamic compliance matrix to the load uncertainty space. The outer-loop optimization problem is solved by a gradient-based mathematical programming method. To this end, the sensitivity analysis of the worst-case objective function value is derived with the adjoint variable method.

2.1 Robust topology optimization formulation

2.1.1 Structural frequency response under uncertain excitation

The load uncertainty is the most significant type of uncertainties in many practical structural design problems. The ellipsoid convex models are suitable to describe uncertain-but-bounded load variations [151]. Recently, a mathematical formulation for constructing the minimum-volume ellipsoidal model from measured data was proposed by Kang and Zhang [152].

Two types of bounded uncertain external loads may be encountered in structural design problems, namely those with zero and nonzero nominal values, as shown in Fig. 2.1. The latter ones are more common in practice but more difficult to handle. In this study, we consider the robust topology design of structures under uncertain-but-bounded harmonic excitations with nonzero nominal values. Here, the loading condition with zero nominal values can be regarded as a specific case.

Uncertain load with zero nominal value   **Uncertain load with nonzero nominal value**
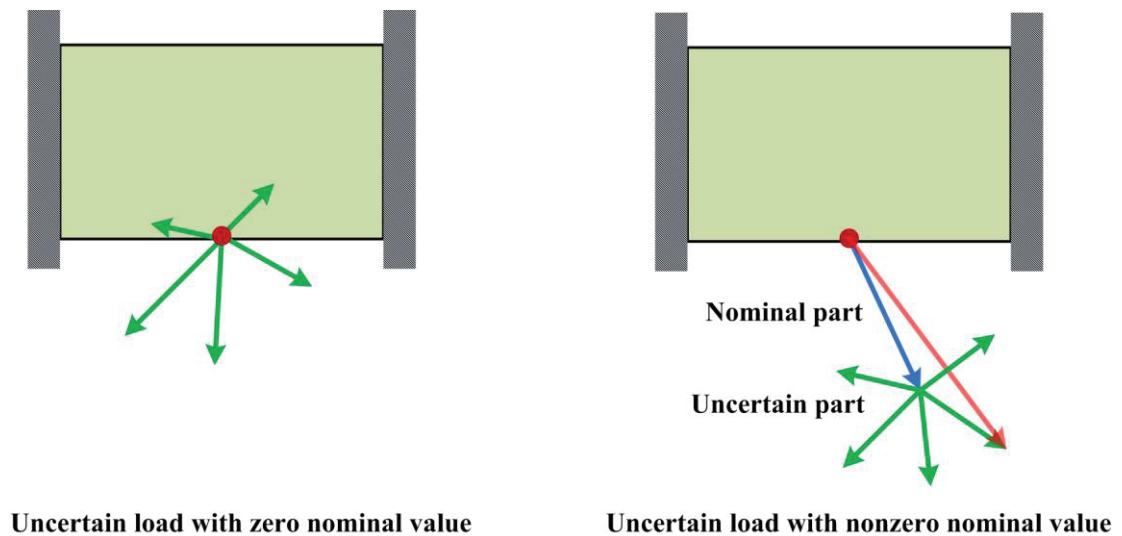
Fig. 2.1 Uncertain loads with zero and nonzero nominal values

In this study, we consider a structural design problem under uncertain-but-bounded harmonic external excitation or ground acceleration, as shown in Fig. 1.11.

(a) Uncertain external excitations

Based on the ellipsoidal convex models, an uncertain harmonic excitation $\mathbf{p}e^{i\omega t}$ can be divided into a nominal part $\mathbf{p}_0 e^{i\omega t}$ and a bounded variation part $\mathbf{W}\mathbf{q}e^{i\omega t}$, as

$$\mathbf{p}e^{i\omega t} = (\mathbf{p}_0 + \mathbf{W}\mathbf{q})e^{i\omega t}, \quad \|\mathbf{q}\| \leq 1. \tag{2.1}$$

Clearly, the bound of the uncertain loads expressed by Eq. (1) forms an ellipsoid in the uncertainty space. Here, $\mathbf{q} \in \mathbf{R}^3$ is referred to as the normalized uncertain load vector defined in the standard uncertainty space; $\mathbf{W} \in \mathbf{R}^{3\times3}$ is a positive semi-definite matrix defining the orientation and specific ratio of the ellipsoidal model [1].

We consider an n-DOF dynamic system, thus the global excitation vector $\mathbf{f}(t) = \mathbf{F}e^{i\omega t}$ has the dimension $n \times 1$. The global load magnitude vector $\mathbf{F}$ can be related to the mentioned load magnitude vector by introducing a matrix $\mathbf{H}_{\mathrm{p}} \in \mathbf{R}^{n\times3}$ as

$$\mathbf{F}e^{i\omega t} = \mathbf{H}\mathbf{p}e^{i\omega t} = \mathbf{H}_{\mathrm{p}}(\mathbf{p}_0 + \mathbf{W}\mathbf{q})e^{i\omega t}, \tag{2.2}$$

$$\mathbf{H}_{\mathrm{p}} = \begin{bmatrix} 0 & \cdots & 1 & 0 & 0 & \cdots & 0 \\ 0 & \cdots & 0 & 1 & 0 & \cdots & 0 \\ 0 & \cdots & 0 & 0 & 1 & \cdots & 0 \end{bmatrix}^{\mathrm{T}}, \tag{2.3}$$

where $\mathbf{H}$ has value 1 at the entries of loaded degrees of freedoms and 0 elsewhere.

The governing equation for the finite element model of a damping-free structure under uncertain external excitations is

$$\mathbf{M}\ddot{\mathbf{u}}(t) + \mathbf{K}\mathbf{u}(t) = \mathbf{F}e^{i\omega t} = \mathbf{H}_{\mathrm{p}}(\mathbf{p}_0 + \mathbf{W}\mathbf{q})e^{i\omega t}, \tag{2.4}$$

where $\mathbf{M} \in \mathbf{R}^{n \times n}$ and $\mathbf{K} \in \mathbf{R}^{n \times n}$ are the mass matrix and the stiffness matrix, respectively; $\mathbf{u}(t) \in \mathbf{C}^{n \times 1}$ and $\ddot{\mathbf{u}}(t) \in \mathbf{C}^{n \times 1}$ are the vectors of displacement and acceleration, respectively. We are concerned with only the steady-state response $\mathbf{u}(t)$, which can be expressed as $\mathbf{u}(t) = \mathbf{U}e^{i\omega t}$, with the vibration amplitude $\mathbf{U} \in \mathbf{R}^{n \times 1}$. Thus the governing equations of the dynamic system can be simplified as

$$\left(-\omega^2 \mathbf{M} + \mathbf{K}\right)\mathbf{U} = \mathbf{F} = \mathbf{H}_p\left(\mathbf{p}_0 + \mathbf{Wq}\right), \tag{2.5}$$

where the expression $\left(-\omega^2 \mathbf{M} + \mathbf{K}\right)$ is known as the structural dynamic stiffness matrix.

(b) Uncertain ground accelerations

For the ground acceleration case, after introducing a connecting matrix $\mathbf{H}_a \in \mathbf{R}^{n \times 3}$, we express the load vector $\mathbf{f}(t)$ as

$$\mathbf{f}(t) = \mathbf{F}e^{i\omega t} = \mathbf{M}\mathbf{H}_a(\mathbf{a}_0 + \mathbf{Wa}_1)e^{i\omega t}, \quad \|\mathbf{a}_1\| \leq 1, \tag{2.6}$$

$$\mathbf{H}_a = \begin{bmatrix} 1 & 0 & 0 & \cdots & 1 & 0 & 0 \\ 0 & 1 & 0 & \cdots & 0 & 1 & 0 \\ 0 & 0 & 1 & \cdots & 0 & 0 & 1 \end{bmatrix}^{\mathrm{T}}. \tag{2.7}$$

Here, $\mathbf{a}_1$ is the normalized uncertainty vector of the ground acceleration.

Furthermore, the governing equation for the steady-state response can be rewritten as

$$\left(-\omega^2 \mathbf{M} + \mathbf{K}\right)\mathbf{U} = \mathbf{F} = \mathbf{M}\mathbf{H}_a(\mathbf{a}_0 + \mathbf{Wa}_1). \tag{2.8}$$

Equations (2.5) and (2.8) can be solved with the model superposition method [40, 49] or the direct method [153]. In this study, we employ the latter approach.

2.1.2 Optimization formulation

We intend to optimize the structural topology for minimizing the frequency response under the worst-case dynamic excitation. The dynamic compliance $C = \mathbf{U}^{\mathrm{T}}\left(\mathbf{K} - \omega^2\mathbf{M}\right)\mathbf{U}$ has been used by many researchers in dynamic topology optimization. However, the dynamic stiffness $\left(\mathbf{K} - \omega^2\mathbf{M}\right)$ may become negative semi-definite if the excitation frequency ω is sufficiently higher than the fundamental frequency of the structure. This will make the dynamic compliance negative [154]. Considering this possibility in the optimization formulation, we chose the absolute value of the dynamic compliance as the objective function:

$$f = |C| = \left|\mathbf{U}^{\mathrm{T}}\left(\mathbf{K} - \omega^2\mathbf{M}\right)\mathbf{U}\right| = \left|\mathbf{F}^{\mathrm{T}}\left(\mathbf{K} - \omega^2\mathbf{M}\right)^{-1}\mathbf{F}\right|. \tag{2.9}$$

Here, minimizing the dynamic compliance is equivalent to maximizing the dynamic stiffness of structures subjected to time-harmonic external loads of given frequency and amplitude. Using the dynamic compliance as the objective function was first proposed by Ma et al. [155] and then extended to represent the damping effect of the vibrating system. Recently, the dynamic compliance has been re-defined as a more general form with a complex function by Takezawa et al. [156]. For the uncertain external excitation case, the absolute dynamic compliance in Eq. (2.9) can be further written as

$$\begin{aligned} |C| &= \left|\left(\mathbf{p}_0 + \mathbf{Wq}\right)^{\mathrm{T}} \mathbf{H}_{\mathrm{p}}^{\mathrm{T}}\left(\mathbf{K} - \omega^2\mathbf{M}\right)^{-1} \mathbf{H}_{\mathrm{p}}\left(\mathbf{p}_0 + \mathbf{Wq}\right)\right| \\ &= \left|\left(\mathbf{p}_0 + \mathbf{Wq}\right)^{\mathrm{T}} \mathbf{Q}_{\mathrm{p}}\left(\mathbf{p}_0 + \mathbf{Wq}\right)\right|, \end{aligned} \tag{2.10}$$

where $\mathbf{Q}_{\mathrm{p}} = \mathbf{Z}_{\mathrm{p}}^{\mathrm{T}}(\mathbf{K} - \omega^2\mathbf{M})\mathbf{Z}_{\mathrm{p}}$ with $\mathbf{Z}_{\mathrm{p}} = (\mathbf{K} - \omega^2\mathbf{M})^{-1}\mathbf{H}_{\mathrm{p}}$. In what follows, we refer to the matrix $\mathbf{Q}_{\mathrm{p}}$ as the generalized compliance matrix to map the structural dynamic compliance

matrix to the load uncertainty space.

For the uncertain ground acceleration case, the absolute dynamic compliance reads

$$
\begin{aligned}
|C| &= \left| \left[\mathbf{M}\mathbf{H}_a (\mathbf{a}_0 + \mathbf{W}\mathbf{a}_1) \right]^{\mathrm{T}} (\mathbf{K} - \omega^2 \mathbf{M})^{-1} \mathbf{M}\mathbf{H}_a (\mathbf{a}_0 + \mathbf{W}\mathbf{a}_1) \right| \\
&= \left| (\mathbf{a}_0 + \mathbf{W}\mathbf{a}_1)^{\mathrm{T}} \mathbf{Q}_a (\mathbf{a}_0 + \mathbf{W}\mathbf{a}_1) \right|,
\end{aligned}
\tag{2.11}
$$

where the generalized compliance matrix $\mathbf{Q}_a = \mathbf{Z}_a^{\mathrm{T}} (\mathbf{K} - \omega^2 \mathbf{M}) \mathbf{Z}_a$, with $\mathbf{Z}_a = (\mathbf{K} - \omega^2 \mathbf{M})^{-1} \mathbf{M}\mathbf{H}_a$.

Taking the uncertain ground acceleration case as example (which is more complex), we state the robust topology optimization problem as

$$
\begin{aligned}
\min_{\mathbf{x}} \quad & f = \max_{\|\mathbf{a}_1\| \le 1} |C| = \max_{\|\mathbf{a}_1\| \le 1} \left| (\mathbf{a}_0 + \mathbf{W}\mathbf{a}_1)^{\mathrm{T}} \mathbf{Q}_a (\mathbf{a}_0 + \mathbf{W}\mathbf{a}_1) \right|, \\
\text{s.t.} \quad & \sum_{e=1}^{N_e} x_e V_e - f_v \sum_{e=1}^{N_e} V_e \le 0, \\
& 0 < \underline{x} \le x_e \le 1 \quad \left(e = 1, 2, ..., N_e \right) ,
\end{aligned}
\tag{2.12}
$$

where the vector $\mathbf{x} = \left\{ x_1, x_2, ..., x_{N_e} \right\}^{\mathrm{T}}$ denotes the element-wise density design variables describing the structural layout, with N_e being the total number of finite elements in the design domain. The symbol f_v is the volume fraction ratio and V_e denotes the volume of the eth element. The lower bound of the design variables is set to be $\underline{x} = 10^{-6}$ in this study.

The conventional power-law penalization model in the Solid Isotropic Material with Penalization (SIMP) model may result in spurious local vibration modes due to inconsistent penalization of the stiffness and the mass matrices [5].Hence the Rational Approximation of Material Properties (RAMP) model [32] is adopted in the optimization formulation. It has a nonzero gradient for the zero density value, and is thus capable of removing localized vibration modes in low density value elements. In the RAMP model, the Young's modulus is interpolated as

$$E(x_e) = E_{\text{void}} + \frac{x_e}{1 + p_{\text{E}}(1 - x_e)}(E_{\text{solid}} - E_{\text{void}}).\tag{2.13}$$

Here, E_{void} and E_{solid} denote the Young's modulus in void elements and fully solid elements, respectively. x_{solid} is the interpolated mass density, and the material density penalization coefficient is set to be $p_{\text{E}} = 4$. The RAMP model provides a consistent penalization of the stiffness and the mass matrices in the areas of low density elements, which can avoid the local vibration modes

Thus, the global stiffness matrix $\mathbf{K}$ and mass matrix $\mathbf{M}$ are given by

$$\mathbf{K} = \sum_{e=1}^{N_e} \left(\underline{x} + \frac{x_e}{1 + p_{\text{E}}(1 - x_e)}(1 - \underline{x}) \right)\mathbf{K}_e,$$

$$\mathbf{M} = \sum_{e=1}^{N_e} x_e \mathbf{M}_e.\tag{2.14}$$

Here, $\mathbf{K}_e$ and $\mathbf{M}_e$ are the element stiffness matrix and element mass matrix computed with the properties of the fully solid material, respectively.

$$\mathbf{K}^e = \int_{\Omega^e} \mathbf{B}^{\text{T}}\mathbf{D}\mathbf{B}|J|\,\mathrm{d}\Omega,$$

$$\mathbf{M}^e = \int_{\Omega^e} \rho_{\text{solid}}\mathbf{N}^{\text{T}}\mathbf{N}|J|\,\mathrm{d}\Omega.\tag{2.15}$$

Here, $\mathbf{B}$ and $\mathbf{N}$ are the displacement-strain matrix and shape function matrix in the local coordinate system, respectively. The notation $\mathbf{D}$ is the usual elasticity matrixes of the solid material, and $|J|$ is determinant of the Jacobian matrix of the corresponding iso-parametric transformation."

2.2 Single-loop reformulation with inhomogeneous eigenvalue problem

The robust optimization problem (2.12) is by definition a nested double-loop optimization

problem. The inner-loop problem $\max_{\|\mathbf{a}_1\| \leq 1} |(\mathbf{a}_0 + \mathbf{W}\mathbf{a}_1)^T \mathbf{Q}_a (\mathbf{a}_0 + \mathbf{W}\mathbf{a}_1)|$ is often called "anti-optimization" and aims to find the worst-case excitation combination (usually strongly depending on the structural topology), while the outer-loop is to optimize the material distribution under such a worst-case loading condition with a gradient-based mathematical programming algorithm. In particular, the inner-loop problem should be solved to the global optimum, in order to ensure that the "real" worst-case scenario is found. This presents a great challenge to the solution of the robust topology optimization. This thus motivates the study of a solvable reformulation of the originally nested optimization problem, which will be elaborated in what follows.

Without loss of generality, we now consider the uncertain ground acceleration case. The objective function of problem (2.12) needs to find both the maximum and the minimum values. The Lagrange function of the dynamic compliance reads

$$C = (\mathbf{a}_0 + \mathbf{W}\mathbf{a}_1)^T \mathbf{Q}_a (\mathbf{a}_0 + \mathbf{W}\mathbf{a}_1) - \lambda \left(\mathbf{a}_1^T \mathbf{a}_1 - 1 \right). \tag{2.16}$$

The Karush-Kuhn-Tucker optimality condition can be established by differentiating the Lagrangian function (2.16) with respect $\mathbf{a}_1$ as

$$\frac{\partial C}{\partial \mathbf{a}_1} = 2\mathbf{W}\mathbf{Q}_a \mathbf{W}\mathbf{a}_1 + 2\mathbf{W}\mathbf{Q}_a \mathbf{a}_0 - 2\lambda \mathbf{I}\mathbf{a}_1. \tag{2.17}$$

Thus, the extreme values of Eq. (2.16) can be obtained by solving the following problem

$$\begin{cases} \left(\lambda \mathbf{I} - \mathbf{W}^T \mathbf{Q}_a \mathbf{W} \right) \mathbf{a}_1 = \mathbf{W}^T \mathbf{Q}_a \mathbf{a}_0, \\ \mathbf{a}_1^T \mathbf{a}_1 = 1. \end{cases} \tag{2.18}$$

To show the nature of Eq. (2.18), we simplify it as $\mathbf{A}\boldsymbol{\phi} - \lambda\boldsymbol{\phi} = \mathbf{b}$ where $\mathbf{A} = \mathbf{W}^T \mathbf{Q}_a \mathbf{W}$, $\boldsymbol{\phi} = \mathbf{a}_0$ and $\mathbf{b} = \mathbf{W}^T \mathbf{Q}_a \mathbf{a}_0$. Eq. (2.18) is called an inhomogeneous

eigenvalue in literature [157]. Effective solution methods of inhomogeneous eigenvalue problem have been developed [158].

It has been proved by Kocvara [149] and Thore et al. [159], the extreme values of the objective function can be obtained by the eigenvectors $\mathbf{a}_1^{\max}$ and $\mathbf{a}_1^{\min}$ associated with the maximum eigenvalue $\lambda^{\max}$ and the minimum eigenvalue $\lambda^{\min}$ of the eigenvalue problem (2.18) as

$$
\begin{aligned}
\left|C_{\max}\right| &= \left|(\mathbf{a}_0 + \mathbf{W}\mathbf{a}_1^{\max})^{\mathrm{T}} \mathbf{Q}_a (\mathbf{a}_0 + \mathbf{W}\mathbf{a}_1^{\max})\right|, \\
\left|C_{\min}\right| &= \left|(\mathbf{a}_0 + \mathbf{W}\mathbf{a}_1^{\min})^{\mathrm{T}} \mathbf{Q}_a (\mathbf{a}_0 + \mathbf{W}\mathbf{a}_1^{\min})\right|.
\end{aligned}
\tag{2.19}
$$

If the nominal part of the uncertain excitation is a zero vector ($\mathbf{a}_0 = \mathbf{0}$), Eq. (2.18) degenerates into a standard eigenvalue problem. The topology optimization of a structure under static loads that have zero nominal values and are bounded by a circle has been treated by Takezawa et al. [147]. However, in presence of non-zero nominal part ($\mathbf{a}_0 \neq \mathbf{0}$), Eq. (2.18) takes the form of the aforementioned inhomogeneous eigenvalue problem.

A simple way to compute all the eigenvalues of such an inhomogeneous eigenvalue problem is to convert it into a quadratic eigenvalue problem expressed by [158]

$$
\begin{bmatrix}
\mathbf{0} & \mathbf{I} \\
\left(\mathbf{W}^{\mathrm{T}}\mathbf{Q}\mathbf{a}_0\right)^{\mathrm{T}} \mathbf{W}^{\mathrm{T}}\mathbf{Q}\mathbf{a}_0 - \mathbf{W}^{\mathrm{T}}\mathbf{Q}_a\mathbf{W}\left(\mathbf{W}^{\mathrm{T}}\mathbf{Q}\mathbf{W}\right)^{\mathrm{T}} & 2\mathbf{W}^{\mathrm{T}}\mathbf{Q}_a\mathbf{W}
\end{bmatrix}
\begin{bmatrix}
\tilde{\mathbf{a}}_1 \\
\tilde{\mathbf{a}}_2
\end{bmatrix}
= \lambda
\begin{bmatrix}
\tilde{\mathbf{a}}_1 \\
\tilde{\mathbf{a}}_2
\end{bmatrix}.
\tag{2.20}
$$

After the eigenvalues of the original inhomogeneous eigenvalue problem (2.18) are obtained by solving the eigenvalue problem (2.20), the eigenvectors $\mathbf{a}_1$ of the corresponding eigenvalues can be further evaluated as follows

$$
\begin{cases}
\tilde{\mathbf{a}} = -\left(\mathbf{W}^{\mathrm{T}}\mathbf{Q}_a\mathbf{W} - \lambda\mathbf{I}\right)^{-1} \mathbf{W}^{\mathrm{T}}\mathbf{Q}_a\mathbf{a}_0, \\
\mathbf{a}_1 = \dfrac{\tilde{\mathbf{a}}}{\|\tilde{\mathbf{a}}\|}.
\end{cases}
\tag{2.21}
$$

38

The non-symmetric eigenvalue problem (2.20) can be solved with a standard algorithm, and the computational cost would be very low since the dimension of the problem is usually small. For instance, the dimension of the inhomogeneous eigenvalue problem is at most 6×6, which is the case when uncertainties arising from both transitional and rotational excitations are considered in a 3D problem. On the contrary, such a case would be extreme difficult to be treated with conventional double-loop approaches relying on anti-optimization techniques to find the worst-case scenario.

Through above derivation and solution procedures, we can determine the extreme dynamic compliance with $\mathbf{a}_1^{\max}$ and $\mathbf{a}_1^{\min}$ in Eq. (2.19), and thus we rewrite the objective function in optimization problem (2.12) with

$$\max f = \max\left(|C_{\max}|, |C_{\min}|\right). \tag{2.22}$$

Such an objective function is not smooth and this poses a major difficulty when solving the optimization problem with a gradient-based algorithm. To circumvent this, the K-S aggregation function [160], which provides a sufficiently smooth conservative envelope, is adopted to approximate the maximum value of the objective function as

$$\max f = \mathrm{KS}\left(|C_{\max}|, |C_{\min}|\right) = \frac{1}{\eta}\ln\left(\mathrm{e}^{\eta|C_{\max}|} + \mathrm{e}^{\eta|C_{\min}|}\right), \tag{2.23}$$

where η is the aggregation parameter. The choice of aggregation parameter has been discussed in detail in Poon and Martins [161]. We set $\eta=10$ in the numerical examples.

With the objective function (2.23), the nested double-loop optimization problem (2.12) reduces to a differentiable single-loop optimization problem as

$$\min_{\mathbf{x}} \quad f = \frac{1}{\eta} \ln \left(e^{\eta \left| (\mathbf{a}_0 + \mathbf{W} \mathbf{a}_1^{max})^{\mathrm{T}} \mathbf{Q}_{\mathrm{a}} (\mathbf{a}_0 + \mathbf{W} \mathbf{a}_1^{max}) \right|} + e^{\eta \left| (\mathbf{a}_0 + \mathbf{W} \mathbf{a}_1^{min})^{\mathrm{T}} \mathbf{Q}_{\mathrm{a}} (\mathbf{a}_0 + \mathbf{W} \mathbf{a}_1^{min}) \right|} \right),$$

$$\text{s.t.} \quad \left(\lambda \mathbf{I} - \mathbf{W}^{\mathrm{T}} \mathbf{Q}_{\mathrm{a}} \mathbf{W} \right) \mathbf{a}_1 = \mathbf{W}^{\mathrm{T}} \mathbf{Q}_{\mathrm{a}} \mathbf{a}_0,$$

$$\mathbf{a}_1^{\mathrm{T}} \mathbf{a}_1 = 1,$$

$$\sum_{e=1}^{N_{\mathrm{e}}} x_e V_e - f_{\mathrm{v}} \sum_{e=1}^{N_{\mathrm{e}}} V_e \leq 0,$$

$$0 < \underline{x} \leq x_e \leq 1, \quad \left(e = 1, 2, ..., N_{\mathrm{e}} \right).$$

(2.24)

This method achieves a relatively high efficiency mainly due to the fact that the dimension of the eigenvalue problem to determine the worst-case load combination is only the number of uncertain loads. As comparison, in the double-loop methods [1], the computational model of the gradients of the objective function w.r.t. the uncertain load is of the order of the total degree of freedom. The comparison between the two methods will be given in the numerical examples.

2.3 Sensitivity analysis

The optimization problem in (2.24) is solved by a gradient-based mathematical programming algorithm, which requires sensitivity analysis of the objective function with respect to the design variables. For a specified excitation, the sensitivity of the absolute dynamic compliance to the eth element gives (taking ground acceleration as example)

$$\frac{\partial |C|}{\partial x_e} = \left| \frac{\partial (\mathbf{a}_0 + \mathbf{W} \mathbf{a}_1)^{\mathrm{T}} \mathbf{Q}_{\mathrm{a}} (\mathbf{a}_0 + \mathbf{W} \mathbf{a}_1)}{\partial x_e} \right|$$

$$= \left| (\mathbf{a}_0 + \mathbf{W} \mathbf{a}_1)^{\mathrm{T}} \frac{\partial \mathbf{Q}_{\mathrm{a}}}{\partial x_e} (\mathbf{a}_0 + \mathbf{W} \mathbf{a}_1) + 2 (\mathbf{a}_0 + \mathbf{W} \mathbf{a}_1)^{\mathrm{T}} \mathbf{Q}_{\mathrm{a}} \mathbf{W} \frac{\partial \mathbf{a}_1}{\partial x_e} \right|.$$

(2.25)

Here, only terms $\partial \mathbf{Q} / \partial x_e$ and $\partial \mathbf{a}_1 / \partial x_e$ need to be further derived.

(a) Derivative of the generalized compliance matrix $\partial \mathbf{Q} / \partial x_e$

The term $\mathbf{Q}_a = \mathbf{Z}_a^T (\mathbf{K} - \omega^2 \mathbf{M}) \mathbf{Z}_a$ (with $\mathbf{Z}_a = (\mathbf{K} - \omega^2 \mathbf{M})^{-1} \mathbf{M} \mathbf{H}_a$) cannot be easily evaluated directly. To overcome this difficulty, we rewrite the matrix $\mathbf{Q}$ by including the product of an adjoint matrix $\mathbf{L} \in \mathbf{R}^{n \times 3}$ and the governing equation as

$$\mathbf{Q}_a = \mathbf{Z}_a^T (\mathbf{K} - \omega^2 \mathbf{M}) \mathbf{Z}_a + \mathbf{L}^T \left(-(\mathbf{K} - \omega^2 \mathbf{M}) \mathbf{Z}_a + \mathbf{M} \mathbf{H}_a \right). \tag{2.26}$$

Differentiating the matrix $\mathbf{Q}$ with respect to the design variable x_e ($e = 1, 2, ..., N_e$) gives

$$\frac{\partial \mathbf{Q}_a}{\partial x_e} = \left((\mathbf{M} \mathbf{H}_a)^T - \mathbf{L}^T (\mathbf{K} - \omega^2 \mathbf{M}) \right) \frac{\partial \mathbf{Z}_a}{\partial x_e} + \frac{\partial (\mathbf{M} \mathbf{H}_a)^T}{\partial x_e} \mathbf{Z}_a - \mathbf{L}^T \frac{\partial (\mathbf{K} - \omega^2 \mathbf{M})}{\partial x_e} \mathbf{Z}_a + \mathbf{L}^T \frac{\partial \mathbf{M}}{\partial x_e} \mathbf{H}_a. \tag{2.27}$$

Let $\mathbf{L} = \mathbf{Z}_a = (\mathbf{K} - \omega^2 \mathbf{M})^{-1} \mathbf{M} \mathbf{H}_a$, we rewrite Eq. (2.27) as

$$\frac{\partial \mathbf{Q}_a}{\partial x_e} = \mathbf{H}_a^T \frac{\partial \mathbf{M}}{\partial x_e} \mathbf{Z}_a - \mathbf{Z}_a^T \left(\frac{\partial \mathbf{K}}{\partial x_e} - \omega^2 \frac{\partial \mathbf{M}}{\partial x_e} \right) \mathbf{Z}_a + \mathbf{Z}_a^T \frac{\partial \mathbf{M}}{\partial x_e} \mathbf{H}_a. \tag{2.28}$$

Here, the derivatives of the mass matrix and the stiffness matrix with respect to the design variables can be calculated as

$$\frac{\partial \mathbf{M}}{\partial x_e} = \sum_{e=1}^{N_e} \mathbf{M}_e, \tag{2.29}$$

$$\frac{\partial \mathbf{K}}{\partial x_e} = \sum_{e=1}^{N_e} \left(\frac{1}{1 + p_E(1 - x_e)} + \frac{p_E x_e}{(1 + p_E(1 - x_e))^2} \right) (1 - \underline{x}) \mathbf{K}_e. \tag{2.30}$$

(b) Derivative of the normalized uncertainty vector of ground acceleration $\partial \mathbf{a}_1 / \partial x_e$

Differentiating both sides of the first equation in Eq. (2.18) with respect to the design variable x_e ($e = 1, 2, ..., N_e$), it yields

$$\frac{\partial \mathbf{a}_1}{\partial x_e} = \left(\lambda \mathbf{I} - \mathbf{W}^{\mathrm{T}} \mathbf{Q}_a \mathbf{W} \right)^{-1} \left(\mathbf{W}^{\mathrm{T}} \frac{\partial \mathbf{Q}_a}{\partial x_e} \left(\mathbf{a}_0 + \mathbf{W} \mathbf{a}_1 \right) - \frac{\partial \lambda}{\partial x_e} \mathbf{I} \mathbf{a}_1 \right), \tag{2.31}$$

where the term $\partial \lambda / \partial x_e$ can be calculated as follows.

Differentiating both sides of the second equation in Eq. (2.18) with respect to x_e $(e = 1, 2, ..., N_e)$, one can rewrite Eq. (2.18) as

$$\mathbf{a}_1 = \left(\lambda \mathbf{I} - \mathbf{W}^{\mathrm{T}} \mathbf{Q}_a \mathbf{W} \right)^{-1} \mathbf{W}^{\mathrm{T}} \mathbf{Q}_a \mathbf{a}_0, \tag{2.32}$$

$$\mathbf{a}_1^{\mathrm{T}} \frac{\partial \mathbf{a}_1}{\partial x_e} = 0. \tag{2.33}$$

Substituting (2.32) into (2.33) yields

$$\mathbf{a}_1^{\mathrm{T}} \left(\frac{\partial \left(\lambda \mathbf{I} - \mathbf{W}^{\mathrm{T}} \mathbf{Q}_a \mathbf{W} \right)^{-1}}{\partial x_e} \mathbf{W}^{\mathrm{T}} \mathbf{Q}_a \mathbf{a}_0 + \left(\lambda \mathbf{I} - \mathbf{W}^{\mathrm{T}} \mathbf{Q}_a \mathbf{W} \right)^{-1} \mathbf{W}^{\mathrm{T}} \frac{\partial \mathbf{Q}}{\partial x_e} \mathbf{a}_0 \right) =$$

$$-\mathbf{a}_1^{\mathrm{T}} \left(\lambda \mathbf{I} - \mathbf{W}^{\mathrm{T}} \mathbf{Q}_a \mathbf{W} \right)^{-2} \left(\frac{\partial \lambda}{\partial x_e} \mathbf{I} - \mathbf{W}^{\mathrm{T}} \frac{\partial \mathbf{Q}_a}{\partial x_e} \mathbf{W} \right) \left(\lambda \mathbf{I} - \mathbf{W}^{\mathrm{T}} \mathbf{Q}_a \mathbf{W} \right) \mathbf{a}_1 + \mathbf{a}_1^{\mathrm{T}} \left(\lambda \mathbf{I} - \mathbf{W}^{\mathrm{T}} \mathbf{Q}_a \mathbf{W} \right)^{-1} \mathbf{W}^{\mathrm{T}} \frac{\partial \mathbf{Q}_a}{\partial x_e} \mathbf{a}_0 = 0.$$

$$\tag{2.34}$$

Then the expression of $\partial \lambda / \partial x_e$ can be given as

$$\frac{\partial \lambda}{\partial x_e} = \frac{\mathbf{a}_1^{\mathrm{T}} \left(\lambda \mathbf{I} - \mathbf{W}^{\mathrm{T}} \mathbf{Q} \mathbf{W} \right)^{-1} \mathbf{W}^{\mathrm{T}} \frac{\partial \mathbf{Q}_a}{\partial x_e} \mathbf{W} \mathbf{a}_1 + \mathbf{a}_1^{\mathrm{T}} \left(\lambda \mathbf{I} - \mathbf{W}^{\mathrm{T}} \mathbf{Q}_a \mathbf{W} \right)^{-1} \mathbf{W}^{\mathrm{T}} \frac{\partial \mathbf{Q}_a}{\partial x_e} \mathbf{a}_0}{\mathbf{a}_1^{\mathrm{T}} \left(\lambda \mathbf{I} - \mathbf{W}^{\mathrm{T}} \mathbf{Q}_a \mathbf{W} \right)^{-1} \mathbf{a}_1}. \tag{2.35}$$

By substituting Eqs. (2.27), (2.31) and (2.35) into (2.25), we can obtain the derivative of the absolute dynamic compliance.

For the aggregated function of the maximum/minimum absolute dynamic compliance, its derivative becomes

$$\frac{\partial f}{\partial x_e} = \left(\mathrm{e}^{\eta |C_{\max}|} \frac{\partial |C_{\max}|}{\partial x_e} + \mathrm{e}^{\eta |C_{\min}|} \frac{\partial |C_{\min}|}{\partial x_e} \right) \bigg/ \left(\mathrm{e}^{\eta |C_{\max}|} + \mathrm{e}^{\eta |C_{\min}|} \right). \tag{2.36}$$

2.4 Numerical examples

In this section, numerical examples are presented to illustrate the validity of the proposed sensitivity analysis procedures and the topology optimization formulation. In all the examples, four-node quadrilateral (Q4) elements are used in the finite element modeling. The GCMMA optimizer [162] is employed for solving the optimization problem. The optimization process will be terminated when the relative difference of the objective function values between two adjacent iteration steps satisfies the convergence criterion $\left\| (f_{\mathrm{new}} - f_{\mathrm{old}})/f_{\mathrm{old}} \right\| < 5 \times 10^{-4}$.

2.4.1. Sensitivity analysis of a clamped bracket with uncertain ground acceleration

The first example considers the sensitivity analysis of the upper-edge clamped rectangle bracket under bounded ground accelerations, as shown in Fig. 2.2. The design domain has geometrical dimensions $l_1 = 3$ m and $l_2 = 2$ m. The material (aluminum) has the Young's modulus $E_{\mathrm{solid}} = 6.9 \times 10^{10}$ N/m^2, Poisson's ratio $v_{\mathrm{solid}} = 0.33$, and the mass density $\rho_{\mathrm{solid}} = 2700$ Kg/m^3. An uncertain time-harmonic ground acceleration is applied, which has a nominal part $\mathbf{a}_0 \mathrm{e}^{i\omega t}$ ($\mathbf{a}_0 = [0, 10]^{\mathrm{T}}$ m/s^2, $\omega = 2\pi f_{\mathrm{p}}$ and $f_{\mathrm{p}} = 40$ Hz) and a variation part $\mathbf{W}\mathbf{a}_1 \mathrm{e}^{i\omega t}$ ($\left\| \mathbf{a}_1 \right\| \leq 1$, $\mathbf{W} = \begin{bmatrix} 8 & 0 \\ 0 & 6 \end{bmatrix}$ m/s^2).

In order to verify the sensitivity analysis algorithm, we first calculate the derivative of the absolute dynamic compliance. The structure is discretized with $N_e = 216$ uniform-sized Q4

elements, with a total number of DOFs $n = 494$, and the element numbers are arranged in an ascending order from the lower left to the upper right. Such a coarse mesh is employed here for ease of graphical illustration of the sensitivity analysis results. The relative densities of all the elements are given a uniform value of 0.5.

The predicted values of the sensitivities $\partial |C|_{max} / \partial x_e$ $(e = 1, 2, ..., 216)$ by using the present method are shown in Fig. 2.3. For the purpose of comparison, the sensitivity results obtained using the finite difference method (FDM) with 0.1% perturbation are also given in Fig. 5. It's found that the sensitivity results obtained by the present method agree very well with those by the FDM, while the computational time cost ratio between the present method and the FDM is 1:30.07. Indeed, this ratio increases rapidly as the number of elements increases.
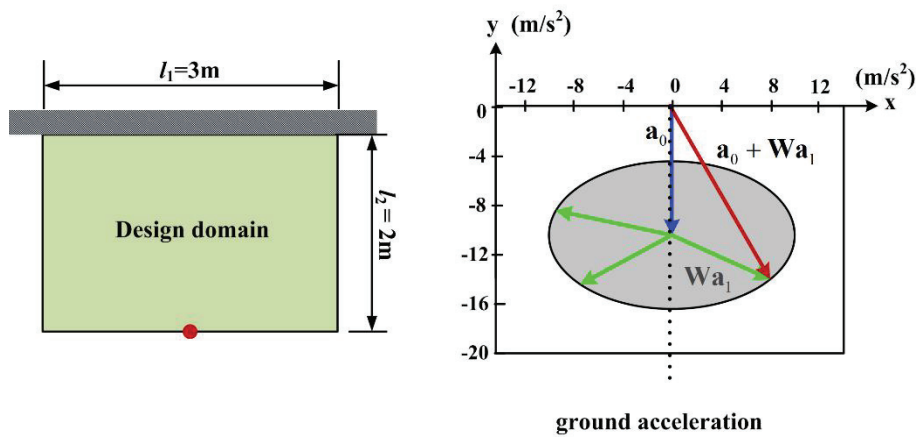
Fig.2.2 Clamped rectangle bracket under uncertain ground acceleration.
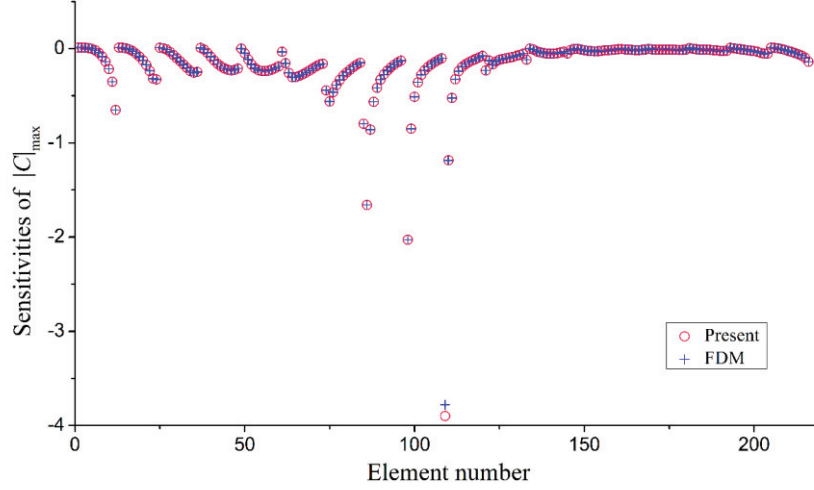
Fig. 2.3 Sensitivities of the maximum absolute dynamic compliance $\left|C\right|_{\max}$ with respect to element densities.

2.4.2 Topology optimization of the clamped bracket with uncertain ground acceleration

We consider the same structure as in the pervious subsection. The same uncertain time-harmonic ground acceleration as in the pervious subsection is considered, and a concentrate mass $m = 200 \text{ Kg}$ is added at the middle point of the lower edge (red point in Fig. 2.2). The design domain is discretized now into a 60×40 finite element mesh with the total number of DOFs $n = 5002$. The upper limit of the volume fraction ratio of the damping material is given as $f_v = 0.5$ and the initial values of the design variables are set to be $x_e = 0.5 \ (e = 1, 2, ..., 2400)$. The sensitivity filter technique [30] with a radius of $r_{\min} = 0.075$ m is applied for suppressing the checkerboard patterns and mesh dependency of the solution. For improving the convergence and numerical stability of the dynamic topology optimization, the Young's modulus of the void phase E_{void} is chosen to be $E_{\text{void}} = 0.1 E_{\text{solid}}$, and an artificial damping $C_{\text{damping}} = 0.001(\mathbf{K} + \mathbf{M})$ is applied at the beginning of the optimization process. They then gradually decrease after 20 iterations until reaching zero, and

it affects the final optimal solution very slightly.

The optimization process converged after 40 iterations. The iteration histories of the objective function and the material volume are presented in Fig. 2.4, which shows a steady decrease of the objective function value during the iterations. In fact, the objective function value has decreased from $2.272 \times 10^{-2} \mathrm{N} \cdot \mathrm{m}$ for the initial design to $0.685 \times 10^{-2} \mathrm{N} \cdot \mathrm{m}$ for the final optimal solution. Some intermediate designs and the final optimal design (the 40th iteration) are given in Fig. 2.5. In the figures, the arrows indicate the directions of the worst-case acceleration within the given uncertainty bound of the ellipsoid model (The blue arrow, green arrow and red arrow indicate the nominal part, variation part and total uncertain excitation, respectively). It can be observed that designs of two adjacent iteration steps may have different worst-case load directions but very similar topologies and shapes. It can be observed that there are two symmetrical extreme load cases for the initial design (there is still a little different due to the modelling and numerical errors), the procedure chose one of them as the worst-case one and optimized it. In the second iteration, the worst-case load changed to the other side, the optimization had to minimize the response for the case. Then in the following iterations, the optimal solutions switched between the two cases, as well as the differences of the two designs were decreasing during the process. And finally, both the two designs came to the same one. This trend can be also noted in Table 2.1, in which the objective function and the worst-case acceleration direction for the last ten iterations are summarized. Despite of the frequently switching of the worst-case excitation directions, the optimization process still achieved a steady convergence. Moreover, the optimized structure exhibits perfect symmetry, which implies effectiveness of the present method.
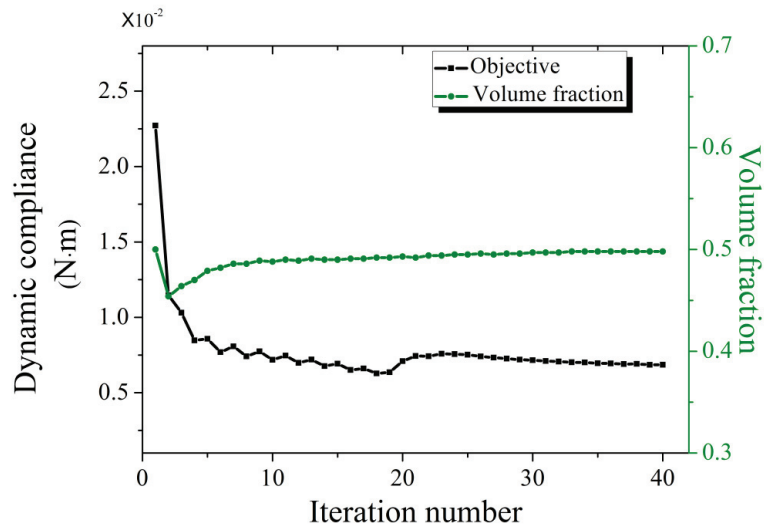
Fig. 2.4 Iteration histories of objective function and volume fraction ratio.
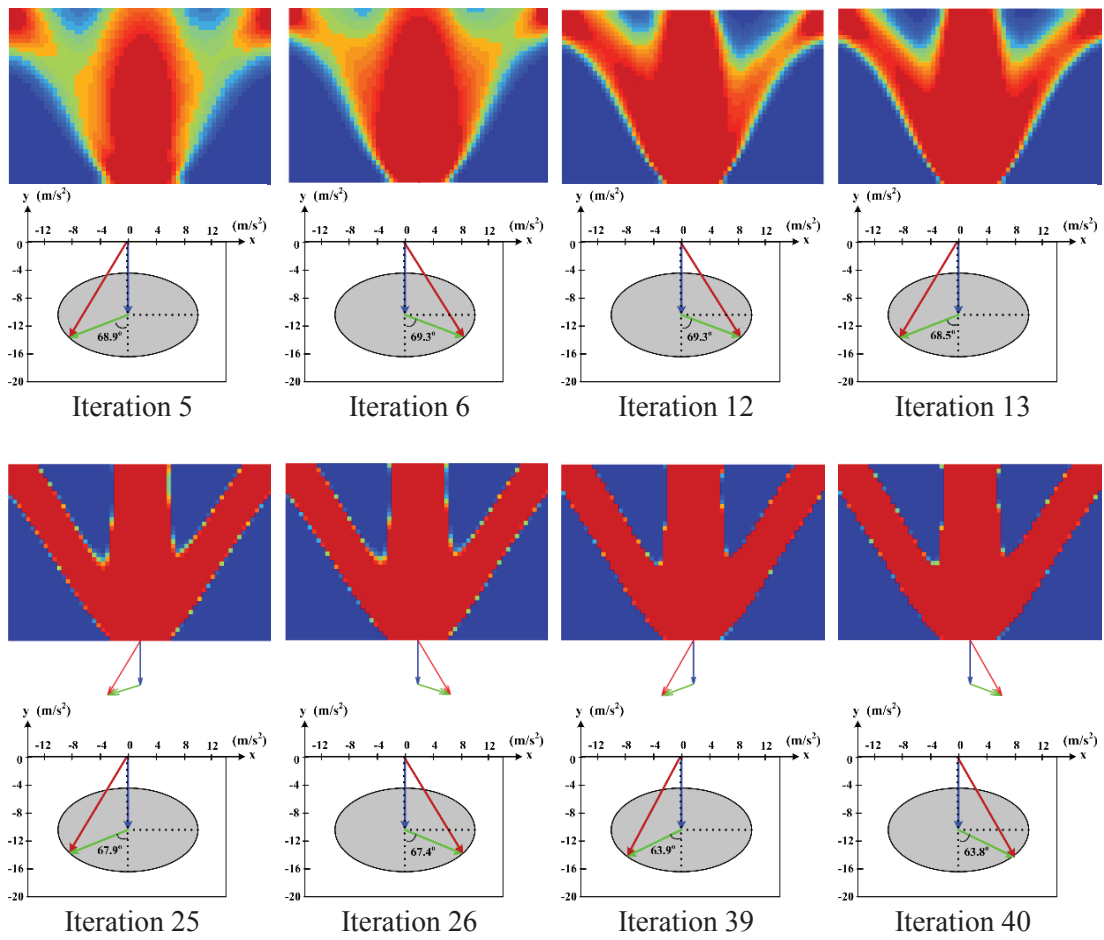
Fig. 2.5 Some intermediate designs and the final robust optimal design.

Table 2.1 Objective function and worst-case acceleration direction for last ten iterations.

Iter. Num.	Obj. ($\times 10^{-2}$ N·m)	Direction of variation part	Iter. Num.	Obj. ($\times 10^{-2}$ N·m)	Direction of variation part
31	0.710	$(-0.911, -0.413)^{\mathrm{T}}$	32	0.707	$(0.909, -0.416)^{\mathrm{T}}$
33	0.702	$(-0.907, -0.421)^{\mathrm{T}}$	34	0.701	$(0.906, -0.424)^{\mathrm{T}}$
35	0.695	$(-0.904, -0.428)^{\mathrm{T}}$	36	0.694	$(0.902, -0.431)^{\mathrm{T}}$
37	0.690	$(-0.900, -0.435)^{\mathrm{T}}$	38	0.691	$(0.900, -0.440)^{\mathrm{T}}$
39	0.685	$(-0.898, -0.440)^{\mathrm{T}}$	40	0.685	$(0.897, -0.442)^{\mathrm{T}}$

For comparison, the optimal design for the same structures under deterministic acceleration (the nominal part) is shown in Fig. 2.6. Apparently, there are obvious differences between this deterministic optimal design and the robust optimal design shown in Fig. 2.5.
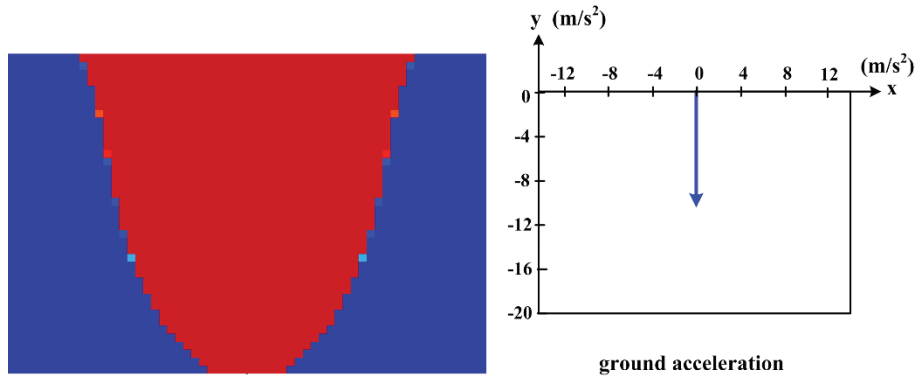
Fig. 2.6 Deterministic optimal design under nominal ground acceleration.

For further evaluating the change of the structural dynamic performance after optimization, the eigenfrequencies for the initial design and optimal design are summarized in Table 2.2. It is

found that the first eight eigenfrequencies all increase after optimization, and move far away from the specified excitation frequency (60 Hz). The absolute dynamic compliance sweep of the robust optimal design (obtained under $f_P = 60$ Hz excitation) under the worst-case ground accelerations for each individual excitation frequency point in the range of $f_P = 20\text{-}100$ Hz are plotted in Fig. 2.7. For comparison, the curve of the absolute dynamic compliance for a fully solid design ($x_e = 1.0$ for $e = 1, 2, ..., 2400$) is also given. It is seen that the optimal design has a better dynamic propriety than the fully solid design in this wide frequency range. The worst-case accelerations and the optimal design both change as the excitation frequency increases. The influence of the excitation frequency will be further discussed later.

Table 2.2 Comparisons of eigenvalue analysis results of the initial design and the robust optimal design.

Order	Natural frequencies of initial design (Hz)	Natural frequencies of robust optimal design (Hz)
1	156.0	222.2
2	241.7	387.6
3	365.3	405.8
4	469.2	565.6
5	476.7	721.0
6	571.6	807.9
7	664.9	908.0
8	715.8	1025.9
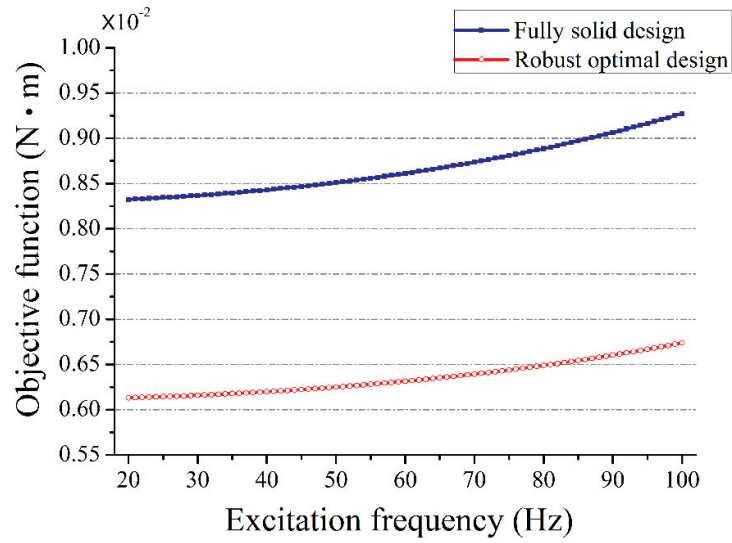
Fig. 2.7 Absolute dynamic compliance sweep of the robust optimal design and the fully solid design for different excitation frequencies.

In the following, we study the dependence of the optimal topology on the excitation frequency. Here, we consider the same structure and uncertain ground acceleration magnitude as mentioned, but four different excitation frequencies f_p =40, 90, 130 and 180 Hz. The obtained optimal solutions are shown in Fig. 2.8. It is found that the optimal design undergoes significant changes as the excitation frequency increases. This can be explained by the fact that higher-order eigenmodes may be excited by a higher excitation frequency.

(a)

(b)

(c)

(d)
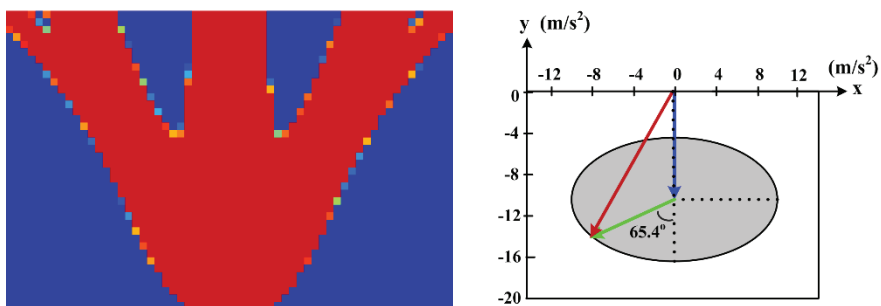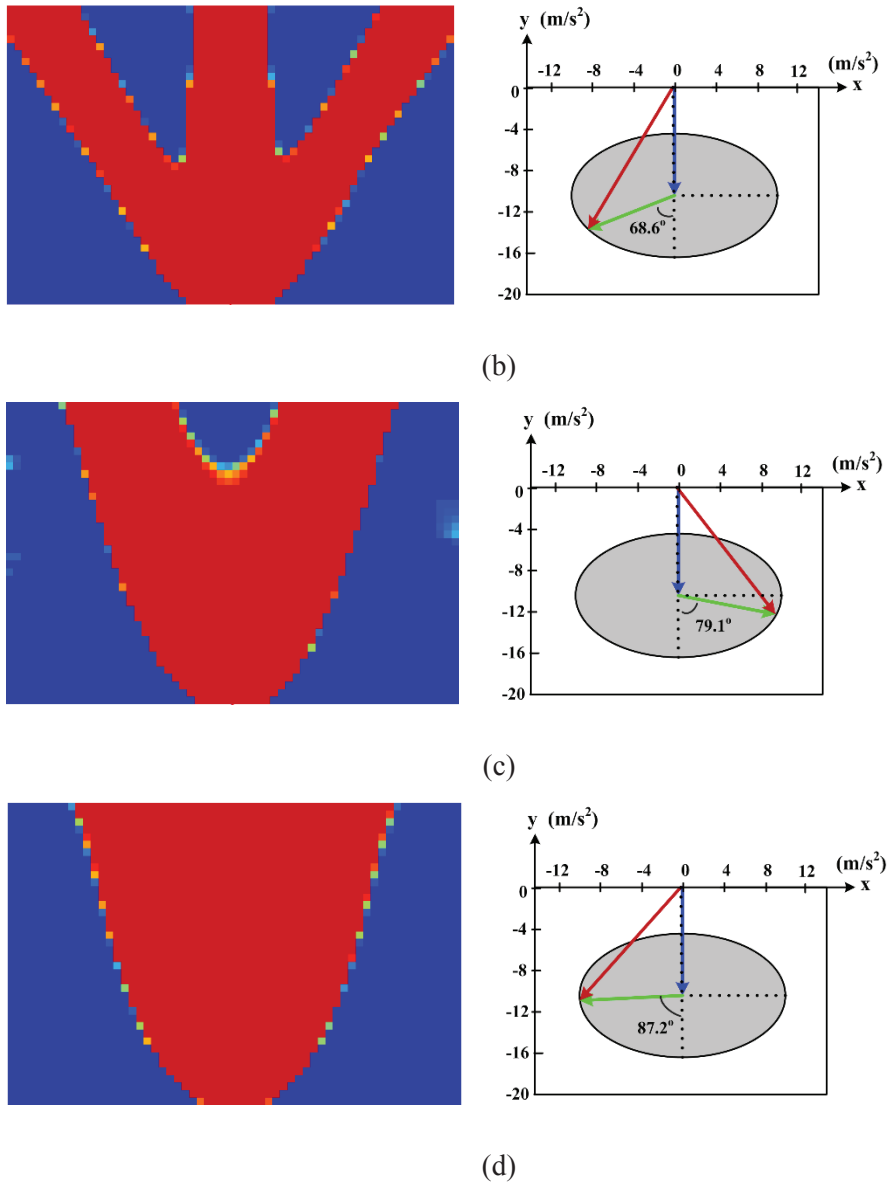
Fig. 2.8 Robust optimal designs and worst-case ground accelerations obtained under different excitation frequencies: (a) $f_p = 40$ Hz; (b) $f_p = 90$ Hz; (c) $f_p = 130$ Hz; (d) $f_p = 180$ Hz.

2.4.3. Robust topology optimization of a cantilever beam with uncertain external excitation

In this example, we consider a rectangular cantilever beam, as shown in Fig. 2.9. The design domain has geometrical dimensions $l_1 = 2$ m and $l_2 = 1$ m. The structure is composed of the same material as in the previous examples. An uncertain external excitation is

applied at the bottom-right corner, and it has the nominal part $\mathbf{p}_0 e^{i\omega t}$

($\mathbf{p}_0 = 2 \times 10^5 \times \left[\sin 30°, \cos 30° \right]^T$ N) and variation part $\mathbf{Wq}e^{i\omega t}$ ($\|\mathbf{q}\| \leq 1$, $\mathbf{W} = 10^5 \times \begin{bmatrix} 1 & 0 \\ 0 & 0.5 \end{bmatrix}$ N),

with the excitation frequency $f_p = 60$ Hz ($\omega = 2\pi f_p$). The design domain is discretize by a

60×40 finite element mesh with the total number of DOFs $n = 5002$. The upper limit of the

volume fraction ratio of the material is given as $f_v = 0.5$ and the initial values of the design

variables are set to be $x_e = 0.5$ $(e = 1, 2, ..., 2400)$.
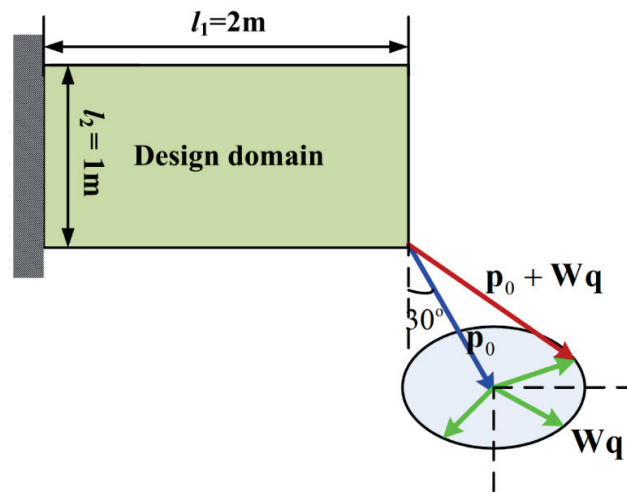
Fig. 2.9 Cantilever beam under uncertain external excitation.

The optimization process converged after 107 iterations. The iteration histories of the

objective function and the material volume are presented in Fig. 2.10, which shows a steady

decrease of the objective function value during the iterations. In fact, the objective function

value has decreased from 2292.8 N·m for the initial design to 470.4 N·m for the final

optimal design. The optimization solution and the worst-case load are given in Fig. 2.11. Again,

the arrows indicate the directions of the worst-case excitation within the given ellipsoidal bound.

Here, the worst-case direction of the variation part is $(-0.4904, -0.8715)^T$. The fundament

frequency of the structure moves from 100.8 Hz for the initial design to 202.4 Hz for the optimal

design.
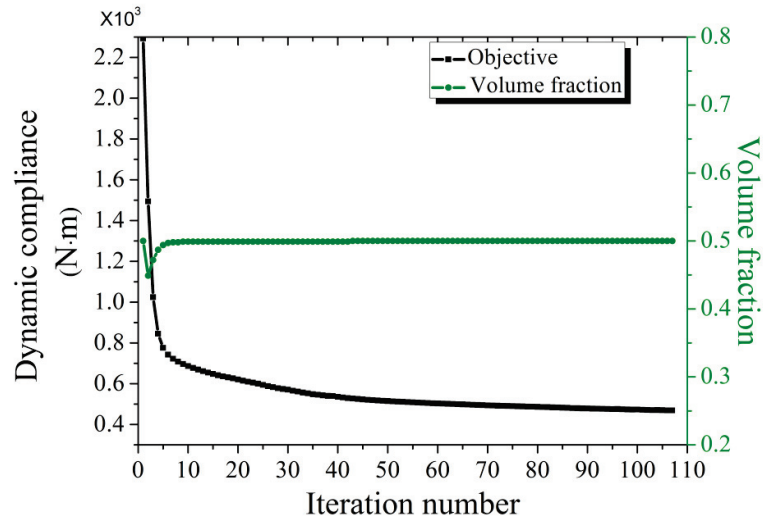
Fig. 2.10 Iteration histories of objective function and volume fraction ratio.
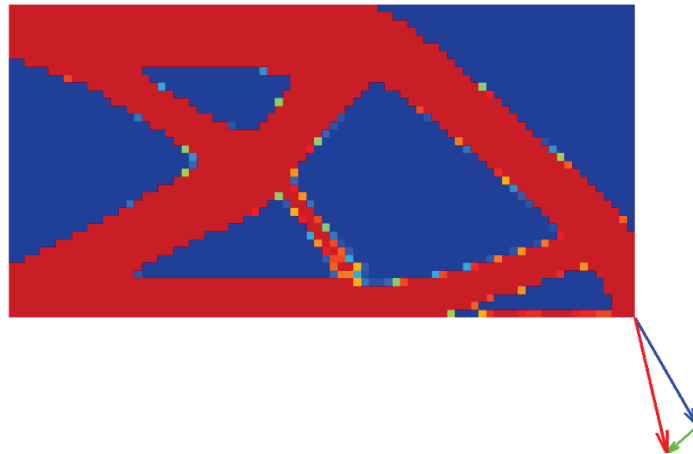
Fig. 2.11 Robust optimal design and worst-case excitation direction.

For comparisons, we now consider two cases with deterministic loading conditions: (1) vertical excitation $\mathbf{p}e^{i\omega t}$ ($\mathbf{p}=2\times10^5\times[0,1]^{\mathrm{T}}$ N, $\omega=2\pi f_{\mathrm{p}}$, $f_{\mathrm{p}}=60$ Hz); (2) nominal excitation $\mathbf{p}_0 e^{i\omega t}$ ($\mathbf{p}_0=2\times10^5\times\left[\sin30°,\cos30°\right]^{\mathrm{T}}$ N, $f_{\mathrm{p}}=60$ Hz). The optimal solutions for the two

53

deterministic cases are given in Fig. 14. The dynamic compliances for the robust design and the two deterministic optimal designs are compared in Table 2.3. As can be seen, the robust optimal topology (Fig. 2.11) is similar to that obtained under the deterministic vertical excitation, but it has an improved dynamic compliance value in presence of uncertain excitations. Moreover, the robust optimal solution exhibits a different force transmission path as compared with the deterministic optimal solution obtained under the nominal excitation.

(a)   (b)
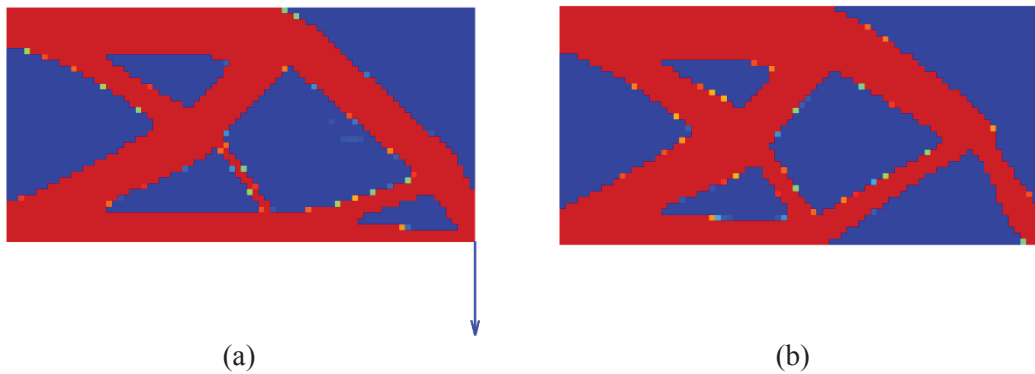
Fig. 2.12 Deterministic optimal designs under (a) vertical excitation; (b) nominal excitation

Table 2.3 Comparisons of optimal designs for the robust design and deterministic designs (f_p =60 Hz).

Dyn. compl.($\mathrm{N \cdot m}$)	Roubst opt. design (Fig. 13)	Deter. opt. design under vertical excitation (Fig. 14 (a))	Deter. opt. design under nominal excitation (Fig. 14 (b))
uncertain excitation (worst-case)	**470.4**	475.0	1013.1
vertical excitation	526.3	500.3	4230.5
nominal excitation	262.1	266.3	235.2

The double-loop method is now added to provide a comparison. As usual, the worst-load case is obtained with a gradient-based optimization algorithm and the adjoint sensitivity method. For comparison, we implement the double-loop method for this example and present the results in Fig. 2.13. The optimization results and the worst-case excitation obtained with the double-loop method are basically the same with that by the present method shown in Fig. 2.11 It is shown that optimization process with the double-loop method converged after 104 iterations, and the objective function value for the optimal design is $470.18\,\mathrm{N\cdot m}$,which is nearly same with the objective value obtained with the proposed method. However, the double-loop method totally calls 3983 times of finite element analysis for finding the worst-case excitation during the optimization process, while the proposed method only needs to solve the low-dimension inhomogeneous eigenvalue problem for 107 times.
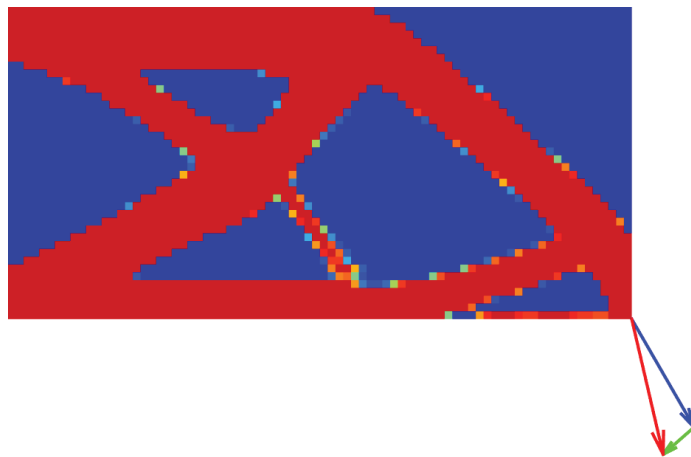
Fig. 2.13 The optimal design and worst-case excitation direction for the double-loop method.

The frequency response sweeps of the absolute dynamic compliance for the robust optimal design (Fig. 2.11) and the deterministic optimal design (Fig. 2.12(a)) in the respective worst-excitation case are compared in Fig. 2.14. As shown in the figure, the robust optimal design is better than the deterministic design when the structures is under an uncertain dynamic

excitation in the whole frequency range between 40 Hz and 80 Hz.
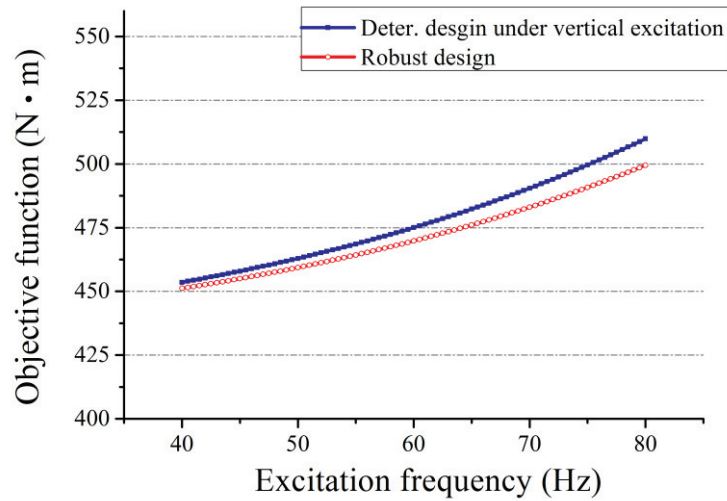
Fig. 2.14 Absolute dynamic compliance sweep of the robust optimal design (Fig. 2.11) and the deterministic optimal design (Fig. 2.12(a)) in the respective worst-case excitation.

2.5 Summary

This chapter deals with robust topology optimization of structures under bounded uncertain excitations. The uncertain excitations are modeled with a non-probabilistic ellipsoidal convex model. The aim of the optimization design is to minimize the absolute dynamic compliance for the worst-case dynamic excitation. We define the objective function by introducing a generalized compliance matrix. The considered robust design problem takes the form of a nested double-loop optimization problem, which can be hardly treated directly with general solution methods (in particular, the inner loop requires global optima to be found). To overcome this inherent difficulty, we propose a reformulation of the robust optimization problem by replacing the inner-loop with an inhomogeneous eigenvalue analysis for finding the maximum absolute dynamic compliance and convert the originally nested problem into a single-loop optimization problem. This reformulation ensures that the globally worst-case

combinations of the uncertain load variations can be found at a low cost. Thus, the worst-case dynamic compliance can be minimized with a gradient-based mathematical programming method. To this end, we have also derived the adjoint-variable sensitivity scheme of the inhomogeneous eigenvalue problem. Numerical examples are presented to illustrate the effectiveness and efficiency of the proposed framework. The obtained optimal topologies are also compared with conventional deterministic solutions, which shows the significance of the robust topology optimization.

It should be pointed out that we consider the unknown-but-bounded dynamic loads/accelerations with three different components, which is a typical case in practical applications (for instance, all the acceleration forces acted on a structure are normally correlated). The proposed method is not limited by the dimensionality of the convex model and thus can be employed to problems with more uncertain load parameters. However, it is unusual to assume that the magnitudes of multiple excitations are bounded by a high-dimensional ellipsoidal convex model in practice. In the cases of multiple uncertain excitations, multiple low-dimensional ellipsoidal models can be employed to represent the uncertainties.

3 Robust topological microstructures design of phononic crystals considering material distribution uncertainty

Most existing topology optimization methods for PnCs are implemented under deterministic conditions. In practical applications, however, PnCs usually exhibit a random distribution of material properties resulting from manufacturing processes (e.g. selective electron beam melting [163] and e-beam lithography[164]). It has been found that the band gap properties of photonic/phononic materials are sensitive to the microstructure configuration and material properties [165]. Unavoidable uncertainties may greatly change or even eliminate band gaps. There is thus a need for a more realistic topology optimization method with which to generate a robust PnC configuration that is less sensitive to the material distribution uncertainty.

The topology optimization of phononic band gaps with uncertainties has seldom been studied [102]. To date, the only attempt made for the topology optimization of PnCs with uncertainties is based on the nonprobability interval model and genetic algorithm [166]. There has been little research on the robust topology optimization of PnCs with random field material properties.

This chapter provides a robust topology optimization framework for achieving a wide band gap design that is insensitive to the uncertain material distribution. Herein, the random material property field is assumed to consist of the density function determining the mean value/standard deviation and a covariance function describing the spatial variability of the random field, and the Young's modulus fields of PnCs are assumed to be a Gaussian random field. Such uncertainties may considerably affect the band gaps of PnCs, as illustrated in Fig. 3.1. To predict the stochastic band gap, the EOLE method is first introduced to discretize the random Young's modulus fields into several uncorrelated uncertain variables, and the mean width of the band gap and the standard deviation are then calculated with the non-intrusive PCE method. Herein,

the PCE coefficients are obtained from the deterministic band gap analysis results obtained with the finite element method (FEM) at specified quadrature points, and the deterministic band gaps of PnCs are aggregated with the Kreisselmeier–Steinhauser (KS) function [167] of the frequency data for each wave vector. Furthermore, the robust topology optimization problem is formulated using the rational approximation of material properties (RAMP) model [32], where the objective is defined as a weighted sum of the mean value and the negative of the standard deviation of the band gaps. The sensitivity analysis schemes for the stochastic band gap response and deterministic band gaps at sampling points of PCE are derived, and the optimization problem is solved with a gradient-based mathematical programming algorithm.
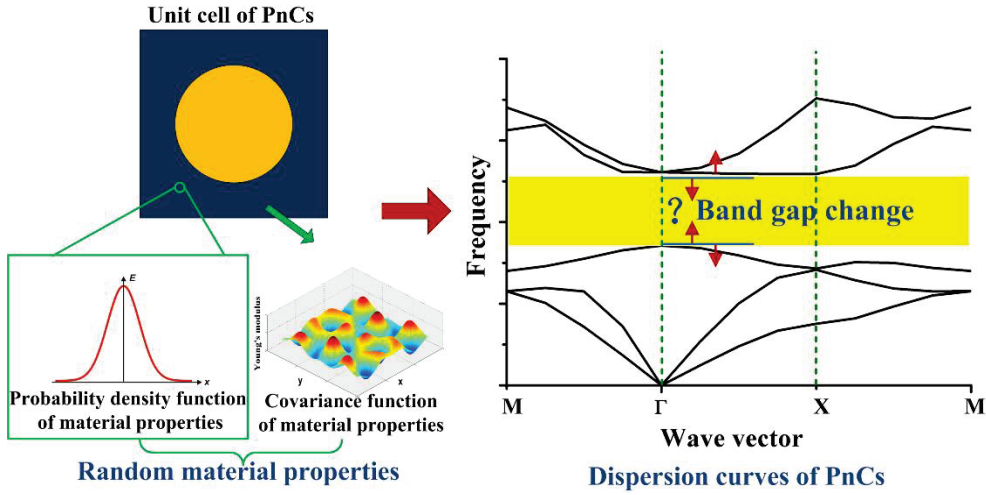
Fig.3.1 Schematic of the band gap variation of PnCs due to the random distribution of material properties.

3.1 Deterministic band analysis of PnCs with the FEM

The governing equation for wave propagation in a three-dimensional inhomogeneous isotropic elastic continuum can be expressed as

$$\rho(\mathbf{r})\ddot{\mathbf{U}} = \nabla\left(\lambda(\mathbf{r}) + \mu(\mathbf{r})\right)\nabla\cdot\mathbf{U} + \nabla\cdot\mu(\mathbf{r})\nabla\mathbf{U}, \qquad (3.1)$$

where $\mathbf{r} = \{x, y\}$ is the position vector, $\mathbf{U} = \{u, v, w\}^{\mathrm{T}}$ is the displacement vector along coordinate directions x, y, and z, $\rho(\mathbf{r})$ is the material density, ∇ is the gradient operator, $\lambda(\mathbf{r})$ and $\mu(\mathbf{r})$ are Lamé coefficients, and Young's modulus E and shear modulus G are respectively expressed as $E = (3\lambda + 2\mu)\mu / (\lambda + \mu)$ and $G = \mu$.

We consider that elastic waves only propagate on the x–y plane (i.e., $\partial \mathbf{U} / \partial z = 0$). Governing equation (3.1) can thus be split into two coupled in-plane modes in Eq. (3.2) and one out-of-plane mode in Eq. (3.3):

$$\begin{cases} \rho(\mathbf{r})\dfrac{\partial^2 u}{\partial t^2} = \dfrac{\partial}{\partial x}\left[(2\mu(\mathbf{r}) + \lambda(\mathbf{r}))\dfrac{\partial u}{\partial x} + \lambda(\mathbf{r})\dfrac{\partial v}{\partial y}\right] + \dfrac{\partial}{\partial y}\left[\mu(\mathbf{r})\left(\dfrac{\partial u}{\partial y} + \dfrac{\partial v}{\partial x}\right)\right] \\ \rho(\mathbf{r})\dfrac{\partial^2 v}{\partial t^2} = \dfrac{\partial}{\partial x}\left[\mu(\mathbf{r})\left(\dfrac{\partial v}{\partial x} + \dfrac{\partial u}{\partial y}\right)\right] + \dfrac{\partial}{\partial y}\left[(2\mu(\mathbf{r}) + \lambda(\mathbf{r}))\dfrac{\partial v}{\partial y} + \lambda(\mathbf{r})\dfrac{\partial u}{\partial x}\right] \end{cases}, \tag{3.2}$$

$$\rho(\mathbf{r})\frac{\partial^2 w}{\partial t^2} = \frac{\partial}{\partial x}\left[\mu(\mathbf{r})\frac{\partial w}{\partial x}\right] + \frac{\partial}{\partial y}\left[\mu(\mathbf{r})\frac{\partial w}{\partial y}\right]. \tag{3.3}$$

For the band calculation of an infinitely periodic structure, the global problem can be solved by analyzing the smallest repetitive unit cell. According to the Floquet–Bloch theorem, the displacement vector gives

$$\mathbf{U}(\mathbf{r}, \mathbf{k}) = \tilde{\mathbf{U}}(\mathbf{r}) e^{i\mathbf{k}^{\mathrm{T}}\mathbf{r}} e^{i\omega t}, \tag{3.4}$$

$$\mathbf{U}(\mathbf{r} + \mathbf{R}, \mathbf{k}) = \mathbf{U}(\mathbf{r}, \mathbf{k}) e^{i\mathbf{k}^{\mathrm{T}}\mathbf{R}}. \tag{3.5}$$

Here, $\tilde{\mathbf{U}}(\mathbf{r})$ is a periodic displacement field of $\mathbf{r}$ with the same periodicity as the structure, $\mathbf{k} = \{\mathbf{k}_x, \mathbf{k}_y\}$ is the plane wave vector limited to the first Brillouin zone (Bloch wave vector), ω is the angular frequency ($\omega = 2\pi f$, f is the circular frequency), and $\mathbf{R} = [a_c, a_c]$ is the lattice periodicity vector of the square PnC unit cell with width a_c.

By substituting (3.4) into (3.2) or (3.3) and through finite element discretization, the generalized eigenvalue equation is obtained as

$$\left(\mathbf{K}(\mathbf{k}) - \omega^2 \mathbf{M}\right)\mathbf{U} = 0, \tag{3.6}$$

where $\mathbf{K}(\mathbf{k})$ and $\mathbf{M}$ are respectively the stiffness and mass matrices of the periodic unit cell.

The band structure of elastic waves can be obtained by solving the generalized complex eigenvalue problem (3.6) for any values of wave vector $\mathbf{k}$. Owing to periodicity in the Bloch–Floquet condition and symmetry of the unit cell structure, the whole band structure can be determined from the irreducible Brillouin zone; i.e., the wave vector $\mathbf{k}$ can be restricted to the boundary of the curve of the triangular $\Gamma\mathrm{XM}$ zone shown in Fig. 3.2.
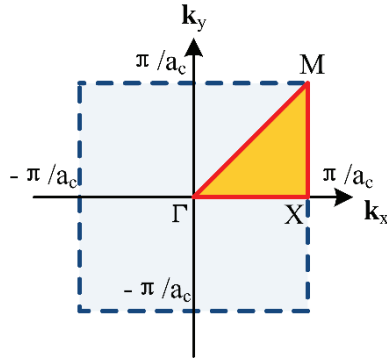
Figure 3.2. Schematic illustration of the irreducible Brillouin zone $\Gamma\mathrm{XM}$.

The band structure for homogeneous single-phase materials shows that eigenmodes exist for all frequencies [103], which means elastic waves within all frequencies may propagate through the structure. To achieve a band gap structure, a multi-phase material cell (two material phases in the present study) should be introduced.

3.2 Stochastic band gap analysis with material distribution uncertainty

The random field is usually characterized by means of a probability density function $p(\mathbf{r})$ (from which the mean value and the standard deviation at a fixed position $\mathbf{r}$ can be determined) and a spatial covariance function $\mathbf{C}(\mathbf{r}_1, \mathbf{r}_2)$ describing how the random field varies in space.

In this study, we consider the material distribution uncertainty of a two-material (two-phase) phononic crystal. Herein, the mass densities of the two materials are regarded as deterministic over the whole cell domain; the Young's modulus fields of PnCs are uncertain and assumed to satisfy a Gaussian random field with mean values μ_{E_1} and μ_{E_2} and standard deviations σ_{E_1} and σ_{E_2}.

The random Young's modulus field $\tilde{E}(\mathbf{r})$ can be further expressed as

$$\tilde{E}(\mathbf{r}) = \mu_E(\mathbf{r}) + \eta(\mathbf{r}), \tag{3.7}$$

where $\eta(\mathbf{r})$ is a standard zero-mean, homogeneous Gaussian random field with standard deviation σ_E.

The relationship between values of Young's modulus at any two positions $\mathbf{r}_1$ and $\mathbf{r}_2$ may be determined by a squared exponential covariance function as

$$\mathbf{C}_E(\mathbf{r}_1, \mathbf{r}_2) = \sigma_E^2 \exp\left(-\frac{\|\mathbf{r}_1 - \mathbf{r}_2\|^2}{L^2}\right), \tag{3.8}$$

where $\|\cdot\|$ denotes the Euclidean distance and L is the correlation length.

3.2.1 Discretization of random material property fields with EOLE

It is common practice to use several random variables instead of random fields to represent the uncertainty in material properties. The standard Gaussian random field $\eta(\mathbf{r})$ can be discretized with the EOLE method (similar to K-L expansion-based methods). Here, N representative nodal points $\mathbf{r}_s = \{\mathbf{r}_1, \mathbf{r}_2, ..., \mathbf{r}_N\}^T$ are first selected in the random field domain, and the dimensions of the infinite random material property fields can be reduced into an N-dimensional vector $\mathbf{v} = \{\eta(\mathbf{r}_1), \eta(\mathbf{r}_2), ..., \eta(\mathbf{r}_N)\}^T$, and the random field $\eta(\mathbf{r})$ can be expressed as

$$\eta(\mathbf{r}) \approx \sum_{k=1}^{N} \frac{1}{\sqrt{\lambda_k}} \boldsymbol{\psi}_i^T \mathbf{C}_{\mathbf{v}\eta}(\mathbf{r}) \xi_k, \tag{3.9}$$

where $\mathbf{C}_{\mathbf{v}\eta}(\mathbf{r}) = \{C_\eta(\mathbf{r}_1 - \mathbf{r}), C_\eta(\mathbf{r}_2 - \mathbf{r}), ..., C_\eta(\mathbf{r}_N - \mathbf{r})\}^T$. $\xi_k (k = 1, 2, ..., N)$ denotes uncorrelated Gaussian random variables; i.e., $E(\xi_k) = 0$, $E(\xi_k \xi_j) = \delta_{kj}$ ($E(\cdot)$ is the mathematical expectation, δ_{kj} is the Kronecker delta). λ_k and $\boldsymbol{\psi}_k$ are the eigenvalues and eigenvectors of the covariance matrix $\mathbf{C}_{\mathbf{v}}$ ($\mathbf{C}_{\mathbf{v}} \boldsymbol{\psi}_k = \lambda_k \boldsymbol{\psi}_k$), and the matrix $\mathbf{C}_{\mathbf{v}}$ is defined as

$$\mathbf{C}_{\mathbf{v}} = \begin{bmatrix} C_\eta(\mathbf{r}_1, \mathbf{r}_1) & \cdots & C_\eta(\mathbf{r}_1, \mathbf{r}_N) \\ \vdots & \ddots & \vdots \\ C_\eta(\mathbf{r}_N, \mathbf{r}_1) & \cdots & C_\eta(\mathbf{r}_N, \mathbf{r}_N) \end{bmatrix}. \tag{3.10}$$

To reduce the dimensionality of the problem, the series expressed by Eq. (3.9) can be truncated into M terms ($M \leq N$) with the M largest eigenvalues. Approximating the expression of the random field, $\eta(\mathbf{r})$ is then reformulated as

$$\tilde{\eta}(\mathbf{r}) \approx \sum_{k=1}^{M} \frac{1}{\sqrt{\lambda_k}} \boldsymbol{\psi}_i^T \mathbf{C}_{\mathbf{v}\eta}(\mathbf{r}) \xi_k. \tag{3.11}$$

The uncertain Young's moduli of the two materials in the PnCs cell are considered. In this study, the nodal points of EOLE are fixed at all finite element centers (where the finite elements of the unit cell are discretized with uniform square elements), and the two random fields for the two material components share the same discrete points. The locations of the nodal points in the PnCs unit cell are shown in Fig. 2.3. It is noted that the two materials of PnCs are assumed to have independent random fields of Young's modulus. Therefore, if M terms of uncorrelated random variables are truncated in each material phase, a total of $N_{EOLE} = 2M$ uncorrelated random variables will be used in the discretization of the random field of the material property.

Material 1 (epoxy)　　　Material 2 (plumbum)
○ EOLE points of Phase 1　＋ EOLE points of Phase 2
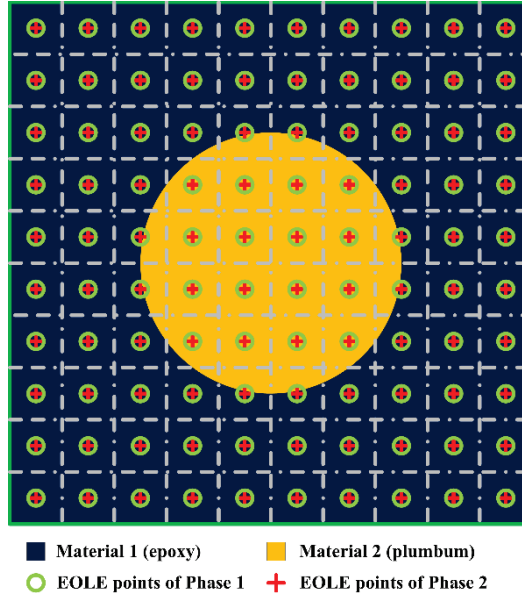
Fig. 2.3 Locations of the EOLE nodal points in the PnC unit cell

The average error variance $\bar{e}_{EOLE}$ over the design domain can be employed to evaluate the accuracy of the random field discretization; it can be expressed as [168]

$$\bar{e}_{EOLE} = \frac{1}{s_D} \int_D \frac{\text{Var}\left[\eta(\mathbf{r}) - \tilde{\eta}(\mathbf{r})\right]}{\text{Var}\left[\eta(\mathbf{r})\right]} \, d\mathbf{r} = \sum_{j=1}^{N} \left(1 - \sum_{k=1}^{M} \frac{\left(\boldsymbol{\psi}_k^T \mathbf{C}_{vj}\right)^2}{\lambda_k}\right), \quad (3.12)$$

where S_D is the area of the domain of the unit cell and $\mathbf{C}_{vj}$ is the jth column of the

covariance matrix $\mathbf{C_v}$. The term S_D vanishes owing to the use of the uniform nodal points and mesh.

3.2.2 Stochastic response analysis with PCE

After discretizing the random field of input material properties $\tilde{E}(\mathbf{r})$ with several uncorrelated random variables $\boldsymbol{\xi} = \{\xi_1,...,\xi_{N_{EOLE}}\}$ (recalling $N_{EOLE} = 2M$)via the EOLE method, the stochastic response $g(\boldsymbol{\xi})$ of the PnCs (i.e., the band structure in this study) can be predicted employing polynomial chaos (PC) expansion. PC-expansion-based uncertainty analysis is summarized as [139, 169]

$$g(\boldsymbol{\xi}) = \sum_{i=0}^{\infty} g_i \Phi_i (\boldsymbol{\xi}), \tag{3.13}$$

where $\Phi_i(\boldsymbol{\xi})$ denotes PC bases, which are orthogonal with respect to the probability density of the random variables. If the input fields are Gaussian variables, the PC bases should be Hermite polynomials (where general PC bases for different types of random variables can be found in [170]). The orthogonal property of PC bases is expressed as

$$\mathrm{E}\left(\Phi_i \Phi_j\right) = \mathrm{E}\left(\Phi_i^2\right)\delta_{ij}. \tag{3.14}$$

In practice, a few PC terms are enough to maintain the prediction accuracy and are able to reduce the computational cost. The expression of (3.13) can be truncated as

$$g(\boldsymbol{\xi}) \approx \sum_{i=0}^{N_{PCE}} g_i \Phi_i (\boldsymbol{\xi}), \tag{3.15}$$

where $N_{PCE} + 1$ is the number of coefficients, which depends on the number of random variables N_{EOLE} and the polynomial order P. N_{PCE} can be determined as

65

$$N_{\text{PCE}} + 1 = \frac{(N_{\text{EOLE}} + P)!}{N_{\text{EOLE}}! P!}. \tag{3.16}$$

A nonintrusive approach [139] for calculating the PC coefficients g_i of the response $g(\xi)$ is employed. By post-multiplying Φ_k in Eq. (3.15) and introducing the orthogonal property (3.14), the coefficients g_i give

$$g_k = \frac{\text{E}\left(g(\xi)\Phi_k\right)}{\text{E}\left(\Phi_k^2\right)}, \quad k = 0, 1, \dots, N_{\text{PCE}}. \tag{3.17}$$

Here, the value of $\text{E}\left(\Phi_k^2\right)$ can be easily obtained because there are analytical expressions for orthogonal polynomials, and the term $\text{E}\left(g(\xi)\Phi_k\right)$ is calculated as

$$E\left(g(\xi)\Phi_k(\xi)\right) = \int_{\Omega} g(\xi)\Phi_k(\xi)\rho(\xi)\,d\xi \approx \sum_{g=1}^{N_g} g\left(\xi^g\right)\Phi_k\left(\xi^g\right)w^g, \tag{3.18}$$

where $\rho(\xi)$ is the probability density of the uncorrelated random variables ξ, $\xi^g = \left\{\xi_1^g, \xi_2^g, \dots, \xi_{N_{\text{EOLE}}}^g\right\}$ and w^g are the gth quadrature point and the corresponding weight coefficient, N_g is the total number of quadrature points, and Ω is the integration domain. For the stochastic response analysis of PnCs consisting of two materials, the number of dimensions of the random variables via the EOLE method is usually not low ($N_{\text{ELOE}} \geq 4$), and the sparse grids quadrature techniques [171] can thus be used to reduce the number of quadrature points.

After obtaining the polynomial expansion of (3.15), the mean value $\mu\left(g(\xi)\right)$ and the standard deviation $\sigma\left(g(\xi)\right)$ of the response $g(\xi)$ (band gap in this study) can be evaluated as

$$\mu\left(g(\xi)\right) = \int_D g(\xi)\rho(\xi)\,d\xi = g_0, \tag{3.19}$$

$$\sigma\big(g(\xi)\big)=\sqrt{\int_D\big[g(\xi)-\mu\big(g(\xi)\big)\big]^2\rho(\xi)\mathrm{d}\xi}=\sqrt{\sum_{i=1}^{N_{\mathrm{PCE}}}g_i^2(\xi)\mathrm{E}\big(\Phi_i^2(\xi)\big)}. \qquad (3.20)$$

3.3 Robust topology optimization of PnCs with a random-field material property

3.3.1 Objective function

For the deterministic design optimization of PnCs, it is desired to achieve the largest possible wavelength through the design of the specific unit cell. There are several choices of objective functions, including maximizing the band gap [172, 173] or relative band gap [103, 105] between two consecutive orders of frequencies, and minimizing the wave magnitudes at specified points subjected to the external excitation loads within a frequency range [174]. We here choose maximizing the band gap between bands j and $j+1$ as the objective function, which can be expressed as [172]

$$\max:\ f_{\mathrm{D}}=\min_{i=1}^{n_k}\omega_{j+1}\big(\mathbf{k}_i\big)-\max_{i=1}^{n_k}\omega_j\big(\mathbf{k}_i\big), \qquad (3.21)$$

where n_k and $\mathbf{k}_i$ are the number of considered wave vectors and the ith considered wave vector of $\mathbf{k}$ for the generalized eigenvalue problem (3.6), and $\omega_{j+1}\big(\mathbf{k}_i\big)$ and $\omega_j\big(\mathbf{k}_i\big)$ are the $j+1$th and jth eigenvalues of the generalized eigenvalue problem with $\mathbf{k}_i$. Such a min-max objective function is generally differentiable, which presents difficulties when solving the optimization problem with gradient-based algorithms. We thus employ the K-S aggregated function [167], which is sufficiently smooth and provides an envelope surface of the minimum and maximum function values. In this way, the objective function for the band gap is rewritten as

$$\max : \tilde{f}_{\mathrm{D}} = \frac{1}{\eta_1} \ln\left(\sum_{i=1}^{n_k} e^{\eta_1 \cdot \omega_{j+1}(\mathbf{k}_i)} \right) - \frac{1}{\eta_2} \ln\left(\sum_{i=1}^{n_k} e^{\eta_1 \cdot \omega_j(\mathbf{k}_i)} \right), \tag{3.22}$$

where η_1 and η_2 are the aggregation parameters of the K-S function. Herein, η_1 should be a negative real number so as to achieve the minimum envelope and η_2 is a positive number so as to have the maximum envelope. The magnitudes of η_1 and η_2 have a crucial effect on the approximation accuracy of the K-S function, and the choice of values of aggregation parameters can be found in the literature [111].

The above objective function (3.22) can be used in the deterministic topology optimization. For robust design optimization problems of PnCs, the robustness index can be formulated by the weighted sum of the mean value and the negative of the standard deviation of the K-S function with respect to the uncertain parameters as [126]

$$\max : f(\mathbf{x}, \boldsymbol{\xi}) = \mu\left(\tilde{f}_{\mathrm{D}}(\mathbf{x}, \boldsymbol{\xi}) \right) - \alpha \cdot \sigma\left(\tilde{f}_{\mathrm{D}}(\mathbf{x}, \boldsymbol{\xi}) \right), \tag{3.23}$$

where $\mathbf{x}$ and $\boldsymbol{\xi}$ are respectively the design variables (which will be discussed in the next subsection) and uncertainty parameters. The mean value and standard deviation of the band gap can be obtained from Eqs. (3.19) and (3.20). α is a positive weight coefficient, which can be considered to balance the mean value and standard deviation and affects the optimization result remarkably.

3.3.2 Robust topology optimization formulation

The task of robust structural design optimization is to minimize the variability of the structural performance, thus the standard deviation of the structural performance is usually introduced into the design objective along with the mean value, rendering a multi-criteria optimization problem [175]. In this study, a prescribed relative weight factor α is employed

to investigate the trade-offs between the mean value and the standard deviation.

With the above objective function (3.23), we propose the robust topology optimization formulation that aims to find a maximum band gap design that is less sensitive to uncertainty in the material distribution. The optimization formulation is written as

$$
\begin{aligned}
\max : f\left(\mathbf{x}, \boldsymbol{\xi}\right) &= \mu\left(\tilde{f}_{\mathrm{D}}\left(\mathbf{x}, \boldsymbol{\xi}\right)\right) - \alpha \cdot \sigma\left(\tilde{f}_{\mathrm{D}}\left(\mathbf{x}, \boldsymbol{\xi}\right)\right), \\
\text{s.t.} \quad : \tilde{f}_{\mathrm{D}} &= \frac{1}{\eta_1} \ln\left(\sum_{i=1}^{n_k} e^{\eta_1 \cdot \omega_{j+1}(\mathbf{k}_i)}\right) - \frac{1}{\eta_2} \ln\left(\sum_{i=1}^{n_k} e^{\eta_1 \cdot \omega_j(\mathbf{k}_i)}\right), \\
&\left(\mathbf{K}(\mathbf{k}) - \omega^2 \mathbf{M}\right) \mathbf{U} = 0, \\
&0 \le x_e \le 1, \quad e = 1, 2, ..., N_e.
\end{aligned}
\tag{3.24}
$$

Here, the vector $\mathbf{x} = \left\{x_1, x_2, ..., x_{N_e}\right\}$ denotes the element-wise design variables describing the distribution of material 1 (epoxy) and material 2 (plumbum) of the PnC unit cell, with N_e being the total number of finite elements in the unit cell. Here, $x_e = 1$ indicates that the element is filled with material 2 while $x_e = 0$ indicates that the element is filled with material 1. For the topology optimization, interpolation models should be employed to relate the material properties with the design variables. Here, the RAMP model [32] is adopted, and Young's modulus $E_e\left(x_e, \boldsymbol{\xi}\right)$ and the mass density ρ_e of the eth element (with the element center located at $\mathbf{r}_e$) are expressed by

$$
E_e\left(x_e, \boldsymbol{\xi}\right) = E_1\left(\mathbf{r}_e, \boldsymbol{\xi}\right) + \frac{x_e}{1 + p\left(1 - x_e\right)}\left(E_2\left(\mathbf{r}_e, \boldsymbol{\xi}\right) - E_1\left(\mathbf{r}_e, \boldsymbol{\xi}\right)\right),
\tag{3.25}
$$

$$
\rho_e = \rho_1 + \frac{x_e}{1 + p\left(1 - x_e\right)}\left(\rho_2 - \rho_1\right),
\tag{3.26}
$$

where E_1, E_2, ρ_1, and ρ_2 are respectively the Young's moduli and mass densities of materials 1 and 2. The parameter p is set to 4 to penalize intermediate density such that there is a clear

0/1 material distribution in the optimal solution. In addition, the Heaviside density filter [176] is adopted to produce a clearer boundary shape of the design. It is recalled that Young's moduli of the two materials are considered as random field functions, while the mass densities of the materials are assumed to be deterministic in the present study. Here, the RAMP interpolation model is employed. It is capable of avoiding spurious local vibration modes, which usually appear in low-density regions when the traditional power-law SIMP model is used (some numerical techniques can be adopted to bypass this issue, see e.g. Du and Olhoff [177]).

The optimization problems can be solved with a gradient-based mathematical programming algorithm, which requires sensitivity analysis of the band gap with respect to the design variables; sensitivity analysis is discussed in the following subsection.

3.4 Sensitivity analysis

Combining the EOLE method with PC expansions, the mean value and standard deviation of the objective function are obtained using the band gaps at the specified deterministic sampling points ξ^g in Eqs. (3.18)–(3.20). Sensitivity analysis for the optimization problem (3.24) can therefore be conducted in two steps: (1) analysis of the deterministic sensitivity of the band gap at specified sampling points and (2) analysis of the mean value and standard deviation of the band gap via PC expansion.

3.4.1 Deterministic band gap sensitivity at the specified sampling points

The deterministic band gap sensitivity of the K-S function-aggregated objective function at the kth sampling point ξ^k of the random variables ξ in the PC expansion can be calculated as

$$\frac{\partial \tilde{f}_{\mathrm{D}}\left(\mathbf{x},\boldsymbol{\xi}^{g}\right)}{\partial x_{e}} = \frac{\displaystyle\sum_{i=1}^{N_{k}}\left(\mathrm{e}^{\eta_{1}\cdot\omega_{j+1}(\mathbf{k}_{i})}\,\dfrac{\partial \omega_{j+1}\left(\mathbf{k}_{i},\boldsymbol{\xi}^{g}\right)}{\partial x_{e}}\right)}{\displaystyle\sum_{i=1}^{N_{\mathrm{p}}}\mathrm{e}^{\eta_{1}\cdot\omega_{j+1}(\mathbf{k}_{i})}} - \frac{\displaystyle\sum_{i=1}^{N_{k}}\left(\mathrm{e}^{\eta_{2}\cdot\omega_{j}(\mathbf{k}_{i})}\,\dfrac{\partial \omega_{j}\left(\mathbf{k}_{i},\boldsymbol{\xi}^{g}\right)}{\partial x_{e}}\right)}{\displaystyle\sum_{i=1}^{N_{\mathrm{p}}}\mathrm{e}^{\eta_{2}\cdot\omega_{j+1}(\mathbf{k}_{i})}}. \tag{3.27}$$

Herein, only the sensitivities of the two consecutive eigenfrequencies ($\mathrm{d}\omega_{j+1}\left(\mathbf{k}_{i},\boldsymbol{\xi}^{g}\right)/\mathrm{d}x_{e}$

and $\mathrm{d}\omega_{j}\left(\mathbf{k}_{i},\boldsymbol{\xi}^{g}\right)/\mathrm{d}x_{e}$) at each wave vector $\mathbf{k}_{i}$ need to be further calculated. They can be

obtained as follows.

In the case that there are no repeated eigenfrequencies, the sensitivity of the jth

eigenfrequency with respect to the eth design variable can be easily obtained as

$$\frac{\partial \omega_{j}\left(\mathbf{k}_{i},\boldsymbol{\xi}^{g}\right)}{\partial x_{e}} = \frac{\mathbf{U}_{j}^{\mathrm{T}}\left(\dfrac{\partial \mathbf{K}\left(\mathbf{k}_{i},\boldsymbol{\xi}^{g}\right)}{\partial x_{e}} - \omega_{j}^{2}\dfrac{\mathrm{d}\mathbf{M}}{\mathrm{d}x_{e}}\right)\mathbf{U}_{j}}{2\omega_{j}}, \tag{3.28}$$

where $\mathbf{U}_{j}$ is the eigenvector corresponding to the eigenvalue ω_{j} of the generalized

eigenvalue problem (3.6), and has been normalized by the mass matrix $\mathbf{M}$ so that

$\mathbf{U}_{j}^{\mathrm{T}}\mathbf{M}\mathbf{U}_{j}=1$.

In some configurations of PnCs, one eigenfrequency may correspond to two eigenvectors.

We suppose that a repeated eigenfrequency ω has two normalized orthogonal eigenvectors

$\mathbf{U}_{1}$ and $\mathbf{U}_{2}$ ($\mathbf{U}_{1}^{\mathrm{T}}\mathbf{M}\mathbf{U}_{2}=0$). Because any linear combination of the two eigenvectors is also an

eigenvector with the same eigenfrequency, the eigenvector $\bar{\mathbf{U}}$ can be expressed as

$$\bar{\mathbf{U}} = c_{1}\mathbf{U}_{1} + c_{2}\mathbf{U}_{2}, \tag{3.29}$$

$$\bar{\mathbf{U}}^{\mathrm{T}}\mathbf{M}\bar{\mathbf{U}}=1 \quad \left(\text{when } c_{1}^{2}+c_{2}^{2}=1\right). \tag{3.30}$$

By substituting (3.29) into (3.28), we get

$$\frac{\partial \omega^2}{\partial x_e} = c_1^2 g_{11} + c_2^2 g_{22} + 2c_1 c_2 g_{12}, \tag{3.31}$$

with

$$g_{ab} = \mathbf{U}_a^{\mathrm{T}} \left(\frac{\partial \mathbf{K}\left(\mathbf{k}_i, \boldsymbol{\xi}^g\right)}{\partial x_e} - \omega_j^2 \frac{\mathrm{d}\mathbf{M}}{\mathrm{d}x_e} \right) \mathbf{U}_b, \quad a, b = 1, 2. \tag{3.32}$$

The extreme values of $\partial \omega^2 / \partial x_e$ can be evaluated by introducing a Lagrange function $L = c_1^2 g_{11} + c_2^2 g_{22} + 2c_1 c_2 g_{12} + \lambda^{\mathrm{sub}}\left(c_1^2 + c_2^2 - 1\right)$ with the Lagrange multiplier λ^{sub}. By differentiating the Lagrange function with respect to the two constants c_1 and c_2, we have the eigenfrequency sub-problem

$$\begin{bmatrix} g_{11} & g_{12} \\ g_{21} & g_{22} \end{bmatrix} \begin{Bmatrix} c_1 \\ c_2 \end{Bmatrix} + \lambda^{\mathrm{sub}} \begin{Bmatrix} c_1 \\ c_2 \end{Bmatrix} = \begin{Bmatrix} 0 \\ 0 \end{Bmatrix}, \tag{3.33}$$

the solution of which gives eigenvalues and corresponding eigenvectors:

$$\begin{cases} \lambda_1^{\mathrm{sub}} & \text{with } \mathbf{c}_1 = \left\{\mathbf{c}_{11}, \mathbf{c}_{12}\right\}^{\mathrm{T}} \\ \lambda_h^{\mathrm{sub}} & \text{with } \mathbf{c}_h = \left\{\mathbf{c}_{h1}, \mathbf{c}_{h2}\right\}^{\mathrm{T}} \end{cases} \tag{3.34}$$

The sensitivities of the repeated eigenfrequency can be obtained from λ_1^{sub} and λ_h^{sub} as

$$\frac{\partial \omega\left(\mathbf{k}_i, \boldsymbol{\xi}^g\right)}{\partial x_e} = \begin{cases} \lambda_1^{\mathrm{sub}}\left(\mathbf{k}_i, \boldsymbol{\xi}^g\right) & \text{with eigenvector } \bar{\mathbf{U}}_1 = c_{11}\mathbf{U}_1 + c_{12}\mathbf{U}_2 \\ \lambda_h^{\mathrm{sub}}\left(\mathbf{k}_i, \boldsymbol{\xi}^g\right) & \text{with eigenvector } \bar{\mathbf{U}}_h = c_{h1}\mathbf{U}_1 + c_{h2}\mathbf{U}_2 \end{cases} \tag{3.35}$$

We can now obtain the sensitivities of single and repeated eigenfrequencies with respect to the design variables. Furthermore, the sensitivity of the deterministic band gap at a specified sampling point can be evaluated by substituting (3.28) or (3.35) into (3.27).

3.4.2 Stochastic band gap analysis with PC expansions

Having obtained the band gap sensitivity $\partial \tilde{f}_{\mathrm{D}}\left(\mathbf{x},\xi^{g}\right)/\partial x_{e}$ at the specified sampling points, the stochastic band gap sensitivity $\partial \tilde{f}_{\mathrm{D}}\left(\mathbf{x},\xi\right)/\partial x_{e}$ can be defined as

$$\frac{\partial \tilde{f}_{\mathrm{D}}\left(\mathbf{x},\xi\right)}{\partial x_{e}} = \sum_{i=0}^{N_{\mathrm{PCE}}} \frac{\partial \tilde{f}_{\mathrm{D}i}\left(\mathbf{x}\right)}{\partial x_{e}} \Phi_{i}\left(\xi\right). \tag{3.36}$$

By employing the nonintrusive differentiation approach [139], the coefficient terms $\partial \tilde{f}_{\mathrm{D}i}\left(\mathbf{x}\right)/\partial x_{e}$ are evaluated as

$$\frac{\partial \tilde{f}_{\mathrm{D}i}\left(\mathbf{x}\right)}{\partial x_{e}} = \frac{\mathrm{E}\left(\dfrac{\partial \tilde{f}_{\mathrm{D}}\left(\mathbf{x},\xi\right)}{\partial x_{e}} \Phi_{i}\right)}{\mathrm{E}\left(\Phi_{i}^{2}\right)} = \frac{\displaystyle\sum_{g=1}^{N_{g}} \dfrac{\partial \tilde{f}_{\mathrm{D}}\left(\mathbf{x},\xi^{g}\right)}{\partial x} \Phi_{i}\left(\xi^{g}\right) w^{g}}{\mathrm{E}\left(\Phi_{i}^{2}\right)}, \quad i=0,1,...,N_{\mathrm{PCE}}. \tag{3.37}$$

Furthermore, the mean value and standard deviation of the stochastic band gaps are obtained as

$$\begin{aligned}
\frac{\partial \mu\left(\tilde{f}_{\mathrm{D}}\left(\mathbf{x},\xi\right)\right)}{\partial x_{e}} &= \frac{\partial \int_{\Omega} \tilde{f}_{\mathrm{D}}\left(\mathbf{x},\xi\right)\rho\left(\xi\right)\mathrm{d}\xi}{\partial x_{e}} = \int_{\Omega} \frac{\partial \tilde{f}_{\mathrm{D}}\left(\mathbf{x},\xi\right)}{\partial x_{e}} \rho\left(\xi\right)\mathrm{d}\xi \sqrt{b^{2}-4ac} \\
&= \frac{\partial \tilde{f}_{\mathrm{D}0}\left(\mathbf{x}\right)}{\partial x_{e}} = \frac{\partial\left(\displaystyle\sum_{g=1}^{N_{g}} \dfrac{\partial \tilde{f}_{\mathrm{D}}\left(\mathbf{x},\xi^{g}\right)}{\partial x} \Phi_{0}\left(\xi^{g}\right) w^{g} \Big/ \mathrm{E}\left(\Phi_{0}^{2}\right)\right)}{\partial x_{e}},
\end{aligned} \tag{3.38}$$

$$
\frac{\partial \sigma\left(\tilde{f}_{\mathrm{D}}(\mathbf{x}, \xi)\right)}{\partial x_e} = \frac{1}{2\sigma\left(\tilde{f}_{\mathrm{D}}(\mathbf{x}, \xi)\right)} \cdot \frac{\partial \int_{\Omega}\left[\tilde{f}_{\mathrm{D}}(\mathbf{x}, \xi) - \tilde{f}_{\mathrm{D}0}(\mathbf{x})\right]^2 \rho(\xi)\,\mathrm{d}\xi}{\partial x_e}
$$

$$
= \frac{1}{\sigma\left(\tilde{f}_{\mathrm{D}}(\mathbf{x}, \xi)\right)} \int_{\Omega}\left(\tilde{f}_{\mathrm{D}}(\mathbf{x}, \xi) - \tilde{f}_{\mathrm{D}0}(\mathbf{x})\right)\left(\frac{\partial \tilde{f}_{\mathrm{D}}(\mathbf{x}, \xi)}{\partial x_e} - \frac{\partial \tilde{f}_{\mathrm{D}0}(\mathbf{x})}{\partial x_e}\right)\rho(\xi)\,\mathrm{d}\xi \quad (3.39)
$$

$$
= \sum_{i=1}^{N_{\mathrm{PCE}}} \frac{\tilde{f}_{\mathrm{D}i}(\mathbf{x})\dfrac{\partial \tilde{f}_{\mathrm{D}i}(\mathbf{x})}{\partial x_e}\mathrm{E}\left(\Phi_i^2\right)}{\sigma\left(\tilde{f}_{\mathrm{D}}(\mathbf{x}, \xi)\right)}.
$$

With the above derivation, the sensitivity of the objective function of the topology optimization problem (3.24) can finally be obtained as

$$
\frac{\partial f(\mathbf{x}, \xi)}{\partial x_e} = \frac{\partial \mu\left(\tilde{f}_{\mathrm{D}}(\mathbf{x}, \xi)\right)}{\partial x_e} - \alpha \cdot \frac{\partial \sigma\left(\tilde{f}_{\mathrm{D}}(\mathbf{x}, \xi)\right)}{\partial x_e}
$$

$$
= \frac{\partial \tilde{f}_{\mathrm{D}0}(\mathbf{x})}{\partial x_e} - \alpha \cdot \sum_{i=1}^{N_{\mathrm{PCE}}} \frac{\tilde{f}_{\mathrm{D}i}(\mathbf{x})\dfrac{\partial \tilde{f}_{\mathrm{D}i}(\mathbf{x})}{\partial x_e}\mathrm{E}\left(\Phi_i^2\right)}{\sigma\left(\tilde{f}_{\mathrm{D}}(\mathbf{x}, \xi)\right)} \quad (3.40)
$$

$$
= \frac{\partial \left(\displaystyle\sum_{g=1}^{N_g} \frac{\partial \tilde{f}_{\mathrm{D}}(\mathbf{x}, \xi^g)}{\partial x}\Phi_0(\xi^g)w^g \Big/ \mathrm{E}\left(\Phi_0^2\right)\right)}{\partial x_e} - \alpha \cdot \sum_{i=1}^{N_{\mathrm{PCE}}} \frac{\tilde{f}_{\mathrm{D}i}(\mathbf{x})\dfrac{\partial \tilde{f}_{\mathrm{D}i}(\mathbf{x})}{\partial x_e}\mathrm{E}\left(\Phi_i^2\right)}{\sigma\left(\tilde{f}_{\mathrm{D}}(\mathbf{x}, \xi)\right)}.
$$

3.5 Numerical Implementations

The robust topology optimization procedure is implemented on the MATLAB platform; a flowchart is presented in Fig. 3.4. At the beginning of the procedure, the periodic displacement boundary conditions based on the Floquet–Bloch theorem in Eq. (3.4) are set, and the design variables that indicate the epoxy/plumbum distribution in the unit cell of PnCs are initialized. The random fields of Young's modulus are then discretized with the EOLE method according to Eq. (3.11). Next, Young's modulus sampling quadrature points in the PC expansions (3.18) for both material components are determined. After analyzing the deterministic target band gaps

and the corresponding sensitives at the specified sampling points, the mean value and standard deviation of the band gap and corresponding sensitivity can be obtained with PCE from Eqs. (3.23) and (3.40). The design variables are updated by the globally convergent method of moving asymptotes (GCMMA) [162] optimizer. The iteration procedure is repeated until the difference between values of the objective function in two adjacent iteration steps falls below a prescribed value.
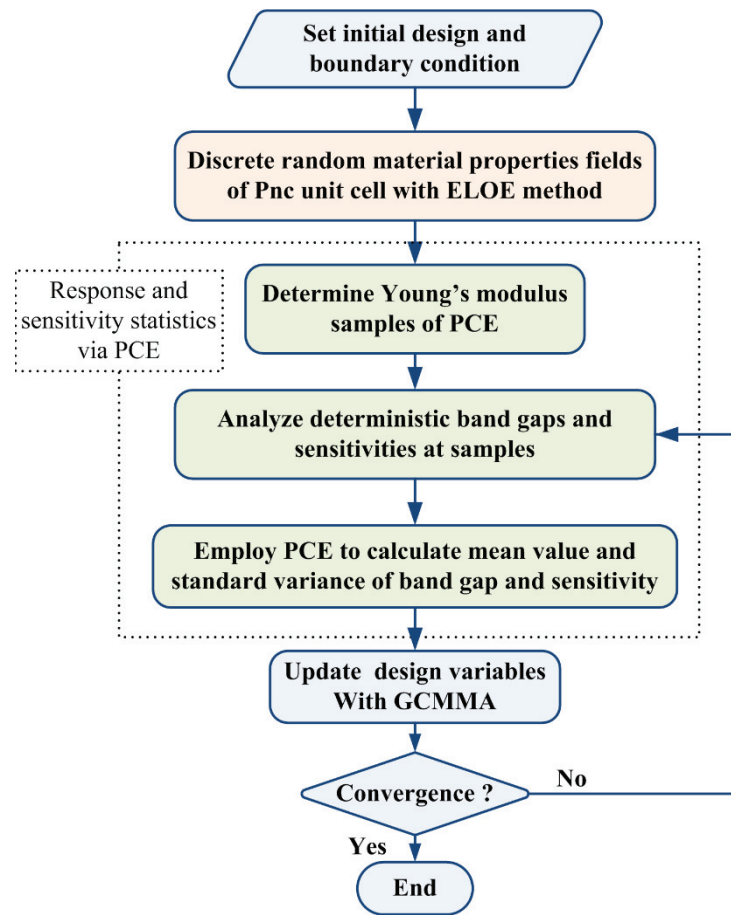
Fig. 3.4 Flowchart of the robust topology optimization for PnCs considering stochastic material property uncertainties.

3.6 Numerical examples

3.6.1 Verification of the stochastic response analysis

Before presenting the robust optimization design procedure, we first provide an example that verifies the effectiveness of the stochastic response analysis method based on EOLE and PCE. Herein, a typical PnC unit cell design with a square plumbum inclusion (material 2) surrounded by the epoxy matrix (material 1) is considered. The unit cell has width $a_c = 0.02\text{m}$ and the length of the inclusion is 0.002 m. The mean values of Young's moduli of the two materials are $E_1 = 4.35\text{GPa}$ and $E_2 = 40.8\text{GPa}$, and they have the same coefficient of variation $\gamma = \sigma_E / \mu_E = 0.1$ and correlation length $L = 0.04\text{m}$; the deterministic Poisson ratio and mass densities of the two materials are respectively $v_1 = v_2 = 0.37$, $\rho_1 = 1180 \text{ kg} \cdot \text{m}^3$, and $\rho_2 = 11600 \text{ kg} \cdot \text{m}^3$. The unit cell is discretized with a 20×20 coarse mesh in this verification example to reduce the computational cost.

Random fields of Young's modulus for the two materials of the PnC unit cell are first represented by N_{EOLE} random variables with the EOLE method. The practical measure of checking whether the number of truncations is sufficient is given by Eq. (3.12). The average error variance when using $N_{\text{EOLE}} = 4$ terms (where each material phase has two terms) is $\bar{e}_{\text{EOLE}} = 3.96\%$, which can be considered sufficient for balancing the computational precision and computational cost.

In the stochastic response analysis with PCE, we choose the polynomial order $P = 3$ and the total number of coefficient terms of PCE in Eq. (3.16) is $N_{\text{PCE}} + 1 = 35$. To reduce the computational cost of the quadruple integrations (due to $N_{\text{EOLE}} = 4$) in Eq. (3.18), sparse grids with third-order precision [171] are adopted, and the total number of quadrature points reduces to $N_g = 41$. The computational results of the mean value and standard deviation of the third

frequencies of the PnC unit cell with different plane wave vectors **k** are summarized in Table 3.1, and Monte-Carlo (MC) simulations with 10,000 samples are performed for comparison. It is found that the mean values of the current PCE method agree well with the MC results with a maximum difference of 0.02%. The difference in standard deviations for the two methods is a larger but still under 1%. We thus deem that the current polynomial order and the coefficient terms are enough to provide sufficient computational precision.

Table 3.1 Comparisons of the third frequencies of PnCs between PCE and MC simulation.

Wave vector $(\mathbf{k} = \mathbf{k}_0 / a_c)$	Mean value (kHz)			Standard deviation (kHz)		
	PCE	MC	Diff.	PCE	MC	Diff.
$\mathbf{k}_0 = \{\pi, \pi\}$	39.321	39.313	0.02%	1.847	1.864	-0.91%
$\mathbf{k}_0 = \{0.8\pi, 0.8\pi\}$	39.970	39.962	0.02%	1.869	1.886	-0.90%
$\mathbf{k}_0 = \{0.6\pi, 0.6\pi\}$	40.986	40.979	0.02%	1.898	1.915	-0.89%
$\mathbf{k}_0 = \{0.4\pi, 0.4\pi\}$	40.732	40.725	0.02%	1.866	1.883	-0.90%
$\mathbf{k}_0 = \{0.2\pi, 0.2\pi\}$	39.278	39.275	0.01%	1.788	1.804	-0.89%
$\mathbf{k}_0 = \{0, 0\}$	39.321	39.313	0.02%	1.847	1.864	-0.91%
$\mathbf{k}_0 = \{0.2\pi, 0\}$	40.203	40.194	0.02%	1.877	1.895	-0.95%
$\mathbf{k}_0 = \{0.4\pi, 0\}$	41.475	41.467	0.02%	1.934	1.952	-0.92%
$\mathbf{k}_0 = \{0.6\pi, 0\}$	43.556	43.546	0.02%	2.027	2.046	-0.93%
$\mathbf{k}_0 = \{0.8\pi, 0\}$	46.201	46.191	0.02%	2.123	2.143	-0.93%
$\mathbf{k}_0 = \{\pi, 0\}$	46.832	46.824	0.02%	2.139	2.159	-0.93%
$\mathbf{k}_0 = \{\pi, 0.2\pi\}$	44.668	44.660	0.02%	2.053	2.073	-0.96%
$\mathbf{k}_0 = \{\pi, 0.4\pi\}$	40.465	40.456	0.02%	1.866	1.884	-0.96%
$\mathbf{k}_0 = \{\pi, 0.6\pi\}$	35.811	35.804	0.02%	1.651	1.667	-0.96%
$\mathbf{k}_0 = \{\pi, 0.8\pi\}$	38.399	38.396	0.01%	1.750	1.766	-0.91%

3.6.2 Robust topology optimization results

This subsection presents robust topology optimization results and discusses important factors in the design of the PnC unit cell. In all examples, the unit cell is discretized into 40×40 uniform square elements. The material properties of the two components are the same as those in the previous subsection. The aggregation parameters of the Kreisselmeier–Steinhauser function (3.22) are set as $\eta_1 = -5$ and $\eta_2 = 5$ initially and their absolute values are increased by 0.5 per optimization iteration until they reach 30. The optimization iterations stop when the difference between two consecutive objective functions is less than 5×10^{-4}.

We first optimized the stochastic band gap of coupled in-plane modes (in Eq. (3.2)) between the sixth and seventh bands of the PnC. Here, both materials are assumed to have a variation $\gamma = 0.1$ in Young's moduli, and the correlation length $L = 0.04$m. The weight factor in the objective function (3.23) is taken as $\alpha = 4$. The initial design is chosen such that the unit cell has a circular plumbum inclusion (with radius of 0.004 m) surrounded by epoxy matrix, as shown in Fig. 3.5(a), and the mean dispersion curves of the in-plane modes are illustrated in Fig. 3.5 (b). Figure 5 shows that the initial design has no band gap between the sixth and seventh bands of the PnC, but a narrow band gap between the third and fourth bands. The optimization process converged after 54 iterations. Changes in the mean value and standard deviation of the band gap during the optimization process are presented in Fig. 3.6, and the optimal solution of the PnC unit cell and its dispersion curves are presented in Fig. 3.7. It is found that a sixth band gap (i.e., a band gap between the sixth and seventh bands) emerges and its mean value increases during the optimization. Although the standard deviation increases in the first few iterations, it decreases after the appearance of the sixth band gap, realizing a design insensitive to uncertainty in the material distribution. The optimal design has a mean band gap of 29.69 kHz and a standard deviation of 1.16 kHz. For comparisons, a deterministic optimization design is also implemented, with the optimal solution presented in Fig. 3.8. In terms of the material

uncertainty for the obtained deterministic design, the design has a mean band gap of 34.68 kHz and a standard deviation of 2.41 kHz. Although the deterministic design has a larger mean value of the band gap, the robust design still has better stochastic performance in terms of the objective function (3.23) and is less sensitive to uncertainty in the input material distribution. A remarkable difference can be found between the robust design in Fig. 3.7 and the deterministic design in Fig. 3.8.

(a)   (b)
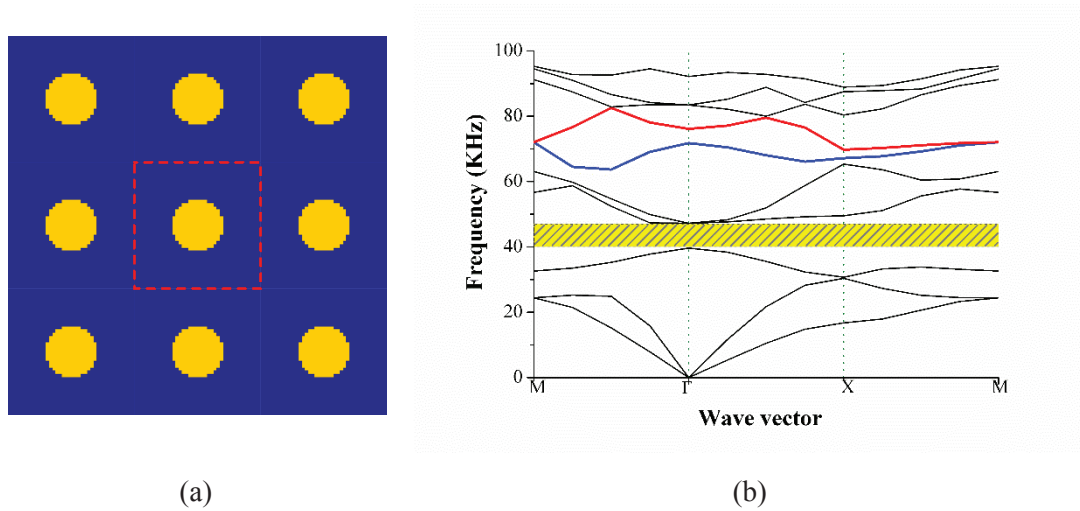
Fig. 3.5. Initial design and its dispersion curves. (a) Initial design of PnC with nine unit cells and (b) mean value of dispersion curves of coupled in-plane modes.
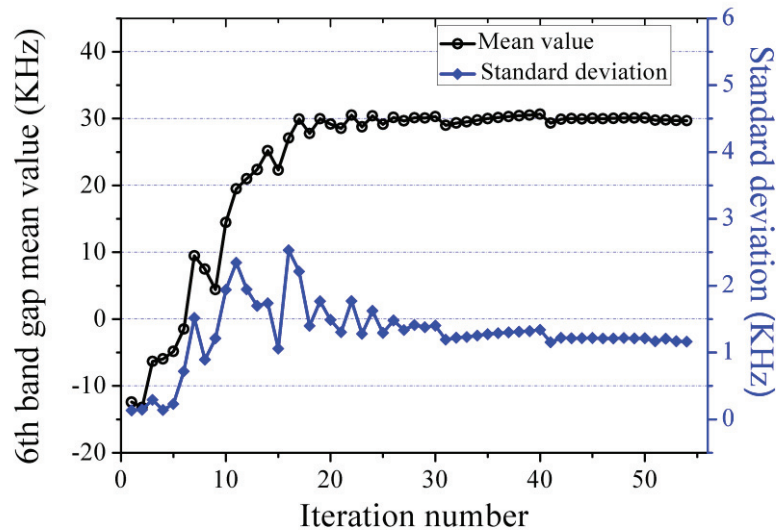
Fig. 3.6. Iteration histories of the mean value and standard deviation of the sixth band gap.

(a)   (b)
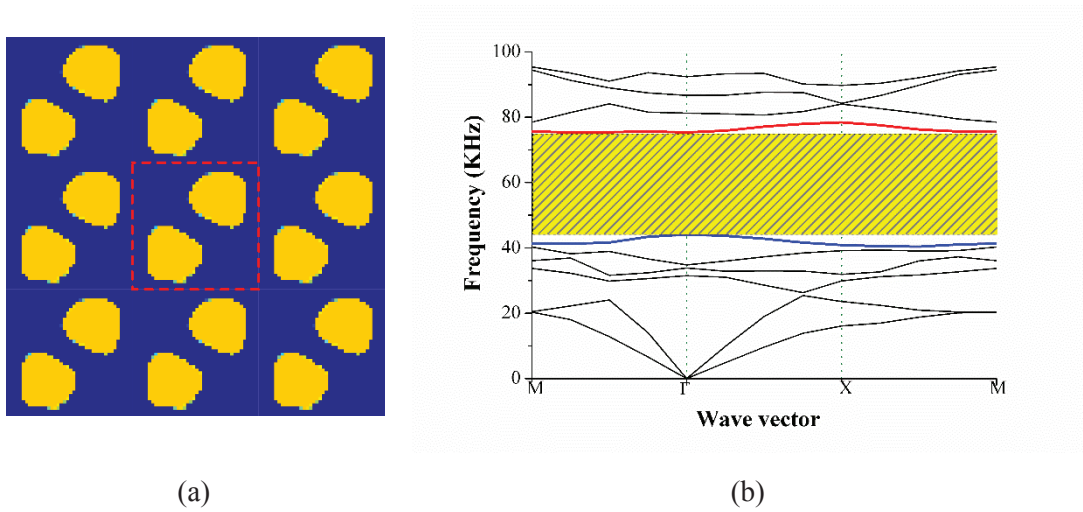
Fig. 3.7 Robust optimal design for the sixth band gap of coupled in-plane modes and its dispersion curves. (a) Optimal design with nine unit cells; (b) mean value of dispersion curves.

(a)   (b)
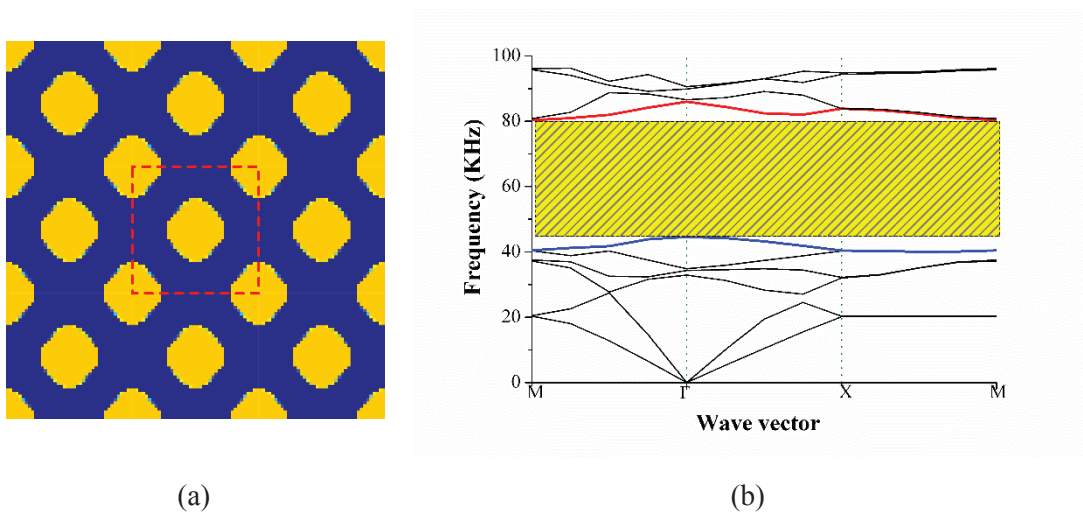
Fig. 3.8 Deterministic optimal design for the sixth band gap of coupled in-plane modes and its dispersion curves when considering uncertainty in the material distribution. (a) Optimal design with nine unit cells; (b) mean value of dispersion curves.

We further study the optimal design for other coupled in-plane modes. Another two band

gaps, the third band gap (i.e., the band gap between third and fourth bands) and the eighth band gap, are considered, and the optimal solutions and corresponding mean values of dispersion curves are given in Fig. 3.9. For optimization of the third band gap, the optimal design in Fig. 3.9 (a) and (b) can provide an in-plane mode band gap with a mean value of 21.46 kHz and a standard deviation of 0.90 kHz, and the eighth-order band gap with a mean value of 4.56 kHz and a standard deviation of 0.29 kHz is obtained from Fig. 3.9 (c) and (d). It is noted that not every order of the band gaps can be easily achieved because it is nearly impossible to open the first six band gaps except the third band gap of the plumbum/epoxy PnCs [105].
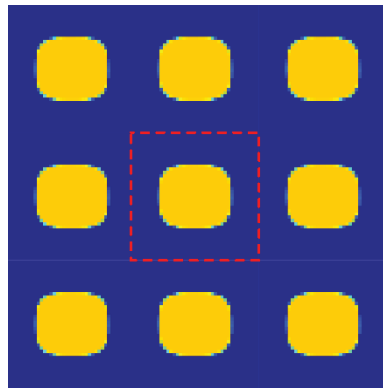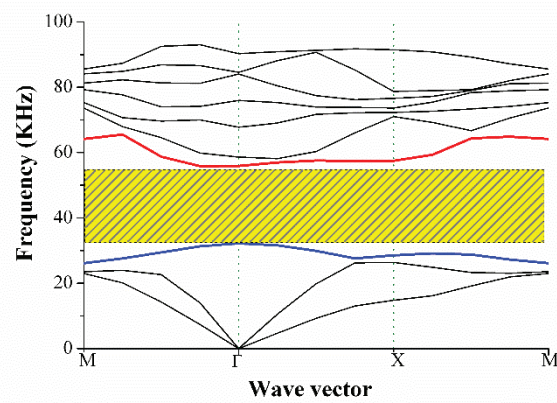
(a)   (b)
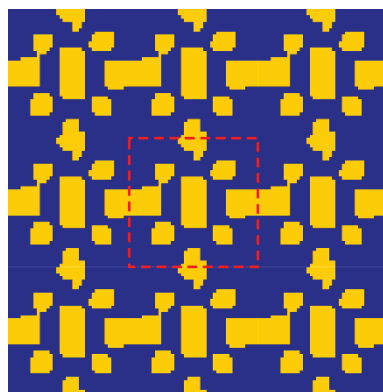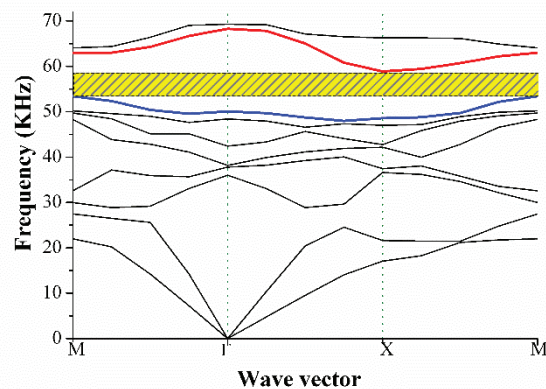
(c)   (d)

Fig. 3.9 Robust optimal design for the third and eighth band gaps of coupled in-plane modes and their dispersion curves. (a) Optimal design for the third band gap; (b) mean value

of dispersion curves of the third band gap design; (c) optimal design for the eighth band gap; (d) mean value of dispersion curves of the eighth band gap design.

In the following, we present the robust optimization of a PnC in the case of the out-of-plane mode. Unlike the case of the in-plane mode, the optimal designs can be obtained with different band gap orders. Here, seven robust optimal designs and their dispersion curves for the different orders of band gaps (from the second order to the eighth order) are presented in Fig. 3.10, and the mean values of the band gap property and the standard deviations are summarized in Table 3.2. It is found that some of the optimized designs exhibit an asymmetrical material distribution (such as Fig. 3.9 (c), Fig. 3.10 (g), and Fig. 3.10 (i)). This is natural because the proposed optimization method imposes no symmetric-related design constraints. In addition, asymmetrical PnC designs have been shown to have larger band gaps than the optimal symmetrical structures [178].

(a)   (b)

82
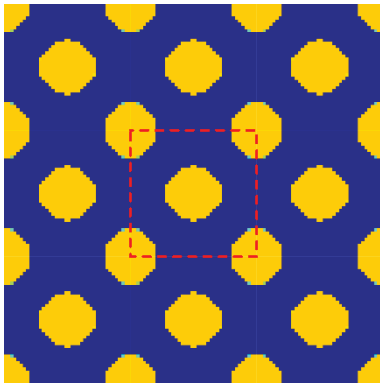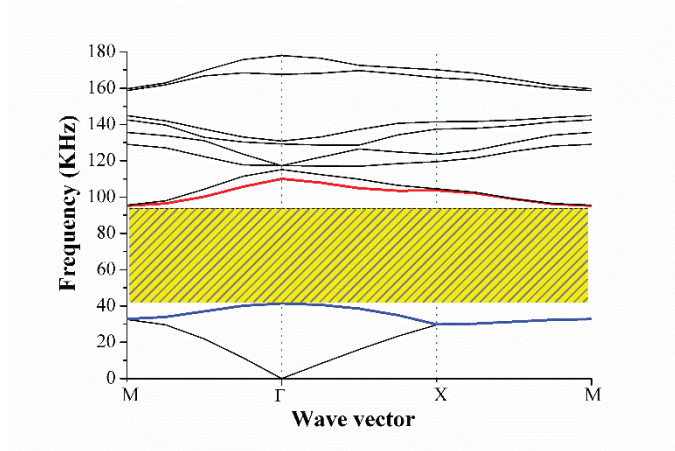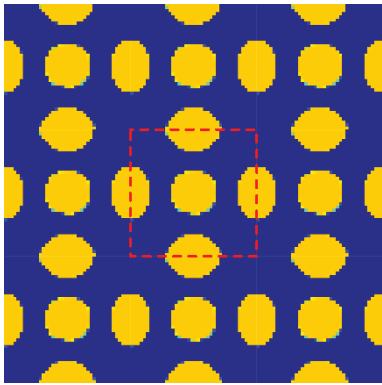
(c)
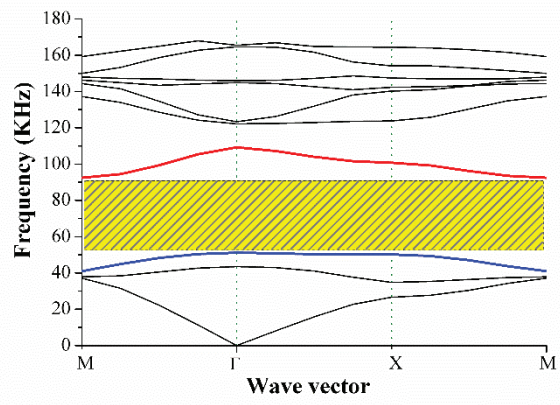
(d)
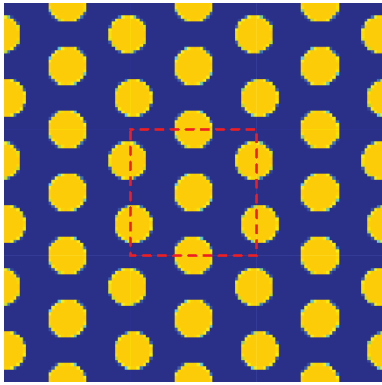
(e)
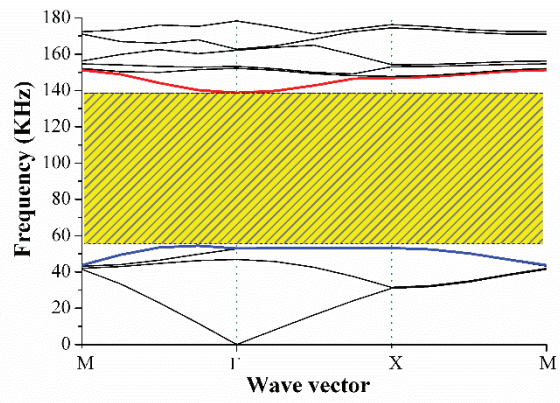
(f)
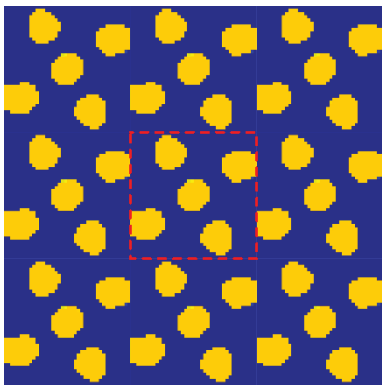
(g)
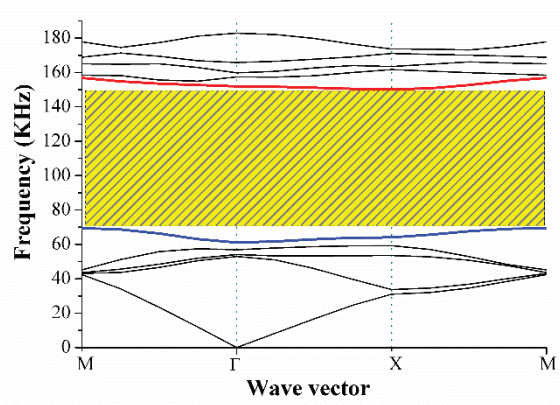
(h)
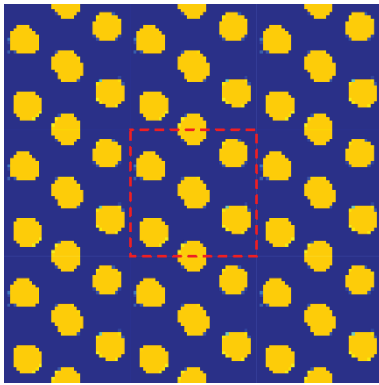
(i)
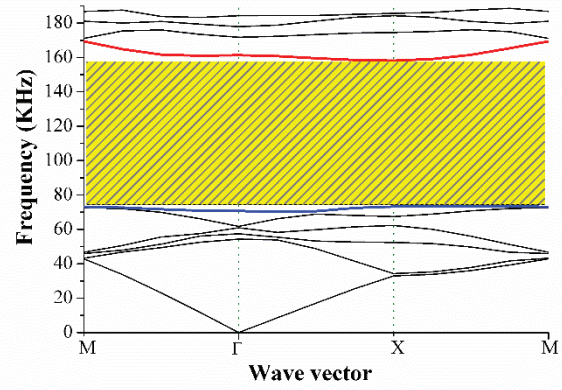
(j)
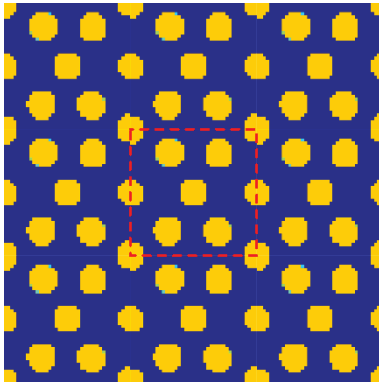
(k)
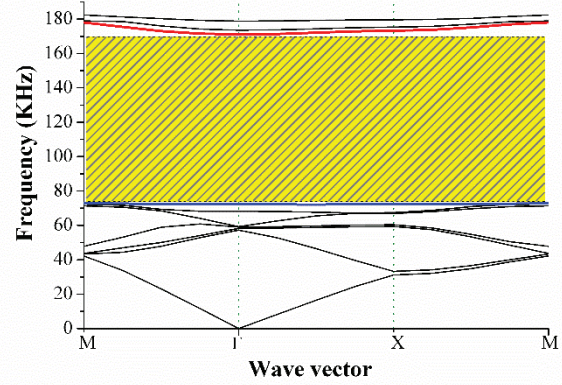
(l)
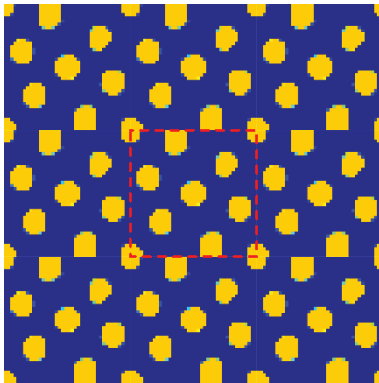
(m)
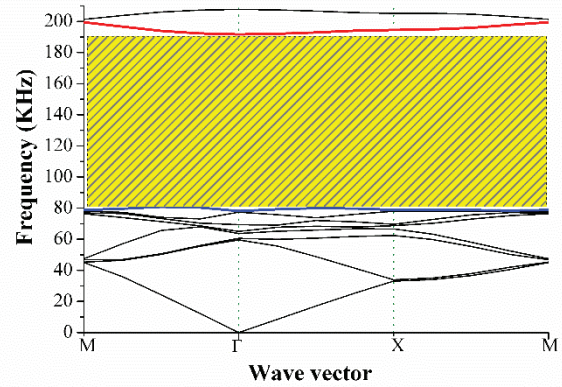
(n)

Fig. 3.10 Robust optimal design of coupled in-plane modes and their dispersion curves: (a)–(b) second band gap, (c)–(d) third band gap, (e)–(f) fourth band gap, (g)–(h) fifth band gap, (i)–(j) sixth band gap, (k)–(l) seventh band gap, and (m)–(n) seventh band gap.

Table 3.2 Mean and standard deviation of robust designs with different orders of band gaps.

Orders of band gap	Mean higher band bottom (kHz)	Mean lower band top (kHz)	Mean band gap width (kHz)	Std. deviation of band gap width (kHz)
2-3 band	95.15	41.33	53.82	2.04
3-4 band	92.46	51.15	41.31	1.56
4-5 band	138.76	54.42	84.34	4.02
5-6 band	150.15	69.50	80.65	3.24
6-7 band	158.19	73.36	84.83	3.51
7-8 band	171.04	72.95	98.09	3.53
8-9 band	191.68	80.81	110.87	4.45

We now investigate the effect of the weight coefficient α in Eq. (3.23), which balances the band gap width and the robustness of the design in the presence of a random material distribution. The robust optimizations of the sixth in-plane mode band gap are implemented with nine different weight coefficients; the mean values and standard deviations of band gaps for these designs are summarized in Table 3.3. Table 3.3 shows a conflict between the mean band gap and the standard deviation: a less sensitive but narrower band gap design is obtained as the weight coefficient α increases. However, if α is too large (e.g., $\alpha = 14$ in this example), a PnC unit cell without a band gap property will be achieved. Two optimal solutions with $\alpha = 0$ and 4 are respectively given in Figs. 3.8 (a) and 3.7 (a); optimal configurations of the PnC unit cells with other weight coefficients are illustrated in Fig. 3.11. Remarkable differences can be observed from these optimized designs, indicating that the weight coefficient α plays an important role in the robust topology optimization formulation.

Table 3.3 Mean values and standard deviations of the optimized designs obtained with different values of weight coefficient α.

Weight Coefficient α	Mean value of bandgap (kHz)	Standard deviation (kHz)
0	34.68	2.41
0.1	34.50	2.69
1	34.44	2.03
4	29.69	1.16
5.5	9.32	0.63
6.5	8.35	0.51
8.5	6.83	0.36
12.5	0.95	0.16
14	-2.82(no bandgap)	0.12

(a)   (b)   (c)

(d)   (e)   (f)
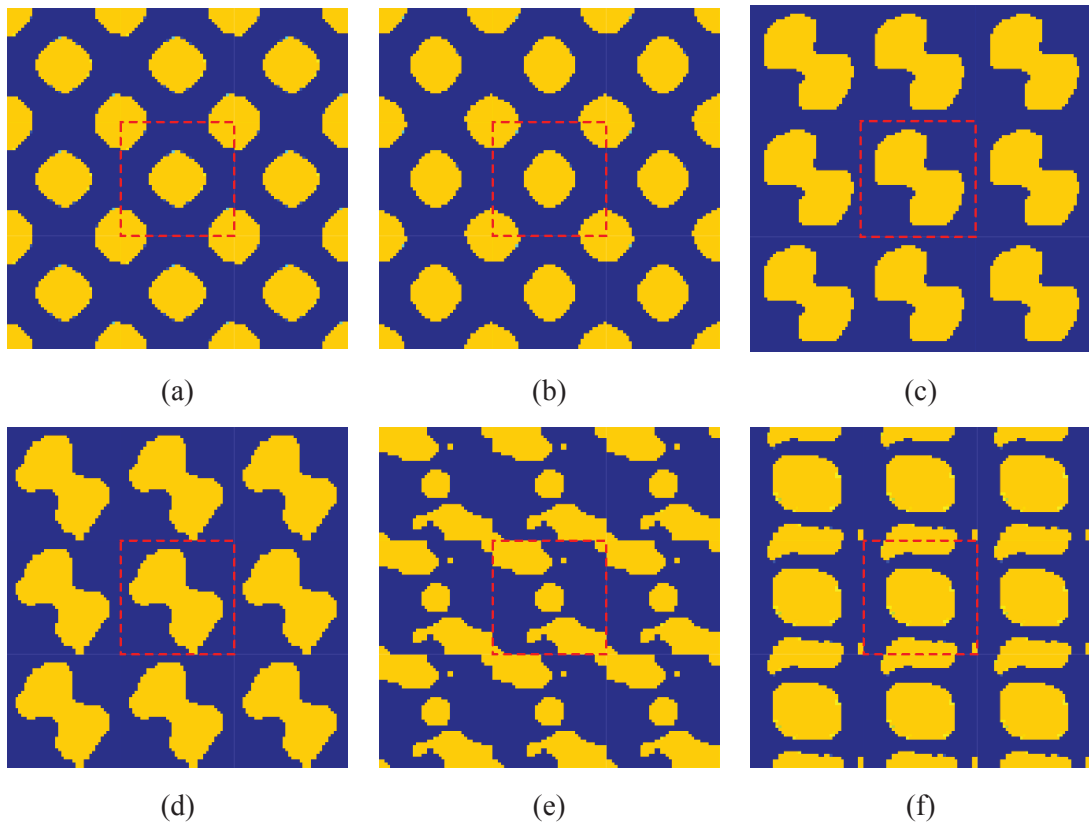
Fig. 3.11 Robust optimal solutions for the sixth in-plane band gap with different values of the weight coefficient α: (a) $\alpha = 0.1$, (b) $\alpha = 1.0$, (c) $\alpha = 5.5$, (d) $\alpha = 6.5$, (e) $\alpha = 8.5$, and (f) $\alpha = 12.5$.

The effect of the variation coefficient γ of Young's moduli of the two materials is studied

for the present example (where $\gamma = 0.1$ in all previous examples). The seventh band gap of the out-of-plane modes is considered as the target band, and the weight coefficient of the objective function is fixed at $\alpha = 4$. Changes in the mean band gap and the standard deviation with an increase in the coefficient of variation is shown in Fig. 12, and five representative optimal solutions ($\gamma = 0.02, \ 0.08, \ 0.20, \ 0.30$ and 0.40) are given in Fig. 13. Figure 12 shows that as the variation coefficient increases from 0.02 to 0.46, the mean value of the band gap reduces about 20% while the standard deviation increases by a factor of 12.59, and the optimal solutions in Fig. 13 are similar to each other. These results imply that the optimal solution for achieving a specified band gap actually consists of a basic configuration obtained by maximizing the mean band gap design and detailed modifications based on the standard deviation caused by the random material field.
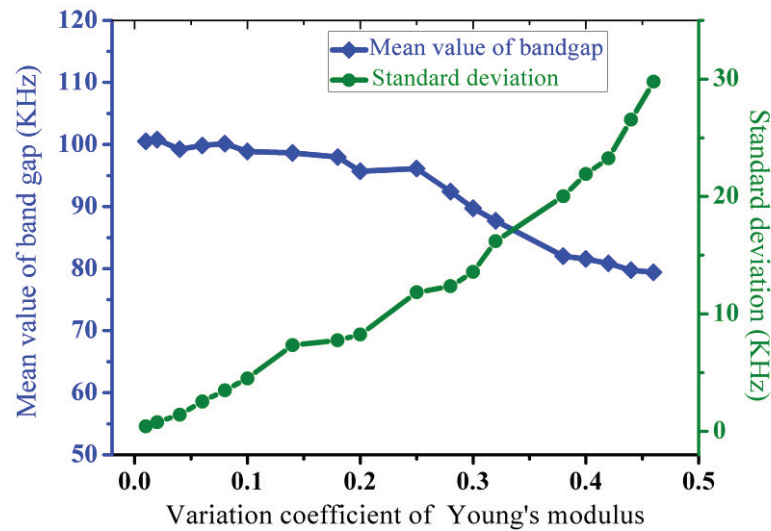
Fig. 3.12 Mean band gaps and standard deviations of the optimal designs obtained for different coefficients of variation of Young's moduli.
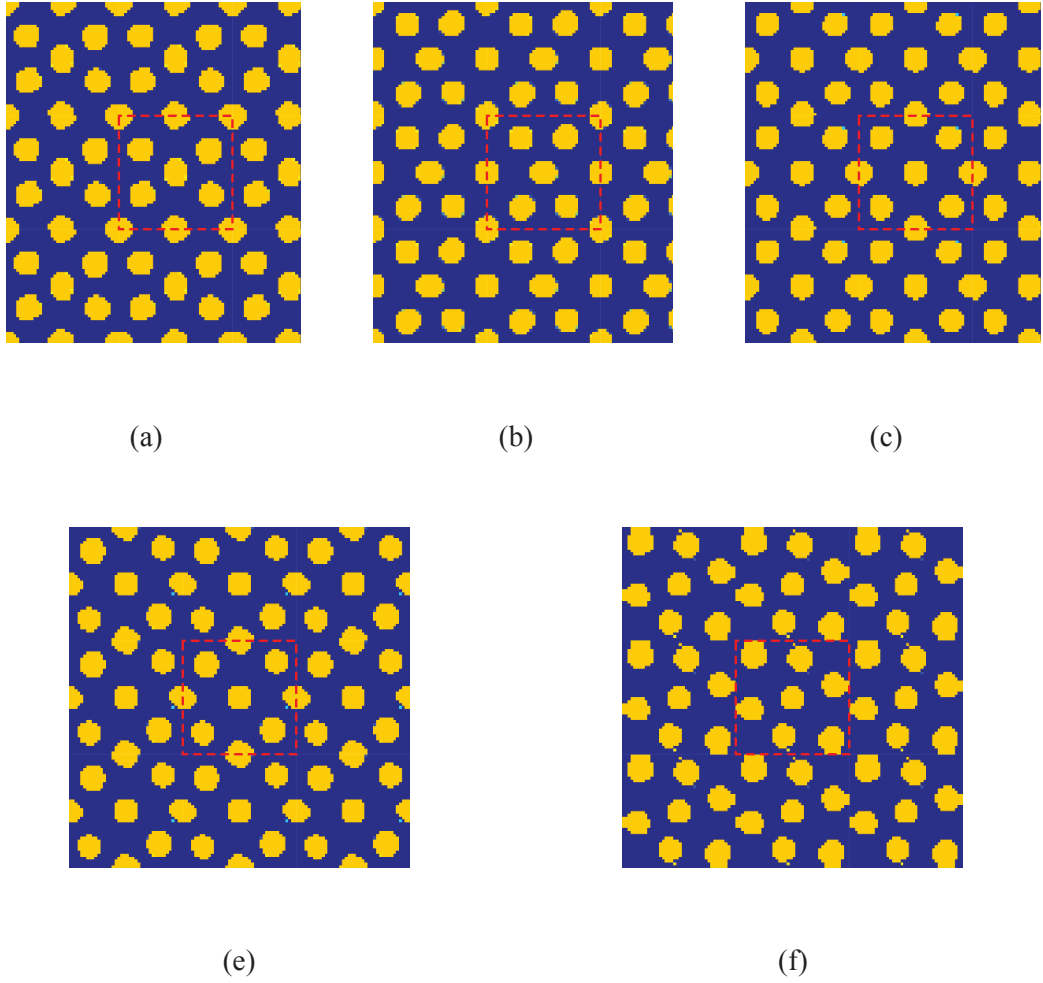
Fig. 3.13. Robust optimal designs obtained for different variation coefficients of Young's moduli: (a) $\gamma = 0.02$, (b) $\gamma = 0.08$, (c) $\gamma = 0.20$, (d) $\gamma = 0.30$, and (e) $\gamma = 0.40$.

3.7. Summary

This chapter proposed a robust topology optimization method for designing the microstructure of PnCs under a random distribution of material properties. Uncertainty in the material properties is a nonnegligible factor in the design of the PnC microstructures. We here employ the EOLE method to discretize the random material Young's modulus fields into several uncorrelated uncertain variables. The stochastic band gap response is then predicted with the PCE method, where the PCE coefficients are determined by calculating the band gap of PnCs

with the FEM at specified quadrature points. A new robust topology optimization formulation is proposed to achieve an insensitive PnC microstructure design by introducing an objective function balances the mean band gap and standard deviation.

Numerical examples were presented to illustrate the effectiveness and efficiency of the proposed framework. A comparison with the deterministic PnC optimal design shows that the proposed robust optimization method can provide a PnC microstructure design with a relatively wide band gap that is less sensitive to random material uncertainties. Additionally, the weight factor of the objective function was shown to be able to effectively balance a broad mean band gap and a small band gap variation.

4 Phase-field based robust topology optimization of vibrating structures with random field uncertainty

For structures composed of multiple material phases, there are usually continuous diffuse regions between material phases in real applications, and it is thus necessary to introduce diffuse regions into the optimization model when considering manufacturing-related uncertainties. Phase field-based topology optimization involves the diffuse region naturally and the random widths of the diffuse region between different material phases can be simulated by evaluating the phase-field function with a given spatially varying field of the diffuse region width, allowing convenient stochastic response analysis and corresponding optimization.

The present work develops a phase-field-based topology optimization method of vibrating structures that reduces the dynamic performance variability under diffuse-region uncertainties. Herein, the diffuse regions between two material phases are assumed to satisfy a spatial stochastic field and are discretized into uncorrelated stochastic variables using the EOLE method; stochastic structural dynamic response analysis is then conducted with PCE. To achieve a less-sensitive optimal design, a robust topology optimization formulation that minimizes the weighted sum of the mean value and standard deviation of the structural dynamic performance is formulated. The structural dynamic compliance, fundamental frequency/frequency gap, and transient responses. In the framework of the phase-field method, the structural shape is represented by the phase-field function defined in the design domain, and initial non-uniform diffuse regions are generated by evolving the phase-field function. With the stochastic structural dynamic responses and the corresponding sensitivities obtained employing the PCE method for each sampling point, the phase-field function is updated using a time-dependent reaction–diffusion equation called the Allen–Cahn equation [179]. An artificial double-well potential used in the equation is derived from sensitivity analysis to move

the front in the direction of the decreasing objective function.

4.1 Objective functions of dynamic topology optimization problems

The governing equations of the finite element model of a structure subjected to dynamic loads are

$$
\begin{aligned}
&\mathbf{M}\ddot{\mathbf{u}}(T) + \mathbf{C}\dot{\mathbf{u}}(T) + \mathbf{K}\mathbf{u}(T) = \mathbf{f}(T), \\
&\dot{\mathbf{u}}\big|_{T=0} = \mathbf{v}_0, \quad \mathbf{u}\big|_{T=0} = \mathbf{u}_0,
\end{aligned}
\tag{4.1}
$$

where T is the real time; $\mathbf{M} \in \mathbf{R}^{n\times n}$, $\mathbf{C} \in \mathbf{R}^{n\times n}$ and $\mathbf{K} \in \mathbf{R}^{n\times n}$ are respectively the mass matrix, damping matrix, and stiffness matrix; $\mathbf{u}(T) \in \mathbf{R}^{n\times 1}$, $\dot{\mathbf{u}}(T) \in \mathbf{R}^{n\times 1}$, and $\ddot{\mathbf{u}}(T) \in \mathbf{R}^{n\times 1}$ are respectively vectors of transient displacement, velocity, and acceleration; $\mathbf{f}(T)$ is the external excitation; and $\mathbf{u}_0 \in \mathbf{R}^{n\times 1}$ and $\mathbf{v}_0 \in \mathbf{R}^{n\times 1}$ are respectively the initial displacement and initial velocity. Here, n is the number of degrees of freedom (DOFs). The structural damping $\mathbf{C}$ is assumed to be Rayleigh damping:

$$
\mathbf{C} = \alpha_1 \mathbf{M} + \alpha_2 \mathbf{K},
\tag{4.2}
$$

where α_1 and α_2 are Rayleigh damping coefficients.

The topology optimization of dynamic structures usually focuses on three types of structural dynamic behavior functions: (a) the frequency response under harmonic/periodical excitations, (b) the fundamental frequency or frequency gaps, and (c) the transient response under impact loads. We thus consider three types of objective functions as follows.

(a) Frequency response under harmonic/periodical excitations

91

When the excitation $\mathbf{f}(T)$ in Eq. (4.1) is a harmonic load $\mathbf{f}(T) = \mathbf{F}e^{i\theta T}$ or periodic load (it can be expressed by a series of harmonic loads), and only the steady-state response is of interest, the steady-state displacement response $\mathbf{u}(T)$ can be expressed as $\mathbf{u}(T) = \mathbf{U}e^{i\theta T}$ with the complex amplitude of vibration $\mathbf{U} \in \mathbf{R}^{n \times 1}$. The governing equations (4.1) can then be rewritten as

$$\mathbf{WU} = \mathbf{F}, \tag{4.3}$$

with

$$\mathbf{W} = -\theta^2 \mathbf{M} + i\theta \mathbf{C} + \mathbf{K}, \tag{4.4}$$

where $\mathbf{W}$ is called the dynamic stiffness matrix [180], and θ is the frequency of the external excitation $\mathbf{f}(T)$. Equation (4.3) can be solved with the mode superposition method [40] or the full method (i.e., by calculating $\mathbf{U} = \mathbf{W}^{-1}\mathbf{F}$) [153], and the latter method is adopted in the present study because it provides higher accuracy.

In the topology optimization problem for reducing the structural frequency response, the dynamic compliance and displacement at a specified position are frequently used as effective measures of the vibration level for a given excitation frequency or frequency range. We here take the dynamic compliance defined by Ma et al. [180] and Yoon [40] as the first type of objective function in the optimization model:

$$J_1 = \sqrt{\left(\mathbf{F}^{\mathrm{T}}\mathbf{U}^{\mathrm{R}}\right)^2 + \left(\mathbf{F}^{\mathrm{T}}\mathbf{U}^{\mathrm{I}}\right)^2}, \tag{4.5}$$

where $\mathbf{U}^{\mathrm{R}}$ and $\mathbf{U}^{\mathrm{I}}$ are respectively real and imaginary parts of the displacement vector $\mathbf{U}$.

(b) Fundamental frequency or frequency gap

92

In problems of topological design for maximizing the fundamental eigenfrequencies and the gap between two consecutive eigenfrequencies, the structural damping is usually neglected and governing equations (4.1) of the dynamic problems can be reformulated into an equation for the eigenvalue problem as

$$\left(\mathbf{K} - \omega^2 \mathbf{M}\right)\boldsymbol{\varphi} = \mathbf{0},$$

(4.6)

where ω is the eigenfrequency and $\boldsymbol{\Phi}$ is the corresponding eigenmode. Usually, only the first N_j real eigenfrequencies need to be considered, and the governing equation can be rewritten as

$$\begin{cases} \mathbf{K}\boldsymbol{\varphi}_j = \omega_j^2 \mathbf{M}\boldsymbol{\varphi}_j, & j = 1, ..., N_j, \\ \boldsymbol{\varphi}_j \mathbf{M}\boldsymbol{\varphi}_k = \delta_{jk}, & j = 1, ..., N_j. \end{cases}$$

(4.7)

It is here assumed that the corresponding eigenvectors $\boldsymbol{\varphi}_j \left(j = 1, ..., N_j\right)$ are $\mathbf{M}$ orthonormalized, and δ_{jk} is the Kronecker delta.

To obtain the maximum value of the fundamental frequency, the design objective can be chosen to minimize the negative minimum value of the first N_j real eigenvalues as

$$J_2 = -\omega_1^2.$$

(4.8)

In some applications, to reduce the undesirable vibration and noise emission levels, the objective function of the optimization problem is chosen to be the gap between two adjacent eigenvalues ω_n^2 and ω_{n-1}^2 of specified orders n and $n-1$:

$$J_2 = -\Delta\left(\omega^2\right) = \omega_{n-1}^2 - \omega_n^2.$$

(4.9)

(c) Transient dynamic response with respect to the impact load

When the structure is excited by an external impact load, governing equations (4.1) can be solved with direct time-integration methods under given initial conditions. The unconditionally stable Newmark algorithm is employed for this purpose in the present study.

The aim of the optimal design for the structural transient dynamic optimization problem is usually to reduce the vibration level over a specified time interval $[T_1, T_2]$. Considering the dynamic response that is only directly related to displacement $\mathbf{u}(T)$ and time T, the objective function can be formulated in the form $\int_{T_1}^{T_2} g(\mathbf{u}(T), T) \mathrm{d}T$. Several types of structural behaviors can be considered in real applications for different requirements [119, 181]. We here focus on the optimization problem of reducing the vibration response at a specified position, and the objective function can thus be chosen to minimize the squared displacement response of a target DOF u_a in the time interval $[T_1, T_2]$, which is expressed as

$$J_3 = \int_{T_1}^{T_2} u_a^2(T) \, \mathrm{d}T. \tag{4.10}$$

Using the above objective functions (4.5) and (4.8)–(4.10) and the phase-field-based description model, the deterministic topology optimization problem for structural vibration can be stated as

$$
\begin{aligned}
&\underset{\phi}{\text{Minimize}} \;\; J_1(\phi), J_2(\phi) \text{ or } J_3(\phi),\\
&\text{subject to } \sum_{e=1}^{N_f} \phi_e V_e - V_0 \leq 0,\\
&\qquad\quad \phi = \left[\phi_1, \ldots, \phi_{N_f}\right],\\
&\qquad\quad 0 \leq \phi_e \leq 1, \;\; e = 1, \ldots, N_f.
\end{aligned}
\tag{4.11}
$$

Here, V_0 denotes the upper limit of the allowable volume of material 1 in the bi-material

distribution optimization problem and $V_e \left(e = 1,\ 2, ..., \ N_\text{f} \right)$ is the volume occupied by the e th phase-field calculation point. The symbol N_f denotes the total number of phase-field calculation points used in the topology optimization model. The present study selects phase-field calculation points at all element centers of the finite element model; therefore, N_f is equal to the total number of finite elements N_e in the design domain.

4.2 Phase-field-based robust topology optimization considering uncertain diffuse regions

4.2.1 Modeling of non-uniform diffuse regions via the evolution of phase-field functions

In existing topology optimization studies based on the phase-field description, diffuse regions between two material phases are usually considered to have deterministic and uniform widths throughout the design domain.

We consider the case that the diffuse regions between two candidate materials are nonuniform and their widths are a random Gaussian field. We first study the modeling of the diffuse region for a deterministic but nonuniform diffuse region width distribution; i.e., the width of the diffuse region $\tilde{\xi}_{i,j}$ has an independent value at each point $\chi_{i,j}$. In the stage of setting up the phase-field method, the design domain is first assigned using two candidate material phases with two different values of $\phi_{i,j} = 1$ or 0 without diffuse regions (as shown in Fig. 3), and the phase-field functions are then evolved by solving Eq. (1.11) using the finite difference method. Here, the time step Δt needs to satisfy the Courant–Friedrich–Levy condition ($\varepsilon^2 \left(\Delta t / \left(\Delta x \right)^2 + \Delta t / \left(\Delta y \right)^2 \right) \le 0.5$ in the two-dimensional case) to achieve stable

convergence. A semi-implicit discretizing scheme is introduced to keep the value of the phase-field function within the range $0 \leq \phi \leq 1$, and the evolutional equation of the phase-field function $\phi_{i,j}^{n+1}$ in the ($n+1$)th iteration at point $\chi_{i,j}$ is then obtained as

$$\frac{\phi_{i,j}^{n+1} - \phi_{i,j}^{n}}{\Delta t} = \varepsilon_{i,j}^{2} \left(\frac{\phi_{i-1,j}^{n} - 2\phi_{i,j}^{n} + \phi_{i+1,j}^{n}}{(\Delta x)^{2}} + \frac{\phi_{i,j-1}^{n} - 2\phi_{i,j}^{n} + \phi_{i,j+1}^{n}}{(\Delta y)^{2}} \right) + \begin{cases} \phi_{i,j}^{n+1}\left(1-\phi_{i,j}^{n}\right)r\left(\phi_{i,j}^{n}\right) & \text{for } r\left(\phi_{i,j}^{n}\right) < 0, \\ \phi_{i,j}^{n}\left(1-\phi_{i,j}^{n+1}\right)r\left(\phi_{i,j}^{n}\right) & \text{for } r\left(\phi_{i,j}^{n}\right) \geq 0, \end{cases}$$

(4.12)

where

$$r\left(\phi_{i,j}^{n}\right) = \phi_{i,j}^{n} - \frac{1}{2} - 30\eta \frac{J'(t)}{\|J'(t)\|}\phi(1-\phi).$$
(4.13)

Here, Δx and Δy are respectively the spatial steps in the x and y directions. The coefficient $\varepsilon_{i,j}$ at point $\chi_{i,j}$ can be expressed in terms of the diffuse-region width $\tilde{\xi}_{i,j}$ as $\varepsilon_{i,j} = \tilde{\xi}_{i,j}/6$ for the current selection of the double-potential function in Eq. (1.8) [182].

In Eq. (4.13), the second term, which includes the sensitivity of the objective function, drives the phase-field functions to the optimal solution, while the first term only controls the diffuse-region part. If one wants to obtain a design with a specified diffuse region from the current design (with or without a diffuse region), the evolution of the phase-field function is only driven with the diffuse-region term (i.e., the first term in Eq.(4.12)) by specifying $\varepsilon_{i,j}$ at each calculation point. Equation (4.12) thus reduces to

$$\frac{\phi_{i,j}^{n+1} - \phi_{i,j}^{n}}{\Delta t} = \varepsilon_{i,j}^{2} \left(\frac{\phi_{i-1,j}^{n} - 2\phi_{i,j}^{n} + \phi_{i+1,j}^{n}}{(\Delta x)^{2}} + \frac{\phi_{i,j-1}^{n} - 2\phi_{i,j}^{n} + \phi_{i,j+1}^{n}}{(\Delta y)^{2}} \right).$$
(4.14)

At the beginning of optimization, the initial design is obtained by the diffuse-region evolution of Eq. (4.14) with a design without diffuse regions and a field of the diffuse region

width as shown in Fig. 4.1, and the corresponding material properties in the uncertain diffuse region are interpolated with Eqs. (1.12) and (1.13).

Initial PF setting without diffuse region

Specified diffuse region width field
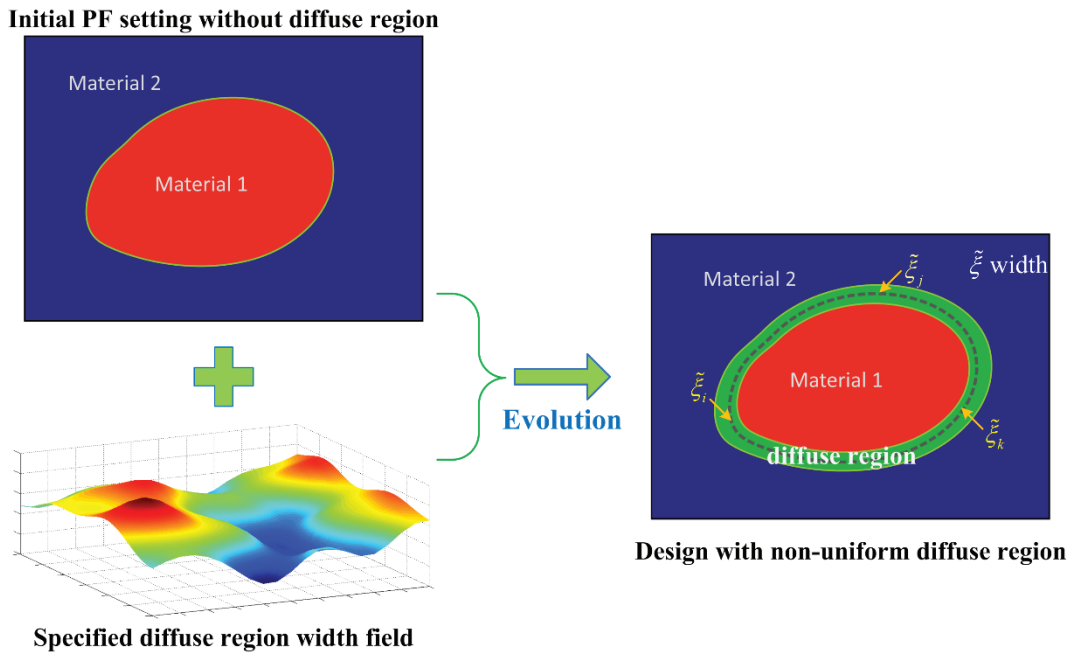
Fig. 4.1. Sketch of setting the initial design with the nonuniform diffuse region employing the phase-field method.

The numerical experience of the authors is that the diffuse-region evolution of Eq. (4.14) usually converges within 20–40 steps in obtaining the initial design. (The convergence criterion is set as the maximum relative difference in all phase-field functions between two consecutive evolutions being less than 10^{-3}). Fig. 4.2 gives two examples of the diffuse-region evolution results for square design domains with a circular/square core and different values of specified diffuse-region widths in four quadrants; the evolution results are obtained after 34 and 42 iterations, respectively. In addition, the evolution of the diffuse region may have much faster convergence during the optimization process because the change in design variables between two consecutive steps is usually not large.
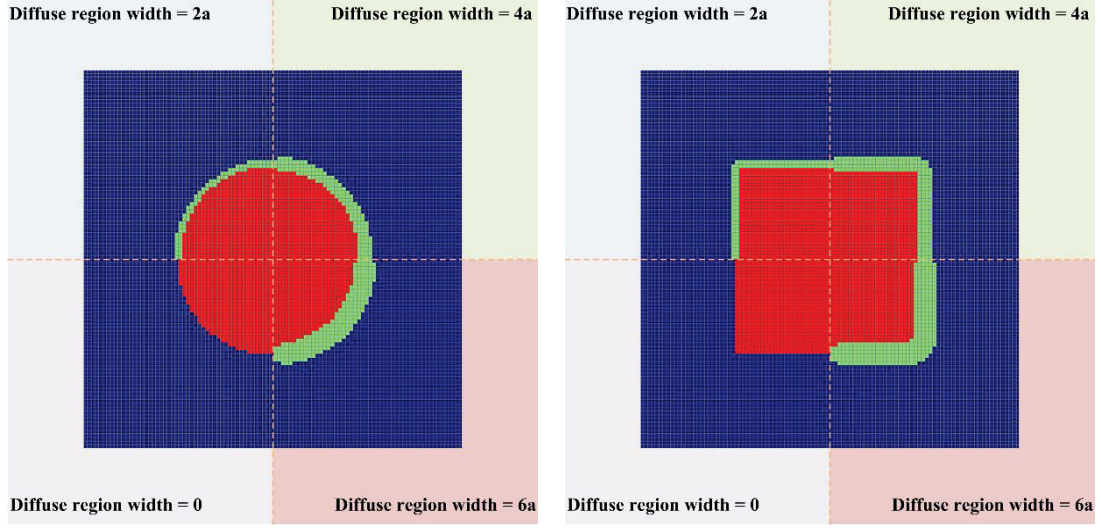
Fig. 4.2 Diffuse-region evolution with specified nonuniform diffuse-region widths.

4.2.2 Robust topology optimization formulation

The task of current robust optimization is to find the best vibration performance design that is less sensitive to the random diffuse-region width field for two material components [133]. The robustness measure (i.e., the objective function) is thus formulated as the weighted sum of the mean value $\mu\left(J\left(\phi,\tilde{\xi}\right)\right)$ and standard deviation $\sigma\left(J\left(\phi,\tilde{\xi}\right)\right)$ of the structural dynamic performance function $J\left(\phi,\tilde{\xi}\right)$ in Eqs. (4.5) and (4.8)–(4.10):

$$\text{Minimize}: \ f\left(\phi,\tilde{\xi}\right) = \mu\left(J\left(\phi,\tilde{\xi}\right)\right) + \alpha \cdot \sigma\left(J\left(\phi,\tilde{\xi}\right)\right), \tag{4.15}$$

where
$$J\left(\phi,\tilde{\xi}\right) = J_1\left(\phi,\tilde{\xi}\right), \ J_2\left(\phi,\tilde{\xi}\right), \text{or } J_3\left(\phi,\tilde{\xi}\right). \tag{4.16}$$

Here, the positive weight coefficient α is used to balance the mean value and standard deviation in the optimization formulation.

The present study considers the uncertain width of the diffuse region as a random field $\tilde{\xi}$

over the whole design domain, while the random field only affects the material distribution of the two candidate materials inside the diffuse region ξ. In fact, it can be formulated as the uncertain parameters of the phase-field functions. The material property functions k and m with respect to the elasticity tensor and mass in the diffuse interface domain in Eq. (1.14) are then rewritten as

$$
\begin{aligned}
k\left(\phi, \tilde{\xi}\right) &= \phi\left(\tilde{\xi}\right)^{p_1}, \\
m\left(\phi, \tilde{\xi}\right) &= \phi\left(\tilde{\xi}\right)^{p_2}.
\end{aligned}
\tag{4.17}
$$

The virtual elasticity tensor $\mathbf{D}^*\left(\phi, \tilde{\xi}\right)$ and mass density $\rho^*\left(\phi, \tilde{\xi}\right)$ in Eqs. (1.12) and (1.13) are thus both related to the random diffuse region field $\tilde{\xi}$. Furthermore, the stiffness matrix $\mathbf{K}\left(\phi, \tilde{\xi}\right)$, mass matrix $\mathbf{M}\left(\phi, \tilde{\xi}\right)$, and damping matrix $\mathbf{C}\left(\phi, \tilde{\xi}\right)$ in the governing equations (4.1), (4.3), and (4.6) are affected by the random field. The global stiffness and mass matrices can be further expressed with the phase-field function value at each element ϕ_e as

$$
\mathbf{K}\left(\phi, \tilde{\xi}\right) = \sum_{e=1}^{N_e} \left[\phi_e\left(\tilde{\xi}\right)^{p_1} \mathbf{k}_e^{(1)} + \left(1 - \phi_e\left(\tilde{\xi}\right)^{p_1}\right) \mathbf{k}_e^{(2)} \right],
\tag{4.18}
$$

$$
\mathbf{M}\left(\phi, \tilde{\xi}\right) = \sum_{e=1}^{N_e} \left[\phi_e\left(\tilde{\xi}\right)^{p_2} \mathbf{m}_e^{(1)} + \left(1 - \phi_e\left(\tilde{\xi}\right)^{p_2}\right) \mathbf{m}_e^{(2)} \right],
\tag{4.19}
$$

where $\mathbf{k}_e^{(1)}, \mathbf{m}_e^{(1)}$, $\mathbf{k}_e^{(2)}$, and $\mathbf{m}_e^{(2)}$ are respectively the elemental stiffness and mass matrices for materials phase 1 and 2.

With the above definitions of the objective function and random field, we formulate the robust optimization problem as

$$\underset{\phi}{\text{Minimize}} \ f\left(\phi,\tilde{\xi}\right) = \mu\left(J\left(\phi,\tilde{\xi}\right)\right) + \alpha \cdot \sigma\left(J\left(\phi,\tilde{\xi}\right)\right),$$

$$\text{subject to} \ \begin{cases} \left(-\theta^2 \mathbf{M}\left(\phi,\tilde{\xi}\right) + i\theta \mathbf{C}\left(\phi,\tilde{\xi}\right) + \mathbf{K}\left(\phi,\tilde{\xi}\right)\right)\mathbf{U} = \mathbf{F}, \\ \qquad\qquad \text{or} \\ \left(\mathbf{K}\left(\phi,\tilde{\xi}\right) - \omega^2 \mathbf{M}\left(\phi,\tilde{\xi}\right)\right)\mathbf{\Phi} = \mathbf{0}, \\ \qquad\qquad \text{or} \\ \mathbf{M}\left(\phi,\tilde{\xi}\right)\ddot{\mathbf{u}}\left(T\right) + \mathbf{C}\left(\phi,\tilde{\xi}\right)\dot{\mathbf{u}}\left(T\right) + \mathbf{K}\left(\phi,\tilde{\xi}\right)\mathbf{u}\left(T\right) = \mathbf{f}\left(T\right), \end{cases}$$

$$\sum_{e=1}^{N_f} \phi_e V_e - V_0 \leq 0, \tag{4.20}$$

$$\phi = \left[\phi_1,...,\phi_{N_f}\right],$$

$$0 \leq \phi_e \leq 1, \quad e = 1,....,N_f.$$

The structural stochastic dynamic response and sensitivity analysis techniques are addressed to solve the phase-field-based robust topology optimization problem in the following section.

4.3 Sensitivity analysis of the stochastic dynamic response

In the stochastic dynamic response analysis scheme based on the EOLE and PCE, the objective function is obtained using the structural dynamic response at the specified deterministic sampling points $\mathbf{\eta}^g$. Sensitivity analysis for the optimization problem (4.20) can therefore be conducted in two steps.

4.3.1 Deterministic sensitivity of structural dynamic responses

The present study considers three different types of structural dynamic performances in Eq. (4.16). The deterministic sensitivities of the structural dynamic response $J\left(\phi,\mathbf{\eta}\right)$ at specified sampling points can be derived with direct or adjoint variable approaches. The

deterministic sensitivity of the frequency response $J_1(\phi, \mathbf{\eta}^g)$, the natural frequency or

frequency gap $J_2(\phi, \mathbf{\eta}^g)$, and the transient dynamic response $J_3(\phi, \mathbf{\eta}^g)$ with respect to the

phase-field functions (design variables) at the gth sampling point $\mathbf{\eta}^g$ of the random variables

$\mathbf{\eta}$ are respectively presented in the followings.

(a) Sensitivity analysis of the frequency response

In the case of steady-state response optimization, the structural dynamic compliance J_1

in Eq. (4.5) only explicitly depends on the amplitude of the displacement response $\mathbf{U}(\phi, \mathbf{\eta}^g)$

(in Eq. (4.3)), which depends on the phase-field function value ϕ and the specified gth

sampling point $\mathbf{\eta}^g$. The sensitivity of $J_1(\mathbf{U}(\phi, \mathbf{\eta}^g))$ can then be derived with the adjoint

variable-based sensitivity analysis scheme as follows.

First, two adjoint vectors $\mathbf{\mu}_1$ and $\mathbf{\mu}_2$ are introduced and the objective function

$J_1(\mathbf{U}(\phi, \mathbf{\eta}^g))$ can be rewritten as

$$J = J_1(\mathbf{U}) + \mathbf{\mu}_1^{\mathrm{T}}(\mathbf{WU} - \mathbf{F}) + \mathbf{\mu}_2^{\mathrm{T}}(\overline{\mathbf{W}}\,\overline{\mathbf{U}} - \overline{\mathbf{F}}), \tag{4.21}$$

where $\overline{\mathbf{W}}$ and $\overline{\mathbf{F}}$ respectively denote the conjugates of the dynamic stiffness matrix $\mathbf{W}$

and excitation amplitude vector $\mathbf{F}$.

Differentiating Equation (4.21) with respect to phase-field functions at the eth element

gives

$$\frac{\mathrm{d}J}{\mathrm{d}\phi_e} = \boldsymbol{\mu}_1^{\mathrm{T}} \frac{\partial \mathbf{W}}{\partial \phi_e} \mathbf{U} + \boldsymbol{\mu}_2^{\mathrm{T}} \frac{\partial \overline{\mathbf{W}}}{\partial \phi_e} \overline{\mathbf{U}} + \frac{\partial \mathbf{U}^{\mathrm{R}}}{\partial \phi_e} \left(\frac{\partial J_1}{\partial \mathbf{U}^{\mathrm{R}}} + \boldsymbol{\mu}_1^{\mathrm{T}} \mathbf{W} + \boldsymbol{\mu}_2^{\mathrm{T}} \overline{\mathbf{W}} \right) + $$

$$\frac{\partial \mathbf{U}^{\mathrm{I}}}{\partial \phi_e} \left(\frac{\partial J_1}{\partial \mathbf{U}^{\mathrm{I}}} + i\,\boldsymbol{\mu}_1^{\mathrm{T}} \mathbf{W} - i\,\boldsymbol{\mu}_2^{\mathrm{T}} \overline{\mathbf{W}} \right). \tag{4.22}$$

Let the adjoint variables satisfy the equations

$$\boldsymbol{\mu}_1^{\mathrm{T}} \mathbf{S} = \frac{1}{2} \left(-\frac{\partial J_1}{\partial \mathbf{U}^{\mathrm{R}}} + i\frac{\partial J_1}{\partial \mathbf{U}^{\mathrm{I}}} \right) = \frac{1}{2} \left(-\frac{\mathbf{F}^{\mathrm{T}} \mathbf{U}^{\mathrm{R}} \mathbf{F}^{\mathrm{T}}}{\sqrt{\left(\mathbf{F}^{\mathrm{T}} \mathbf{U}^{\mathrm{R}}\right)^2 + \left(\mathbf{F}^{\mathrm{T}} \mathbf{U}^{\mathrm{I}}\right)^2}} + i\frac{\mathbf{F}^{\mathrm{T}} \mathbf{U}^{\mathrm{I}} \mathbf{F}^{\mathrm{T}}}{\sqrt{\left(\mathbf{F}^{\mathrm{T}} \mathbf{U}^{\mathrm{R}}\right)^2 + \left(\mathbf{F}^{\mathrm{T}} \mathbf{U}^{\mathrm{I}}\right)^2}} \right)$$

$$= -\frac{1}{2\sqrt{\left(\mathbf{F}^{\mathrm{T}} \mathbf{U}^{\mathrm{R}}\right)^2 + \left(\mathbf{F}^{\mathrm{T}} \mathbf{U}^{\mathrm{I}}\right)^2}} \mathbf{F}^{\mathrm{T}} \overline{\mathbf{U}} \mathbf{F}^{\mathrm{T}},$$

$$\tag{4.23}$$

$$\boldsymbol{\mu}_2^{\mathrm{T}} \overline{\mathbf{S}} = \frac{1}{2} \left(-\frac{\partial J_1}{\partial \mathbf{U}^{\mathrm{R}}} - i\frac{\partial J_1}{\partial \mathbf{U}^{\mathrm{I}}} \right) = \frac{1}{2} \left(-\frac{\mathbf{F}^{\mathrm{T}} \mathbf{U}^{\mathrm{R}} \mathbf{F}^{\mathrm{T}}}{\sqrt{\left(\mathbf{F}^{\mathrm{T}} \mathbf{U}^{\mathrm{R}}\right)^2 + \left(\mathbf{F}^{\mathrm{T}} \mathbf{U}^{\mathrm{I}}\right)^2}} - i\frac{\mathbf{F}^{\mathrm{T}} \mathbf{U}^{\mathrm{I}} \mathbf{F}^{\mathrm{T}}}{\sqrt{\left(\mathbf{F}^{\mathrm{T}} \mathbf{U}^{\mathrm{R}}\right)^2 + \left(\mathbf{F}^{\mathrm{T}} \mathbf{U}^{\mathrm{I}}\right)^2}} \right)$$

$$= -\frac{1}{2\sqrt{\left(\mathbf{F}^{\mathrm{T}} \mathbf{U}^{\mathrm{R}}\right)^2 + \left(\mathbf{F}^{\mathrm{T}} \mathbf{U}^{\mathrm{I}}\right)^2}} \mathbf{F}^{\mathrm{T}} \mathbf{U} \mathbf{F}^{\mathrm{T}}.$$

$$\tag{4.24}$$

With the adjoint vector solutions to Eqs. (4.23) and (4.24), the derivative of the objective function for the gth sampling point $\boldsymbol{\eta}^g$ can be determined using

$$\frac{\mathrm{d}J\left(\boldsymbol{\eta}^g\right)}{\mathrm{d}\phi_e} = 2\,\mathrm{Re}\left(\boldsymbol{\mu}_1^{\mathrm{T}} \left(-\theta^2 \frac{\partial \mathbf{M}\left(\boldsymbol{\eta}^g\right)}{\partial \phi_e} + i\,\theta \frac{\partial \mathbf{C}\left(\boldsymbol{\eta}^g\right)}{\partial \phi_e} + \frac{\partial \mathbf{K}\left(\boldsymbol{\eta}^g\right)}{\partial \phi_e} \right) \mathbf{U}\left(\boldsymbol{\eta}^g\right) \right). \tag{4.25}$$

Here, $\mathrm{Re}(\ \cdot\ )$ denotes the real part of the complex vector.

(b) Sensitivity analysis of the structural natural frequency

In the case that the structure has no repeated eigenfrequencies, the sensitivity of the jth eigenfrequency with respect to the phase-field function value assigned to the eth element for the gth sampling point $\mathbf{\eta}^g$ can be easily obtained as

$$\frac{\partial \omega_j\left(\mathbf{\eta}^g\right)}{\partial \phi_e} = \frac{\mathbf{\varphi}_j^{\mathrm{T}}\left(\dfrac{\partial \mathbf{K}\left(\mathbf{\eta}^g\right)}{\partial \phi_e} - \omega_j^2 \dfrac{\partial \mathbf{M}\left(\mathbf{\eta}^g\right)}{\partial \phi_e}\right)\mathbf{\varphi}_j}{2\omega_j}. \tag{4.26}$$

For some structural configurations, one eigenfrequency may correspond to two eigenvectors. The repeated eigenfrequency ω can be assumed to have two normalized orthogonal eigenvectors $\mathbf{\varphi}_1$ and $\mathbf{\varphi}_2$ ($\mathbf{\varphi}_1^{\mathrm{T}}\mathbf{M}\mathbf{\varphi}_2 = 0$). The eigenvector $\overline{\mathbf{\varphi}}$ can thus be expressed with a linear combination of $\mathbf{\varphi}_1$ and $\mathbf{\varphi}_2$ as

$$\overline{\mathbf{\varphi}} = c_1\mathbf{\varphi}_1 + c_2\mathbf{\varphi}_2, \tag{4.27}$$

and $c_1^2 + c_2^2 = 1$ we have $\overline{\mathbf{\varphi}}^{\mathrm{T}}\mathbf{M}\overline{\mathbf{\varphi}} = 1$ when $c_1^2 + c_2^2 = 1$. Substituting (3.29) into (3.28) gives

$$\frac{\partial \omega^2}{\partial \phi_e} = c_1^2\mathbf{\varphi}_1^{\mathrm{T}}\left(\frac{\partial \mathbf{K}\left(\mathbf{\eta}^g\right)}{\partial \phi_e} - \omega_j^2 \frac{\partial \mathbf{M}\left(\mathbf{\eta}^g\right)}{\partial \phi_e}\right)\mathbf{\varphi}_1 + c_2^2\mathbf{\varphi}_2^{\mathrm{T}}\left(\frac{\partial \mathbf{K}\left(\mathbf{\eta}^g\right)}{\partial \phi_e} - \omega_j^2 \frac{\partial \mathbf{M}\left(\mathbf{\eta}^g\right)}{\partial \phi_e}\right)\mathbf{\varphi}_2$$
$$+ 2c_1 c_2\mathbf{\varphi}_1^{\mathrm{T}}\left(\frac{\partial \mathbf{K}\left(\mathbf{\eta}^g\right)}{\partial \phi_e} - \omega_j^2 \frac{\partial \mathbf{M}\left(\mathbf{\eta}^g\right)}{\partial \phi_e}\right)\mathbf{\varphi}_2. \tag{4.28}$$

The extreme values of $\partial \omega^2/\partial x_e$ can be evaluated by introducing a Lagrange function $L = \dfrac{\partial \omega^2}{\partial \phi_e} + \lambda^{\mathrm{sub}}\left(c_1^2 + c_2^2 - 1\right)$ with the Lagrange multiplier λ^{sub}. By differentiating the Lagrange function with respect to the two constants c_1 and c_2, we have the eigenfrequency sub-problem

103

$$\begin{bmatrix} \boldsymbol{\varphi}_1^{\mathrm{T}}\left(\dfrac{\partial \mathbf{K}\left(\boldsymbol{\eta}^g\right)}{\partial \phi_e} - \omega_j^2 \dfrac{\partial \mathbf{M}\left(\boldsymbol{\eta}^g\right)}{\partial \phi_e}\right)\boldsymbol{\varphi}_1 & \boldsymbol{\varphi}_1^{\mathrm{T}}\left(\dfrac{\partial \mathbf{K}\left(\boldsymbol{\eta}^g\right)}{\partial \phi_e} - \omega_j^2 \dfrac{\partial \mathbf{M}\left(\boldsymbol{\eta}^g\right)}{\partial \phi_e}\right)\boldsymbol{\varphi}_2 \\[3mm] \boldsymbol{\varphi}_2^{\mathrm{T}}\left(\dfrac{\partial \mathbf{K}\left(\boldsymbol{\eta}^g\right)}{\partial \phi_e} - \omega_j^2 \dfrac{\partial \mathbf{M}\left(\boldsymbol{\eta}^g\right)}{\partial \phi_e}\right)\boldsymbol{\varphi}_1 & \boldsymbol{\varphi}_2^{\mathrm{T}}\left(\dfrac{\partial \mathbf{K}\left(\boldsymbol{\eta}^g\right)}{\partial \phi_e} - \omega_j^2 \dfrac{\partial \mathbf{M}\left(\boldsymbol{\eta}^g\right)}{\partial \phi_e}\right)\boldsymbol{\varphi}_2 \end{bmatrix} \begin{Bmatrix} c_1 \\ c_2 \end{Bmatrix} + \lambda^{\mathrm{sub}}\begin{Bmatrix} c_1 \\ c_2 \end{Bmatrix} = \begin{Bmatrix} 0 \\ 0 \end{Bmatrix},$$

$$(4.29)$$

the solution of which gives eigenvalues and corresponding eigenvectors:

$$\begin{cases} \lambda_1^{\mathrm{sub}} & \text{with } \mathbf{c}_1 = \left\{\mathbf{c}_{11}, \mathbf{c}_{12}\right\}^{\mathrm{T}}, \\ \lambda_{\mathrm{h}}^{\mathrm{sub}} & \text{with } \mathbf{c}_{\mathrm{h}} = \left\{\mathbf{c}_{\mathrm{h1}}, \mathbf{c}_{\mathrm{h2}}\right\}^{\mathrm{T}}. \end{cases}$$

$$(4.30)$$

The sensitivities of the repeated eigenfrequency can be obtained from λ_1^{sub} and $\lambda_{\mathrm{h}}^{\mathrm{sub}}$ as

$$\frac{\partial \omega\left(\boldsymbol{\eta}^g\right)}{\partial \phi_e} = \begin{cases} \lambda_1^{\mathrm{sub}}\left(\boldsymbol{\eta}^g\right) & \text{with eigenvector } \overline{\boldsymbol{\varphi}}_1 = c_{11}\boldsymbol{\varphi}_1 + c_{12}\boldsymbol{\varphi}_2, \\ \lambda_{\mathrm{h}}^{\mathrm{sub}}\left(\boldsymbol{\eta}^g\right) & \text{with eigenvector } \overline{\boldsymbol{\varphi}}_{\mathrm{h}} = c_{\mathrm{h1}}\boldsymbol{\varphi}_1 + c_{\mathrm{h2}}\boldsymbol{\varphi}_2. \end{cases}$$

$$(4.31)$$

The sensitivities of single and repeated eigenvalues of the objective function $J_2\left(\phi, \boldsymbol{\eta}^g\right)$

in (4.8) with respect to the eth phase-field calculation point at the gth sampling point $\boldsymbol{\eta}^g$ can

then be obtained. In the case that the objective function is the gap between two adjacent

eigenvalues ω_n^2 and ω_{n-1}^2 in Eq. (4.9), it is only required to calculate the sensitivities of both

orders of the natural frequencies and perform the subtraction operation.

(c) Sensitivity analysis of the structural transient dynamic response

The sensitivity of the transient dynamic behavior function $J_3 = \int_{T_1}^{T_2} u_a^2(T)\,\mathrm{d}T$ with respect

to the phase-field function value assigned to the eth element for the gth sampling point $\boldsymbol{\eta}^g$

can be easily obtained as

$$\frac{\partial J_3\left(\phi, \boldsymbol{\eta}^g\right)}{\partial \phi_e} = \frac{\partial \int_0^{T_2} u_a^2\left(T, \boldsymbol{\eta}^g\right) \mathrm{d}T}{\partial \phi_e} - \frac{\partial \int_0^{T_1} u_a^2\left(T, \boldsymbol{\eta}^g\right) \mathrm{d}T}{\partial \phi_e}, \tag{4.32}$$

where the two terms on the right-hand share the same form but have different end times. Therefore, only the sensitivity of the integral $J_3^*\left(\phi, \boldsymbol{\eta}^g\right) = \int_0^{T^*} u_a^2\left(T, \boldsymbol{\eta}^g\right) \mathrm{d}T$ needs to be calculated. By introducing a time-depended adjoint vector $\boldsymbol{\lambda}(T)$, the Lagrangian function can be obtained as

$$L(\mathbf{u}, \boldsymbol{\lambda}) = \int_0^{T^*} u_a^2\left(T, \boldsymbol{\eta}^g\right) \mathrm{d}t + \int_0^{T^*} \boldsymbol{\lambda}^{\mathrm{T}}\left[\mathbf{M}\ddot{\mathbf{u}} + \mathbf{C}\dot{\mathbf{u}} + \mathbf{K}\mathbf{u} - \mathbf{f}(T)\right] \mathrm{d}T. \tag{4.33}$$

Differentiating the Lagrangian function L with respect to the design variable x_e $(e = 1, 2, ..., N_e)$ using the chain rule (assuming that $\partial \mathbf{f}(T)/\partial \phi_e = 0$) gives

$$\frac{\partial L}{\partial \phi_e} = \int_0^{T^*} \frac{\partial u_a^2}{\partial \mathbf{u}} \frac{\partial \mathbf{u}}{\partial \phi_e} \mathrm{d}T + \int_0^{T^*} \boldsymbol{\lambda}^{\mathrm{T}}\left(\frac{\partial \mathbf{M}}{\partial \phi_e}\ddot{\mathbf{u}} + \frac{\partial \mathbf{C}}{\partial \phi_e}\dot{\mathbf{u}} + \frac{\partial \mathbf{K}}{\partial \phi_e}\mathbf{u}\right) \mathrm{d}T + \int_0^{T^*} \boldsymbol{\lambda}^{\mathrm{T}}\left(\mathbf{M}\frac{\partial \ddot{\mathbf{u}}}{\partial \phi_e} + \mathbf{C}\frac{\partial \dot{\mathbf{u}}}{\partial \phi_e} + \mathbf{K}\frac{\partial \mathbf{u}}{\partial \phi_e}\right) \mathrm{d}T$$

$$. \tag{4.34}$$

Integrating by parts for the last term of Eq. (4.34) and noting that the initial conditions are independent of the design variables, the derivative of the Lagrangian function $\partial L/\partial \phi_e$ becomes

$$\frac{\partial L}{\partial \phi_e} = \int_0^{T^*} \boldsymbol{\lambda}^{\mathrm{T}}\left(\frac{\partial \mathbf{M}}{\phi_e}\ddot{\mathbf{u}} + \frac{\partial \mathbf{C}}{\phi_e}\dot{\mathbf{u}} + \frac{\partial \mathbf{K}}{\phi_e}\mathbf{u}\right) \mathrm{d}t + \int_0^{T^*}\left(\frac{\partial g}{\partial \mathbf{u}} + \ddot{\boldsymbol{\lambda}}^{\mathrm{T}}\mathbf{M} - \dot{\boldsymbol{\lambda}}^{\mathrm{T}}\mathbf{C} + \boldsymbol{\lambda}^{\mathrm{T}}\mathbf{K}\right)\frac{\partial \mathbf{u}}{\partial \phi_e} \mathrm{d}T$$
$$+ \boldsymbol{\lambda}^{\mathrm{T}}(T^*)\mathbf{M}\frac{\partial \dot{\mathbf{u}}(T^*)}{\partial \phi_e} + \left(\boldsymbol{\lambda}^{\mathrm{T}}(T^*)\mathbf{C} - \dot{\boldsymbol{\lambda}}^{\mathrm{T}}(T^*)\mathbf{M}\right)\frac{\partial \mathbf{u}(T^*)}{\partial \phi_e}. \tag{4.35}$$

As equation (4.35) holds for arbitrary $\boldsymbol{\lambda}(T)$, the adjoint vector can be chosen as the solution to the adjoint equations

$$\begin{cases} \ddot{\boldsymbol{\lambda}}^{\mathrm{T}}\mathbf{M} - \dot{\boldsymbol{\lambda}}^{\mathrm{T}}\mathbf{C} + \boldsymbol{\lambda}^{\mathrm{T}}\mathbf{K} &=& -2u_{\mathrm{a}}^2\left(\boldsymbol{\eta}^g\right)\mathbf{p}_0, \\ \boldsymbol{\lambda}^{\mathrm{T}}\left(T^*\right) &=& 0, \\ \dot{\boldsymbol{\lambda}}^{\mathrm{T}}\left(T^*\right) &=& 0, \end{cases} \tag{4.36}$$

where $\mathbf{p}_0 = \{0,...,0,1,0,...,0\} \in \mathbf{R}^{1\times n}$, with 1 at the target DOF entry and 0 elsewhere. The above adjoint equations (4.36) with terminal conditions are first converted into initial-value equations using the time mapping $\tilde{T} = T^* - T$, and they are then readily solved using the implicit Newmark method in a manner similar to the structural transient-response analysis.

By substituting the solution $\boldsymbol{\lambda}^{\mathrm{T}}$ of Eq. (4.36) into (4.35), the derivative of the objective function $J_3^*\left(\phi, \boldsymbol{\eta}^g\right)$ at the gth sampling point $\boldsymbol{\eta}^g$ can be obtained as

$$\begin{aligned} \frac{\partial J_3^*\left(\phi, \boldsymbol{\eta}^g\right)}{\partial \phi_e} = \int_0^{T^*} \boldsymbol{\lambda}^{\mathrm{T}} \Bigg[&p_2 \phi_e\left(\boldsymbol{\eta}^g\right)^{p_2-1}\left(\mathbf{m}_e^{(1)} - \mathbf{m}_e^{(2)}\right)\ddot{\mathbf{u}} + \left(\alpha_1 p_2 \phi_e\left(\boldsymbol{\eta}^g\right)^{p_2-1}\left(\mathbf{m}_e^{(1)} - \mathbf{m}_e^{(2)}\right)\right. \\ &\left. + \alpha_2 p_1 \phi_e\left(\boldsymbol{\eta}^g\right)^{p_1-1}\left(\mathbf{k}_e^{(1)} - \mathbf{k}_e^{(2)}\right)\dot{\mathbf{u}}\right) + p_1 \phi_e\left(\boldsymbol{\eta}^g\right)^{p_1-1}\left(\mathbf{k}_e^{(1)} - \mathbf{k}_e^{(2)}\right)\mathbf{u}\Bigg]\mathrm{d}T. \end{aligned} \tag{4.37}$$

In deterministically obtaining the sensitivity of the different types of the structural dynamic response, the derivatives of the mass matrix and stiffness matrix with respect to the eth phase-field design point at the gth sampling point $\boldsymbol{\eta}^g$ are obtained as

$$\frac{\partial \mathbf{K}\left(\boldsymbol{\eta}^g\right)}{\partial \phi_e} = \frac{\partial \sum\limits_{e=1}^{N_e}\left[\phi_e\left(\boldsymbol{\eta}^g\right)^{p_1}\mathbf{k}_e^{(1)} + \left(1 - \phi_e\left(\boldsymbol{\eta}^g\right)^{p_1}\right)\mathbf{k}_e^{(2)}\right]}{\partial \phi_e} = p_1\phi_e\left(\boldsymbol{\eta}^g\right)^{p_1-1}\left(\mathbf{k}_e^{(1)} - \mathbf{k}_e^{(2)}\right), \tag{4.38}$$

$$\frac{\partial \mathbf{M}\left(\boldsymbol{\eta}^g\right)}{\partial \phi_e} = \frac{\partial \sum\limits_{e=1}^{N_e}\left[\phi_e\left(\boldsymbol{\eta}^g\right)^{p_2}\mathbf{m}_e^{(1)} + \left(1 - \phi_e\left(\boldsymbol{\eta}^g\right)^{p_2}\right)\mathbf{m}_e^{(2)}\right]}{\partial \phi_e} = p_2\phi_e\left(\boldsymbol{\eta}^g\right)^{p_2-1}\left(\mathbf{m}_e^{(1)} - \mathbf{m}_e^{(2)}\right). \tag{4.39}$$

4.3.2 Stochastic sensitivity analysis of dynamic responses via PCE

After obtaining the deterministic sensitivities of different types of the structural dynamic response to each phase-field calculation point $\partial J\left(\phi, \mathbf{\eta}^g\right)/\partial \phi_e$ at the specified sampling points, the sensitivity of the stochastic response function can be calculated using

$$\frac{\partial J\left(\phi, \mathbf{\eta}\right)}{\partial \phi_e} = \sum_{i=0}^{N_{\mathrm{PCE}}} \frac{\partial j_i\left(\phi\right)}{\partial \phi_e} \Phi_i\left(\mathbf{\eta}\right). \tag{4.40}$$

Here, the coefficients $\partial j_i\left(\phi\right)/\partial \phi_e$ can be obtained by using the nonintrusive differentiation approach [59] as

$$\frac{\partial j_i\left(\phi\right)}{\partial \phi_e} = \frac{\mathrm{E}\left(\dfrac{\partial J\left(\phi, \mathbf{\eta}\right)}{\partial \phi_e} \Phi_i\right)}{\mathrm{E}\left(\Phi_i^2\right)} = \frac{\displaystyle\sum_{g=1}^{N_g} \dfrac{\partial J\left(\phi, \mathbf{\eta}^g\right)}{\partial \phi_e} \Phi_i\left(\mathbf{\eta}^g\right) w^g}{\mathrm{E}\left(\Phi_i^2\right)} , \ i = 0,1,...,N_{\mathrm{PCE}}. \tag{4.41}$$

Furthermore, the sensitivities of the mean value and standard deviation of the stochastic dynamic responses with respect to the phase-field function value associated with the *e*th element can be expressed as

$$
\begin{aligned}
\frac{\partial \mu\left(J\left(\phi, \mathbf{\eta}\right)\right)}{\partial \phi_e} &= \int_{\Omega_{\mathrm{r}}} \frac{\partial J\left(\phi, \mathbf{\eta}\right)}{\partial \phi_e} \rho\left(\mathbf{\eta}\right) \mathrm{d}\mathbf{\eta} = \frac{\partial j_0\left(\phi\right)}{\partial \phi_e} \\
&= \frac{\partial \left(\displaystyle\sum_{g=1}^{N_g} J\left(\mathbf{x}, \mathbf{\eta}^g\right) \Phi_0\left(\mathbf{\eta}^g\right) w^g \Big/ \mathrm{E}\left(\Phi_0^2\right) \right)}{\partial \phi_e} ,
\end{aligned}
\tag{4.42}
$$

$$
\begin{aligned}
\frac{\partial \sigma\left(J\left(\phi, \mathbf{\eta}\right)\right)}{\partial \phi_e} &= \frac{1}{\sigma\left(J\left(\phi, \mathbf{\eta}\right)\right)} \int_{\Omega_{\mathrm{r}}} \left(J\left(\phi, \mathbf{\eta}\right) - j_0\left(\phi\right)\right) \left(\frac{\partial \tilde{f}_{\mathrm{D}}\left(\mathbf{x}, \boldsymbol{\xi}\right)}{\partial \phi_e} - \frac{\partial j_0\left(\phi\right)}{\partial \phi_e} \right) \rho\left(\mathbf{\eta}\right) \mathrm{d}\mathbf{\eta} \\
&= \sum_{i=1}^{N_{\mathrm{PCE}}} \frac{j_i \dfrac{\partial j_i\left(\mathbf{x}\right)}{\partial \phi_e} \mathrm{E}\left(\Phi_i^2\right)}{\sigma\left(J\left(\phi, \mathbf{\eta}\right)\right)} .
\end{aligned}
\tag{4.43}
$$

Finally, the sensitivity of the objective function of the robust topology optimization

problem (4.56) is obtained as

$$
\begin{aligned}
\frac{\partial J(\phi,\boldsymbol{\eta})}{\partial \phi_e} &= \frac{\partial \mu\left(J(\phi,\boldsymbol{\eta})\right)}{\partial \phi_e} + \alpha \cdot \frac{\partial \sigma\left(J(\phi,\boldsymbol{\eta})\right)}{\partial \phi_e} \\
&= \frac{\partial\left(\sum_{g=1}^{N_g} J\left(\mathbf{x},\boldsymbol{\eta}^g\right) \Phi_0\left(\boldsymbol{\eta}^g\right) w^g \Big/ \mathrm{E}\left(\Phi_0^2\right)\right)}{\partial \phi_e} + \alpha \cdot \sum_{i=1}^{N_{\mathrm{PCE}}} \frac{j_i \dfrac{\partial j_i(\mathbf{x})}{\partial \phi_e} \mathrm{E}\left(\Phi_i^2\right)}{\sigma\left(J(\phi,\boldsymbol{\eta})\right)}.
\end{aligned}
\tag{4.44}
$$

4.4 Numerical implementations

A flowchart of the robust topology optimization procedure is presented in Fig. 4.3. At the beginning of the procedure, the random field of diffuse-region widths over the design domain is discretized using the EOLE method, and the diffuse-region-width sampling quadrature points used in the PCE are then determined. Next, an initial phase-field function for two material phases is defined over the whole design domain without diffuse regions, and the diffuse regions are then generated by solving the evolutional equation of the phase-field function (4.14) for the sampling quadrature points. After analyzing the deterministic dynamic responses and the corresponding sensitives at the specified sampling points, the mean value and standard deviation of the structural dynamic response and corresponding sensitivity can be obtained with PCE according to Eq. (3.40). The phase-field functions will be updated by solving the Allen–Cahn equation (1.10) with the semi-implicit discretizing scheme (4.12) between iterations and be updated by solving the evolutional equation (4.14) to ensure the sampling quadrature points of the diffuse-region widths satisfy the random-width field within each iteration. Specifically, the phase field is evaluated with the diffuse-region random width field until the maximum relative difference in phase-field functions between two consecutive evolutions is less than 10^{-3} at the beginning of each iteration, and the evolution of the optimization is then implemented by solving the Allen–Cahn equation with the scheme in (4.12) again. These

optimization procedures are repeated until the difference between values of the objective function in two adjacent iteration steps falls below a prescribed value (10^{-4} in the numerical examples).
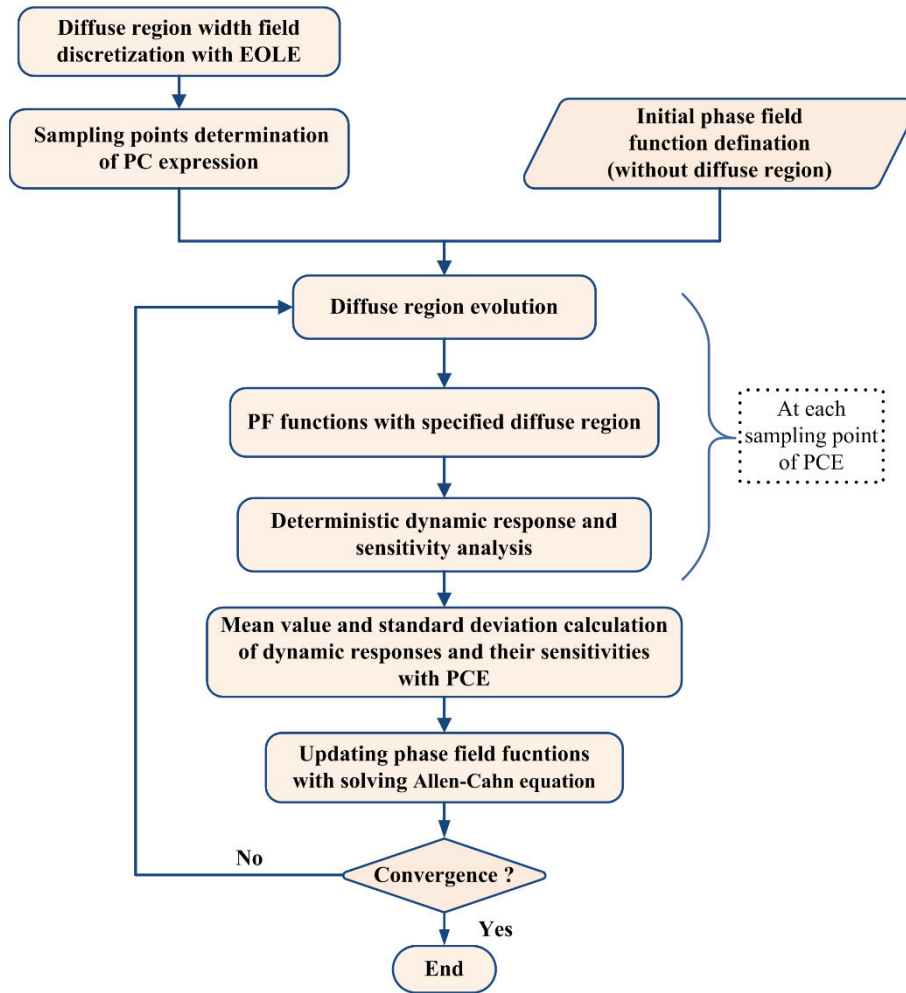
Fig. 4.3 Flowchart of the phase-field-based robust topology optimization for vibrating structures considering stochastic diffuse-region uncertainties.

4.5 Numerical examples of vibrating structures

This section presents numerical examples to show the validity of the proposed optimization formulation. Here, different types of robust objective functions, namely the frequency responses, fundamental frequency, frequency gap, and structural transient dynamic response,

are considered. The effects of important factors on the robust optimization are also discussed.

4.5.1 Robust topology optimization of beam structures for reducing the frequency response

(a) Optimization results of cantilever beams

The first example considers the robust topology optimization of a rectangular cantilever beam under an external harmonic excitation, as shown in Fig. 4.4. The design domain has geometrical dimensions $l_1 = 2$ m and $l_2 = 1$ m. The force $f(T) = Fe^{i\theta T}$ (with $F = 10^6$ N, $\theta = 2\pi f$, and $f = 100$ Hz) is applied at the mid-point of the free edge. The properties of the two candidate materials are that material 1 has a Young's modulus $E_1 = 2.1 \times 10^{11}$ N/m^2, Poisson's ratio $v_1 = 0.3$, and mass density $\rho_1 = 7800$ kg/m^3 while material 2 has a Young's modulus $E_2 = 3.0 \times 10^{10}$ N/m^2, Poisson's ratio $v_2 = 0.3$, and mass density $\rho_2 = 3500$ kg/m^3. The random field of the diffuse-region width satisfies a Gaussian distribution with mean value $\mu_\xi = 0.12$m, coefficient of variation $\gamma = \sigma_\xi/\mu_\xi = 0.15$, and correlation length $L = 1$m. The structure is discretized with $N_e = 5000 \ (100 \times 50)$ uniformly sized Q4 elements, with the total number of DOFs being $n = 10302$.
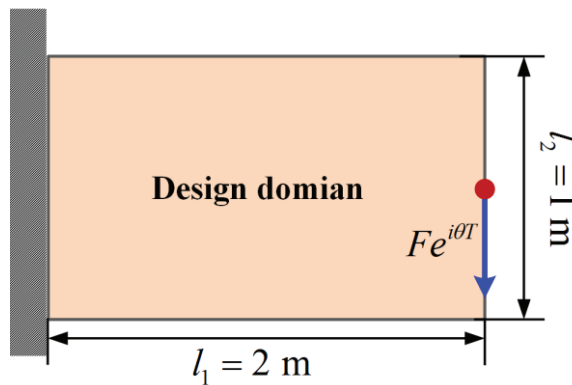
Fig. 4.4 Rectangular cantilever beam under an external harmonic excitation.

In the optimization model, the trade-off weighting factor between the mean value and standard deviation of the frequency response is taken as $\alpha = 10$ in the objective function. The upper limit of the allowable amount of material 1 is set as 50% of the design domain. The initial design is given as circles filled with material 2 and surrounded by material 1. After 19 steps of the diffuse-region evolution with Eq. (4.11), the mean configuration of the initial design with the uncertain diffuse region is that shown in Fig. 4.5(a). In the initial design, the structure has a mean frequency response of 1783.6 N·m and a standard deviation of 29.6 N·m. The optimization process gets convergence after 124 iterations, and the mean configuration of the optimal design is obtained as in Fig. 4.5(b). The history of the objective function of the optimization process is shown in Fig. 4.6, showing that the mean and standard deviation of the frequency response for optimal design are respectively 365.73 N·m and 0.98 N·m. The mean values of first five orders of eigenfrequencies for the initial design and optimal design are summarized in Table 4.1, showing the first three eigenfrequencies have moved away from the external excitation frequency remarkably.

(a)   (b)
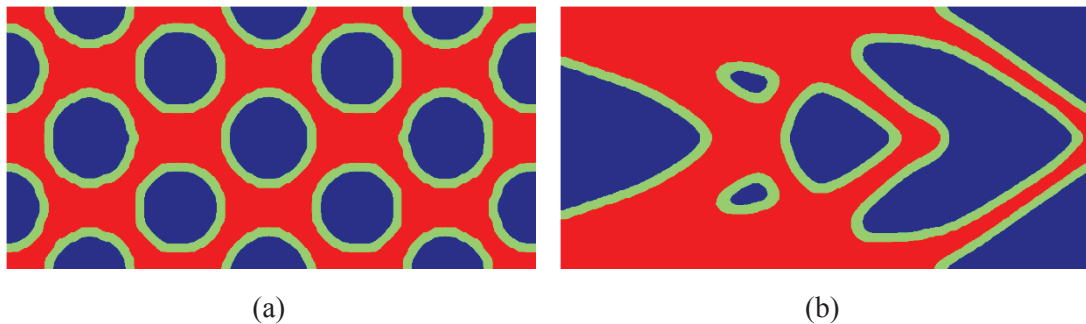
Fig. 4.5 Initial mean design and optimal mean design for the cantilever beam under harmonic excitation.
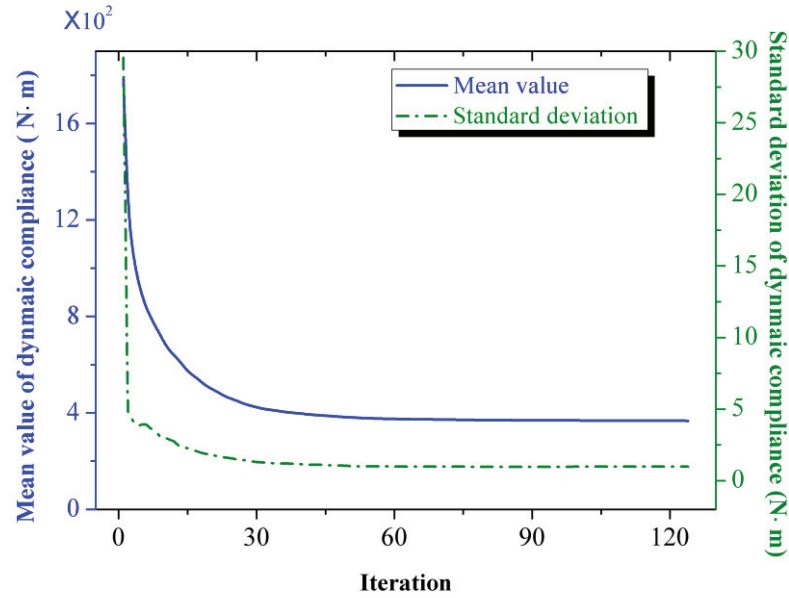
Fig. 4.6 Iteration histories of the mean value and standard deviation of the structural dynamic compliance.

Table 4.1 Comparison of mean values of eigenfrequencies of the initial and optimized designs.

Order	Initial design (Hz)	Optimized design (Hz)
1	120.6	192.9
2	425.0	537.2
3	475.7	587.7
4	999.7	1046.3
5	1280.0	1140.7

(c) Influencing factors

This subsection discusses several parameters that affect the optimal solutions. We first consider the effect of the weighting factor α for the mean value and standard deviation. All settings and parameters are selected the same as those in the previous example except for four

112

different cases of weighting factors: $\alpha = 1,\ 30,\ 50,$ and 100. The optimized designs are shown in Fig. 4.7. The mean values and standard deviations for these cases are summarized in Table 4.2. It is seen that as the weighting factor increases (i.e., the standard deviation plays a more important role), the solution changes remarkably and the optimization ends with larger mean dynamic compliances and smaller standard deviations. $\alpha = 100$ Sawtooth-like boundaries appear in the optimized design for a very large weighting factor $\alpha = 100$, as shown in Fig. 4.7(d).

(a)   (b)

(c)   (d)
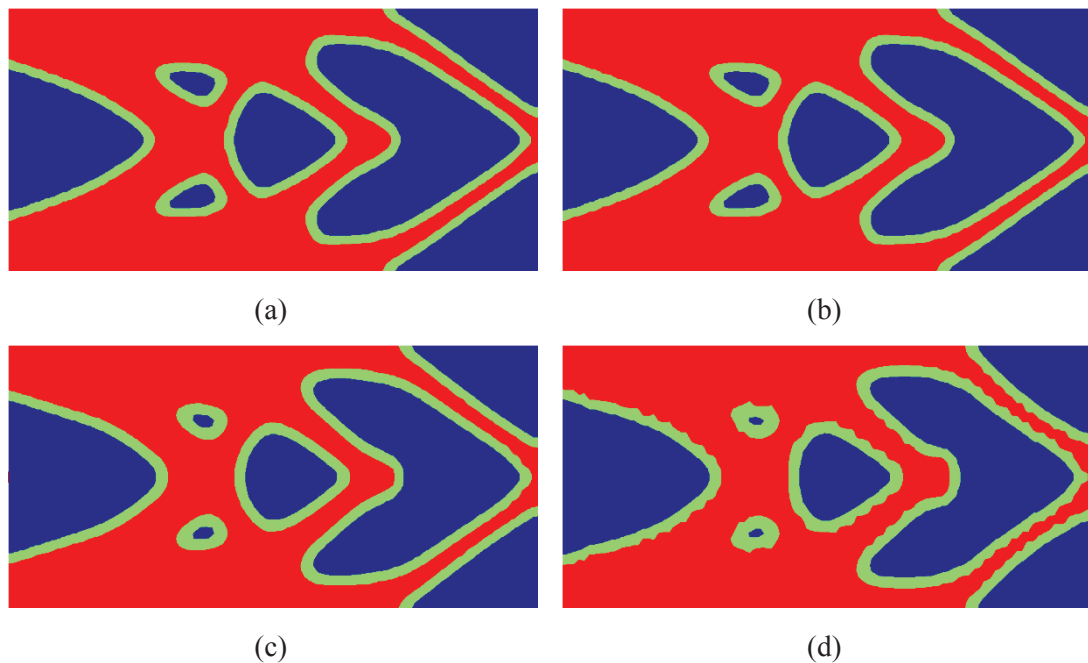
Fig. 4.7 Optimized designs of a cantilever beam obtained with different weighting factors: (a) $\alpha = 1$; (b) $\alpha = 30$; (c) $\alpha = 50$; (d) $\alpha = 100$.

Table 4.2 Comparison of the mean value and standard variance of dynamic compliance for different weighting factors

Weighting factor α	Mean value of dyn. compl. (N·m)	Standard variance of dyn. compl. (N·m)
1	365.62	1.04
10	365.73	0.98

30	369.07	0.90
50	372.58	0.84
100	379.03	0.68

The effect of the coefficient of variation (COV) γ is then studied. The same parameters are used in this example except for four different COV values: $\gamma = 0.05,\ 0.15,\ 0.25,$ and 0.35. The optimization solutions are presented in Fig. 4.8, and the mean values and standard deviations of the dynamic compliance are compared in Table 4.3. Figures 4.5(b) and 4.8 show that nearly the same topologies are obtained for different values of the COV, while Table 3 shows the mean value becomes a little larger and the standard deviation increases nearly linearly with the COV. This implies that a change in the COV may not change the optimization solution obviously but can still affect structural robustness.

(a)　　　　　　　　　　　(b)　　　　　　　　　　　(c)
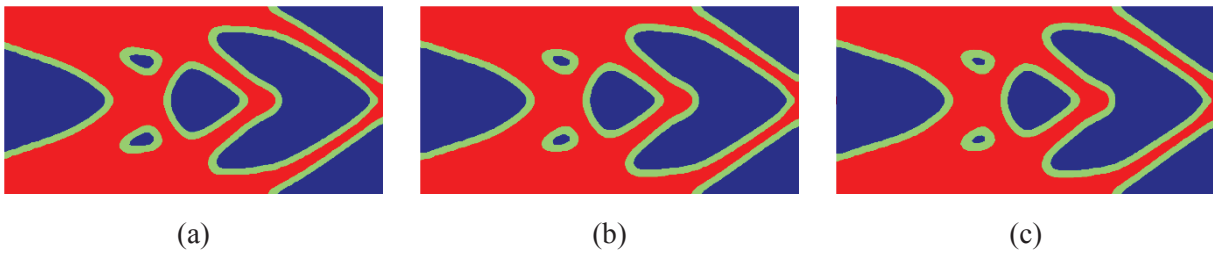
Fig. 4.8 Optimized designs of a cantilever beam obtained with different COVs: (a) $\gamma = 0.05$; (b) $\gamma = 0.25$; (c) $\gamma = 0.35$.

Table 4.3 Comparison of the mean value and standard variance of dynamic compliance for different COVs.

COV γ	Mean value of dyn. compl. ($\mathrm{N \cdot m}$)	Standard variance of dyn. compl. ($\mathrm{N \cdot m}$)
0.05	364.07	0.46
0.15	365.73	0.98
0.25	368.02	2.07
0.35	370.43	2.87

The effect of the mean value of the diffuse-region width is also studied. The COV is now fixed at $\gamma = 0.15$, and all parameters are the same as those in the pervious example except for the different diffuse-region widths. Here, four other mean values of the diffuse-region width $\mu_\xi = 0.04, 0.08, 0.16,$ and 0.20m are considered. The optimization solutions are given in Fig. 4.9 and the corresponding mean value and standard deviation are listed in Table 2.4. It is found that the mean value of the dynamic compliance increases with that of the diffuse-region width, and some structural members with the 'strong' material (i.e., material 1) become thinner. This is because there is a larger relatively-weak region in the final design when the diffuse region broadens, which may weaken the structural dynamic performance.

| (a) | (b) |

| (c) | (d) |
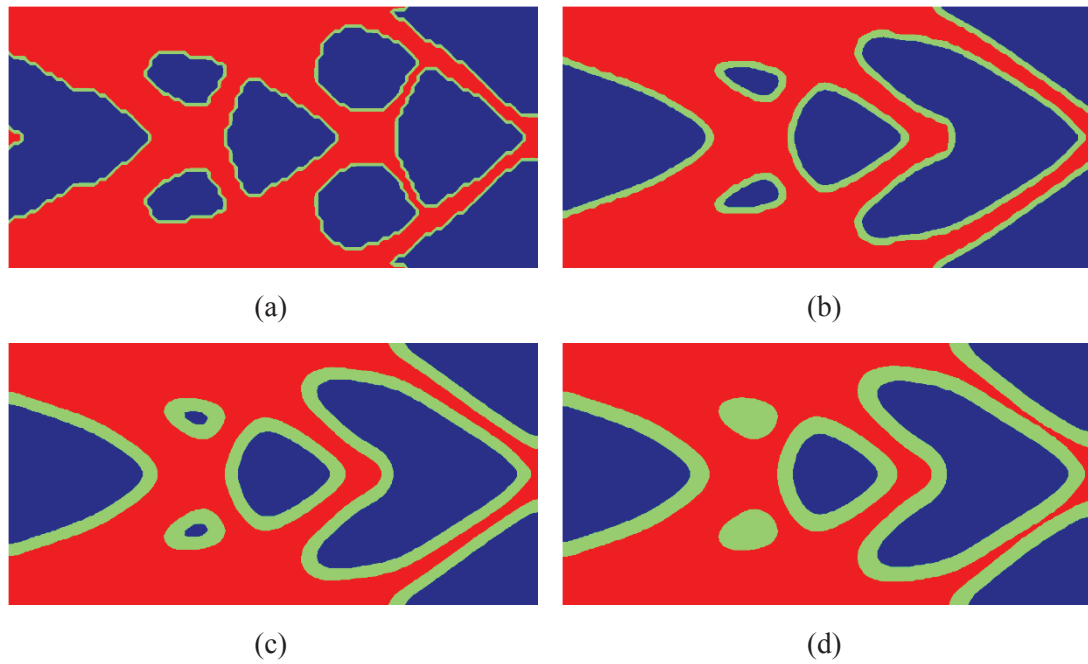
Fig. 4.9 Optimization solutions of a cantilever beam obtained for different diffuse-region widths: (a) $\mu_\xi = 0.04\text{m}$; (b) $\mu_\xi = 0.08\text{m}$; (c) $\mu_\xi = 0.16\text{m}$; (d) 0.20m.

Table 2.4 Mean value and standard deviation of dynamic compliance for different diffuse-region widths.

Mean diffuse region width μ_ξ	Mean value of dyn.	Standard deviation of dyn.

	compl. (N·m)	compl. (N·m)
0.04	353.70	0.97
0.08	355.10	1.12
0.12	365.73	0.98
0.16	378.53	0.84
0.20	391.39	0.72

(b) Robust design obtained under different excitation frequencies

The effect of the excitation frequency on the optimal design is studied in this subsection. The same structure as used in the pervious example considered, and the optimizations are made under four different external excitations f_p = 1000, 2000, 3000, and 4000 Hz. The optimization solutions are shown in Fig. 4.10. It is seen that as the excitation frequency increases, the optimal solution tends to become a more complex shape and the load transmission path becomes less clear. This can be explained as that the higher vibration modes are excited by higher-frequency excitation, and the 'strong' material tends to distribute in the more isolated areas to suppress local vibrations. Because the current optimization problem is a bi-material optimization problem without any void phase in the design domain, the loading path has no risk of interruption with such material distributions. For the case of external frequency f_p = 2000 Hz (i.e., the optimized design in Fig. 4.10(b)), vibration amplitude contours of the mean initial design and the mean optimal design are shown in Fig. 4.11. It is seen that the mean maximum vibration amplitude reduces by a factor of about 5, and the local vibration modes vanish after the optimization.
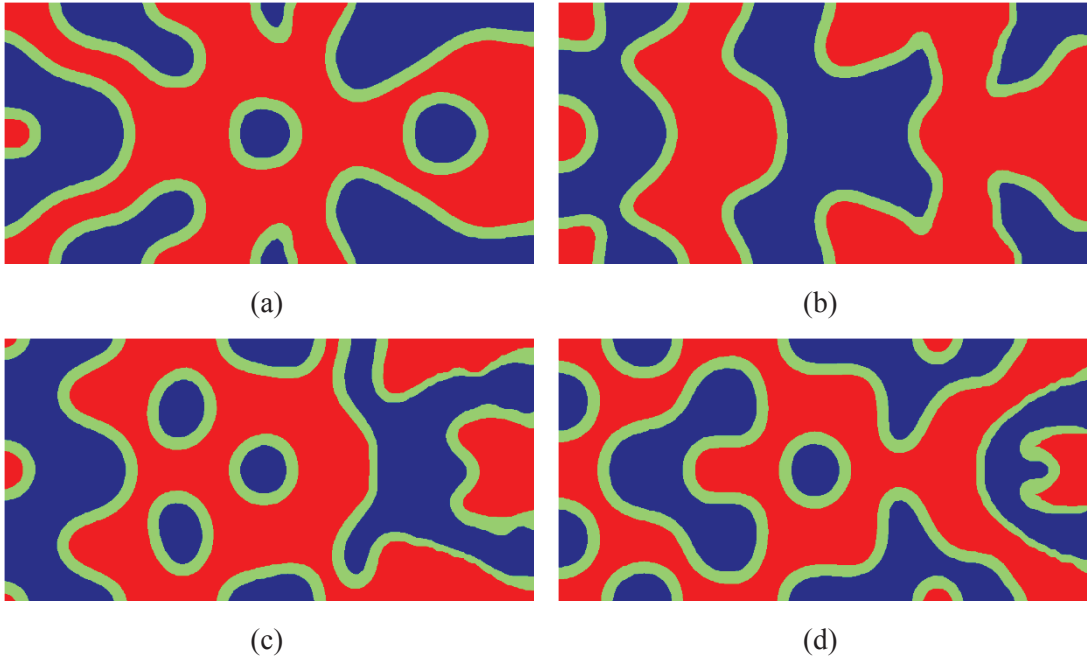
Fig. 4.10 Optimized design obtained under different excitation frequencies: (a) $f_p =$ 1000 Hz; (b) $f_p = 2000$ Hz; (c) $f_p = 3000$ Hz; (d) $f_p = 4000$ Hz.
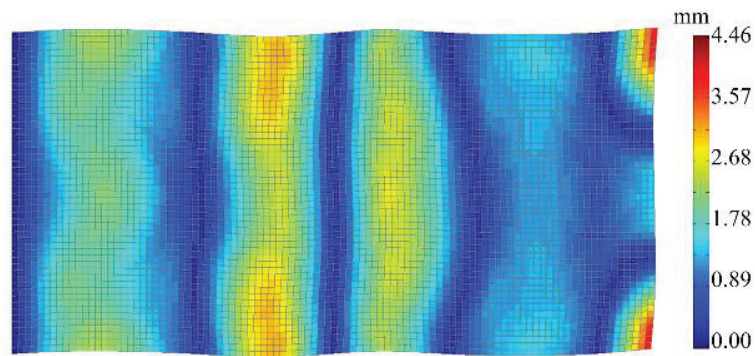
(a)
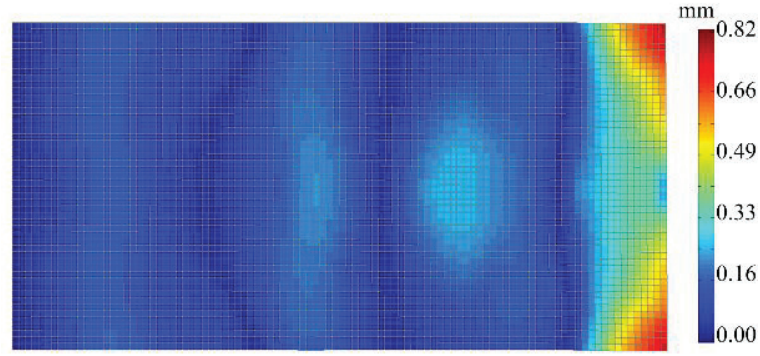
(b)

Fig. 4.11 Mean vibration level of the cantilever beam under excitation at $f_p = 2000$ Hz

for (a) the initial design and (b) the optimized design.

4.5.2 Robust topological design for structural eigenfrequencies

(a) Optimization for the structural fundamental frequency

We now study the robust topology optimization for structural eigenfrequencies. A two-edge fixed rectangular beam is considered as shown in Fig. 4.12. The design domain consists of two candidate materials, namely materials 1 and 2, and the geometrical dimensions of the beam are $l_1 = 5$ m and $l_2 = 1$ m. The uncertain width of the diffuse region between the two material phases is assumed to satisfy a Gaussian distribution with a mean width of $\mu_\xi = 0.2$m, COV of $\gamma = 0.15$, and correlation length of $L = 1$m. The structure is discretized with $N_e = 4500 \ (150 \times 30)$ uniformly sized Q4 elements and $N_f = N_e = 5000$ phase-field calculation points located at each element center. In the optimization model, the fundamental eigenfrequency (4.8) of the beam is excepted to be maximized, and the weighting factor is taken as $\alpha = 10$ in the objective function (4.15). The volume constraint for material 1 is 50%.

118
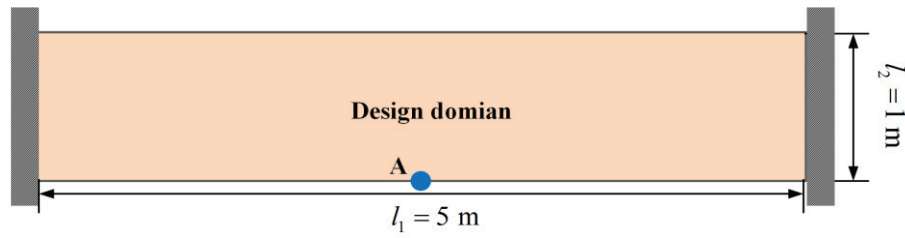
Fig. 4.12 Two-edge fixed rectangular beam.

The optimization process can not get a fast convergence in this example since some orders of eigenfrequencies become repeated during the optimization. Thus, the optimization process is terminated after 200 iterations (the change of the objective functions between two consecutive iterations has become relatively small), the weighted objective function increases from 737 Hz (where the mean value is 715 Hz and the standard deviation is 2.18 Hz) for the initial design to 1074.7 Hz (where the mean value is 1065.4 Hz and the standard deviation is 0.93 Hz) for the optimized design after the optimization process. The iteration history and optimal solution are respectively given in Figs. 4.13 and 4.14. Compared with the benchmark optimal result given by Du and Olhoff [41] for optimization of the bi-material structure topology in the deterministic case, the optimal result obtained with the proposed method has the same tendency of the material distribution but some small bars and local bulk areas vanish. This is naturally due to the optimal design having greater robustness, while the local and small material patches are usually easily affected by uncertainty inputs (i.e., the diffuse-region field in this study). The iteration histories of the mean values of the first three eigenfrequencies are given in Fig. 4.15, showing that all mean values of the first three eigenfrequencies increase after optimization.
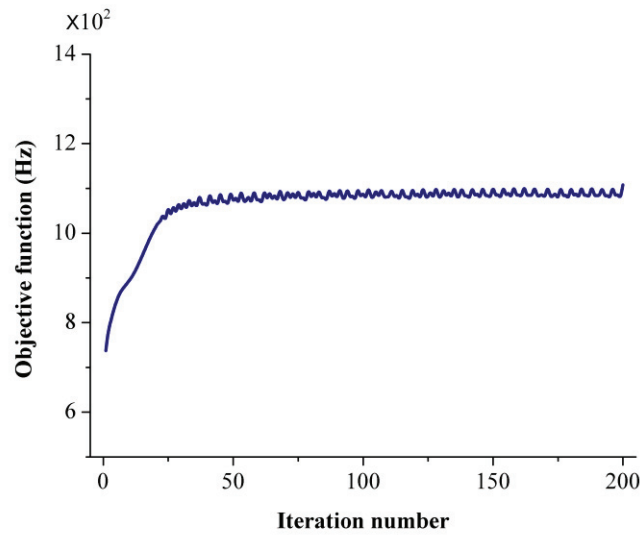
Fig. 4.13 Iteration history of the objective function of the eigenfrequency optimization.
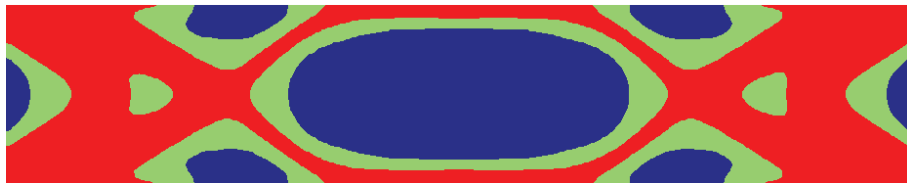
Fig. 4.14 Optimization solution of the two-edge fixed beam maximizing the fundamental frequency.
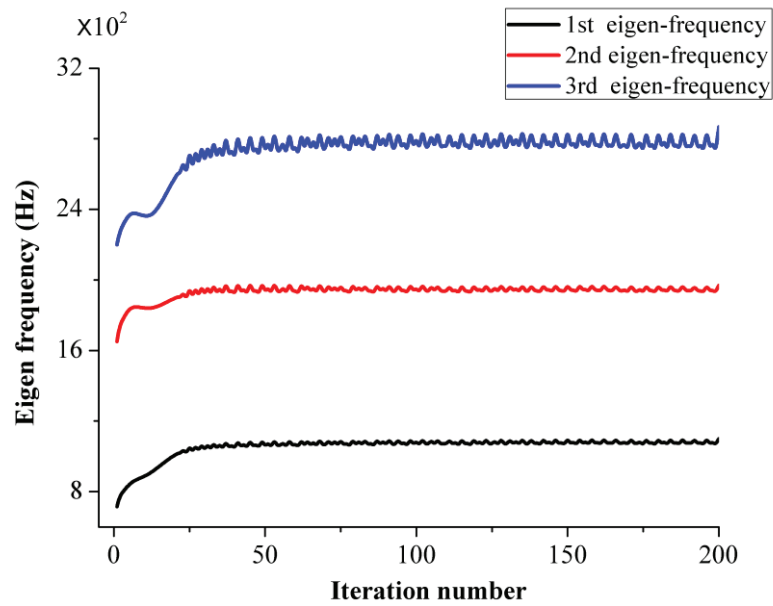
Fig. 4.15 Iteration histories of the mean values of the first three eigenfrequencies.

The effects of the mean diffuse-region width are also studied. The optimization solutions obtained with three other mean diffuse-region widths $\mu_\xi = 0.1, 0.3$, and 0.4m are shown in Fig. 4.16. The mean values and standard deviations of the fundamental frequencies for the optimal designs obtained with different diffuse-region widths are summarized in Table 4.5. A higher mean fundamental frequency is obtained for a narrower diffuse region because the effect of the uncertain field is weak and there are larger areas of diffuse material in the case of a wider diffuse region (e.g., Fig. 4.16(c)), which may affect the mechanical properties of the whole structure.

(a)

(b)

(c)
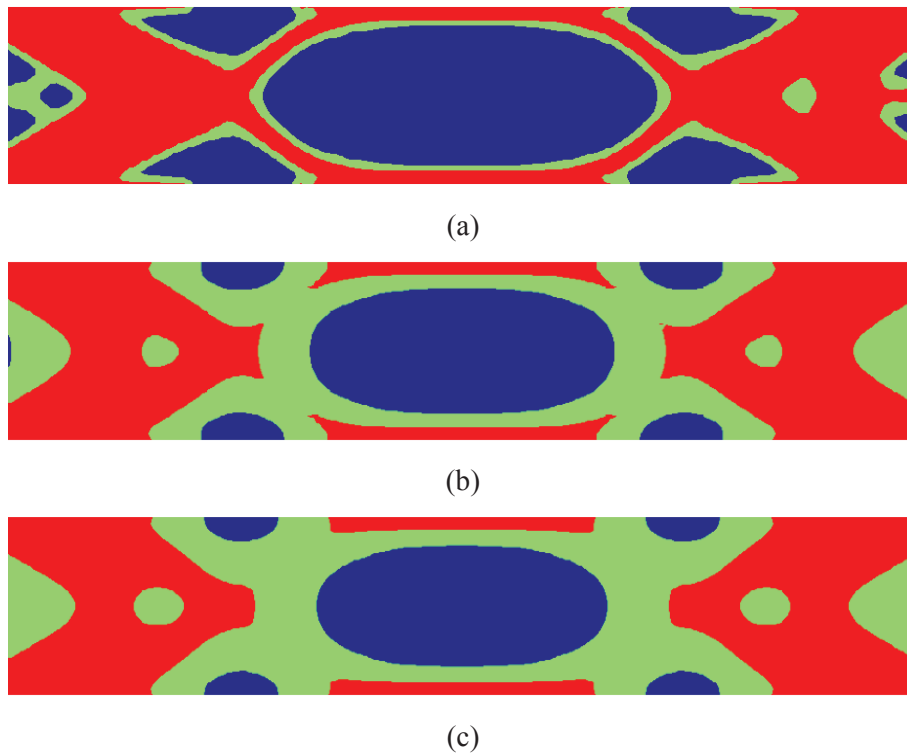
Fig. 4.16 Optimization solutions for eigenfrequency optimization with different diffuse region widths: (a) $\mu_\xi = 0.1$m; (b) $\mu_\xi = 0.3$m; (c) $\mu_\xi = 0.4$m.

Table 4.5 Mean values and standard deviations of the fundamental frequencies for
optimized designs obtained for different mean diffuse-region widths.

Mean diffuse region width μ_ξ	Mean value of fundamental eigenfrequency (Hz)	Standard deviation of fundamental eigenfrequency (Hz)
0.1	1132.6	1.77
0.2	1100.4	0.78
0.3	1022.3	0.56
0.4	1006.5	0.46

(b) Optimization for the frequency gap

This subsection implements the robust optimization of maximizing the gap between two adjacent frequencies. A two-edge clamped beam structure with a concentrated mass $m_c = 2 \times 10^4$ kg attached at the midpoint of the lower edge (point A) is considered as shown in Fig. 2.12. The same materials and geometrical dimensions of the beam are chosen as in the pervious example.

In the optimization model, the gap between the second and third eigenfrequencies is maximized, the weighting factor is taken as $\alpha = 1$, and the volume constraint for material 1 is 50%. The diffuse region width is assumed to have a mean width $\mu_\xi = 0.2$m, COV $\gamma = 0.15$, and correlation length $L = 1$m. The optimization solution is shown in Fig. 4.17. The optimization changes the mean value and standard deviation of the eigenfrequency gap from 678.1 and 0.84 Hz to 1863.8 and 1.96 Hz, respectively. The iteration histories of the mean values of the first four eigenfrequencies are given in Fig. 4.18. The eigenfrequency gap between the second and third eigenfrequencies is clearly increased by the optimization. Meanwhile, the third and fourth eigenfrequencies become approximately repeated and alternately rise after

about 50 iterations, demonstrating that the proposed sensitivity analysis and optimization model work well.

Fig. 4.17 Robust optimal design of the two-edge clamped beam for maximizing the frequency gap between the second and third frequencies.
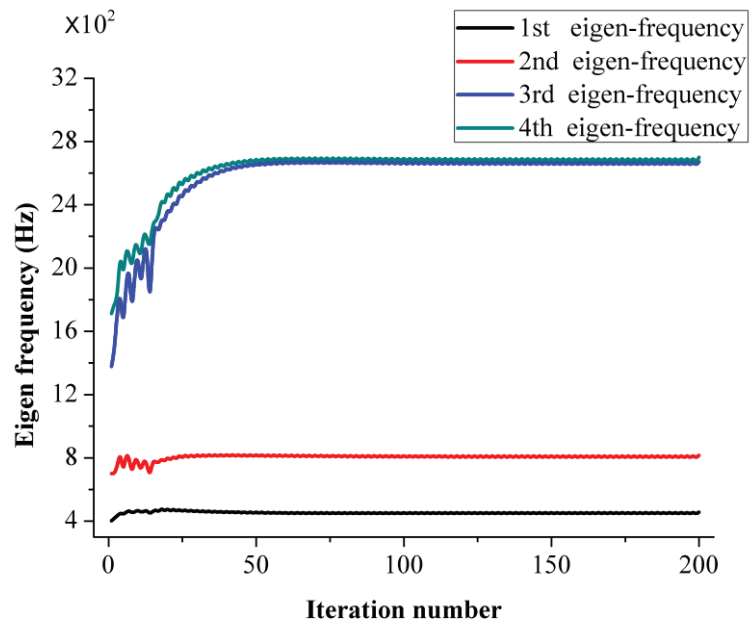
Fig. 4.18 Iteration histories of the mean values of eigenfrequencies.

Two mean diffuse-region widths $\mu_\xi = 0.1$ and 0.3 m are further studied. The optimal solutions are shown in Fig. 4.19. Figures 19 and 21 show that the main configuration of the optimal design changes only very slightly for different mean diffuse-region widths except for the boundary-layer widths. The mean values of the frequency gap between the second and third frequencies for the cases $\mu_\xi = 0.1$, 0.2, and 0.3 m are respectively 1906.5, 1863.8, and 1798.1

Hz while the standard deviations are respectively 0.83, 1.96, and 3.52 Hz. The results show that a higher mean value of the diffuse-region width reduces both the mean frequency gaps of the optimal designs and structural robustness.

(a)

(b)
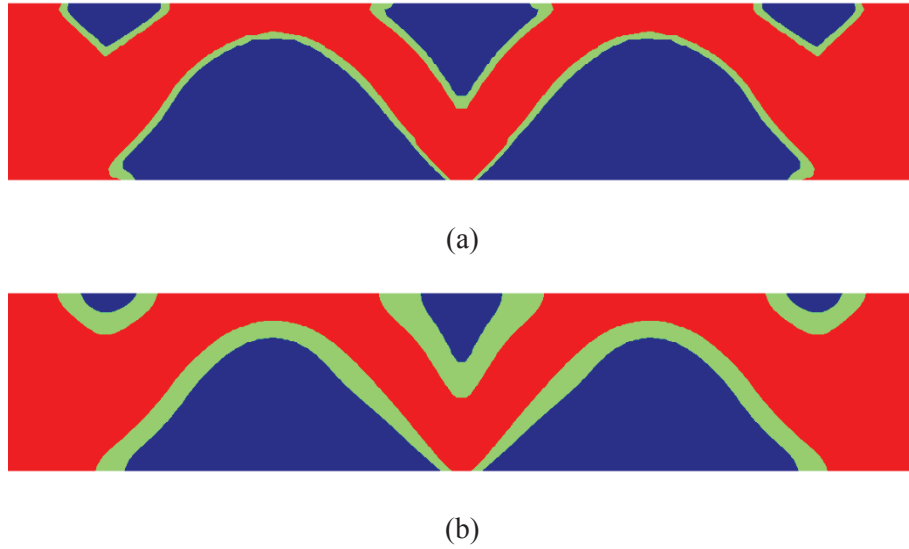
Fig. 4.19 Robust optimal designs for maximizing the frequency gap for different mean diffuse-region widths: (a) $\mu_\varsigma = 0.1$ m; (b) $\mu_\varsigma = 0.3$ m.

4.5.3 Robust topology optimization of the damping material coverage over plate structures under impact loads

We now study the robust topological design of structures under impact loads. A cantilever plate structure with a damping material covering both faces excited by an impact force $\mathbf{F}(T)$ at the mid-point of the free end (point I) is considered as shown in Fig. 4.20. Here, the base structure is considered as the non-design domain while the distribution of the damping material is designable, which implies the optimization problem considered in this example is a solid–void phase robust topology optimization problem. The plate has geometrical dimensions $a = 1.2$ m , $b = 0.8$ m , and $t_b = 1 \times 10^{-2}$ m for the host layer and $t_d = 5 \times 10^{-3}$ m for the

damping layer. The material properties of the base structure are $E_b = 2.1 \times 10^{11}$ N/m^2, $\rho_b = 7800$ kg/m^3, and $v_b = 0.3$ while the material properties of the damping layer are $E_d = 2.2 \times 10^8$ N/m^2, $\rho_d = 980$ kg/m^3, and $v_d = 0.49$. The damping coefficients of the base structure are $\alpha = \beta = 1 \times 10^{-6}$. The time history of the impact force $\mathbf{F}(T)$ is shown in Fig. 4.21. The terminal time considered in the objective function is $T = 0.1$ s and the time step used in the time integration is $\Delta T = 2 \times 10^{-4}$ s.

The structure is discretized with $N_e = 2400 \, (60 \times 40)$ uniformly sized four-node quadrilateral Mindlin shell elements and $N_f = N_e = 2400$ phase-field calculation points located at each element center. The Gaussian distribution of the uncertain diffuse regions between two material phases is assumed to have a mean width of $\mu_\xi = 0.12$m, COV of $\gamma = 0.15$, and correlation length of $L = 1$m.
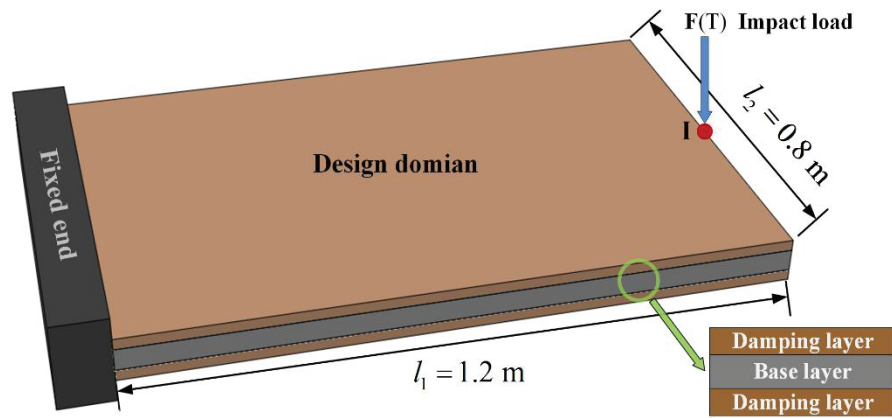
Fig. 4.20 Cantilever damping plate excited by an impact force.
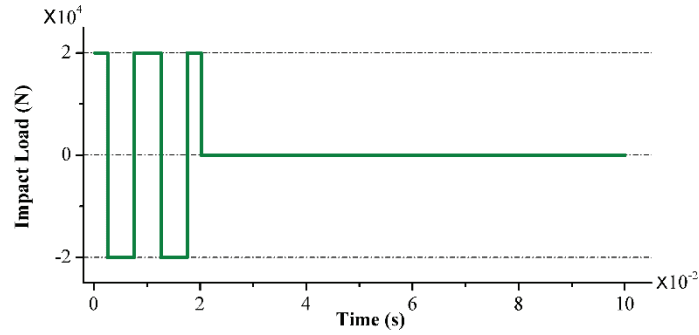
Fig. 4.21 Time history of the impact load.

In the optimization model, the squared displacement response of the load point in the time interval $[0, 0.1s]$ is chosen as the target dynamic response index, and the objective function with a weighting factor of $\alpha = 10$ is minimized. The volume constraint for material 1 is taken as 50%. The optimal solution and suggested damping material coverage (obtained by extracting phase-field function boundaries at the mid-line of the diffuse region) are shown in Fig. 4.21. The mean value and standard deviation of the squared displacement of the load point decrease from $1.96\,\text{m}^2$ and $2 \times 10^{-2}\,\text{m}^2$ to $1.39\,\text{m}^2$ and $7 \times 10^{-4}\,\text{m}^2$, respectively. The time histories of the mean displacement at the load point for the initial design and optimized design are shown in Fig. 4.22, revealing that the vibration level at the load point is reduced remarkably by optimization. The first five eigenfrequencies of the plate structures are summarized in Table 4.6. It is seen that these eigenfrequencies change very little during the optimization process, which can be explained as that the lower-order eigenfrequencies of the structure have no remarkable effect on the transient-response optimization under impact loads. Additionally, robust optimization with two other values ($\mu_\xi = 0.06\text{m}$ and 0.18 m) of the mean diffuse-region width are also implemented; the optimal designs are shown in Fig. 4.24. Compared with the optimal solutions of the frequency response (Figs. 4.5 and 4.7) and fundamental frequency (Figs. 4.14 and 4.16) for different diffuse-region widths, the differences among the optimal designs

126

of the transient response for different diffuse-region widths are much more obvious, possible because the transient dynamic optimization problems have more local solutions and are more readily affected by uncertain parameters.

(a)   (b)
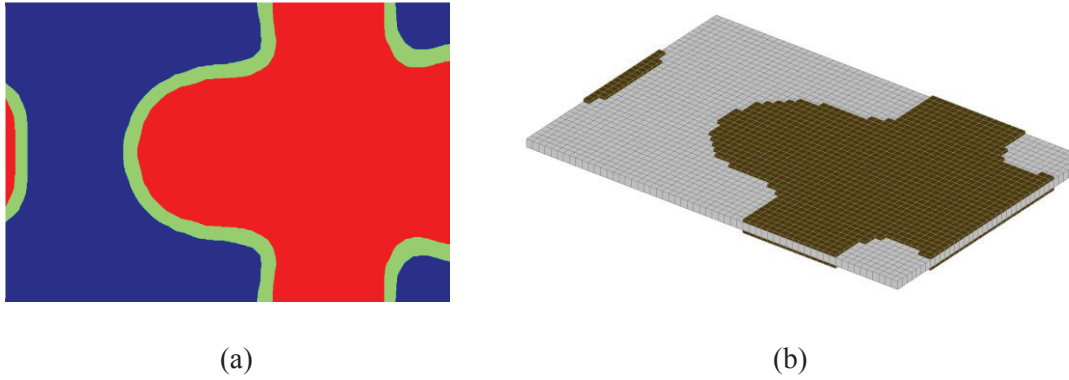
Fig. 4.22 Optimized design of the cantilever damping plate under impact loads: (a) optimal solution; (b) suggested damping coverage (obtained by extracting the mid-line of the diffuse region).
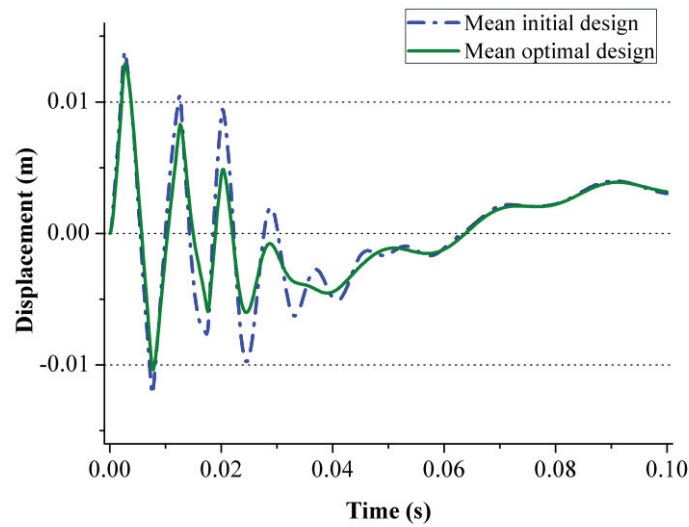
Fig. 4.23 Time history of the mean displacement at the load point.

Table 4.6 Eigenfrequencies of the plate structures for the initial design and optimized design.

Order	Initial design (Hz)	Optimized design (Hz)
1	7.81	7.74

2	26.21	26.17
3	48.49	48.43
4	88.39	89.13
5	120.60	119.87

<div align="center">(a)   (b)</div>
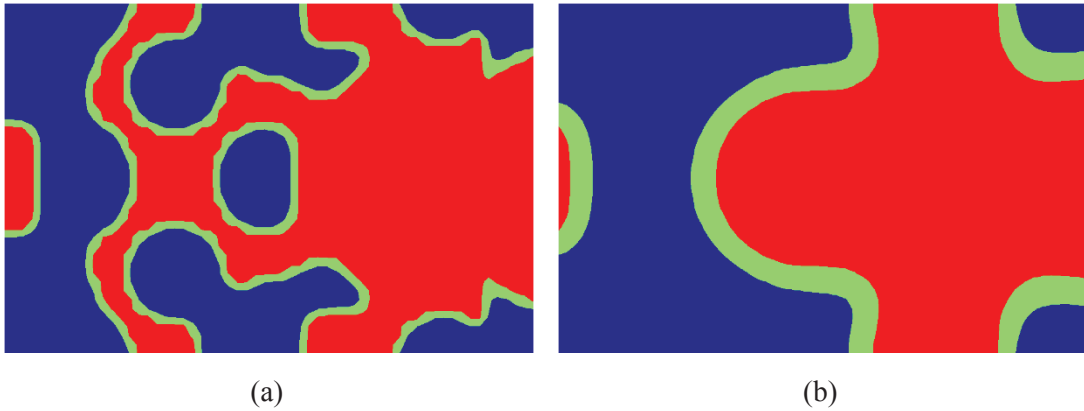
Fig. 4.24 Optimal solutions for the cantilever damping plate obtained with different values of the mean diffuse-region width: (a) $\mu_\xi = 0.06\text{m}$; (b) $\mu_\xi = 0.18$ m.

In the following, we consider the same plate as in the previous example but with different load times $T^{\text{load}} = 0.01$ and 0.03 s, while the mean diffuse-region width is fixed as $\mu_\xi = 0.12\text{m}$. The optimized designs and suggested damping coverage are shown in Fig. 4.25. The load time has a remarkable effect on the final optimal solution. This is a natural consequence of the different external loads exciting different modes of vibrations, and the optimization process driving the evolution of phase-field function to a design that suppresses the corresponding vibration modes.

<div style="text-align:center">(a)</div>

<div style="text-align:center">(b)</div>

<div style="text-align:center">(c)</div>

<div style="text-align:center">(d)</div>
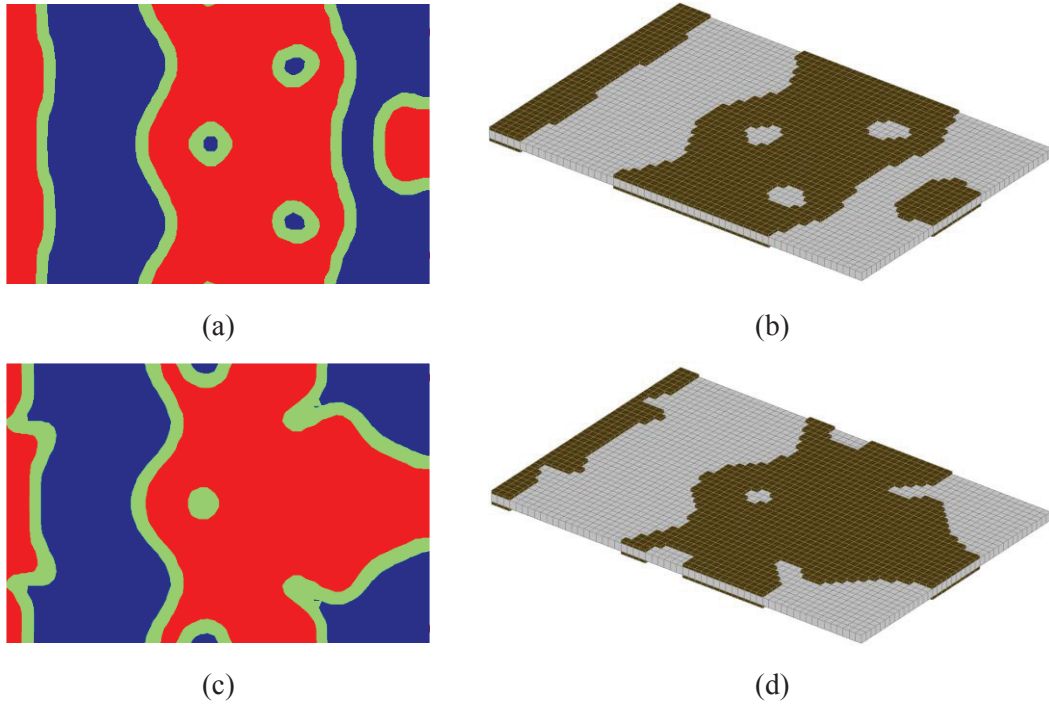
Fig. 4.25 Optimized designs of cantilever plates under different impact loads: (a) $T^{\mathrm{load}} = 0.01$ s; (b) $T^{\mathrm{load}} = 0.03$ s.

4.6 Robust topology design of phononic crystals with random diffuse via phase-field method

The manufacturing errors uncertainties can remarkably affect the band gap properties of PnCs, thus it is necessary to considering uncertainties in the design and optimization of the microstructures of the unit cell. The material property uncertainty of PnCs is from the inherent material inhomogeneity and also affected by the changing of the environment. While the manufacturing errors may include the uncertainties of the boundary geometry and diffuse regions between material phases of PnCs. How to efficiently handle the diffuse region uncertainties of PnCs and implement the corresponding topology optimization are major tasks of this chapter.

The chapter aims to develop a phase field-based topology optimization framework for

achieving a robust microstructural design of PnCs under diffuse region uncertainties. Herein, the diffuse regions between two material phases are assumed to satisfy a spatial Gaussian random field and discretized into uncorrelated stochastic variables with the EOLE method; then stochastic band gap analysis is conducted with the PCE. Herein, the PCE coefficients are obtained from the deterministic band gap analysis results obtained with the finite element method (FEM) at specified quadrature points, and the deterministic band gaps of PnCs are aggregated with the Kreisselmeier–Steinhauser (KS) function of the frequency data for each wave vector. For achieving a less sensitive optimal design of PnCs, a phase-field based robust topology optimization formulation to minimize the weighted sum of the mean value and standard deviation of the specified band gap is formulated.

4.6.1 Material distribution presentation of PnCs via phase-filed model

We first introduce the phase field method into the representation of the unit cell of a 2D phononic crystal composed of plumbum inclusions (represented with Ω_1), epoxy matrix (represented with Ω_2), and a diffuse layer ξ between the material phases. The whole design domain (the unit cell) thus can be formulated with with the phase-field function ϕ as

$$\left\{ \begin{array}{lll} \phi = 1 & \Leftrightarrow & \chi \in \Omega_1, \\ 0 < \phi < 1 & \Leftrightarrow & \chi \in \xi, \\ \phi = 0 & \Leftrightarrow & \chi \in \Omega_2. \end{array} \right. \tag{4.45}$$

Here, $\phi = 1$ means that material 1 is chosen while $\phi = 0$ means that material 2 is chosen. A value within the range $0 < \phi < 1$ means that there is a diffuse region (denoted ξ), which consists of both candidate materials. The illustration of a unit cell of PnCs with diffuse regions represented by the phase-field model is shown in Fig. 4.26.
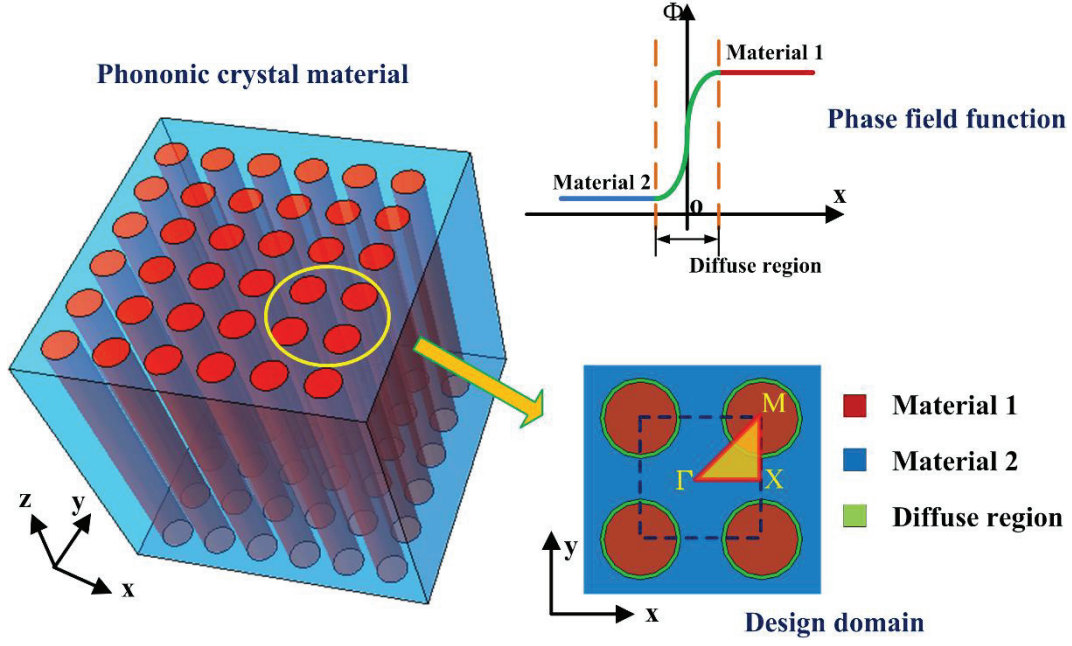
Fig. 4.26. The outline of a phononic crystal and its unit cell considering diffuse region represented by the phase-field model . The triangle in the unit cell represents the Brillouin zone.

In evaluating the band gap analysis of PnCs, the virtual elasticity tensor $\mathbf{D}^*(\phi)$ and the mass density $\rho^*(\phi)$ in the design domain can be defined by introducing the interpolation functions $k(\phi)$ and $m(\phi)$ as

$$\mathbf{D}^*(\phi) = \begin{cases} \mathbf{D}^{(1)} & \text{if } \chi \in \Omega_1, \\ k(\phi)\mathbf{D}^{(1)} + (1-k(\phi))\mathbf{D}^{(2)} & (0<k(\phi)<1) \quad \text{if } \chi \in \xi, \\ \mathbf{D}^{(2)} & \text{if } \chi \in \Omega_2, \end{cases} \tag{4.46}$$

$$\rho^*(\phi) = \begin{cases} \rho^{(1)} & \text{if } \chi \in \Omega_1, \\ m(\phi)\rho^{(1)} + (1-m(\phi))\rho^{(2)} & (0<\rho(\phi)<1) \quad \text{if } \chi \in \xi, \\ \rho^{(2)} & \text{if } \chi \in \Omega_2, \end{cases} \tag{4.47}$$

where, $\mathbf{D}^{(1)}$, $\mathbf{D}^{(2)}$, $\rho^{(1)}$ and $\rho^{(2)}$ are respectively the usual elasticity matrices and mass

density for each material. Here, the interpolation functions are chosen as the RAMP model for its ability to avoid spurious local modes in dynamic optimization problem, they are expressed by

$$k(\phi) = \frac{\phi}{1+p(1-\phi)}, \quad m(\phi) = \frac{\phi}{1+p(1-\phi)}, \tag{4.48}$$

In Eq. (4.48), the parameter p is used to penalize the intermediate value of the phase-field function, it is usually set to be $p=4$.

4.6.2 Design variables evolution of the unit cell of PnCs

In this study, the material distribution of two candidate material phases in the unit cell are represented and evaluated by solving the Allen–Cahn equation. In the practical application of the phase-filed method, the unit cell is first assigned using two candidate material phases with two different values of $\phi_{i,j}=1$ or 0 without diffuse regions in the setting up stage. Here, the diffuse regions between two candidate materials are assumed to have a nonuniform diffuse region width distribution; i.e., the width of the diffuse region $\tilde{\xi}_{i,j}$ has an independent value at each point $\chi_{i,j}$. For obtaining a design with a specified diffuse region from the current design (with or without a diffuse region), the evolution of the phase-field function is only driven with the diffuse-region term by specifying $\varepsilon_{i,j}$ at each calculation point. By using the finite difference method, the evolutional equation of the phase-field function $\phi_{i,j}^{n+1}$ in the $(n+1)$ th iteration at point $\chi_{i,j}$ is then expressed as

$$\frac{\phi_{i,j}^{n+1} - \phi_{i,j}^{n}}{\Delta t} = \varepsilon_{i,j}^{2} \left(\frac{\phi_{i-1,j}^{n} - 2\phi_{i,j}^{n} + \phi_{i+1,j}^{n}}{(\Delta x)^{2}} + \frac{\phi_{i,j-1}^{n} - 2\phi_{i,j}^{n} + \phi_{i,j+1}^{n}}{(\Delta y)^{2}} \right). \tag{4.49}$$

132

Here, Δx and Δy are respectively the spatial steps in the x and y directions. The coefficient $\varepsilon_{i,j}$ at point $\chi_{i,j}$ can be expressed in terms of the diffuse-region width $\tilde{\xi}_{i,j}$ as $\varepsilon_{i,j} = \tilde{\xi}_{i,j}/6$ for the current selection of the double-potential function. After the diffuse-region evolution of Eq. (4.49), one can obtain a unit cell design consisting with two material phases and a nonuniform diffuse region layer.

In the following evolution process of design variables for the topology optimization of PnCs, the evolutional equation of the phase-field function can be formulated from Eq. (4.50) with the finite difference method as

$$\frac{\phi_{i,j}^{n+1} - \phi_{i,j}^{n}}{\Delta t} = \varepsilon_{i,j}^2 \left(\frac{\phi_{i-1,j}^{n} - 2\phi_{i,j}^{n} + \phi_{i+1,j}^{n}}{(\Delta x)^2} + \frac{\phi_{i,j-1}^{n} - 2\phi_{i,j}^{n} + \phi_{i,j+1}^{n}}{(\Delta y)^2} \right) + \begin{cases} \phi_{i,j}^{n+1} \left(1 - \phi_{i,j}^{n}\right) r\left(\phi_{i,j}^{n}\right) & \text{for } r\left(\phi_{i,j}^{n}\right) < 0, \\ \phi_{i,j}^{n} \left(1 - \phi_{i,j}^{n+1}\right) r\left(\phi_{i,j}^{n}\right) & \text{for } r\left(\phi_{i,j}^{n}\right) \geq 0, \end{cases}$$

(4.50)

with
$$r\left(\phi_{i,j}^{n}\right) = \phi_{i,j}^{n} - \frac{1}{2} - 30\eta \frac{J'(t)}{\|J'(t)\|} \phi(1-\phi).$$
(4.51)

Here, the time step Δt needs to satisfy the Courant–Friedrich–Levy condition ($\varepsilon^2 \left(\Delta t/(\Delta x)^2 + \Delta t/(\Delta y)^2 \right) \leq 0.5$ in the two-dimensional case) to achieve stable convergence.

In this study, we consider the case that the diffuse regions between two candidate materials satisfies a random Gaussian field. Thus, the phase-field functions will be updated with the sensitivity of the objective function in the second term of Eq. (4.50) and the uncertain diffuse region width field which affects the first term of (4.50) until the evolution process achieves a convergence.

4.6.3 Robust topology optimization formulation

The task of current robust optimization is to find the band gap structure design of PnCs that is less sensitive to the random diffuse-region width field for two material components. Here, the robustness index can be formulated by the weighted sum of the mean value $\mu\left(J\left(\phi,\tilde{\xi}\right)\right)$ and the negative of the standard deviation $\sigma\left(J\left(\phi,\tilde{\xi}\right)\right)$ with respect to the uncertain parameters as

$$\text{maximize}: f\left(\phi,\tilde{\xi}\right)=\mu\left(J\left(\phi,\tilde{\xi}\right)\right)-\alpha\cdot\sigma\left(J\left(\phi,\tilde{\xi}\right)\right), \tag{4.52}$$

where the positive weight coefficient α is used to balance the mean value and standard deviation in the optimization formulation.

The present study considers the uncertain width of the diffuse region as a random field $\tilde{\xi}$ in the whole unit cell, while the random field only affects the material distribution of the two candidate materials inside the diffuse region ξ. Thus, the interpolation functions of Eq. (4.48) related to the random diffuse region field $\tilde{\xi}$ can be further rewritten as

$$k\left(\phi,\tilde{\xi}\right)=\frac{\phi\left(\tilde{\xi}\right)}{1+p\left(1-\phi\left(\tilde{\xi}\right)\right)}, \quad m\left(\phi,\tilde{\xi}\right)=\frac{\phi\left(\tilde{\xi}\right)}{1+p\left(1-\phi\left(\tilde{\xi}\right)\right)}, \tag{4.53}$$

Furthermore, the stiffness matrix $\mathbf{K}\left(\phi,\tilde{\xi}\right)$, mass matrix of the unit cell are affected by the random field. The global stiffness and mass matrices can be further expressed with the phase-field function value at each element ϕ_e as

$$\mathbf{K}\left(\phi,\tilde{\xi}\right)=\sum_{e=1}^{N_e}\left[\frac{\phi_e\left(\tilde{\xi}\right)}{1+p\left(1-\phi_e\left(\tilde{\xi}\right)\right)}\mathbf{k}_e^{(1)}+\left(1-\frac{\phi_e\left(\tilde{\xi}\right)}{1+p\left(1-\phi_e\left(\tilde{\xi}\right)\right)}\right)\mathbf{k}_e^{(2)}\right], \tag{4.54}$$

$$\mathbf{M}\left(\phi,\tilde{\xi}\right) = \sum_{e=1}^{N_e}\left[\frac{\phi_e\left(\tilde{\xi}\right)}{1+p\left(1-\phi_e\left(\tilde{\xi}\right)\right)}\mathbf{m}_e^{(1)} + \left(1 - \frac{\phi_e\left(\tilde{\xi}\right)}{1+p\left(1-\phi_e\left(\tilde{\xi}\right)\right)}\right)\mathbf{m}_e^{(2)}\right], \qquad (4.55)$$

where $\mathbf{k}_e^{(1)}, \mathbf{m}_e^{(1)}$, $\mathbf{k}_e^{(2)}$, and $\mathbf{m}_e^{(2)}$ are respectively the elemental stiffness and mass matrices for materials phase 1 (plumbum) and phase 2 (epoxy).

With the above definitions of the objective function and random field, we formulate the robust optimization problem as

$$\operatorname*{Maximize}_{\phi} : f\left(\phi,\tilde{\xi}\right) = \mu\left(J\left(\phi,\tilde{\xi}\right)\right) - \alpha \cdot \sigma\left(J\left(\phi,\tilde{\xi}\right)\right),$$

$$\text{subject to} : J = \frac{1}{\eta_1}\ln\left(\sum_{i=1}^{n_k}e^{\eta_1 \cdot \omega_{j+1}(\mathbf{k}_i)}\right) - \frac{1}{\eta_2}\ln\left(\sum_{i=1}^{n_k}e^{\eta_1 \cdot \omega_j(\mathbf{k}_i)}\right),$$

$$\left(\mathbf{K}\left(\mathbf{k}\right) - \omega^2\mathbf{M}\right)\mathbf{U} = 0, \qquad (4.56)$$

$$\phi = \left[\phi_1,...,\phi_{N_f}\right],$$

$$0 \le \phi_e \le 1, \quad e = 1,....,N_f.$$

The symbol N_f denotes the total number of phase-field calculation points used in the topology optimization model. The present study selects phase-field calculation points at all element centers of the finite element model; therefore, N_f is equal to the total number of finite elements N_e in the design domain. The above problem (4.56) can be solved with a gradient-based mathematical programming algorithm, which requires band gap and corresponding sensitivity analysis. Thus, the following subsection will address the band gap and sensitivity calculation procedure under random diffuse region widths of the unit cell of PnCs.

4.7 Numerical examples of Robust topology optimization of PnCs

4.7.1 Influence of the diffusion region width

We first provide an example that shows the influence of the diffuse region width on the dispersion curves of the phononic crystals. Herein, a typical PnC unit cell design with a circle plumbum inclusion (material 2) surrounded by the epoxy matrix (material 1) is considered. The material 1 has the Young's modulus $E_1 = 4.35 \text{GPa}$, Poisson's ratio $v_1 = 0.37$, and the mass density $\rho_1 = 1180 \text{ kg} \cdot \text{m}^3$, the material properties of material 2 are $E_2 = 40.8 \text{GPa}$, $v_2 = 0.37$, and $\rho_2 = 11600 \text{ kg} \cdot \text{m}^3$. The unit cell has width $a_c = 0.02 \text{m}$ and the radius of the circular inclusion is 0.005 m. Here, three different cases of diffuse region widths are considered as shown in Fig.4.27: (a) without diffuse region, (b) with a uniform diffuse region (diffuse region width $h_{\text{diffuse}} = 4 \times 10^{-4} \text{m}$), and (c) with non-uniform diffuse region (diffuse region width is $0 \sim 8 \times 10^{-4} \text{m}$). For verifying the influence of the diffuse region, the second band gap (i.e., a band gap between the second and third bands) and the fourth band gap of out-of-plane modes for the three reference designs are shown in Fig. 4.28. It is seen that, the diffuse region width has remarkably effect on the dispersion curves of the of the phononic crystals, this also proves the importance of robust optimization of the phononic crystals considering the diffuse region width.
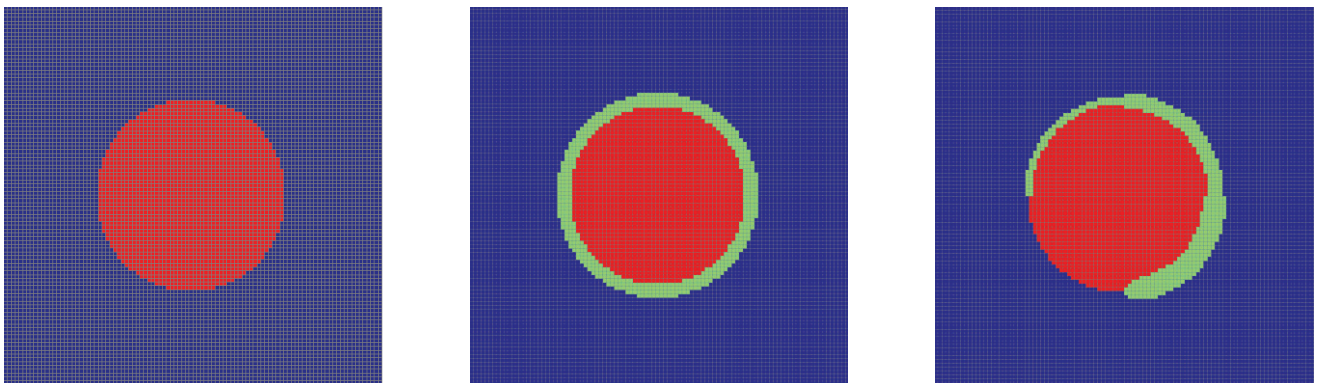
Fig. 4.27 Unit cells of phononic crystals with different diffuse regions: (a) without diffuse region; (b) with uniform diffuse regions; (c) with non-uniform diffuse regions.
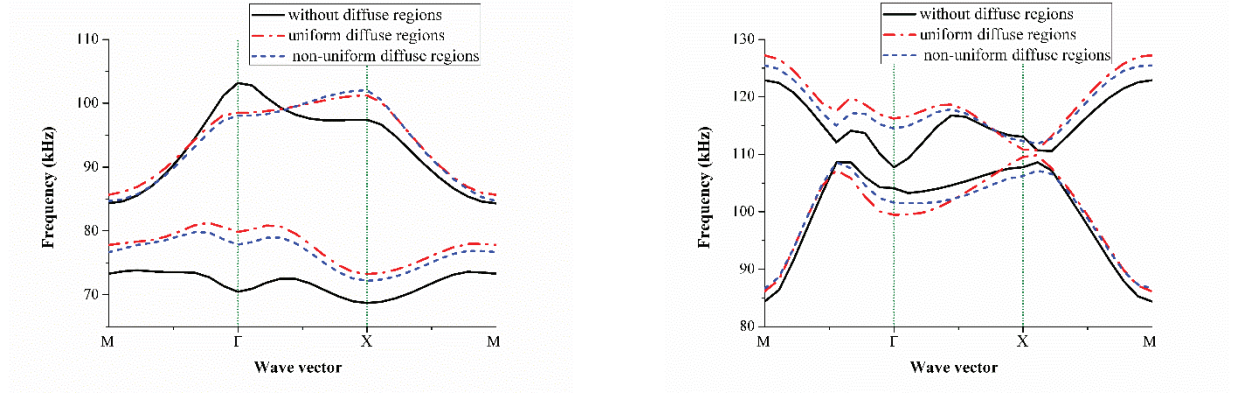
(a)   (b)

Fig. 4.28 Dispersion curves of out-of-plane modes for different reference designs: (a) the second band gap; (b) the fourth band gap.

4.7.2 Robust topology optimization of out-of-plane mode

We first present robust topology optimization results and discusses important factors in the design of out-of-plane modes of the PnC unit cell. Here, the unit cell consists of two kinds of candidate materials: epoxy (material 1) and plumbum (material 2). The material properties of the two components are the same as those in the previous subsection. The unit cell has width $a_c = 0.02\text{m}$ and is discretized into 100×100 uniform square elements. The K-S aggregation parameters are set as $\eta_1 = -5$ and $\eta_2 = 5$ initially and their absolute values are increased by 0.5 per iteration until they reach 30. The optimization iterations stop when the difference between two consecutive objective functions is less than 1×10^{-4}.

In the robust optimization problem, the random field of the diffuse-region width between two material phases satisfies a Gaussian distribution with mean value $\mu_\xi = 8 \times 10^{-4}\text{m}$,

137

coefficient of variation $\gamma = \sigma_\xi / \mu_\xi = 0.2$, and correlation length $L = 0.02\text{m}$. Here, the fifth

stochastic band gap of the PnCs is considered as the optimization target, and the weight factor

between the mean band gap and the standard deviation is taken as $\alpha = 1$. The initial design is

chosen such that the unit cell has seven circular plumbum inclusions (with radius of 0.002 m)

and the diffuse regions with the a mean width of $\mu_\xi = 8 \times 10^{-4}\text{m}$, the initial design and its

dispersion curves of out-of-plane modes are shown in Fig. 4.29. It can be seen that there is not

band gap between the fifth and sixth bands. The optimization process converged after 46

iterations, the history of the objective function is given in Fig.4.30. After optimization, an

optimized design with the mean and standard deviation of the band gap 51.50 kHz and 0.285

kHz respectively can be obtained as shown in Fig. 4.31(a) and its dispersion curves are given

in Fig 4.32(b).In the robust optimized design, the total volume ratio of the plumbum inclusions

is 27.2%. It is found that a relatively wide mean band gap can be achieved after the optimization

process.

(a)   (b)
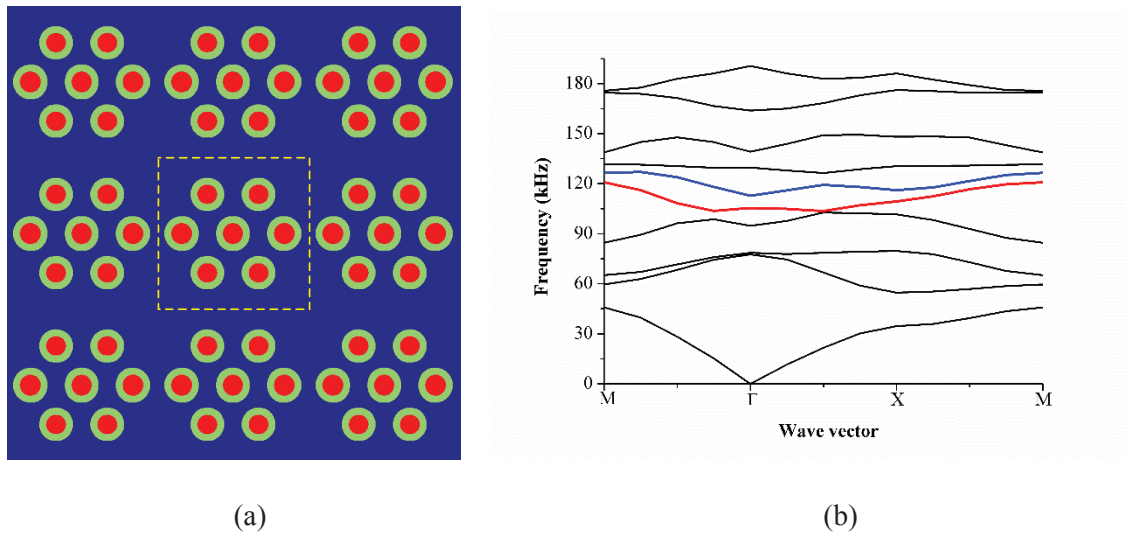
Fig. 4.29 Initial design and its dispersion curves. (a) Initial design of PnC with nine unit
cells and (b) mean value of dispersion curves of out-of-plane modes.
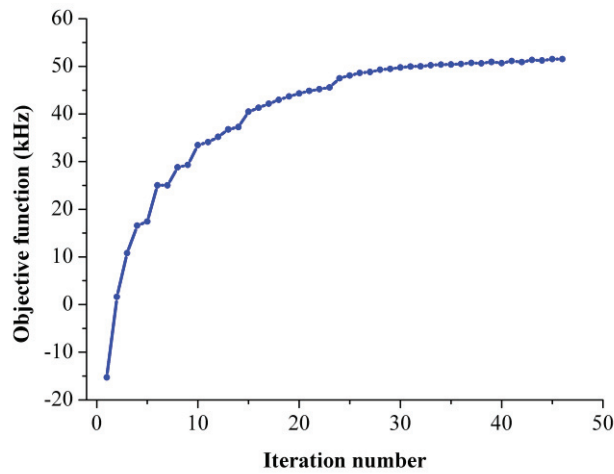
Fig. 4.30 Iteration history of the weighted objective function of the fifth band gap.

(a)   (b)
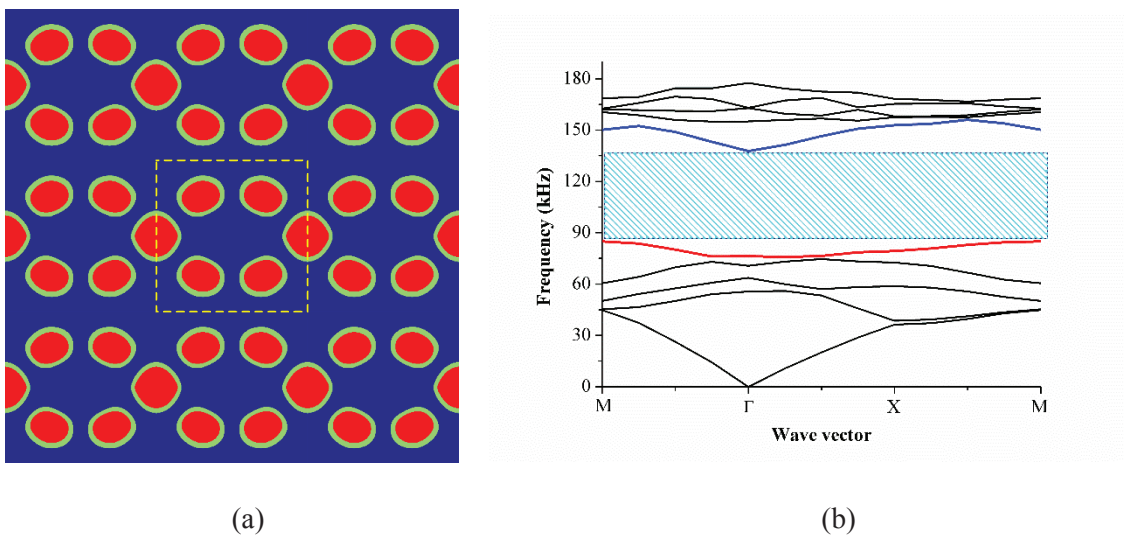
Fig. 4.31 Optimized design and its dispersion curves. (a) Initial design of PnC with nine
unit cells and (b) mean value of dispersion curves of out-of-plane modes.

Next, we examine the effect of the weight factor in the objective function (4.52). Another
two weight factors $\alpha = 30$ and $\alpha = 50$ are considered, and the optimized solutions are given
in Fig.4.32. The mean values and standard deviations of the band gap for designs with different
weight factors are summarized in Table 4.7. It is seen that as the weighting factor increases, the

optimized unit cell solution changes remarkably, and a relatively narrow mean band gap design is obtained for achieving a smaller standard variance of band gap

(a)   (b)
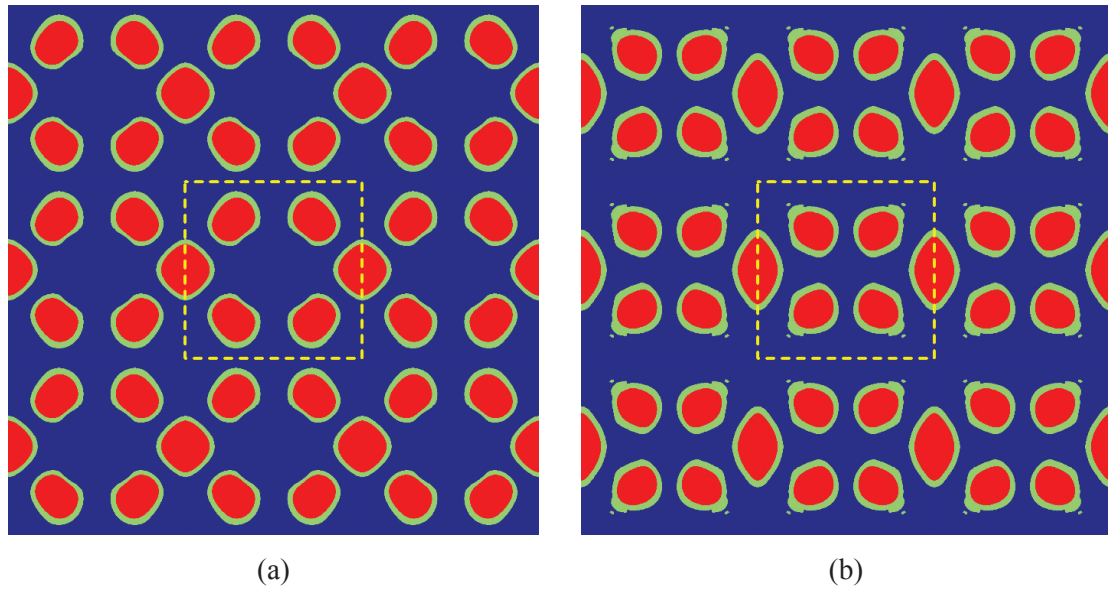
Fig. 4.32 Optimized designs of nine unit cells with different weighting factors: (a) $\alpha = 30$; (b) $\alpha = 50$.

Table 4.7 Comparison of the mean value and standard variance of band gap for different weighting factors

Weighting factor α	Mean value of band gap (kHz)	Standard variance of band gap (kHz)
1	51.50	0.285
30	48.15	0.249
50	20.62	0.168

The effect of the mean diffuse region width is then studied. Two different mean diffuse region values $\mu_\xi = 4 \times 10^{-4}\,\text{m}$ and $1.6 \times 10^{-3}\,\text{m}$ are considered. The optimization solutions are given in Fig.4.33, and the mean value and standard deviation for different diffuse region widths are summarized in Table 4.8. It can be observed that the optimized solutions for different cases

share the similar distribution tendency, and for the case with thinner diffuse region can achieve a relatively wider band gap.

(a)   (b)
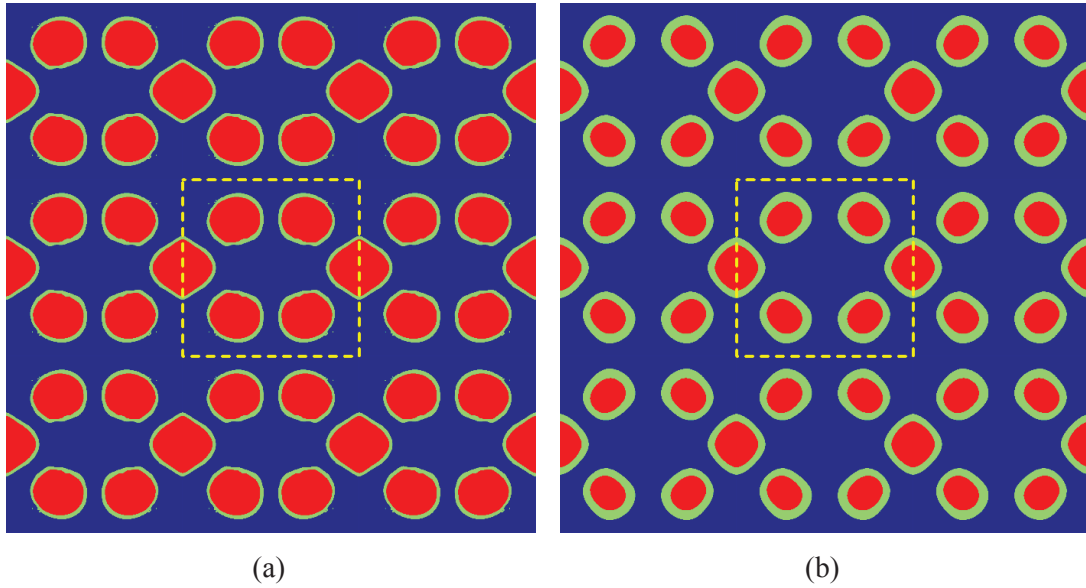
Fig. 4.33 Optimization solutions of a cantilever beam obtained for different diffuse-region widths: (a) $\mu_\xi = 4 \times 10^{-4}\,\mathrm{m}$; (b) $\mu_\xi = 1.6 \times 10^{-3}\,\mathrm{m}$.

Table 4.8 Mean value and standard deviation of band gap for different diffuse-region widths

Mean width of diffuse layer μ_ξ (m)	Mean value of band gap (kHz)	Standard variance of band gap (kHz)
4×10^{-4}	57.42	0.196
8×10^{-4}	48.15	0.249
1.6×10^{-3}	37.96	0.233

In the following, we present the robust optimization of a PnC for different band gap orders.

Here, another five robust optimal designs and their dispersion curves for the different orders of band gaps (from the second order to the seventh order) are presented in Fig. 4.34. The mean value and standard deviation of the band gap for the optimized solutions obtained by respective orders are given in Table 4.9, the total volume ratios of the plumbum inclusions are also listed in Table 4.9. it can be easily found that the designs show significant difference for different orders and exhibit different dispersion curves.
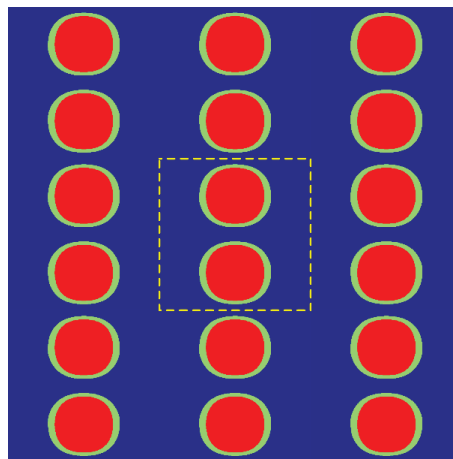
(a)
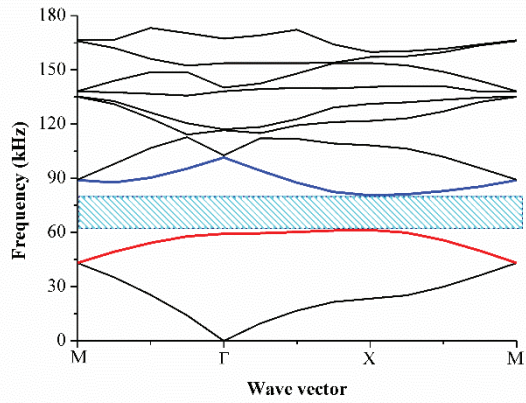
(b)
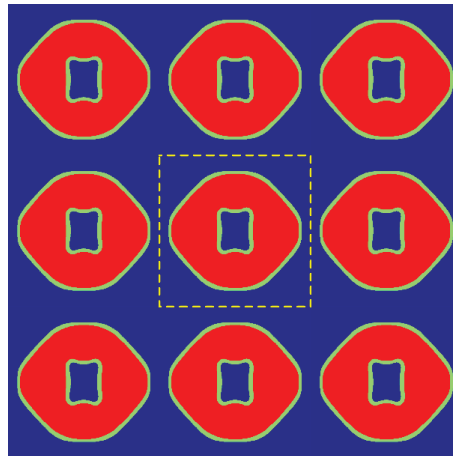
(c)
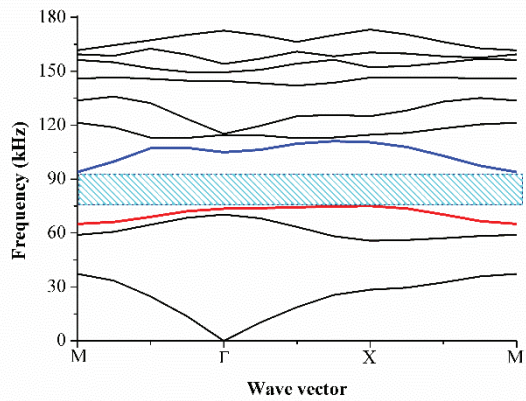
(d)
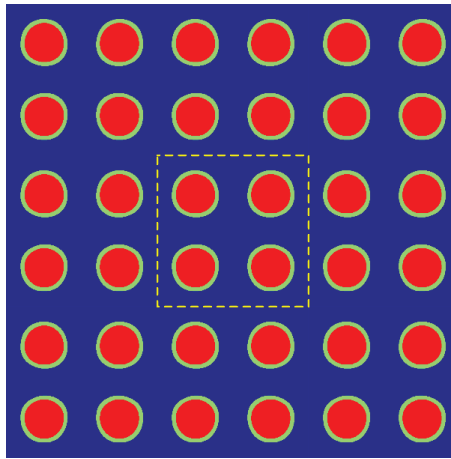
(e)
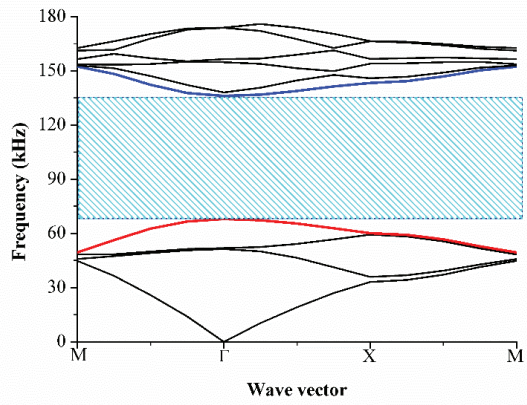
(f)
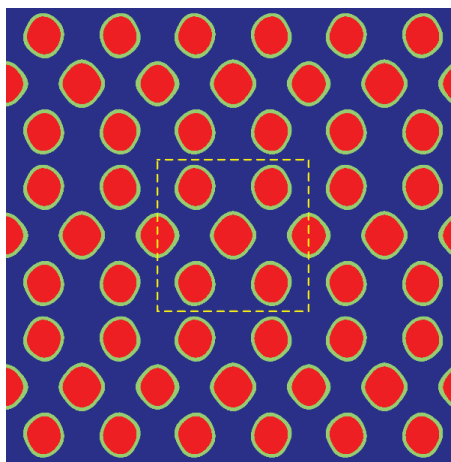
(g)
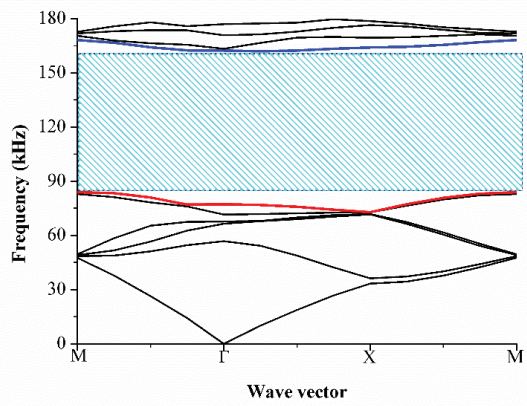
(h)
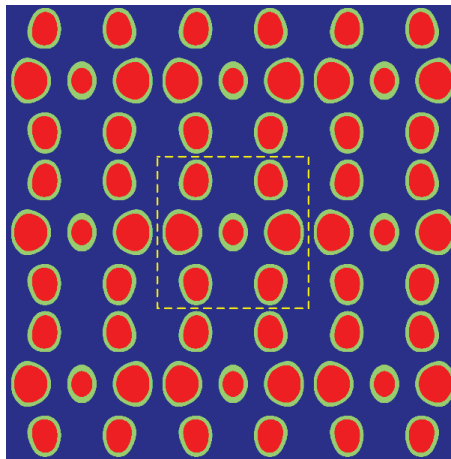
(i)
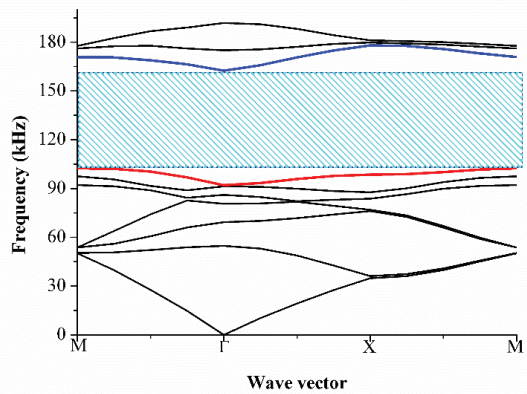
(j)

Fig. 4.34 Robust optimized design of out-of-plane modes and their dispersion curves: (a)–(b) second band gap, (c)–(d) third band gap, (e)–(f) fourth band gap, (g)–(h) sixth band gap, (i)–(j) seventh band gap.

143

Table 4.9 comparisons of robust optimized designs with different orders of band gaps

Orders of band gap	Volume ratios of the plumbum inclusions	Mean band gap width (kHz)	Std. deviation of band gap width (kHz)
2-3 band	27.0%	18.12	0.171
3-4 band	40.2%	17.84	0.053
4-5 band	24.9%	67.28	0.105
5-6 band	27.2%	48.15	0.249
6-7 band	31.2%	76.97	0.323
7-8 band	28.2%	59.10	0.307

4.7.3 Robust topology optimization of in-plane mode

In this subsection, we further study the optimal design for other coupled in-plane modes. The unit cell is discretized into 80×80 uniform square elements. The material properties of the two components are the same as those in the previous subsection. In the Gaussian random distribution field model of the diffuse-region, the mean width is $\mu_\xi = 2.7 \times 10^{-4}$ m, coefficient of variation $\gamma = \sigma_\xi / \mu_\xi = 0.2$, and correlation length $L = 0.02$m. In the robust optimization formulation, the sixth band gap (i.e., the band gap between sixth and seventh bands) is considered, and the weight factor between the mean band gap and the standard deviation is taken as $\alpha = 1$. The initial design is chosen same with the pervious example that the unit cell has seven circular plumbum inclusions (with radius of 6.7×10^{-5} m), its design and dispersion curves of in-plane modes are plotted in Fig.4.35. It is observed that there is no band gap between the sixth and seventh bands, after optimization process, a band gap with the mean and standard deviation of the band gap 7.61 kHz and 0.06 kHz respectively in the optimal design. The optimal solutions and corresponding mean values of dispersion curves are given in Fig. 4.36.

In the optimal design, the volume ratio of the plumbum inclusions is 30.7%.

(a)   (b)
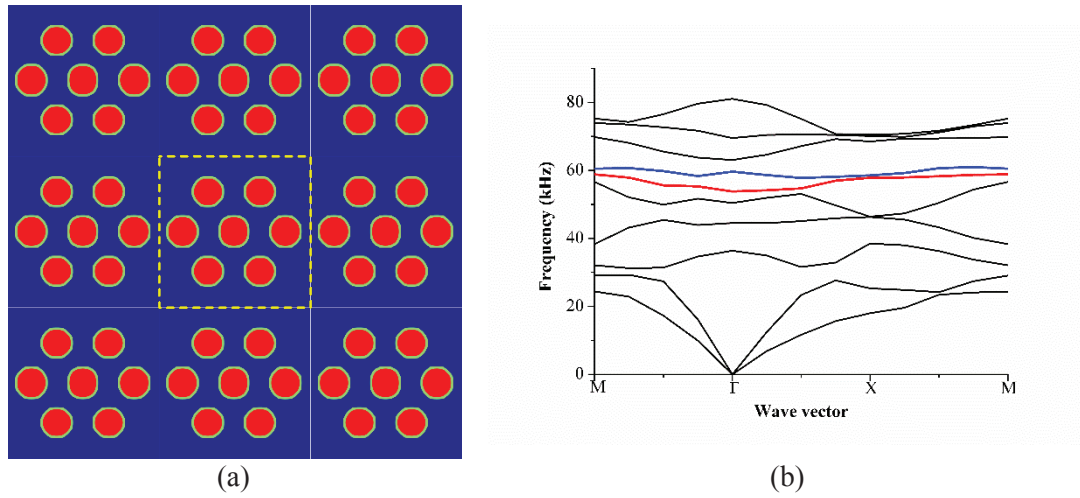
Fig. 4.35 Initial design and its dispersion curves of coupled in-plane modes. (a) Initial

design of PnC with nine unit cells and (b) mean value of dispersion curves.

(a)   (b)
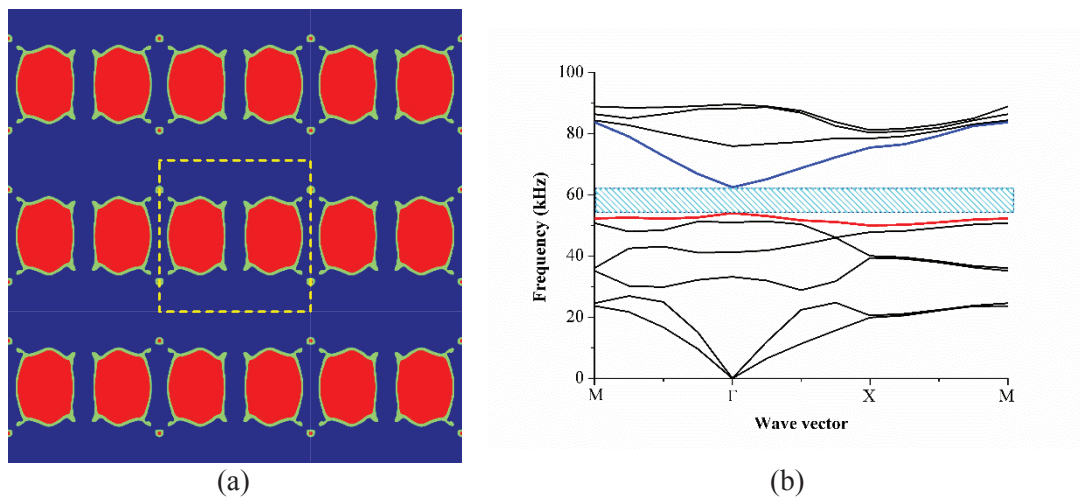
Fig. 4.36 Optimal design and its dispersion curves of coupled in-plane modes. (a) Initial
design of PnC with nine unit cells and (b) mean value of dispersion curves.

4.8 Summary

We proposed a phase-field-based topology optimization method for minimizing dynamic

responses of structures with diffuse-region width uncertainty. Herein, a diffuse region between two material phases was assumed as a spatial stochastic field and discretized into uncorrelated stochastic variables employing the EOLE method. Stochastic structural dynamic response analysis was then conducted with PCE. To produce a less-sensitive optimal design, a robust topology optimization formulation with a weighted objective function handling the mean value and standard deviation of the structural dynamic performance was formulated. The structural dynamic performance can be chosen as structural frequency responses, frequency proprieties, and transient responses. These correspond respectively with the dynamic compliance, structural fundamental frequency or frequency gap, and the transient displacement under impact loads. In the framework of the phase-field method, the bi-material design domain is represented with the phase-field function, and initial non-uniform diffuse regions are generated by evolving the phase-field functions. The proposed phase field-based robust topology optimization method has also applied into the microstructure design of PnCs against random diffuse regions between material phases. Numerical examples demonstrated that the proposed phase-field-based topology optimization can handle different types of structural dynamic robust optimization problems. The numerical results showed that the characteristics of the external excitations (e.g., the excitation frequency and the action time) have remarkable effects on the optimal solutions.

The results also show that the phase-field based approach can provide a relatively wide band gap design that is less sensitive to random diffuse region uncertainties between material phases.

5 Topology optimization of piezoelectric smart structures for minimum energy consumption

Smart structural systems with piezoelectric actuators and sensors are considered an effective method to reduce structural vibration for avoiding possible structural failure or system performance degradation. Piezoelectric actuators are often used for providing active damping in active vibration control system. The control effectiveness is one of the major concerns in the design of an active control system. Another important criterion of the active control system is the power consumption. In many practical cases (such as miniature devices and aerospace smart structures), only a limited energy supply may be available. Thus, achieving the desired structural vibration level using as little energy as possible is considered ideal for active control systems.

Many attempts have been made to improve the effectiveness of piezoelectric active control structures, including designing high performance controller algorithms [183], choosing suitable type of amplifiers [184], and finding the optimal placement/configuration of piezoelectric patches [185]. It is clear that the active control effect can be promoted by optimizing the numbers and positions of piezoelectric actuators. Early studies mostly focused on exhaustive search [54] or heuristic optimization strategies [55] to find the optimal positions and sizes of the piezoelectric patches. In more recent works, Bruant et al. [57] and Xu et al. [186] studied the optimal placement of piezoelectric patches using genetic algorithms. However, the number of design variables is very limited because of the high computational cost when using heuristic optimization strategies. Thus it may be difficult to obtain a realistic optimal design with genetic algorithms. This just demonstrates the need for topology optimization in the conceptual design of piezoelectric smart structures. Existing studies have primarily focused on improvement of the vibration control effectiveness with the topology optimization techniques and no energy

consumption index was considered.

Electrical energy consumption has been discussed in some studies on the vibration control and design optimization of smart piezoelectric structures. Brennan and McGowan [187] first proposed a method for predicting the energy consumption of piezoelectric actuators in active vibration control systems. Mukherjee and Joshi [188] studied the shape optimization of piezoelectric actuators for minimizing the energy consumption to achieve a specified maximum static response. Chevva et al. [189] presented a minimum actuation energy control strategy for minimizing the total input energy in the active control. Zorić et al. [190] optimized the sizes and locations of the piezoelectric patches with Linear-Quadratic Regulator (LQR) control by using exhaustive heuristic search. In more recent works, topology optimization methods have been introduced for reducing both the structural vibration level and control the energy consumption simultaneously with optimal control strategies. For instance, Goncalves et al. [191] proposed a new controllability-based topology optimization method to determine the optimal piezoelectric material distribution in the LQR control system by considering the control spillover effects. Hu et al. [192] investigated topology optimization for piezoelectric thin-shell structures under LQR optimal control by reducing the structural dynamic compliance and energy consumption simultaneously. Howerver, topology optimization methods based on the optimal control strategy actually provide a compromise between the energy consumption and control performance.

This chapter proposes a topology optimization method for obtaining the best electrode coverage of the piezoelectric material layer which requires the minimum energy consumption to achieve a specified vibration level of a plate with active control. As shown in Figure 1, two piezoelectric layers are adhered to the top surface of a thin-walled structure in a collocated manner. In the control system, each sensor patch is connected to a charge amplifier, and the control voltage of the corresponding actuator patch can be obtained from the sensor output by

using the CGVF control algorithm of the controller. The steady-state structural response of the structure under harmonic excitation is evaluated with finite element analysis. In the topology optimization model, the objective function is the total energy consumption of the active control system; the dynamic compliance of the structure is taken as a vibration level measure for the whole structure, and it is imposed by a specified upper bound. With the density-based topology optimization model, the elemental pseudo-densities indicating the presence/absence of electrode coverage of the piezoelectric layer are taken as design variables. The penalization models of the piezoelectric effects and energy consumption are employed to suppress the elements with intermediate pseudo-densities during the optimization process. The stiffness and mass matrices of the host and piezoelectric layers do not change during the optimization process because the changes in the electrode coverage only affect the piezoelectric effect and energy consumption of each piezoelectric patch. The sensitivity analysis scheme for the total energy consumption of the piezoelectric actuators is derived with the adjoint-variable method, and the optimization problem is solved with a gradient-based mathematical programming algorithm.

5.1 Frequency response analysis under CGVF control

5.1.1 Finite element modeling of the piezoelectric laminated plate

We consider a laminated plate with attached piezoelectric material layer and designable electrode coverage, as shown in Fig. 5.1. The constitutive relations for the host layer and piezoelectric layer are

$$\begin{cases} \boldsymbol{\sigma} = \mathbf{C}^{\mathrm{H}}\boldsymbol{\varepsilon} & \text{in host layer,} \\ \boldsymbol{\sigma} = \mathbf{C}^{\mathrm{E}}\boldsymbol{\varepsilon} - \mathbf{e}^{\mathrm{T}}\mathbf{E} & \text{in piezoelectric layer.} \end{cases} \tag{5.1}$$

Here, $\boldsymbol{\sigma}$ and $\boldsymbol{\varepsilon}$ are the mechanical stress vector and the mechanical strain vector, respectively; $\mathbf{C}^{\mathrm{H}}$ and $\mathbf{C}^{\mathrm{E}}$ are the elasticity matrices of the host layer and piezoelectric layers,

respectively; $\mathbf{e}$ is the piezoelectricity matrix and $\mathbf{E}$ is the vector of the applied electric field.
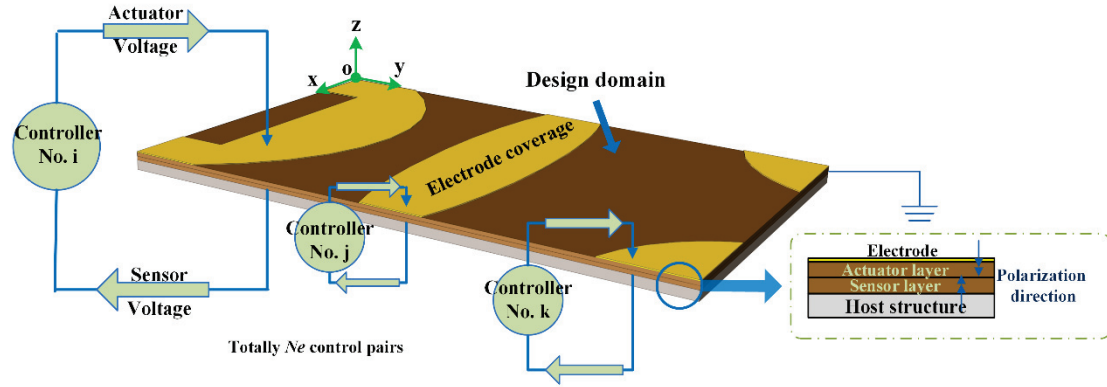
Fig. 5.1 Schematic illustration of a piezoelectric laminated plate under active vibration control.

In the present work, a four-node Mindlin shell element with small strain assumptions is employed. The displacement components u, v and w at point (x, y, z) can be given as

$$
\begin{aligned}
u(x, y, z, t) &= u_0(x, y, t) - z\theta_x(x, y, t), \\
v(x, y, z, t) &= v_0(x, y, t) - z\theta_y(x, y, t), \\
w(x, y, z, t) &= w_0(x, y, t).
\end{aligned}
\tag{5.2}
$$

Here, u_0, v_0 and w_0 are the mid-plane displacement components, and θ_x and θ_y are the rotations of transverse normal about the y and x axes, respectively.

After finite element discretization, the governing equations of a laminated structure with bonded piezoelectric actuator/sensor patches under an external harmonic force $\mathbf{f}(t)$ and piezoelectric control force $\mathbf{f}_a(t)$ are given as

$$
\mathbf{M}\ddot{\mathbf{x}}(t) + \mathbf{C}\dot{\mathbf{x}}(t) + \mathbf{K}\mathbf{x}(t) = \mathbf{f}(t) + \mathbf{f}_a(t),
\tag{5.3}
$$

where $\mathbf{M} \in \mathbf{R}^{n \times n}$, $\mathbf{C} \in \mathbf{R}^{n \times n}$ and $\mathbf{K} \in \mathbf{R}^{n \times n}$ (n is the number of degree of freedom) are the mass matrix, damping matrix and stiffness matrix, respectively; $\mathbf{x}(t) \in \mathbf{R}^{n \times 1}$, $\dot{\mathbf{x}}(t) \in \mathbf{R}^{n \times 1}$, and

$\ddot{\mathbf{x}}(t) \in \mathbf{R}^{n \times 1}$ are the vectors of time-varying displacement, velocity, and acceleration, respectively. The control force $\mathbf{f}_a(t)$ depends on the control algorithm and will be discussed in the following section.

5.1.2 Active control force in CGVF control

The control voltage is applied in the thickness direction. The electric voltage $\boldsymbol{\varphi}_a$ and the electric field intensity $\mathbf{E}_z$ in the actuator layer are expressed as

$$\boldsymbol{\varphi}_a = \left\{ \varphi_a^1, \ \varphi_a^2, \ \dots, \ \varphi_a^{N_e} \right\}^{\mathrm{T}}, \tag{5.4}$$

$$\mathbf{E}_z = \left\{ E_z^1, \ E_z^2, ..., E_z^{N_e} \right\}^{\mathrm{T}} = \left\{ -\frac{\varphi_z^1}{h}, \ -\frac{\varphi_z^2}{h}, ..., \ -\frac{\varphi_z^{N_e}}{h} \right\}^{\mathrm{T}}, \tag{5.5}$$

where N_e is the total number of actuator elements; $\varphi_a^e \ (e = 1, 2, \dots, N_e)$ and $E_z^e \ (e = 1, 2, \dots, N_e)$ are the electric voltage and the electric field intensity, respectively, of the eth actuator elements.

The actuation force $\mathbf{f}_a(t)$ in Eq. (5.3) is

$$\mathbf{f}_a(t) = \mathbf{K}_{u\varphi} \boldsymbol{\varphi}_a(t), \tag{5.6}$$

where $\mathbf{K}_{u\varphi} = \int_{\Omega_a} \mathbf{B}_u^{\mathrm{T}} \mathbf{e} \mathbf{B}_\varphi d\Omega_a$ is the structural electro-mechanical matrix of the actuator layer, $\mathbf{B}_u$ and $\mathbf{B}_\varphi$ are the strain-displacement matrix and the electric field-potential matrix, and Ω_a is the volume occupied by the actuator layer.

The actuator voltage $\boldsymbol{\varphi}_a(t)$, which depends on the output sensor voltage $\boldsymbol{\varphi}_s(t)$ and the constant control gain matrix $\mathbf{G}_a$ in the CGVF control, is written as

$$\boldsymbol{\varphi}_{\mathrm{a}}(t) = -\mathbf{G}_{\mathrm{a}}\boldsymbol{\varphi}_{\mathrm{s}}(t). \tag{5.7}$$

The sensor voltage output vector $\boldsymbol{\varphi}_{\mathrm{s}}(t)$ is expressed as

$$\boldsymbol{\varphi}_{\mathrm{s}}(t) = \mathbf{G}_{\mathrm{s}}\,\mathbf{K}_{\varphi u}\,\dot{\mathbf{x}}(t), \tag{5.8}$$

where $\mathbf{G}_{\mathrm{s}} = \mathrm{diag}(G_{\mathrm{s}}^{1}, G_{\mathrm{s}}^{2}, \ldots, G_{\mathrm{s}}^{N_{\mathrm{e}}})$ is the diagonal gain factors matrix of charge amplifiers. Each diagonal gain of the charge amplifiers matrix stands for an independent control gain for its own sensor/actuator pair, implying that the numbers of sensors and actuators are equal. The gain factors matrix is diagonal means that the control pairs do not affect each other. Here, $\mathbf{K}_{\varphi u} = \int_{\Omega_{\mathrm{s}}} \mathbf{B}_{\Phi}^{\mathrm{T}} \mathbf{e}^{\mathrm{T}} \mathbf{B}_{u} \, d\Omega$ is the mechano-electronic matrix for the sensor layer, with Ω_{s} denoting the volume occupied by the sensor layer.

By substituting Eqs. (5.8) and (5.7) into Eq. (5.6), the control voltage becomes

$$\boldsymbol{\varphi}_{\mathrm{a}}(t) = -\mathbf{G}_{\mathrm{a}}\mathbf{G}_{\mathrm{s}}\mathbf{K}_{\varphi u}\dot{\mathbf{x}}(t). \tag{5.9}$$

Thus, the active control force $\mathbf{f}_{\mathrm{a}}(t)$ can be rewritten as

$$\mathbf{f}_{\mathrm{a}}(t) = -\mathbf{C}_{\mathrm{A}}\dot{\mathbf{x}}(t), \tag{5.10}$$

$$\mathbf{C}_{\mathrm{A}} \equiv \mathbf{K}_{u\varphi}\mathbf{G}_{\mathrm{a}}\mathbf{G}_{\mathrm{s}}\mathbf{K}_{\varphi u}. \tag{5.11}$$

Here, $\mathbf{C}_{\mathrm{A}}$ in Eq. (5.11) is defined as the active damping matrix.

5.1.3 Frequency response analysis

Substituting Eq. (5.10) into Eq. (5.3), we can rewrite the dynamic equation as

$$\mathbf{M}\ddot{\mathbf{x}}(t)+(\mathbf{C}+\mathbf{C}_{\mathrm{A}})\dot{\mathbf{x}}(t)+\mathbf{K}\mathbf{x}(t)=\mathbf{f}(t) \tag{5.12}$$

In this study, the external excitation is a harmonic one in the form of $\mathbf{f}(t)=\mathbf{F}e^{i\theta t}$ (with frequency $\theta=2\pi f$ and amplitude $\mathbf{F}$), and only the frequency response is of concern. The steady-state displacement response $\mathbf{x}(t)$ can be expressed as $\mathbf{x}(t)=\mathbf{X}e^{i\theta t}$, where $\mathbf{X}$ is the vibration displacement amplitude. Thus, the dynamic equation (5.12) can be further expressed as

$$\left(-\theta^2\mathbf{M}+i\theta(\mathbf{C}+\mathbf{C}_{\mathrm{A}})+\mathbf{K}\right)\mathbf{X}=\mathbf{F} \tag{5.13}$$

As mentioned, the mass, stiffness, and damping effects of the electrode coverage are negligible. Thus the matrices $\mathbf{M}$, $\mathbf{K}$, and $\mathbf{C}$ in the governing equation (5.13) are assembled as

$$\begin{aligned}
\mathbf{M} &= \sum_{e=1}^{N_{\mathrm{e}}}\left(\mathbf{M}_{\mathrm{h}}^e+\mathbf{M}_{\mathrm{a}}^e+\mathbf{M}_{\mathrm{s}}^e\right),\\
\mathbf{K} &= \sum_{e=1}^{N_{\mathrm{e}}}\left(\mathbf{K}_{\mathrm{h}}^e+\mathbf{K}_{\mathrm{a}}^e+\mathbf{K}_{\mathrm{s}}^e\right),\\
\mathbf{C} &= \alpha\sum_{e=1}^{N_{\mathrm{e}}}\mathbf{K}_{\mathrm{h}}^e+\beta\sum_{e=1}^{N_{\mathrm{e}}}\mathbf{M}_{\mathrm{h}}^e,
\end{aligned} \tag{5.14}$$

where $\mathbf{K}_{\mathrm{h}}^e$ and $\mathbf{M}_{\mathrm{h}}^e$ are the element stiffness matrix and the element mass matrix of the host structure and remain unchanged during the optimization process; $\mathbf{K}_{\mathrm{s}}^e$, $\mathbf{K}_{\mathrm{a}}^e$, $\mathbf{M}_{\mathrm{s}}^e$ and $\mathbf{M}_{\mathrm{a}}^e$ denote the element stiffness and mass matrices of the piezoelectric actuator/sensor layers. The structural damping of the piezoelectric layers is neglected here, because the structural damping effect of piezoelectric layer is much smaller than that of the base structure, and the active damping effect of the piezoelectric plays a dominate role in the structural vibration reduction [58, 71]. Thus, the total structural damping effect contains only the contribution of the host layer, for which the damping coefficients are denoted by α and β. Here, the damping of the base

structural can effectively avoid undesirable resonance.

The actuator voltage $\varphi_a(t)$ in Eq. (5.9) can also be given as $\varphi_a(t) = \Phi_a e^{i\theta t}$, and the active control voltage amplitude Φ_a, which is a complex number vector, is then

$$\Phi_a = -i\theta \mathbf{G}_a \mathbf{G}_s \mathbf{K}_{\Phi u} \mathbf{X}. \tag{5.15}$$

It is noted that the active damping $\mathbf{C}_A$ and control voltage amplitude Φ_a are related to the structural electro-mechanical matrix of the actuator layer $\mathbf{K}_{u\varphi}$ and the mechano-electronic matrix of the sensor layer $\mathbf{K}_{\Phi u}$, which are affected directly by the electrode coverage. Thus the expressions with the design variables will be presented in the next section.

The response analysis of the non-proportionally damped system in Eq. (5.13) can be efficiently solved with the complex mode superposition method [73] or the direct method [153]. In this study, we employ the latter approach.

5.2. Topology optimization formulation

Our objective is to minimize the electrical energy consumption of the piezoelectric actuators. The total actuator energy consumption $P(\boldsymbol{\rho})$ is given as [187]

$$P(\boldsymbol{\rho}) = \sum_{e=1}^{Ne} P^e(\boldsymbol{\rho}) = \sum_{e=1}^{Ne} \frac{\theta}{2} \overline{C}_{\text{cap}}^e \left\| \Phi_a^e(\boldsymbol{\rho}) \right\|^2, \tag{5.16}$$

where $\overline{C}_{\text{cap}}^e = \overline{\varepsilon} A^e / h$ $(e = 1, 2, ..., N_e)$ is the effective capacitance of each actuator, $\overline{\varepsilon}$ is the permittivity of the piezoelectric material and A^e is the surface area of the eth actuator; all the actuators share the same geometric dimension ; In this study, all of the actuators have the same effective capacitance $C_{\text{cap}} = \overline{C}_{\text{cap}}^e = \overline{\varepsilon} A^e / h$ $(e = 1, 2, ..., N_e)$ because they share the same

geometric dimensions and material; the symbol $\left\|\Phi_a^e\right\|^2$ stands for the norm of the actuator voltage amplitude and can be expressed as

$$\left\|\Phi_a^e(\boldsymbol{\rho})\right\|^2 = \left(\mathrm{Re}\left(\Phi_a^e(\boldsymbol{\rho})\right)\right)^2 + \left(\mathrm{Im}\left(\Phi_a^e(\boldsymbol{\rho})\right)\right)^2. \tag{5.17}$$

Here, the symbols $\mathrm{Re}(\ )$ and $\mathrm{Im}(\ )$ denote the real and imaginary parts of a complex number.

Using the vector and matrix forms, the total actuator energy consumption P can be rewritten as

$$\begin{aligned} P(\boldsymbol{\rho}) &= \frac{\theta}{2} C_{\mathrm{cap}}\left(\mathrm{Re}(\boldsymbol{\Phi}_a)^{\mathrm{T}} \cdot \mathrm{Re}(\boldsymbol{\Phi}_a) + \mathrm{Im}(\boldsymbol{\Phi}_a)^{\mathrm{T}} \cdot \mathrm{Im}(\boldsymbol{\Phi}_a)\right), \\ &= \frac{\theta^3}{2} C_{\mathrm{cap}}\left((\mathbf{X}^{\mathrm{R}})^{\mathrm{T}}\mathbf{A}\mathbf{X}^{\mathrm{R}} + (\mathbf{X}^{\mathrm{I}})^{\mathrm{T}}\mathbf{A}\mathbf{X}^{\mathrm{I}}\right), \end{aligned} \tag{5.18}$$

where the matrix $\mathbf{A} = \left(\mathbf{G}_a\mathbf{G}_s\mathbf{K}_{\Phi u}\right)^{\mathrm{T}}\left(\mathbf{G}_a\mathbf{G}_s\mathbf{K}_{\Phi u}\right)$, and $\mathbf{X}^{\mathrm{R}}$ and $\mathbf{X}^{\mathrm{I}}$ are the real and imaginary parts of the displacement vector $\mathbf{X}$, respectively.

In this study, the dynamic compliance [193] is considered a vibration response measure to be restricted in the optimization model. Its expression is [40]

$$c = \sqrt{\left(\mathbf{F}^{\mathrm{T}}\mathbf{X}^{\mathrm{R}}\right)^2 + \left(\mathbf{F}^{\mathrm{T}}\mathbf{X}^{\mathrm{I}}\right)^2}. \tag{5.19}$$

The dynamic compliance constraint is equivalent to restricting the maximum allowable value of structural dynamic stiffness subjected to time-harmonic external loads of given frequency and amplitude. The details of explanations and discussions on dynamic compliance can be founded in [154].

With the above objective function and constraint, the topology optimization problem is formulated as

155

$$\min_{\boldsymbol{\rho}} \quad P(\boldsymbol{\rho})$$

$$\text{s.t.} \quad \left(-\theta^2 \mathbf{M} + i\theta(\mathbf{C} + \mathbf{C}_\text{A}) + \mathbf{K}\right)\mathbf{X} = \mathbf{F},$$

$$\sqrt{\left(\mathbf{F}^\text{T}\mathbf{X}^\text{R}\right)^2 + \left(\mathbf{F}^\text{T}\mathbf{X}^\text{I}\right)^2} \le c_{\max},$$

$$0 < \underline{\rho} \le \rho_e \le 1, \quad \left(e = 1, 2, ..., N_\text{e}\right). \tag{5.20}$$

Here, the vector $\boldsymbol{\rho} = \left\{\rho_1, \rho_2, ..., \rho_{N_\text{e}}\right\}^\text{T}$ collects the element-wise density design variables describing the electrode layout over the piezoelectric layers, both actuator and sensor layers share the same distribution of electrode coverage and design variables. The symbol $c_{\max}$ denotes the specified highest allowable dynamic compliance value, it can be chosen by considering specific application requirements. The lower bound of the relative density $\underline{\rho}$ is set to be 10^{-6} in this study.

It is noted that, the signs and magnitudes of the actuator voltages are determined by the active control law. To be specific, they are calculated using Eqs. (5.7)-(5.8) for the CGVF control considered in this study. Thus in the final optimal designs, the piezoelectric control pairs only exist at the locations with non-zero densities.

By introducing the piezoelectric property penalization model, the piezoelectricity matrix can be expressed as [194]

$$\mathbf{e}^{\text{piezo}}\left(\rho_e\right) = \rho_e^{p_1}\mathbf{e}. \tag{5.21}$$

Then the active damping matrix $\mathbf{C}_\text{A}$ in Eq. (5.11) can be further given as

$$\mathbf{C}_\text{A} = \sum_{e=1}^{N_e}\left(\rho_e\right)^{p_1}\mathbf{K}_{\text{u}\Phi}^e\mathbf{G}_\text{a}^e\mathbf{G}_\text{s}^e\mathbf{K}_{\Phi\text{u}}^e. \tag{5.22}$$

Here, the symbol p_1 is the penalty factor, and we chose $p_1 = 3$ following the suggestion in [61, 195]. It is noted that the elasticity, piezoelectric and mass matrices of the sensors and

actuators are not penalized and keep unchangeable during the optimization process.

The total energy consumption P can also be expressed with a density-based interpolation model as

$$P = \sum_{e=1}^{Ne} \frac{\theta}{2} C_{\text{cap}} \left\| \Phi_{\text{a}}^e (\boldsymbol{\rho}) \right\|^2 = \frac{\theta^3}{2} C_{\text{cap}} \sum_{e=1}^{Ne} \left(\left(\mathbf{X}_e^{\text{R}} \right)^{\text{T}} \mathbf{A}_e \mathbf{X}_e^{\text{R}} + (\mathbf{X}_e^{\text{I}})^{\text{T}} \mathbf{A}_e \mathbf{X}_e^{\text{I}} \right), \qquad (5.23)$$

with
$$\mathbf{A}^e = \left(\rho_e \right)^{p_2} G_{\text{a}}^e G_{\text{s}}^e \left(\mathbf{K}_{\Phi\text{u}}^e \right)^{\text{T}} \left(\mathbf{K}_{\Phi\text{u}}^e \right) \quad . \qquad (5.24)$$

Recalling Eq. (5.18), one sees that the elemental matrix $\mathbf{A}^e$ in Eq. (5.24) reflects the relation between the displacements and the energy consumption of the e th element. Here, $p_2 \geq 1$ is a penalization factor when computing the energy consumption. Because the total energy consumption in Eq. (5.24) has been indirectly penalized by the penalization factor $p_1 = 3$ through its effect on the elemental dynamic response $\mathbf{X}_e$, we suggest here $p_2 = 1$, though other choices may also work. If the penalization factor p_2 is larger than 1, the energy consumption of the intermediate density element will be artificially reduced by the penalization model and lead to a solution with a 'gray' electrode coverage.

The volume constraint, which is usually considered in the compliance minimization topology optimization, is not included in our optimization model. Comparative results regarding the effects of discarding the volume constraint in the considered problems will be given in a numerical example.

5.3 Sensitivity analysis

In this chapter, the topology optimization problem is solved by a gradient-based mathematical programming algorithm. Thus, the sensitivity analysis of the objective function and constraint

function with respect to the elemental densities needs to be developed. To evaluate the sensitivity of the total energy consumption P, we first introduce two adjoint vectors λ_1 and λ_2 to formulate the Lagrangian function $L(\mathbf{X}, \mathbf{A})$ as

$$L = P(\mathbf{X}, \mathbf{A}) + \lambda_1^\mathrm{T}(\mathbf{W}\mathbf{X} - \mathbf{F}) + \lambda_2^\mathrm{T}(\overline{\mathbf{W}}\overline{\mathbf{X}} - \overline{\mathbf{F}}), \tag{5.25}$$

where $\overline{\mathbf{W}}$ and $\overline{\mathbf{F}}$ denote the conjugates of the dynamic stiffness matrix $\mathbf{W} = -\theta^2\mathbf{M} + i\theta(\mathbf{C} + \mathbf{C}_\mathrm{A}) + \mathbf{K}$ and the excitation amplitude vector $\mathbf{F}$, respectively.

Differentiating Eq. (5.25) with respect to the eth design variable yields

$$\frac{\mathrm{d}L(\mathbf{X}, \mathbf{A})}{\mathrm{d}\rho_e} = \frac{\partial P}{\partial \mathbf{A}} \cdot \frac{\partial \mathbf{A}}{\partial \rho_e} + \lambda_1^\mathrm{T}\frac{\partial \mathbf{W}}{\partial \rho_e}\mathbf{X} + \lambda_2^\mathrm{T}\frac{\partial \overline{\mathbf{W}}}{\partial \rho_e}\overline{\mathbf{X}} + \left(\frac{\partial P}{\partial \mathbf{X}^\mathrm{R}} + \lambda_1^\mathrm{T}\mathbf{W} + \lambda_2^\mathrm{T}\overline{\mathbf{W}}\right)\frac{\partial \mathbf{X}^\mathrm{R}}{\partial \rho_e} \\ + \left(\frac{\partial P}{\partial \mathbf{X}^\mathrm{I}} + i\lambda_1^\mathrm{T}\mathbf{W} - i\lambda_2^\mathrm{T}\overline{\mathbf{W}}\right)\frac{\partial \mathbf{X}^\mathrm{I}}{\partial \rho_e}. \tag{5.26}$$

Letting the fourth and fifth terms on the right-hand side of Eq. (5.26) be equal to zero, the adjoint variables can be obtained by solving the following equations

$$\lambda_1^\mathrm{T}\mathbf{W} = \frac{1}{2}\left(-\frac{\partial P}{\partial \mathbf{X}^\mathrm{R}} + i\frac{\partial P}{\partial \mathbf{X}^\mathrm{I}}\right), \quad \lambda_2^\mathrm{T}\overline{\mathbf{W}} = \frac{1}{2}\left(-\frac{\partial P}{\partial \mathbf{X}^\mathrm{R}} - i\frac{\partial P}{\partial \mathbf{X}^\mathrm{I}}\right). \tag{5.27}$$

The two adjoint variables satisfy $\lambda_1 = \overline{\lambda}_2$, and λ_1 is the solution to the following adjoint equation

$$\lambda_1^\mathrm{T}\mathbf{W} = \frac{1}{2}\left(-\frac{\partial P}{\partial \mathbf{X}^\mathrm{R}} + i\frac{\partial P}{\partial \mathbf{X}^\mathrm{I}}\right) = -\frac{\theta^3}{2}C_\mathrm{cap}\left(\mathbf{X}^\mathrm{R} - i\mathbf{X}^\mathrm{I}\right)^\mathrm{T}\mathbf{A} = -\frac{\theta^3}{2}C_\mathrm{cap}\overline{\mathbf{X}}^\mathrm{T}\mathbf{A}. \tag{5.28}$$

The derivative of the objective function in Eq. (5.26) can be further expressed as

$$\frac{\mathrm{d}L}{\mathrm{d}\rho_e} = \frac{\partial P}{\partial \mathbf{A}} \cdot \frac{\partial \mathbf{A}}{\partial \rho_e} + 2\,\mathrm{Re}\left(\lambda_1^\mathrm{T}\frac{\partial \mathbf{W}}{\partial \rho_e}\mathbf{X}\right), \tag{5.29}$$

in which

$$
\frac{\partial \mathbf{W}}{\partial \rho_e} = \frac{\partial \left(-\theta^2 \mathbf{M} + i\theta(\mathbf{C} + \mathbf{C}_\mathrm{A}) + \mathbf{K} \right)}{\partial \rho_e} = \frac{\partial \mathbf{C}_\mathrm{A}}{\partial \rho_e},
$$

$$
= p_1 \left(\rho_e \right)^{(p_1 - 1)} \mathbf{K}_{\mathrm{u}\Phi}^e G_\mathrm{a}^e G_\mathrm{s}^e \mathbf{K}_{\Phi\mathrm{u}}^e,
$$

(5.30)

and

$$
\frac{\partial P}{\partial \mathbf{A}} \cdot \frac{\partial \mathbf{A}}{\partial \rho_e} = \frac{\theta^3}{2} C_{\mathrm{cap}} \left(\left(\mathbf{X}^\mathrm{R} \right)^\mathrm{T} \frac{\partial \mathbf{A}}{\partial \rho_e} \mathbf{X}^\mathrm{R} + \left(\mathbf{X}^\mathrm{I} \right)^\mathrm{T} \frac{\partial \mathbf{A}}{\partial \rho_e} \mathbf{X}^\mathrm{I} \right),
$$

(5.31)

with

$$
\frac{\partial \mathbf{A}}{\partial \rho_e} = p_2 \left(\rho_e \right)^{p_2 - 1} G_\mathrm{a}^e G_\mathrm{s}^e \left(\mathbf{K}_{\Phi\mathrm{u}}^e \right)^\mathrm{T} \left(\mathbf{K}_{\Phi\mathrm{u}}^e \right).
$$

(5.32)

Substituting Eqs. (5.28) and (5.30)-(5.32) into Eq. (5.29), the derivative of the total energy consumption P can be obtained as

$$
\frac{\partial P}{\partial \rho_e} = \frac{\theta^3}{2} C_{\mathrm{cap}} G_\mathrm{a}^e G_\mathrm{s}^e \left\{ p_2 \left(\rho_e \right)^{p_2 - 1} \left[\left(\mathbf{X}^\mathrm{R} \right)^\mathrm{T} \left(\mathbf{K}_{\Phi\mathrm{u}}^e \right)^\mathrm{T} \left(\mathbf{K}_{\Phi\mathrm{u}}^e \right) \mathbf{X}^\mathrm{R} + \left(\mathbf{X}^\mathrm{I} \right)^\mathrm{T} \left(\mathbf{K}_{\Phi\mathrm{u}}^e \right)^\mathrm{T} \left(\mathbf{K}_{\Phi\mathrm{u}}^e \right) \mathbf{X}^\mathrm{I} \right]
$$
$$
+ 2 p_1 \left(\rho_e \right)^{p_1 - 1} \mathrm{Re} \left[-\mathbf{W}^{-1} \bar{\mathbf{X}}^\mathrm{T} \mathbf{A} \mathbf{K}_{\mathrm{u}\Phi}^e \mathbf{K}_{\Phi\mathrm{u}}^e \mathbf{X} \right] \right\}
$$

(5.33)

The sensitivity of the structural dynamic compliance c can be derived in a similar way and can be found in [40].

5.4 Numerical examples

Numerical examples are presented to confirm the validity of the proposed topology optimization methodology, and the differences between the present optimization model and the minimum-volume optimization model are also discussed. The proposed method is implemented on the Matlab platform, and the globally convergent method of moving asymptotes (GCMMA) [162] algorithm is employed to solve the optimization problem. The optimization process is

terminated when the relative difference between the objective function values of two adjacent iterations becomes less than 10^{-4}.

5.4.1 Topology optimization for four-edge clamped plate

A numerical example involving four-edge clamped squared plate is presented first to confirm the validity of the proposed topology optimization methodology. The four-edge clamped piezoelectric laminated plate with two piezoelectric layers covered with electrodes and attached to the top surface of the host layer is shown in Fig. 5.2. The length and thickness of the host layer are $a = 0.1\text{m}$ and $t_\text{h} = 10^{-4}\text{m}$, respectively. Two piezoelectric layers share the same length with the host layer, and the thicknesses of both layers are $t^\text{s} = t^\text{a} = 10^{-5}\text{ m}$. The geometric parameters are not realistic, though they satisfy the basic assumption that the damping of the piezoelectric layers is much smaller than those of the host structure. The material of the host layer is defined as an isotropic elastic material with aluminum constitutive properties (modulus of elasticity $E^\text{h} = 6.9 \times 10^{10}\text{ N/m}^2$, Poisson's ratio $v^\text{h} = 0.3$ and the mass density $\rho^\text{h} = 2700\text{ kg/m}^3$), and the material properties of the piezoelectric sensor and actuator layers (PZT-5A) are given in Table 5.1. The damping coefficients of the host structure are $\alpha = \beta = 1 \times 10^{-5}$. The sensor charge amplifier has a gain factor of $G_\text{c} = 2 \times 10^4\text{ V/A}$, and the control gain of the CGVF control is $G_\text{a} = 100$. A time-harmonic external force $f(t) = F\text{e}^{i\theta t}$ (with $F = 2\text{N}$, $\theta = 2\pi f$ and $f = 240$ Hz) is applied at the center of the plate.
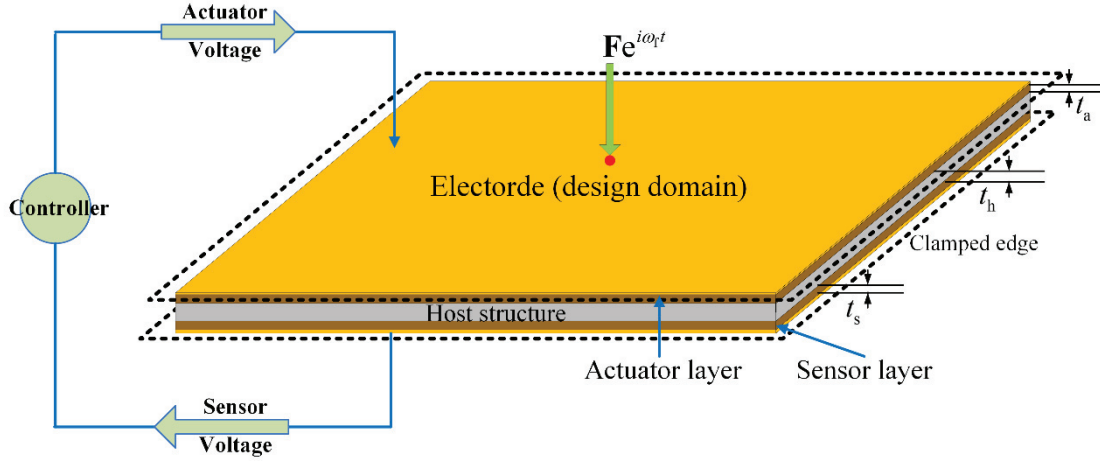
Fig. 5.2 Four-edge clamped piezoelectric laminated plate with designable electrode coverage under an external harmonic excitation at its center.

Table 5.1 Material properties of piezoelectric sensor/actuator layers.

Elasticity constant	$C_{11} = C_{22} = 10.76 \times 10^{10}$ N/m^2, $C_{12} = 6.31 \times 10^{10}$ N/m^2, $C_{13} = C_{23} = 6.39 \times 10^{10}$ N/m^2, $C_{33} = 10.04 \times 10^{10}$ N/m^2, $C_{44} = 1.96 \times 10^{10}$ N/m^2, $C_{66} = 2.22 \times 10^{10}$ N/m^2
Mass density	$\rho^{\text{piezo}} = 7800$ kg/m^3
Piezoelectricity constant	$e_{31} = e_{32} = -9.6$ C/m^2, $e_{33} = 15.1$ C/m^2, $e_{33} = 15.1$ C/m^2 $e_{15} = e_{25} = 12.0$ C/m^2
Dielectric constant	$\bar{\varepsilon} = 1.15 \times 10^{-9}$ F/m

The plate (design domain) is discretized by 50×50 uniform-sized four-node Mindlin shell elements with 2601 nodes and 13005 degree of freedoms (DOFs) (including constrained ones). The first five eigenfrequencies of the laminated plate are 82.6 Hz, 168.5 Hz, 168.5 Hz, 248.1 Hz, and 302.4 Hz. They will not change during the optimization process because only the electrode coverage layout is designable (recall that the mass and stiffness of the electrode are negligible). In the optimization model, the upper limit value of structural dynamic compliance is 5.5×10^{-3} N·m and the initial values of the design variables for indicating the electrode

coverage are set to be $\rho_e = 0.6 \ (e = 1, 2, ..., 2500)$. The well-known sensitivity filter technique [196], with a filter radius of $r_{\min} = 4 \times 10^{-3}$ m, is employed for preventing mesh dependency of the optimal solution.

The optimization process converged after 32 iterations, and the iteration history is given in Figure 3. It can be observed from Fig. 5.3 that the total energy consumption of the active control system decreases from 1.91 W for the initial design to 1.61 W for the optimal design. It is necessary to point out that the compliance dynamic for the initial design ($c = 6.7 \times 10^{-3}$ N·m) is larger than the allowable maximum value ($c = 5.5 \times 10^{-3}$ N·m) and thus the objective function increases in the first four iterations to satisfy the dynamic compliance constraint . The optimal solution (red color denotes density 1 and blue color denotes zero density) and suggested electrode coverage (by deleting low-density elements) are given in Fig 5.4. The electrode coverage over the piezoelectric material layer is 46.2%. The optimal solution is significantly different from the optimal solution for minimizing dynamic compliance [73]. It can be observed that no electrode coverage is distributed in the areas around the loading point; this occurs because the implementation of the piezoelectric control forces around the loading area, which has higher vibration velocity amplitudes, requires more electrical power supply. The vibration amplitude under the CGVF control for the initial design and optimal design is shown in Fig 5.5. This figure indicates that the global vibration level has been reduced uniformly after optimization. Here, the maximum vibration amplitudes for the initial and optimal designs are 0.33 cm and 0.27 cm, respectively. The real and imaginary part of the applied actuator voltage amplitude are shown in Fig 5.6, which shows that the distribution of real and imaginary part of the control voltage agrees very well and they have opposite signs.
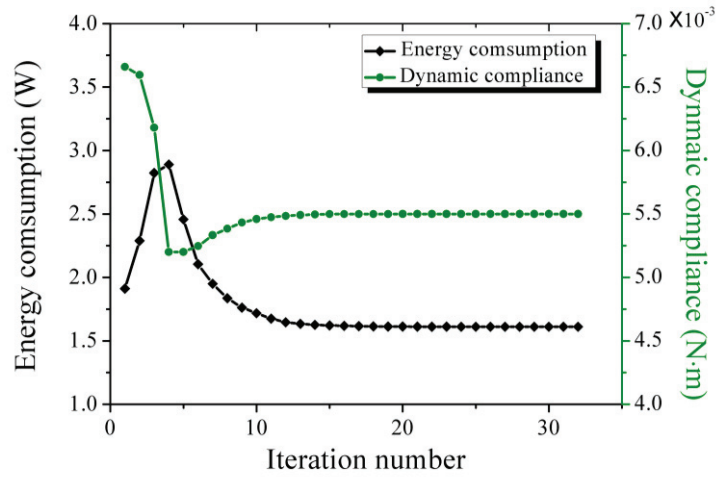
Fig. 5.3 Iteration histories of the energy consumption and dynamic compliance constraint.

(a)

(b)
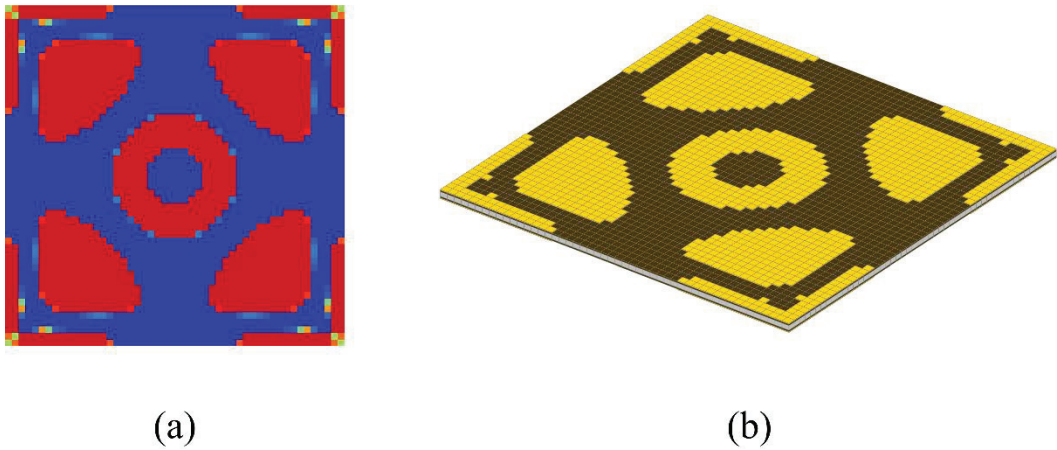
Fig. 5.4 Optimal layout of electrode coverage for the four-edge clamped piezoelectric laminated plate: (a) design variable density contour and (b) optimal distribution of electrode plotted with threshold density value $\rho_{threshold}=0.5$.
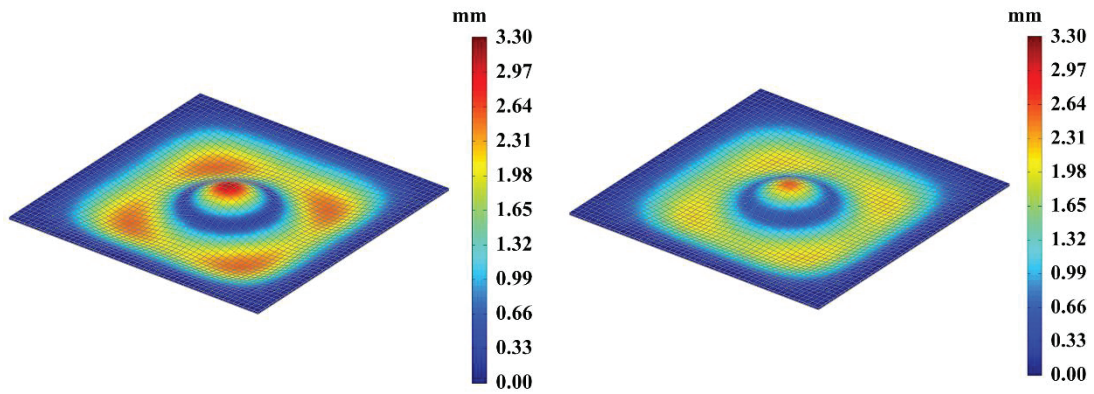
(a)   (b)

Fig. 5.5 Vibration amplitude for the initial and optimal design: (a) initial design
(maximum vibration amplitude is 0.33 cm) and (b) optimal design (maximum vibration
amplitude is 0.27 cm).
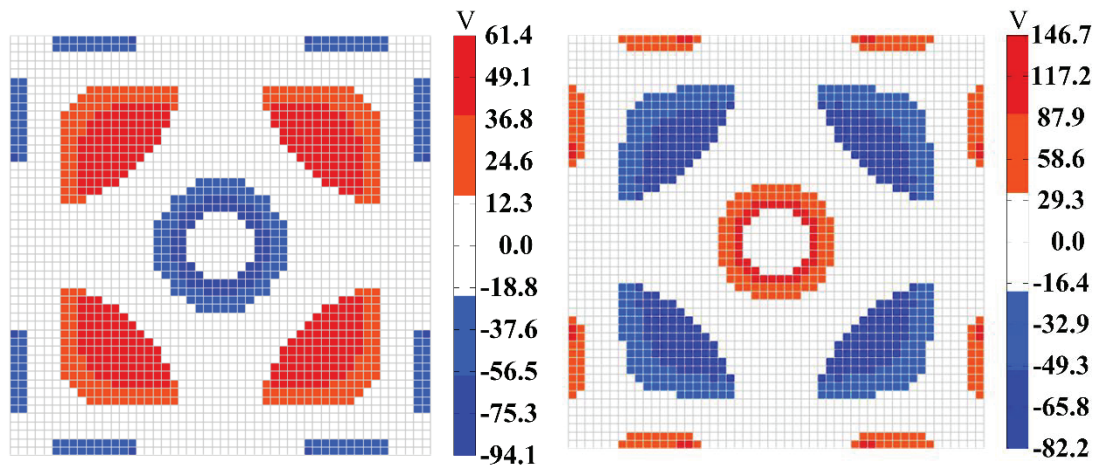
(a)   (b)

Fig. 5.6 Actuator voltage amplitude for optimal design: (a) real part and (b) imaginary
part.

For comparison, we consider three different reference designs with similar area coverage
of electrodes (46.24%~48%) (recall that the optimal solution in Fig. 5.4 has a 46.2% electrode
coverage), as shown in Fig. 5.7. The dynamic compliances and energy consumptions are

summarized in Table 5.2. It is found that the optimal design (Fig. 5.4) has the lowest energy consumption in all the designs that satisfy the dynamic compliance constraint, while the reference designs either have high energy consumptions (the designs in Figs. 5.7(a) and (c)) or violate the dynamic compliance constraint (the design in Fig. 5.7(b)).

(a)　　　　　　　　(b)　　　　　　　　(c)
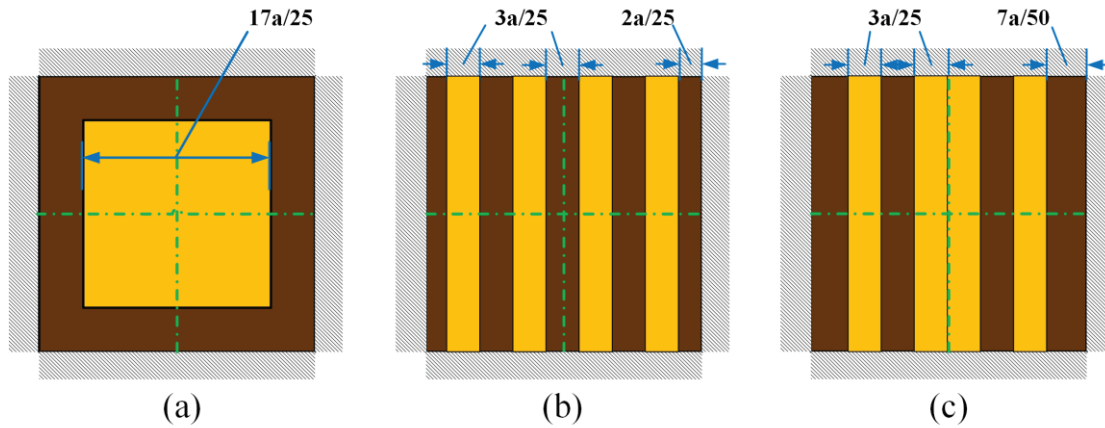
Fig.5.7 Three reference designs: (a) Case A: center electrode coverage design (total electrode coverage ratio is 46.24%), (b) Case B: design with vertical striped electrode coverage (total electrode coverage ratio is 48%) and (c) Case C: design with central and vertical striped electrode coverage (total electrode coverage ratio is 48%).

Table 5.2 Comparisons of the dynamic compliances and energy consumptions for the optimal design and reference designs.

	Electrode coverage ratio	Energy consumption (W)	Dynamic compliance (N•m)
Optimal solution	46.2%	1.61	5.5×10^{-3}
Reference design A	46.24%	3.37	5.2×10^{-3}
Reference design B	48%	1.47	5.8×10^{-3}
Reference design C	48%	3.19	5.2×10^{-3}

The influence of the dynamic compliance constraint on the optimal design is also studied.

The same plate treated in the previous example is considered except with two different limiting values for dynamic compliance $c = 6.0 \times 10^{-3} \, \text{N} \cdot \text{m}$ and $5.0 \times 10^{-3} \, \text{N} \cdot \text{m}$. The optimal designs are illustrated in Fig. 5.8. These optimized topologies are similar, except that some regions become larger as the upper limit of the dynamic compliance decreases. Moreover, the electrode coverages for the piezoelectric layers in the two cases are 32.6% and 59.3%, respectively.

(a) (b)
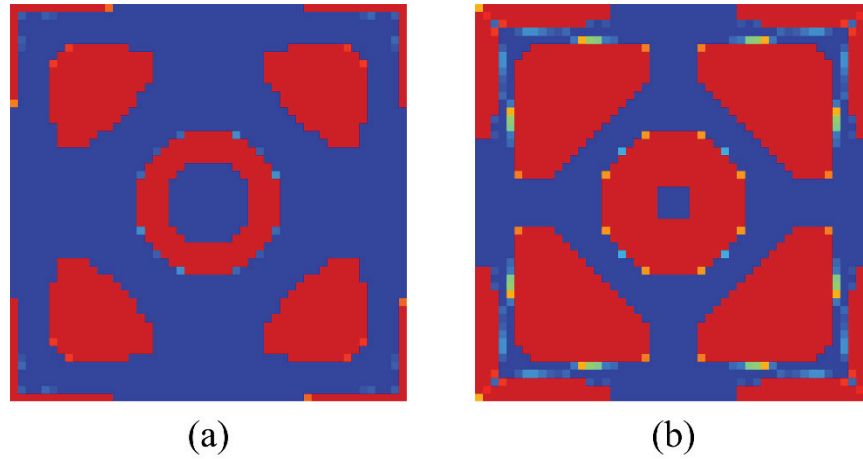
Fig. 5.8 Optimal solutions under different dynamic compliance constraints: (a) $c = 6.0 \times 10^{-3} \, \text{N} \cdot \text{m}$ and (b) $5.0 \times 10^{-3} \, \text{N} \cdot \text{m}$ optimal design.

To explore the influence of the external excitation frequency and dynamic compliance constraint, we also perform the optimal design under excitation of 208Hz excitation (middle point between the third and fourth eigen-frequencies of the structure) and three different dynamic compliance constraints $c_{max} = 2.4 \times 10^{-3}$, 2.6×10^{-3} and $2.8 \times 10^{-3} \, \text{N} \cdot \text{m}$ (it cannot be set to $5.5 \times 10^{-3} \, \text{N} \cdot \text{m}$ because the vibration level under 208 Hz excitation is much smaller than that of 240 Hz excitation). The optimized designs are given in Fig. 5.9. They show some similar patterns but not identical shapes as compared with the solutions obtained at 240Hz excitation frequency (Figs. 5.4 and 5.8). This is because the optimization results under 208Hz excitation are affected by both the third and fourth eigenmodes, while the solutions for 240Hz mainly reflect the influence of the fourth eigenmode.
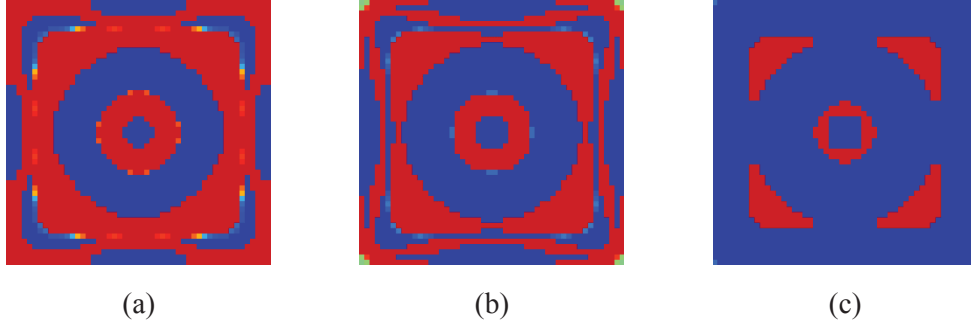
Fig. 5.9 Optimal solutions (red color implies the electrode coverage) under 208 Hz excitation and different dynamic compliance constraints: (a) $c_{max} = 2.4 \times 10^{-3}$ N·m, (b) $c_{max} = 2.6 \times 10^{-3}$ N·m and (c) $c_{max} = 2.8 \times 10^{-3}$ N·m.

5.4.2 Topology optimization for cantilever plate with two different optimization models

(a) Optimization for minimizing energy consumption

We now consider the topological design of the electrode layout in a cantilever piezoelectric laminated plate for minimizing the total energy consumption, as shown in Fig. 5.10. The plate has side lengths $a = 1.6$ m and $b = 0.8$ m, and the thicknesses of the host layer and piezoelectric layers are $t_h = 4 \times 10^{-3}$ m and $t^s = t^a = 5 \times 10^{-4}$ m, respectively. The material properties of the host layer and piezoelectric layers are the same as in the previous example. The damping coefficients of the host structure are $\alpha = \beta = 1 \times 10^{-4}$. The sensor charge amplifier has a gain factor of $G_c = 10^5$ V/A, and the control gain of the CGVF control is $G_a = 150$. A time-harmonic external force $f(t) = Fe^{i\theta t}$ (with $F = 100$ N, $\theta = 2\pi f$ and $f = 7$ Hz) is applied at the mid-point of the free edge. The design domain of the piezoelectric laminated plate is discretized by 80×40 uniformly-sized shell elements with 3321 nodes and 16605 DOFs. The first Eigen frequencies are 1.22 Hz, 5.20 Hz, 7.65 Hz, 16.99 Hz, and 21.46 Hz. The objective function is to minimize the total energy consumption at the excitation frequency f =7 Hz, and the dynamic compliance of the structure is restricted by 4.4 N·m. All the design

167

variables are set as $\rho_e = 0.6 \ (e = 1, 2, ..., 3200)$ in the initial design.
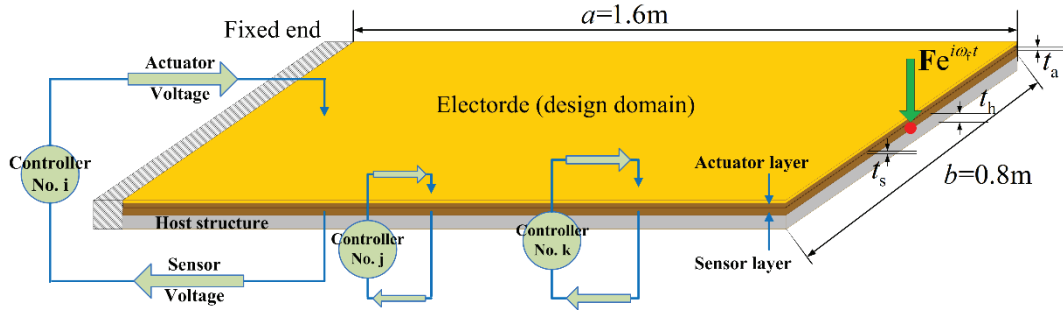
Fig. 5.10   Cantilever piezoelectric laminated plate under an external harmonic excitation at the mid-point of the free edge.

The optimization process converged after 95 iterations, yielding the optimal solution shown in Figure 11. It is found from Fig. 5.9 that the electrode distribution is moved away from the neighborhood area of the loading point to avoid an energy consumption that is too high. Fig. 5.11 shows that some isolated electrode parts are distributed around the inflection points and corner points for reducing the local vibration. The iteration history of the objective function and the dynamic compliance index are plotted in Fig. 5.12. The energy consumption increases in the first iteration to satisfy the dynamic compliance constraint and then decreases from 29.07 W for the second iteration to 18.21 W in the final solution. In the optimized design, the electrode coverage is 46.1%. It can be observed from the vibration level contours of the initial and optimal designs given in Fig. 5.13 that the overall vibration level is notably reduced after optimization. Here, the maximum vibration amplitudes for the initial and optimal designs are 5.21 cm and 4.40 cm, respectively. The applied actuator voltage amplitude is shown in Fig. 5.14, and the maximum absolute values of the real and imaginary parts are 546.4 V and 819.4 V, respectively.

(a)

(b)
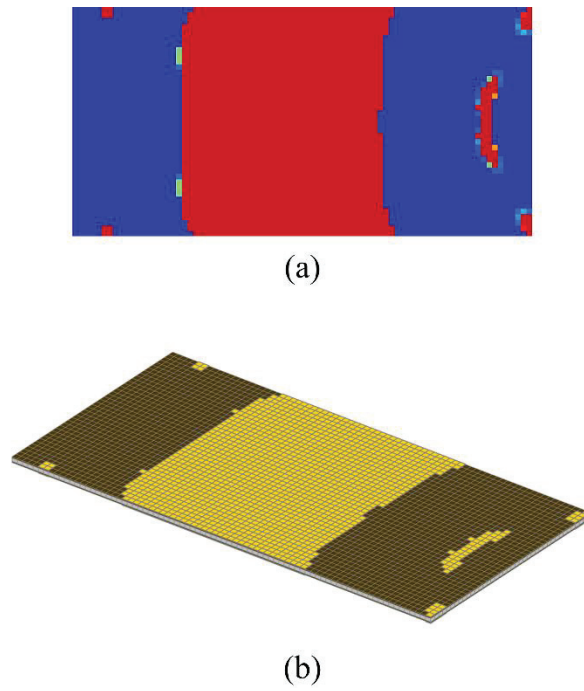
Fig. 5.11 Optimal layout of electrode coverage for the cantilever piezoelectric laminated plate: (a) design variable density contour and (b) optimal distribution of electrode plotted with threshold density value $\rho_{\text{threshold}}=0.5$.
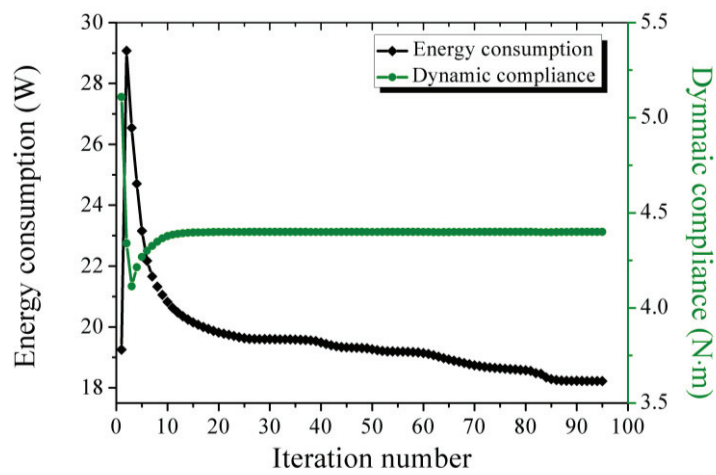
Fig. 5.12 Iteration histories of the energy consumption and dynamic compliance constraint.
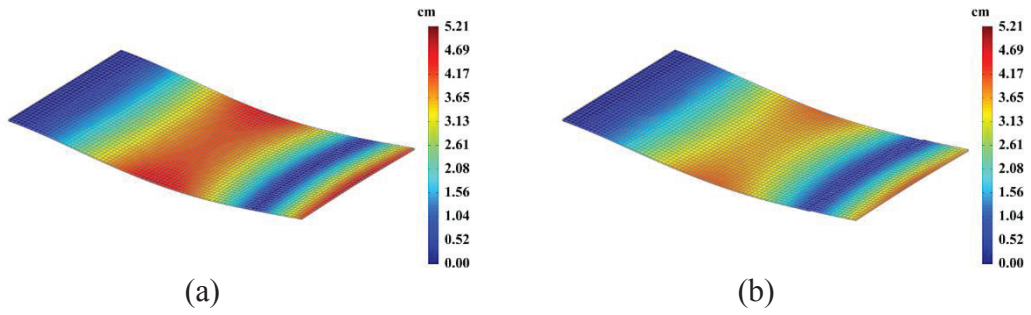
Fig. 5.13 Vibration amplitude for the initial and optimal design: (a) initial design (maximum vibration amplitude is 5.21 cm) and (b) optimal design (maximum vibration amplitude is 4.40 cm).
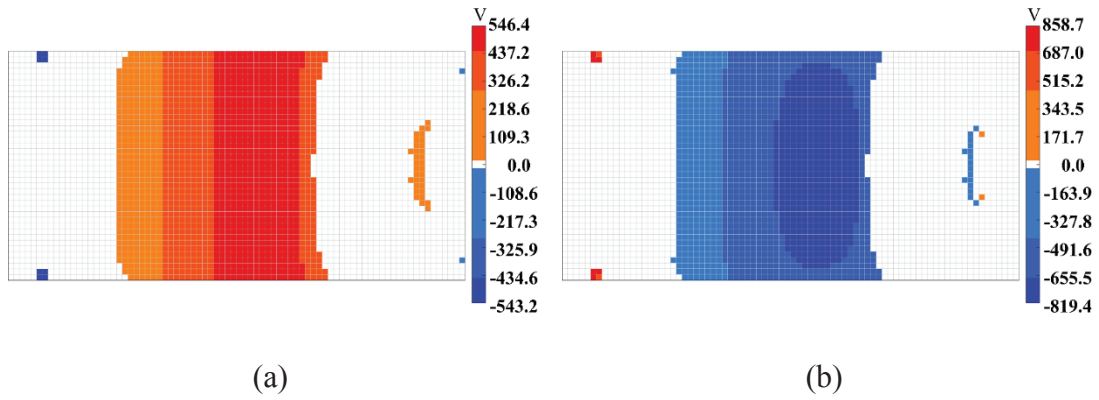
Fig. 5.14 Actuator voltage amplitude for optimal design: (a) real part and (b) imaginary part.

(b) Comparison with minimum-volume design

In this section, we present the topology optimization for minimizing the volume fraction ratio under the constraint of dynamic compliance. The optimization model is expressed as

$$\min_{\boldsymbol{\rho}} \quad f_{\mathrm{v}} = \sum_{e=1}^{N_{\mathrm{e}}} \rho_e V_e \big/ V_0$$

$$\text{s.t.} \quad \left(-\theta^2 \mathbf{M} + i\theta(\mathbf{C} + \mathbf{C}_{\mathrm{A}}) + \mathbf{K}\right)\mathbf{X} = \mathbf{F}$$

$$\sqrt{\left(\mathbf{F}^{\mathrm{T}}\mathbf{X}^{\mathrm{R}}\right)^2 + \left(\mathbf{F}^{\mathrm{T}}\mathbf{X}^{\mathrm{I}}\right)^2} \leq c_{\max}$$

$$0 < \underline{\rho} \leq \rho_e \leq 1 \quad \left(e = 1, 2, ..., N_{\mathrm{e}}\right),$$

(34)

where V_e denotes the volume of the electrode over the eth piezoelectric patch, and V_0 is the total volume of the electrode with the full coverage. This optimization model is employed here for comparing with the proposed energy consumption optimization method. Thus, the same structure as in the pervious subsection is now considered, but the design objective is to minimize the material volume fraction ratio.

The optimization process converges after 72 iterations, and the optimal solution is given in Fig. 5.15. This solution is obviously different from that of the energy consumption optimization (Fig. 5.9). It has a total electrode coverage of 25.5%, which is lower than the energy consumption solution (46.1%), but it has a higher power requirement of 21.44 W (as compared with 18.21 W for the energy consumption optimization). As shown in Fig. 5.16, this design has nearly the same vibration level as the minimum energy consumption design, and the maximum vibration amplitude of the minimum-volume design is 4.40 cm. This is because both solutions reach the upper bound of the allowable structural dynamic compliance. However, a remarkably different control voltage distribution can be observed in Fig. 5.17. In this specific example, although the proposed energy consumption minimization model yields a larger electrode coverage than the volume-minimization design, it substantially reduces the electric power requirement, considering that the peak absolute values of the control voltage are much higher (927.2V for the real part and 1586.8 V for the imaginary part).
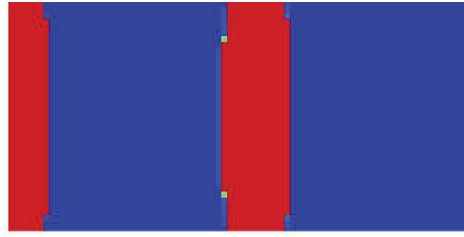
(a)
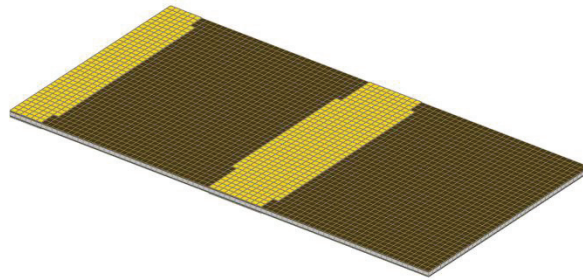
(b)

Fig. 5.15 Optimal electrode coverage layout of a cantilever piezoelectric laminated plate for volume fraction minimization: (a) design variable density contour and (b) optimal distribution of electrode plotted with threshold density value $\rho_{\text{threshold}}=0.5$.
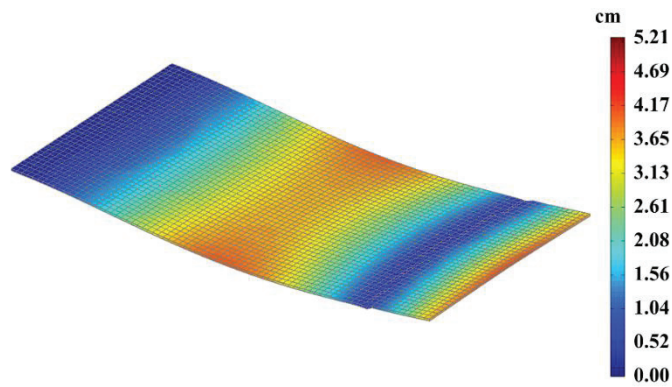
Fig. 5.16 Vibration amplitude for the optimal design of volume minimization optimization (maximum vibration amplitude is 4.40 cm).
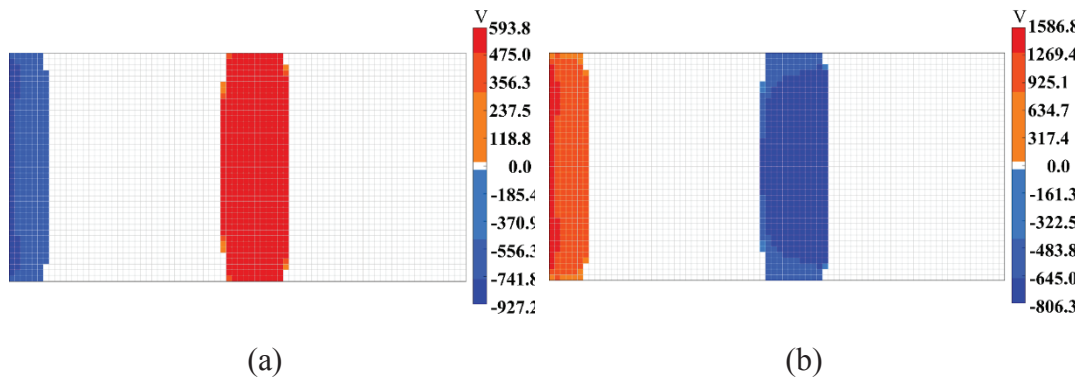
Fig. 5.17 Actuator voltage amplitude for optimal design of volume minimization optimization: (a) real part and (b) imaginary part.

Furthermore, we present another 16 sets of optimization results under different dynamic compliance constraints in the range of $c_{max} = 4 \sim 4.8\,\mathrm{N\cdot m}$ (sampling points are uniformly distributed with an interval of $0.05\,\mathrm{N\cdot m}$). Both optimization models yield larger electrode coverage for providing higher control forces, when the allowable dynamic compliance is assigned a smaller value (corresponding to more stringent vibration reduction requirement). The energy consumption and volume fraction ratio for the optimal designs obtained with the two optimization models are given in Figure 18 and Figure 19, respectively. It can be observed that the energy consumption-minimization designs have lower power requirements in all 16 cases.
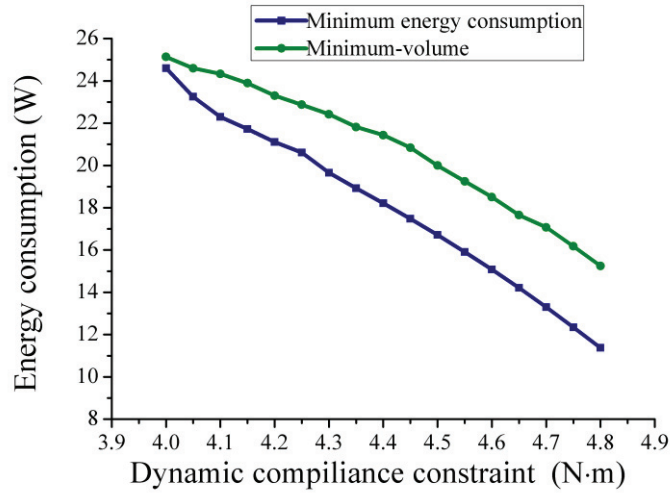
Fig. 5.18 Comparison of the energy consumption with volume-minimization solutions and energy minimization solutions.
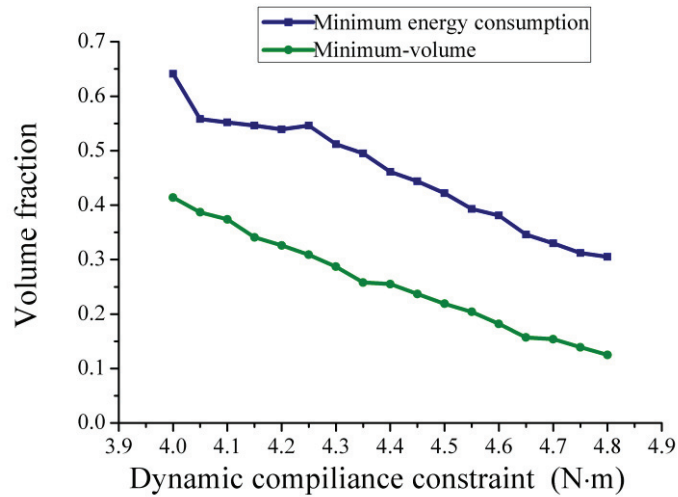
Fig. 5.19 Comparison of the volume fraction of volume-minimization solutions and energy minimization solutions.

5.5 Summary

This chapter proposes a method for topology optimization of piezoelectric laminated plates for

minimizing the energy consumption with CGVF control under harmonic excitation. A new type of objective function, which is to minimize the total energy consumption in the active control system, is introduced into the topology optimization formulation, and the optimization problem is restricted by a upper limit of allowable dynamic compliance. A pseudo-density model with penalization for indicating the absence and presence of surface electrodes is used in the topology optimization model, and artificial models with penalization for both piezoelectric properties and energy consumption calculations are employed for suppressing intermediate density values. In this context, the sensitivity of the total energy consumption with respect to the design variables is derived using the adjoint-variable method. Numerical examples demonstrate the validity of the proposed method. It is shown that the proposed method is capable of reducing the energy consumption of the active vibration control. This highlights the importance of properly considering the energy consumption performance in the design of active control structures, in particular miniature smart devices.

6 Concluding remarks

Topology optimization methods of macrostructures and microstructures against uncertain dynamic loads, random material properties distribution, and random diffuse regions between material phases are proposed in this dissertation. In addition, this dissertation also investigates topology optimization of the piezoelectric structure to reduce the energy consumption of active vibration control. The following results were achieved.

(1) Robust topology optimization methods of structures subjected to unknown-but-bounded dynamic loads/ground accelerations are investigated. Herein, the single-loop reformulation of the originally nested problem on the basis of inhomogeneous eigenvalue analysis is proposed. Sensitivity analysis for the worst-case dynamic response is derived.

(2) A robust topological design method of the microstructures of PnCs considering random-field material properties is proposed. The stochastic response analysis method combining the EOLE method with the PCE approach for the random material property distribution is addressed. The sensitivity analysis for the stochastic band gap response is derived.

(3) A robust phase-field-based topology optimization method is developed for the design of vibrating structures under diffuse-region uncertainties. The design domain is represented with the phase-field function and the explicit phase-field curve is updated by solving the Allen–Cahn equation. Herein, three types of the dynamic performance functions are considered, including the structural dynamic compliance, the fundamental frequency or frequency gap, and the transient displacement under impact loads. The phase-field based robust topology optimization method is also applied into the microstructures design of PnCs considering random diffuse-region widths between different material phases. For achieving a less sensitive optimal design of PnCs, a phase field based robust topology

optimization formulation to minimize the weighted sum of the mean value and standard deviation of the specified band gap is developed.

(4) A topology optimization method is proposed for obtaining the best electrode coverage of the piezoelectric material layer which requires the minimum energy consumption to achieve a specified vibration level of a plate with active control. In the topology optimization model, the objective function is the total energy consumption of the active control system; the dynamic compliance of the structure is taken as a vibration level measure for the whole structure, and it is imposed by a specified upper bound. With the density-based topology optimization model, the elemental pseudo-densities indicating the presence/absence of electrode coverage of the piezoelectric layer are taken as design variables. The sensitivity analysis scheme for the total energy consumption of the piezoelectric actuators is derived with the adjoint-variable method, and the optimization problem is solved with a gradient-based mathematical programming algorithm.

References

[1] Y. Luo, Z. Kang, Z. Luo, A. Li, Continuum topology optimization with non-probabilistic reliability constraints based on multi-ellipsoid convex model, Structural and Multidisciplinary Optimization, 39 (3) (2009) 297-310.

[2] F. Wang, J.S. Jensen, O. Sigmund, Robust topology optimization of photonic crystal waveguides with tailored dispersion properties, JOSA B, 28 (3) (2011) 387-397.

[3] S. Chen, W. Chen, A new level-set based approach to shape and topology optimization under geometric uncertainty, Structural and Multidisciplinary Optimization, 44 (1) (2011) 1-18.

[4] X. Guo, W. Zhang, L. Zhang, Robust structural topology optimization considering boundary uncertainties, Computer Methods in Applied Mechanics and Engineering, 253 (2013) 356-368.

[5] N.L. Pedersen, Maximization of eigenvalues using topology optimization, Structural and Multidisciplinary Optimization, 20 (1) (2000) 2-11.

[6] N. Olhoff, J. Du, Introductory notes on topological design optimization of vibrating continuum structures, in: Topology Optimization in Structural and Continuum Mechanics, Springer, 2014, pp. 259-273.

[7] M.S. Kushwaha, P. Halevi, L. Dobrzynski, B. Djafari-Rouhani, Acoustic band structure of periodic elastic composites, Physical Review Letters, 71 (13) (1993) 2022.

[8] B. Graczykowski, M. Sledzinska, F. Alzina, J. Gomis-Bresco, J. Reparaz, M. Wagner, C.S. Torres, Phonon dispersion in hypersonic two-dimensional phononic crystal membranes, Physical Review B, 91 (7) (2015) 075414.

[9] M. Maldovan, Phonon wave interference and thermal bandgap materials, Nature materials, 14 (7) (2015) 667.

[10] M.R. Wagner, B. Graczykowski, J.S. Reparaz, A. El Sachat, M. Sledzinska, F. Alzina, C.M. Sotomayor Torres, Two-dimensional phononic crystals: Disorder matters, Nano Letters, 16 (9) (2016) 5661-5668.

[11] J. Maire, R. Anufriev, R. Yanagisawa, A. Ramiere, S. Volz, M. Nomura, Heat conduction tuning by wave nature of phonons, Science Advances, 3 (8) (2017) e1700027.

[12] A.G.M. Michell, LVIII. The limits of economy of material in frame-structures, The London, Edinburgh, and Dublin Philosophical Magazine and Journal of Science, 8 (47) (1904) 589-597.

[13] K.-T. Cheng, N. Olhoff, An investigation concerning optimal design of solid elastic plates, International Journal of Solids and Structures, 17 (3) (1981) 305-323.

[14] M.P. Bendsøe, N. Kikuchi, Generating optimal topologies in structural design using a homogenization method, Computer Methods in Applied Mechanics and Engineering, 71 (2) (1988) 197-224.

[15] M.P. Bendsøe, Optimal shape design as a material distribution problem, Structural Optimization, 1 (4) (1989) 193-202.

[16] Y.M. Xie, G.P. Steven, A simple evolutionary procedure for structural optimization, Computers & Structures, 49 (5) (1993) 885-896.

[17] M. Wang, X. Wang, D. Guo, A level set method for structural topology optimization, Computer Methods in Applied Mechanics and Engineering, 192 (1-2) (2003) 227-246.

[18] G. Allaire, F. Jouve, A.-M. Toader, Structural optimization using sensitivity analysis and a level-set method, Journal of Computational Physics, 194 (1) (2004) 363-393.

[19] M. Burger, R. Stainko, Phase-field relaxation of topology optimization with local stress constraints, SIAM Journal on Control and Optimization, 45 (4) (2006) 1447-1466.

[20] A. Takezawa, S. Nishiwaki, M. Kitamura, Shape and topology optimization based on the phase field method and sensitivity analysis, Journal of Computational Physics, 229 (7) (2010) 2697-2718.

[21] W. Zhang, J. Yuan, J. Zhang, X. Guo, A new topology optimization approach based on Moving Morphable Components (MMC) and the ersatz material model, Structural and Multidisciplinary Optimization, 53 (6) (2016) 1243-1260.

[22] G.I. Rozvany, A critical review of established methods of structural topology optimization, Structural and multidisciplinary optimization, 37 (3) (2009) 217-237.

[23] N.P. van Dijk, K. Maute, M. Langelaar, F. Van Keulen, Level-set methods for structural topology optimization: a review, Structural and Multidisciplinary Optimization, 48 (3) (2013) 437-472.

[24] X. Huang, Y.-M. Xie, A further review of ESO type methods for topology optimization, Structural and Multidisciplinary Optimization, 41 (5) (2010) 671-683.

[25] M. Zhou, G. Rozvany, The COC algorithm, Part II: topological, geometrical and generalized shape optimization, Computer Methods in Applied Mechanics and Engineering, 89 (1) (1991) 309-336.

[26] M.P. Bendsøe, O. Sigmund, Material interpolation schemes in topology optimization, Archive of applied mechanics, 69 (9-10) (1999) 635-654.

[27] J. Petersson, M. Patriksson, Topology optimization of sheets in contact by a subgradient method, International Journal for Numerical Methods in Engineering, 40 (7) (1997) 1295-1321.

[28] C.S. Jog, R.B. Haber, Stability of finite element models for distributed-parameter optimization and topology design, Computer Methods in Applied Mechanics and Engineering, 3 (130) (1996) 203-226.

[29] R.B. Haber, C.S. Jog, M.P. Bendsøe, A new approach to variable-topology shape design using a constraint on perimeter, Structural optimization, 11 (1-2) (1996) 1-12.

[30] O. Sigmund, On the design of compliant mechanisms using topology optimization, Journal of Structural Mechanics, 25 (4) (1997) 493-524.

[31] O. Sigmund, K. Maute, Topology optimization approaches, Structural and Multidisciplinary Optimization, 48 (6) (2013) 1031-1055.

[32] M. Stolpe, K. Svanberg, An alternative interpolation scheme for minimum compliance topology optimization, Structural and Multidisciplinary Optimization, 22 (2) (2001) 116-124.

[33] N. Pedersen, Maximization of eigenvalues using topology optimization, Structural and Multidisciplinary Optimization, 20 (1) (2000) 2-11.

[34] J.S. Jensen, Topology optimization of dynamics problems with Padé approximants, International journal for numerical methods in engineering, 72 (13) (2007) 1605-1630.

[35] F.I. Niordson, On the optimal design of a vibrating beam, Quarterly of Applied Mathematics, 23 (1) (1965) 47-53.

[36] N. Olhoff, On singularities, local optima, and formation of stiffeners in optimal design of plates, in: Optimization in Structural Design, Springer, 1975, pp. 82-103.

[37] A.R. Díaaz, N. Kikuchi, Solutions to shape and topology eigenvalue optimization problems using a homogenization method, International Journal for Numerical Methods in Engineering, 35 (7) (1992) 1487-1502.

[38] S. Zargham, T.A. Ward, R. Ramli, I.A. Badruddin, Topology optimization: a review for structural designs under vibration problems, Structural and Multidisciplinary Optimization, 53 (6) (2016) 1157-1177.

[39] A.A. Larsen, B. Laksafoss, J.S. Jensen, O. Sigmund, Topological material layout in plates for vibration suppression and wave propagation control, Structural and Multidisciplinary Optimization, 37 (6) (2009) 585-594.

[40] G.H. Yoon, Structural topology optimization for frequency response problem using model reduction schemes, Computer methods in applied mechanics and engineering, 199 (25) (2010) 1744-1763.

[41] J. Du, N. Olhoff, Minimization of Sound Radiation from Vibrating Bi-Material Structures Using Topology Optimization, Structural and Multidisciplinary Optimization, 33 (4-5) (2007) 305-321.

[42] J. Du, N. Olhoff, Topological design of vibrating structures with respect to optimum sound pressure characteristics in a surrounding acoustic medium, Structural and Multidisciplinary Optimization, 42 (1) (2010) 43-54.

[43] L. Shu, M.Y. Wang, Z. Fang, Z. Ma, P. Wei, Level set based structural topology optimization for minimizing frequency response, Journal of sound and vibration, 330 (24) (2011) 5820-5834.

[44] G. Rosi, R. Paccapeli, F. Ollivier, J. Pouget, Optimization of piezoelectric patch positioning for passive sound radiation control of plates, Journal of Vibration and Control, 19 (5) (2013) 658-673.

[45] B. Xu, Y.J. Jin, Multiobjective dynamic topology optimization of truss with interval parameters based on interval possibility degree, Journal of Vibration and Control, (2012).

[46] E. Sabbatini, G.M. Revel, M. Kobayashi, Vibration reduction using biologically inspired topology optimization method: optimal stiffeners distribution on an acoustically excited plate, Journal of Vibration and Control, (2013).

[47] H. Zheng, C. Cai, G.S.H. Pau, G.R. Liu, Minimizing vibration response of cylindrical shells through layout optimization of passive constrained layer damping treatments, Journal of Sound and Vibration, 279 (3-5) (2005) 739-756.

[48] C.M. Chia, J.A. Rongong, K. Worden, Strategies for using cellular automata to locate constrained layer damping on vibrating structures, Journal of Sound and Vibration, 319 (1-2) (2009) 119-139.

[49] Z. Kang, X. Zhang, S. Jiang, G. Cheng, On topology optimization of damping layer

in shell structures under harmonic excitations, Structural and Multidisciplinary Optimization, 46 (1) (2012) 51-67.

[50] X. Zhang, Z. Kang, Topology optimization of damping layers for minimizing sound radiation of shell structures, Journal of sound and vibration, (2013).

[51] S.Y. Kim, C.K. Mechefske, I.Y. Kim, Optimal damping layout in a shell structure using topology optimization, Journal of sound and vibration, (2013).

[52] H. Tzou, C. Tseng, Distributed piezoelectric sensor/actuator design for dynamic measurement/control of distributed parameter systems: a piezoelectric finite element approach, Journal of Sound and Vibration, 138 (1) (1990) 17-34.

[53] S. Hanagud, M. Obal, A. Calise, Optimal vibration control by the use of piezoceramic sensors and actuators, Journal of Guidance, Control, and Dynamics, 15 (5) (1992) 1199-1206.

[54] S. Devasia, T. Meressi, B. Paden, E. Bayo, Piezoelectric actuator design for vibration suppression-placement and sizing, Journal of Guidance, Control, and Dynamics, 16 (5) (1993) 859-864.

[55] D. Sun, L. Tong, Design optimization of piezoelectric actuator patterns for static shape control of smart plates, Smart Materials and Structures, 14 (6) (2005) 1353.

[56] J. Onoda, R.T. Haftka, An approach to structure/control simultaneous optimization for largeflexible spacecraft, AIAA journal, 25 (8) (1987) 1133-1138.

[57] I. Bruant, L. Gallimard, S. Nikoukar, Optimal piezoelectric actuator and sensor location for active vibration control, using genetic algorithm, Journal of Sound and Vibration, 329 (10) (2010) 1615-1635.

[58] N. Darivandi, K. Morris, A. Khajepour, An algorithm for LQ optimal actuator location, Smart Materials and Structures, 22 (3) (2013) 035001.

[59] A. Takezawa, K. Makihara, N. Kogiso, M. Kitamura, Layout optimization methodology of piezoelectric transducers in energy-recycling semi-active vibration control systems, Journal of Sound and Vibration, 333 (2) (2014) 327-344.

[60] G. Rozvany, Aims, scope, methods, history and unified terminology of computer-aided topology optimization in structural mechanics, Structural and Multidisciplinary Optimization, 21 (2) (2001) 90-108.

[61] M. Kögl, E.C. Silva, Topology optimization of smart structures: design of piezoelectric plate and shell actuators, Smart Materials and Structures, 14 (2) (2005) 387.

[62] Z. Kang, L. Tong, Topology optimization-based distribution design of actuation voltage in static shape control of plates, Computers & Structures, 86 (19) (2008) 1885-1893.

[63] E.C.N. Silva, Topology optimization applied to the design of linear piezoelectric motors, Journal of Intelligent Material Systems and Structures, 14 (4-5) (2003) 309-322.

[64] Z. Kang, X. Wang, Topology optimization of bending actuators with multilayer piezoelectric material, Smart Materials and Structures, 19 (7) (2010) 075018.

[65] B. Zheng, C.-J. Chang, H.C. Gea, Topology optimization of energy harvesting devices using piezoelectric materials, Structural and Multidisciplinary Optimization, 38 (1) (2009) 17-23.

[66] C.J. Rupp, A. Evgrafov, K. Maute, M.L. Dunn, Design of piezoelectric energy

harvesting systems: a topology optimization approach based on multilayer plates and shells, Journal of Intelligent Material Systems and Structures, 20 (16) (2009) 1923-1939.

[67] J.Y. Noh, G.H. Yoon, Topology optimization of piezoelectric energy harvesting devices considering static and harmonic dynamic loads, Advances in Engineering Software, 53 (2012) 45-60.

[68] A. Takezawa, M. Kitamura, S. Vatanabe, E. Silva, Design methodology of piezoelectric energy-harvesting skin using topology optimization, Structural and Multidisciplinary Optimization, 49 (2) (2013) 1-17.

[69] J.-S. Ou, N. Kikuchi, Integrated optimal structural and vibration control design, Structural optimization, 12 (4) (1996) 209-216.

[70] E.C.N. Silva, N. Kikuchi, Design of piezoelectric transducers using topology optimization, Smart Materials and Structures, 8 (3) (1999) 350.

[71] S. Wang, K. Tai, S. Quek, Topology optimization of piezoelectric sensors/actuators for torsional vibration control of composite plates, Smart Materials and Structures, 15 (2) (2006) 253.

[72] L. Mello, A. Takezawa, E. Silva, Designing piezoresistive plate-based sensors with distribution of piezoresistive material using topology optimization, Smart Materials and Structures, 21 (8) (2012) 085029.

[73] X. Zhang, Z. Kang, Topology optimization of piezoelectric layers in plates with active vibration control, Journal of Intelligent Material Systems and Structures, 25 (6) (2014) 697-712.

[74] M. Yalcintas, H. Dai, Magnetorheological and electrorheological materials in adaptive structures and their performance comparison, Smart Materials and Structures, 8 (5) (1999) 560.

[75] M. Yalcintas, H. Dai, Vibration suppression capabilities of magnetorheological materials based adaptive structures, Smart Materials and Structures, 13 (2004) 1-11.

[76] Z. Ying, Y. Ni, Micro-vibration response of a stochastically excited sandwich beam with a magnetorheological elastomer core and mass, Smart Materials and Structures, 18 (9) (2009) 095005.

[77] V. Rajamohan, S. Rakheja, R. Sedaghati, Vibration analysis of a partially treated multi-layer beam with magnetorheological fluid, Journal of Sound and Vibration, 329 (17) (2010) 3451-3469.

[78] R. Manoharan, R. Vasudevan, A. Jeevanantham, Dynamic characterization of a laminated composite magnetorheological fluid sandwich plate, Smart Materials and Structures, 23 (2) (2014) 25022-25037.

[79] M. Hoseinzadeh, J. Rezaeepazhand, Vibration suppression of composite plates using smart electrorheological dampers, International Journal of Mechanical Sciences, 84 (2014) 31-40.

[80] J.-Y. Yeh, Vibration analysis of sandwich rectangular plates with magnetorheological elastomer damping treatment, Smart Materials and Structures, 22 (3) (2013) 035010.

[81] G. Haiqing, L.M. King, T.B. Cher, Influence of a locally applied electro-rheological fluid layer on vibration of a simple cantilever beam, Journal of Intelligent Material Systems

and Structures, 4 (3) (1993) 379-384.

[82] G. Haiqing, L.M. King, Vibration characteristics of sandwich beams partially and fully treated with electro-rheological fluid, Journal of Intelligent Material Systems and Structures, 8 (5) (1997) 401-413.

[83] J. Snamina, Optimal location of an active segment of magnetorheological fluid layer in a sandwich plate, in: Carpathian Control Conference (ICCC), 2011 12th International, IEEE, 2011, pp. 362-365.

[84] V. Rajamohan, R. Sedaghati, S. Rakheja, Optimum design of a multilayer beam partially treated with magnetorheological fluid, Smart Materials and Structures, 19 (6) (2010) 065002.

[85] X. Zhang, Z. Kang, Topology optimization of magnetorheological fluid layers in sandwich plates for semi-active vibration control, Smart Materials and Structures, 24 (8) (2015) 085024.

[86] J.W. Lee, Y.Y. Kim, Topology optimization of muffler internal partitions for improving acoustical attenuation performance, International Journal for Numerical Methods in Engineering, 80 (4) (2009) 455-477.

[87] D. Richards, D.J. Pines, Passive reduction of gear mesh vibration using a periodic drive shaft, Journal of Sound and Vibration, 264 (2) (2003) 317-342.

[88] A. Khelif, A. Choujaa, S. Benchabane, B. Djafari-Rouhani, V. Laude, Guiding and bending of acoustic waves in highly confined phononic crystal waveguides, Applied Physics Letters, 84 (22) (2004) 4400-4402.

[89] B.I. Popa, L. Zigoneanu, S.A. Cummer, Experimental Acoustic Ground Cloak in Air, Physical Review Letters, 106 (25) (2011) 253901.

[90] L.-Y. Zheng, Y. Wu, X. Ni, Z.-G. Chen, M.-H. Lu, Y.-F. Chen, Acoustic cloaking by a near-zero-index phononic crystal, Applied Physics Letters, 104 (16) (2014) 161904.

[91] R. Martinezsala, J. Sancho, J.V. Sánchez, V. Gómez, J. Llinares, F. Meseguer, Sound-attenuation by sculpture, Nature, 378 (6554) (1995) 241-241.

[92] Z. Liu, X. Zhang, Y. Mao, Y. Zhu, Z. Yang, C. Chan, P. Sheng, Locally resonant sonic materials, Science, 289 (5485) (2000) 1734-1736.

[93] O.B. Wright, O. Matsuda, Watching surface waves in phononic crystals, Phil. Trans. R. Soc. A, 373 (2049) (2015) 20140364.

[94] J.H. Oh, Y.E. Kwon, H.J. Lee, Y.Y. Kim, Elastic metamaterials for independent realization of negativity in density and stiffness, Scientific reports, 6 (2016).

[95] M. Farhat, S. Enoch, S. Guenneau, A. Movchan, Broadband cylindrical acoustic cloak for linear surface waves in a fluid, Physical Review Letters, 101 (13) (2008) 134501.

[96] L. Zigoneanu, B.-I. Popa, S.A. Cummer, Three-dimensional broadband omnidirectional acoustic ground cloak, Nature Materials, 13 (4) (2014) 352-355.

[97] J.S. Jensen, Phononic band gaps and vibrations in one-and two-dimensional mass–spring structures, Journal of Sound and Vibration, 266 (5) (2003) 1053-1078.

[98] V.M. García-Chocano, L. Sanchis, A. Díaz-Rubio, J. Martínez-Pastor, F. Cervera, R. Llopis-Pontiveros, J. Sánchez-Dehesa, Acoustic cloak for airborne sound by inverse design,

Applied Physics Letters, 99 (7) (2011) 074102.

[99] C.J. Rupp, A. Evgrafov, K. Maute, M.L. Dunn, Design of phononic materials/structures for surface wave devices using topology optimization, Structural and Multidisciplinary Optimization, 34 (2) (2007) 111-121.

[100] Z.-F. Liu, B. Wu, C.-F. He, Systematic topology optimization of solid–solid phononic crystals for multiple separate band-gaps with different polarizations, Ultrasonics, 65 (2016) 249-257.

[101] Y. Chen, S. Zhou, Q. Li, Multiobjective topology optimization for finite periodic structures, Computers & Structures, 88 (11) (2010) 806-811.

[102] G. Yi, B.D. Youn, A comprehensive survey on topology optimization of phononic crystals, Structural and Multidisciplinary Optimization, 54 (5) (2016) 1315-1344.

[103] O. Sigmund, J.S. Jensen, Systematic design of phononic band–gap materials and structures by topology optimization, Philosophical Transactions of the Royal Society of London A: Mathematical, Physical and Engineering Sciences, 361 (1806) (2003) 1001-1019.

[104] M.I. Hussein, K. Hamza, G.M. Hulbert, R.A. Scott, K. Saitou, Multiobjective evolutionary optimization of periodic layered materials for desired wave dispersion characteristics, Structural and Multidisciplinary Optimization, 31 (1) (2006) 60-75.

[105] H.-W. Dong, X.-X. Su, Y.-S. Wang, C. Zhang, Topological optimization of two-dimensional phononic crystals based on the finite element method and genetic algorithm, Structural and Multidisciplinary Optimization, 50 (4) (2014) 593-604.

[106] H.-W. Dong, X.-X. Su, Y.-S. Wang, Multi-objective optimization of two-dimensional porous phononic crystals, Journal of Physics D: Applied Physics, 47 (15) (2014) 155301.

[107] Y. fan Li, X. Huang, F. Meng, S. Zhou, Evolutionary topological design for phononic band gap crystals, Structural and Multidisciplinary Optimization, 54 (3) (2016) 595-617.

[108] Y.F. Li, X. Huang, S. Zhou, Topological design of cellular phononic band gap crystals, Materials, 9 (3) (2016) 186.

[109] S. Hedayatrasa, M. Kersemans, K. Abhary, M. Uddin, J.K. Guest, W. Van Paepegem, Maximizing bandgap width and in-plane stiffness of porous phononic plates for tailoring flexural guided waves: Topology optimization and experimental validation, Mechanics of Materials, 105 (2017) 188-203.

[110] J. Dahl, J.S. Jensen, O. Sigmund, Topology optimization for transient wave propagation problems in one dimension, Structural and Multidisciplinary Optimization, 36 (6) (2008) 585-595.

[111] J. He, Z. Kang, Achieving directional propagation of elastic waves via topology optimization, Ultrasonics, 82 (2018) 1-10.

[112] A. Asadpoure, M. Tootkaboni, L. Valdevit, Topology optimization of multiphase architected materials for energy dissipation, Computer Methods in Applied Mechanics and Engineering, 325 (2017) 314-329.

[113] J.H. Park, P.S. Ma, Y.Y. Kim, Design of phononic crystals for self-collimation of elastic waves using topology optimization method, Structural and Multidisciplinary Optimization, 51 (6) (2015) 1199-1209.

[114] R.C. Carbonari, E.C. Silva, G.H. Paulino, Multi‐actuated functionally graded piezoelectric micro‐tools design: A multiphysics topology optimization approach, International Journal for Numerical Methods in Engineering, 77 (3) (2009) 301-336.

[115] Z. Kang, R. Wang, L. Tong, Combined optimization of bi-material structural layout and voltage distribution for in-plane piezoelectric actuation, Computer Methods in Applied Mechanics and Engineering, 200 (13) (2011) 1467-1478.

[116] D. Ruiz, J. Bellido, A. Donoso, J. Sánchez-Rojas, Design of in-plane piezoelectric sensors for static response by simultaneously optimizing the host structure and the electrode profile, Structural and Multidisciplinary Optimization, 48 (5) (2013) 1023-1026.

[117] L.A.M. Mello, C.Y. Kiyono, P.H. Nakasone, E.C.N. Silva, Design of quasi-static piezoelectric plate based transducers by using topology optimization, Smart Materials and Structures, 23 (2) (2014) 025035.

[118] A. Donoso, O. Sigmund, Optimization of piezoelectric bimorph actuators with active damping for static and dynamic loads, Structural and Multidisciplinary Optimization, 38 (2) (2009) 171-183.

[119] X. Zhang, Z. Kang, Dynamic topology optimization of piezoelectric structures with active control for reducing transient response, Computer Methods in Applied Mechanics and Engineering, 281 (2014) 200-219.

[120] D.M. Frangopol, R.B. Corotis, Reliability-based structural system optimization: state-of-the-art versus state-of-the-practice, in: Analysis and Computation (1996), ASCE, 1996, pp. 67-78.

[121] M. Papadrakakis, N.D. Lagaros, Reliability-based structural optimization using neural networks and Monte Carlo simulation, Computer Methods in Applied Mechanics and Engineering, 191 (32) (2002) 3491-3507.

[122] I. Doltsinis, Z. Kang, Robust design of structures using optimization methods, Computer Methods in Applied Mechanics and Engineering, 193 (23) (2004) 2221-2237.

[123] H.-G. Beyer, B. Sendhoff, Robust optimization–a comprehensive survey, Computer Methods in Applied Mechanics and Engineering, 196 (33) (2007) 3190-3218.

[124] B.S. Lazarov, M. Schevenels, O. Sigmund, Topology optimization considering material and geometric uncertainties using stochastic collocation methods, Structural and Multidisciplinary optimization, 46 (4) (2012) 597-612.

[125] M. Tootkaboni, A. Asadpoure, J.K. Guest, Topology optimization of continuum structures under uncertainty–A Polynomial Chaos approach, Computer Methods in Applied Mechanics and Engineering, 201 (2012) 263-275.

[126] N. Kogiso, W. Ahn, S. Nishiwaki, K. Izui, M. Yoshimura, Robust topology optimization for compliant mechanisms considering uncertainty of applied loads, Journal of Advanced Mechanical Design, Systems, and Manufacturing, 2 (1) (2008) 96-107.

[127] P.D. Dunning, H.A. Kim, Robust topology optimization: Minimization of expected and variance of compliance, AIAA journal, 51 (11) (2013) 2656-2664.

[128] J. Zhao, C. Wang, Robust structural topology optimization under random field loading uncertainty, Structural and Multidisciplinary Optimization, 50 (3) (2014) 517-522.

[129] J. Liu, G. Wen, Y.M. Xie, Layout optimization of continuum structures considering

the probabilistic and fuzzy directional uncertainty of applied loads based on the cloud model, Structural and Multidisciplinary Optimization, (2015) 1-20.

[130] M. Jalalpour, M. Tootkaboni, An efficient approach to reliability-based topology optimization for continua under material uncertainty, Structural and Multidisciplinary Optimization, 53 (4) (2016) 759-772.

[131] N. Changizi, M. Jalalpour, Robust topology optimization of frame structures under geometric or material properties uncertainties, Structural and Multidisciplinary Optimization, 56 (4) (2017) 791-807.

[132] J. Wu, J. Gao, Z. Luo, T. Brown, Robust topology optimization for structures under interval uncertainty, Advances in Engineering Software, 99 (2016) 36-48.

[133] J. Wu, Z. Luo, H. Li, N. Zhang, Level-set topology optimization for mechanical metamaterials under hybrid uncertainties, Computer Methods in Applied Mechanics and Engineering, 319 (2017) 414-441.

[134] J.K. Guest, T. Igusa, Structural optimization under uncertain loads and nodal locations, Computer Methods in Applied Mechanics and Engineering, 198 (1) (2008) 116-124.

[135] G. Kharmanda, N. Olhoff, A. Mohamed, M. Lemaire, Reliability-based topology optimization, Structural and Multidisciplinary Optimization, 26 (5) (2004) 295-307.

[136] K. Maute, D.M. Frangopol, Reliability-based design of MEMS mechanisms by topology optimization, Computers & Structures, 81 (8) (2003) 813-824.

[137] S. Chen, W. Chen, S. Lee, Level set based robust shape and topology optimization under random field uncertainties, Structural and Multidisciplinary Optimization, 41 (4) (2010) 507-524.

[138] M. Schevenels, B.S. Lazarov, O. Sigmund, Robust topology optimization accounting for spatially varying manufacturing errors, Computer Methods in Applied Mechanics and Engineering, 200 (49-52) (2011) 3613-3627.

[139] V. Keshavarzzadeh, H. Meidani, D.A. Tortorelli, Gradient based design optimization under uncertainty via stochastic expansion methods, Computer Methods in Applied Mechanics and Engineering, 306 (2016) 47-76.

[140] V. Keshavarzzadeh, F. Fernandez, D.A. Tortorelli, Topology optimization under uncertainty via non-intrusive polynomial chaos expansion, Computer Methods in Applied Mechanics and Engineering, 318 (2017) 120-147.

[141] Y. Ben-Haim, I. Elishakoff, Convex models of uncertainty in applied mechanics, Elsevier Science, 198 (1990).

[142] Y. Luo, Z. Kang, A. Li, Structural reliability assessment based on probability and convex set mixed model, Computers & Structures, 87 (21) (2009) 1408-1415.

[143] M. Lombardi, R.T. Haftka, Anti-optimization technique for structural design under load uncertainties, Computer Methods in Applied Mechanics and Engineering, 157 (1) (1998) 19-31.

[144] H.-S. Jung, S. Cho, Reliability-based topology optimization of geometrically nonlinear structures with loading and material uncertainties, Finite elements in analysis and design, 41 (3) (2004) 311-331.

[145] G. Cheng, L. Xu, L. Jiang, A sequential approximate programming strategy for

reliability-based structural optimization, Computers & Structures, 84 (21) (2006) 1353-1367.

[146] E. Cherkaev, A. Cherkaev, Minimax optimization problem of structural design, Computers & Structures, 86 (13) (2008) 1426-1435.

[147] A. Takezawa, S. Nii, M. Kitamura, N. Kogiso, Topology optimization for worst load conditions based on the eigenvalue analysis of an aggregated linear system, Computer Methods in Applied Mechanics and Engineering, 200 (25) (2011) 2268-2281.

[148] K. Brittain, M. Silva, D.A. Tortorelli, Minmax topology optimization, Structural and Multidisciplinary Optimization, 45 (5) (2012) 657-668.

[149] M. Kocvara, On Robustness Criteria and Robust Topology Optimization with Uncertain Loads, arXiv preprint arXiv:1307.7547, (2013).

[150] X. Zhao, W. Song, H.C. Gea, L. Xu, Topology Optimization With Unknown-but-Bounded Load Uncertainty, in: ASME 2014 International Design Engineering Technical Conferences and Computers and Information in Engineering Conference, American Society of Mechanical Engineers, 2014, pp. V02BT03A053-V002BT003A053.

[151] P.D. Dunning, H.A. Kim, G. Mullineux, Introducing loading uncertainty in topology optimization, AIAA journal, 49 (4) (2011) 760-768.

[152] Z. Kang, W. Zhang, Construction and application of an ellipsoidal convex model using a semi-definite programming formulation from measured data, Computer Methods in Applied Mechanics and Engineering, 300 (2016) 461-489.

[153] H. Liu, W. Zhang, T. Gao, A comparative study of dynamic analysis methods for structural topology optimization under harmonic force excitations, Structural and Multidisciplinary Optimization, 51 (6) (2015) 1321-1333.

[154] N. Olhoff, J. Du, Topological design for minimum sound emission from structures under forced vibration, in: Topology Optimization in Structural and Continuum Mechanics, Springer, 2014, pp. 341-357.

[155] Z.-D. Ma, N. Kikuchi, I. Hagiwara, Structural topology and shape optimization for a frequency response problem, Computational mechanics, 13 (3) (1993) 157-174.

[156] A. Takezawa, M. Daifuku, Y. Nakano, K. Nakagawa, T. Yamamoto, M. Kitamura, Topology optimization of damping material for reducing resonance response based on complex dynamic compliance, Journal of Sound and Vibration, 365 (2016) 230-243.

[157] G.H. Golub, Some modified matrix eigenvalue problems, Siam Review, 15 (2) (1973) 318-334.

[158] R.M. Mattheij, G. Söderlind, On inhomogeneous eigenvalue problems. I, Linear Algebra and its Applications, 88 (1987) 507-531.

[159] C.-J. Thore, E. Holmberg, A. Klarbring, Large-scale robust topology optimization under load-uncertainty, in: Proceedings, 11th World Congress on Structural and Multidisciplinary Optimization, 2015.

[160] G. Kreisselmeier, R. Steinhauser, Systematische Auslegung von Reglern durch Optimierung eines vektoriellen Gütekriteriums/Systematic controller design by optimization of a vector performance index, at-Automatisierungstechnik, 27 (1-12) (1979) 76-79.

[161] N.M. Poon, J.R. Martins, An adaptive approach to constraint aggregation using adjoint sensitivity analysis, Structural and Multidisciplinary Optimization, 34 (1) (2007) 61-73.

[162] K. Svanberg, A Class of Globally Convergent Optimization Methods Based on Conservative Convex Separable Approximations, SIAM Journal on Optimization, 12 (2) (2002) 555-573.

[163] J. Schwerdtfeger, P. Heinl, R. Singer, C. Körner, Auxetic cellular structures through selective electron‑beam melting, physica status solidi (b), 247 (2) (2010) 269-272.

[164] N. Zen, T.A. Puurtinen, T.J. Isotalo, S. Chaudhuri, I.J. Maasilta, Engineering thermal conductance using a two-dimensional phononic crystal, Nature Communications, 5 (2014) 3435.

[165] O. Sigmund, Manufacturing tolerant topology optimization, Acta Mechanica Sinica, 25 (2) (2009) 227-239.

[166] L. Xie, B. Xia, G. Huang, J. Lei, J. Liu, Topology optimization of phononic crystals with uncertainties, Structural and Multidisciplinary Optimization, (2017) 1-21.

[167] G. Kreisselmeier, R. Steinhauser, Systematic control design by optimizing a vector performance index, IFAC Proceedings Volumes, 12 (7) (1979) 113-117.

[168] C.-C. Li, A. Der Kiureghian, Optimal discretization of random fields, Journal of Engineering Mechanics, 119 (6) (1993) 1136-1154.

[169] R.G. Ghanem, P.D. Spanos, Stochastic finite elements: a spectral approach, Courier Corporation, 2003.

[170] D. Xiu, G.E. Karniadakis, The Wiener--Askey Polynomial Chaos for Stochastic Differential Equations, SIAM Journal on Scientific Computing, 24 (2) (2002) 619-644.

[171] F. Heiss, V. Winschel, Likelihood approximation by numerical integration on sparse grids, Journal of Econometrics, 144 (1) (2008) 62-80.

[172] J.S. Jensen, N.L. Pedersen, On maximal eigenfrequency separation in two-material structures: the 1D and 2D scalar cases, Journal of Sound and Vibration, 289 (4) (2006) 967-986.

[173] A. Diaz, A. Haddow, L. Ma, Design of band-gap grid structures, Structural and Multidisciplinary Optimization, 29 (6) (2005) 418-431.

[174] J.S. Jensen, Topology optimization problems for reflection and dissipation of elastic waves, Journal of Sound Vibration, 301 (2007) 319-340.

[175] I. Doltsinis, Z. Kang, Robust design of structures using optimization methods, Computer Methods in Applied Mechanics and Engineering, 23 (193) (2004) 2221-2237.

[176] S. Xu, Y. Cai, G. Cheng, Volume preserving nonlinear density filter based on heaviside functions, Structural and Multidisciplinary Optimization, 41 (4) (2010) 495-505.

[177] J. Du, N. Olhoff, Topological design of freely vibrating continuum structures for maximum values of simple and multiple eigenfrequencies and frequency gaps, Structural and Multidisciplinary Optimization, 34 (2) (2007) 91-110.

[178] H.-W. Dong, X.-X. Su, Y.-S. Wang, C. Zhang, Topology optimization of two-dimensional asymmetrical phononic crystals, Physics Letters A, 378 (4) (2014) 434-441.

[179] S.M. Allen, J.W. Cahn, A microscopic theory for antiphase boundary motion and its application to antiphase domain coarsening, Acta Metallurgica, 27 (6) (1979) 1085-1095.

[180] Z.-D. Ma, N. Kikuchi, H.-C. Cheng, Topological design for vibrating structures,

Comput. Methods Appl. Mech. Engrg, 121 (1995) 259-280.

[181] K. Yan, G. Cheng, B.P. Wang, Topology optimization of plate structures subject to initial excitations for minimum dynamic performance index, Structural and Multidisciplinary Optimization, 53 (3) (2016) 623-633.

[182] R. Kobayashi, Modeling and numerical simulations of dendritic crystal growth, Physica D: Nonlinear Phenomena, 63 (3-4) (1993) 410-423.

[183] U. Aridogan, I. Basdogan, A review of active vibration and noise suppression of plate-like structures with piezoelectric transducers, Journal of Intelligent Material Systems and Structures, 26 (12) (2015) 1455-1476.

[184] C. Wallenhauer, A. Kappel, B. Gottlieb, T. Schwebel, T. Lüth, Efficient class-B analog amplifier for a piezoelectric actuator drive, Mechatronics, 19 (1) (2009) 56-64.

[185] F. Peng, A. Ng, Y.-R. Hu, Actuator placement optimization and adaptive vibration control of plate smart structures, Journal of Intelligent Material Systems and Structures, 16 (3) (2005) 263-271.

[186] B. Xu, J. Jiang, J. Ou, Integrated optimization of structural topology and control for piezoelectric smart trusses using genetic algorithm, Journal of Sound and Vibration, 307 (3) (2007) 393-427.

[187] M.C. Brennan, A.-M.R. McGowan, Piezoelectric power requirements for active vibration control, in: Smart Structures and Materials' 97, International Society for Optics and Photonics, 1997, pp. 660-669.

[188] A. Mukherjee, S. Joshi, Design of actuator profiles for minimum power consumption, Smart Materials and Structures, 10 (2) (2001) 305.

[189] K. Chevva, F. Sun, A. Blanc, J. Mendoza, Active vibration control using minimum actuation power, Journal of Sound and Vibration, 340 (2015) 1-21.

[190] N.D. Zorić, A.M. Simonović, Z.S. Mitrović, S.N. Stupar, Optimal vibration control of smart composite beams with optimal size and location of piezoelectric sensing and actuation, Journal of Intelligent Material Systems and Structures, (2012) 1045389X12463465.

[191] J.F. Gonçalves, D.M. De Leon, E.A. Perondi, Topology optimization of embedded piezoelectric actuators considering control spillover effects, Journal of Sound and Vibration, 388 (2017) 20-41.

[192] J. Hu, X. Zhang, Z. Kang, Layout design of piezoelectric patches in structural LQR optimal control using topology optimization, Submitted, (2017).

[193] Z.-D. Ma, N. Kikuchi, H.-C. Cheng, Topological design for vibrating structures, Computer Methods in Applied Mechanics and Engineering, 121 (1) (1995) 259-280.

[194] Z. Kang, L. Tong, Integrated optimization of material layout and control voltage for piezoelectric laminated plates, Journal of Intelligent Material Systems and Structures, (2008).

[195] G.H. Yoon, Acoustic topology optimization of fibrous material with Delany–Bazley empirical material formulation, Journal of Sound and Vibration, 332 (5) (2013) 1172-1187.

[196] O. Sigmund, S. Torquato, Design of materials with extreme thermal expansion using a three-phase topology optimization method, in: Smart Structures and Materials' 97, International Society for Optics and Photonics, 1997, pp. 52-60.

Publications

International Journal Papers (SCI Papers)

[1] Xiaopeng Zhang, Jingjie He, Zhan Kang, Akihiro Takezawa.. Robust topology optimization of phononic crystals with random field uncertainty. International Journal for Numerical Methods in Engineering, (2018). DOI: 10.1002/nme.5839. SCI, IF: 2.162 (Chapter 3)

[2] Xiaopeng Zhang, Zhan Kang, Akihiro Takezawa. Topology optimization of piezoelectric smart structures for minimum energy consumption under active control. Structural and Multidisciplinary Optimization, (2017) DOI: 10.1007/s00158-017-1886-y. SCI. IF: 2.377. (Chapter 6)

[3] **Xiaopeng Zhang**, Zhan Kang, Wenbo Zhang. Robust topology optimization for dynamic compliance minimization under uncertain harmonic excitations with inhomogeneous eigenvalue analysis. Structural and Multidisciplinary Optimization, 54(2016): 1469-1484. SCI. IF: 2.377. (Chapter 2)

[4] **Xiaopeng Zhang**, Akihiro Takezawa, Zhan Kang. Robust topology optimization of vibrating structures considering random diffuse regions via a phase-field method. Submitted. (Chapter 4)

[5] Jun Hu, **Xiaopeng Zhang**, Zhan Kang. Layout design of piezoelectric patches in structural LQR optimal control using topology optimization. Journal of Intelligent Material Systems and Structures, (2018): DOI: 10.1177/1045389X18758178. SCI. IF: 2.255. (Chapter 6)

[6] Akihiro Takezawa, Koshi Takenaka, **Xiaopeng Zhang.** Inverse analysis of giant macroscopic negative thermal expansion of Ca2RuO4−y ceramics based on elasticity and structural topology optimization. Applied Physics Express,11.5 (2018): 055801. SCI.

IF:2.667.

[7] Akihiro Takezawa, Kazuo Yonekura, Yuichiro Koizumi, **Xiaopeng Zhang**, Mitsuru Kitamura. Isotropic Ti-6Al-4V lattice via topology optimization and electron beam melting, Additive Manufacturing (2018), in press.

[8] Zhijun Liu, Shingo Cho, Akihiro Takezawa, **Xiaopeng Zhang**, Mitsuru Kitamura. Two-stage layout–size optimization method for prow stiffeners. International Journal of Naval Architecture and Ocean Engineering (2018). SCI. IF:0.606.

Conference Papers

[1] **Xiaopeng Zhang** (Reporter), Zhan Kang, Akihiro Takezawa. Topology optimization of piezoelectric structures for minimum power consumption with active control. 1 Asian Congress of Structural and Multidisciplinary Optimization 2018. 2018.5.10-5.24, Dalian, China.

[2] **Xiaopeng Zhang** (Reporter), Akihiro Takezawa, Zhan Kang. Robust topology optimization of phononic crystals considering material properties uncertainty during manufacturing process. 10th European Solid Mechanics Conference. 2018.7.2-7.6, Bologna, Italy.

[3] **Xiaopeng Zhang** (Reporter), Zhan Kang, Akihiro Takezawa. Structural robust topology optimization under uncertain dynamic loads. 12th World Congress on Structural and Multidisciplinary Optimization. 2017.6.5-6.9, Braunschweig, Germany.

[4] **Xiaopeng Zhang** (Reporter), Akihiro Takezawa, Zhan Kang. Layout optimization of magnet-orheological fluid patches in plate structures by using semi-active control. 14th U.S. National Congress on Computational Mechanics. 2017.7.17-7.20, Montréal, Canada.